SCALING APPROACH AND THERMAL-HYDRAULIC ANALYSIS IN THE REACTOR CAVITY COOLING SYSTEM OF A HIGH TEMPERATURE GAS –COOLED REACTOR AND THERMAL-JET MIXING IN A SODIUM FAST REACTOR

A Dissertation

Presented in Partial Fulfillment of the Requirements for the

Degree of Doctor of Philosophy

with a

Major in Nuclear Engineering

in the

College of Graduate Studies

University of Idaho

by

Olumuyiwa A. Omotowa

March 2014

Major Professor: Akira Tokuhiro, Ph.D.

AUTHORIZATION TO SUBMIT DISSERTATION

This dissertation of Olumuyiwa A. Omotowa, submitted for the degree of Doctor of Philosophy, with a major in Nuclear Engineering and titled "Scaling Approach and Thermal-hydraulic Analysis in the Reactor Cavity Cooling System of a High Temperature Gas–Cooled Reactor and Thermal-Jet Mixing in a Sodium Fast Reactor" has been reviewed in final form. Permission, as indicated by the signatures and dates given below is now granted for submission of final copies to the College of Graduate Studies for approval.

Major Professor:

_____ Date_____
Prof. Akira T. Tokuhiro

Committee Members:

_____ Date: _____
Prof. Vivek Utgikar

_____ Date: _____
Prof. Will Zimmerman

_____ Date: _____
Prof. Jason Harris

Department Chair:

_____ Date: _____
Prof. John Crepeau

Dean of Engineering:

_____ Date: _____
Prof. Larry Stauffer

Final Approval and Acceptance by the College of Graduate Studies:

_____ Date: _____
Prof. Jie Chen

ABSTRACT

This dissertation develops and demonstrates the application of the top-down and bottom-up scaling methodologies to thermal-hydraulic flows in the reactor cavity cooling system (RCCS) of the high temperature gas reactor (HTGR) and upper plenum of the sodium fast reactor (SFR), respectively. The need to integrate scaled separate effects and integral tests was identified. Experimental studies and computational tools (CFD) have been integrated to guide the engineering design, analysis and assessment of this scaling methods under single and two-phase flow conditions. To test this methods, two applicable case studies are considered, and original contributions are noted.

Case 1: "Experimental Study of RCCS for the HTGR". Contributions include validation of scaling analysis using the top-down approach as guide to a ¼-scale integral test facility. System code, RELAP5, was developed based on the derived scaling parameters. Tests performed included system sensitivity to decay heat load and heat sink inventory variations. System behavior under steady-state and transient scenarios were predicted. Results show that the system has the capacity to protect the cavity walls from over-heating during normal operations and provide a means for decay heat removal under accident scenarios. A full width half maximum statistical method was devised to characterize the thermal-hydraulics of the non-linear two-phase oscillatory behavior. This facilitated understanding of the thermal hydraulic coupling of the loop segments of the RCCS, the heat transfer, and the two-phase flashing flow phenomena; thus the impact of scaling overall.

Case 2: “Computational Studies of Thermal Jet Mixing in SFR”. In the pool-type SFR, susceptible regions to thermal striping are the upper instrumentation structure and the intermediate heat exchanger (IHX). We investigated the thermal mixing above the core to UIS and the potential impact due to poor mixing. The thermal mixing of dual-jet flows at different temperatures and velocities were investigated using COMSOL CFD. CFD simulations show that the flow field is characterized into three regions, and the phenomenon is momentum dominated, thus poor mixing. Thus, the lack of thermal mixing showed CFD can be used as a tool for scaling. Scaling of the SFR pool, IHX and pumps will be important at integral and full-scale.

ACKNOWLEDGEMENTS

Grant for this research work was provided under the US Department of Energy's (US DOE) Nuclear Energy University Programs (NEUP) 09-202 and 09-321(Agreement number 193K340 and contract number DE-AC07-051D14517 respectively). Special thanks to my major advisor Prof. Akira Tokuhiro for his assistance, insightful discussions and encouragement during the course of my research work. Thanks also to my committee members, Prof. Vivek Utgikar, Prof. Will Zimmerman (University of Sheffield, UK), and Prof. Jason Harris (Idaho State University) for their valuable contributions.

To my host at the University of Wisconsin-Madison during my research fellowship, Prof. Mike Corradini and Prof. Mark Anderson, I wish to say thank you. To my friend and colleague Darius Lisowski, your contributions, dedication, long days and nights in the laboratory while experiments were on-going are most appreciated.

I would also like to thank Alice Allen, Debbie Caudle, Sara Moore, Jeff Barnes and all my colleagues in Dr. Akira Tokuhiro's research group especially Richard Skifton and John Downing for their support throughout my academic years in Idaho Falls.

TABLE OF CONTENTS

AUTHORIZATION TO SUBMIT DISSERTATION ..... **ii**

ABSTRACT ..... **iii**

ACKNOWLEDGEMENTS ..... **v**

LIST OF FIGURES ..... **ix**

LIST OF TABLES ..... **xiv**

ACRONYMS AND ABBREVIATIONS ..... **xvi**

NOMENCLATURE ..... **xx**

GREEK SYMBOLS ..... **xxiii**

SUBSCRIPTS ..... **xxiv**

DIMENSIONLESS QUANTITIES ..... **xxv**

CHAPTER 1: INTRODUCTION **1**

1.1. MOTIVATION 10

CHAPTER 2: LITERATURE REVIEW **12**

2.1. SCALING ANALYSIS 12
2.1.1. Empirical Approach 13
2.1.2. Analytical Approach 14
2.1.3. Top-Down Scaling 15
2.1.4. Bottom-up Scaling 16
2.2. INTEGRAL TEST FACILITIES (ITF) 17
2.2.1. Multi-Application Small Light Water Reactor (MASLWR): 18
2.2.2. Passive decay heat removal Assembly (PANDA) 20
2.2.3. Purdue University Multi-Dimensional Integral Test Assembly (PUMA) 21
2.3. SEPARATE EFFECT TESTS (SETS) 26
2.3.1. PAFS Condensation Heat Removal Assessment Loop (PASCAL) 26
2.4. RESEARCH OBJECTIVES 28

CHAPTER 3: NGNP-VHTR CONCEPT- REACTOR CAVITY COOLING SYSTEM **30**

3.1. REACTOR CAVITY COOLING SYSTEM (RCCS) 33
3.1.1. Description 33
3.1.2. Prototype (Conceptual Design) Description 36
Normal Operations 39

3.2. SCALING APPROACH 42
3.2.1. Scaling Methodology (UW-RCCS Test Facility) 42
3.2.2. Similarity Parameters: 48
3.3. SCALED WATER-COOLED RCCS TEST FACILITY 53
3.3.1. Facility Description: 53
3.3.2. Thermal Insulation 58
3.3.3. Instrumentation 60
3.3.3.1. Thermocouples 60
3.3.3.2. Optical Phase Sensor (RBI) 62
OPERATING PRINCIPLE 65
3.3.3.3. Magnetic Flow Meter 72
3.3.4. Data Acquisition System 74
3.3.5. Modeling and Simulation (RELAP5) 75

CHAPTER 4: RCCS EXPERIMENTAL PROCEDURE 78

4.1. OVERVIEW: ESTABLISHED EXPERIMENTAL PROCEDURE 78
4.1.1. Single Phase – Steady-State Tests 79
4.1.2. Two-Phase Transient Tests 82
4.1.2.1. Two-phase Baseline Conditions 85

CHAPTER 5: MIXING IN UPPER PLENUM OF ADVANCED FAST REACTORS 87

5.1. TURBULENCE MODELING 97
5.1.1. Overview: 97
5.1.2. Turbulence Models: 100
5.1.2.1. K-ε Turbulence Model: 104
5.2. BENCHMARK STUDIES: MODEL DESCRIPTION 105
5.2.1. Single-Jet Benchmark: 105
5.2.2. Two-Jet benchmark: 113
5.3. SCALING APPROACH 116

CHAPTER 6: RESULTS AND DISCUSSION 120

6.1. EXPERIMENTAL THERMAL-HYDRAULIC ANALYSIS OF A SCALED RCCS 120
6.1.1. Baseline Conditions (80% tank volume, 15.19 kW decay power) 121
6.1.2. Influence and Effect of Varying Decay Heat Load 126
6.1.3. Influence and Effect of Varying Storage Tank Inventory 136
6.1.4. Influence and Effect of Accelerated Tank Depletion 139
6.2. NUMERICAL THERMAL-HYDRAULIC ANALYSIS OF TURBULENT MIXING IN SFR 141
6.2.1. Baseline Thermo-fluid Simulation: Iso-velocity and Iso-thermal 142
6.2.2. Effect of Temperature on Sodium Turbulent Mixing 144
6.2.4. Effect of Velocity Ratios on Thermal Field 148

6.2.5. Effect of Jet Spacing 151

CHAPTER 7: CONCLUSIONS 154

6.3. THERMAL-HYDRAULIC PERFORMANCE OF THE REACTOR CAVITY COOLING SYSTEM 154
6.4. MODELING OF TURBULENT MIXING IN UPPER PLENUM OF SODIUM FAST REACTORS 157

REFERENCES: 161

APPENDIX A: NEUP-09-202 PROPOSAL 167

APPENDIX B: NEUP-09-202 PROPOSAL 178

APPENDIX C: RCCS EXPERIMENTAL RESULTS 192

APPENDIX D: PUBLICATIONS 199

LIST OF FIGURES

Figure 1-1: Gen-IV Nuclear Systems Roadmap....3

Figure 1-2: Six innovative designs under the Gen-IV Initiative 5

Figure 2-1: Schematic of hierarchical scaling approach for complex systems [adapted from Zuber (1991)]....12

Figure 2-2: External view of the full-scale R4 Marviken Power Plant....18

Figure 2-3: Side view of OSU-MASLWR Test Facility....19

Figure 2-4: Internal view of the PANDA Test Facility....21

Figure 2-5: Top-down view of the PUMA Test Facility....23

Figure 2-6: Integrated scaling approach for integral and separate effect thermal-hydraulic tests for nuclear systems design....25

Figure 2-7: Schematic diagram of the Korean Advanced Power Reactor passive auxiliary feed-water system....27

Figure 2-8: Relevance of scaling to thermal-hydraulic flows in two different nuclear systems....29

Figure 3-1: Schematic Diagram of the Proposed HTGR (NUREG/CR/6944)....31

Figure 3-2: Flow path of the water in the RCCS during active mode of operation (NGNP, 2008)....34

Figure 3-3: Flow path of the water in the RCCS during passive mode of operation (NGNP, 2008)....35

Figure 3-4: General arrangement of Water-Cooled RCCS components (NGNP, 2008)....37

Figure 3-5: Arrangement of A and B trains of water storage tanks, overhead headers for steam release, water inlet to the tank and outlet through the downcomer and piping network for sub-cooled and hot fluid (NGNP, 2008)....38

Figure 3-6: Drawing of the pipe network for a Water RCCS System Configuration..39

Figure 3-7: Reactor power and RCCS heat removal following a design basis accident [HTGR-86-024]....41

Figure 3-8: Sketch illustrates the cold and hot legs described in the integral momentum equation above.....50

Figure 3-9: 5° wedges from the RPV to the concrete wall (*inse*t: risers lining the walls of concrete wall).....54

Figure 3-10: Schematic of a Scaled Water-Cooled RCCS at the University of Wisconsin-Madison.....56

Figure 3-11: (a) Plan view of heated cavity (b) Diagram of heater, pipe and fin configuration within the heated cavity 57

Figure 3-12: (a) Facility overview (b)Heated cavity (c) Well insulated overhead water tank and upper header (d) Lower header and three riser tubes 59

Figure 3-13: (a) Thermocouple welds to riser tube surface and attached fins. (b) Thermocouple welds to capture bulk flow temperature at the lower header.....61

Figure 3-14: Components of RBI two-phase flow optical instrumentation. (a) Dual-tip phase sensor probe with 0.5mm sapphire fibers (b)Opto-electronic unit and (c) data acquisition box 63

Figure 3-15: (a) Schematic of probe positioning in a vertical pipe section (b) Phase indicating function for the gas and liquid phase from individual channels. 64

Figure 3-16: Graphical description of the operating principle of the two phase optical probe.....67

Figure 3-17: Bench-top separate effect test of optical sensor probe i.e. RBI.....68

Figure 3-18: Signal visualization interface. (*Inset: zoomed signals*).....70

Figure 3-19: RBI Probe vertically fixed normal to direction of flow in the upper network.....71

Figure 3-20: (a): Magnetic flow meter and signal converter (b): Showing the location of the magnetic flow meter 73

Figure 3-21: Screenshot of programmed LabVIEW software interface on PC showing details on TCs along the test loop.....75

Figure 3-22: Nodalization diagram for UW ¼ scaled water-cooled Reactor Cavity Cooling System (RCCS) 77

Figure 4-1: Schematic of single phase steady-state operation.....80

Figure 4-2: Temperature difference across the natural circulation loop and average mass flow rate at 4.63, 7.27, 9.91, 12.55 and 15.19 kW decay heat loads during single phase steady-state operations. 81

Figure 4-3: Schematic of two-phase operation after saturation temperature is reached....84

Figure 5-1: Schematic of (a) a pool type JSFR (b) core fuel and blanket zone highlighting core exit conditions and (c) core exit mixing between a fuel zone and blanket zone channels 90

Figure 5-2: Turbulent flow from a planar nozzle [www.ifd.mavt.ethz.ch]] 98

Figure 5-3: Flow realization of the axial normalized temperature field for triple jet fluid interaction in a water test facility, computed from Experiment, Low Reynolds number turbulence stress and heat flux equation models (LRSFM) and RANS based k-ε based models [Kimura et.al]. A cold jet is sandwiched between two hot jets. 102

Figure 5-4: Schematic of vertical planar jet used for numerical simulation benchmark....107

Figure 5-5: Sensitivity study based on grid size for single jet numerical simulations 109

Figure 5-6: Discretization of the fluid domain with 32010 elements and contour plot of the velocity field 110

Figure 5-7: Fully developed turbulent flow: Jet exit velocity profile....110

Figure 5-8: Benchmark series: Numerical and experimental comparison of centerline velocity decay in a single jet....111

Figure 5-9: Benchmark series: Numerical and experimental comparison of jet-half radius in a single jet 112

Figure 5-10: 2-D geometry and grid system used to validate dual-jet numerical simulations 114

Figure 5-11: Benchmark series: Numerical and experimental comparison of centerline velocity decay for two-jets**.** 115

Figure 5-12: Schematic of the in-vessel components in a pool-type SFR configuration 117

Figure 6-1: Full time history of (a) inlet and outlet temperature (b) mass flow rate and (c) pressure drop data, under baseline conditions (15.19 kW heat load and 80% tank volume) 121

Figure 6-2: Three distinct oscillatory modes (a) t=280 to 290 minutes (b) 420 to 450 minutes (c) 510 to 520 minutes, representing mass flow rate, pressure drop and void fraction data during flashing of the baseline scenario test (15.19 kW, 80% tank volume).....124

Figure 6-3: Comparison of system mass flow rate during two-phase regime under baseline conditions and repeat tests.....125

Figure 6-4: Summary of characteristic two-phase (flashing) mass flow rates during 12.55 kW, 15.19 kW, 17.84 kW and 20.49 kW tests 127

Figure 6-5: Mass flow rate oscillatory behavior over a 30 minute window 2.5 hours into the flashing phase. 129

Figure 6-6: Average period of oscillations for 7.27, 9.29, 10.9 and 12.52$\frac{\mathbf{kW}}{\mathbf{m2}}$ tests .130

Figure 6-7: Components of the FWHM statistical analysis with a normal distribution 131

Figure 6-8: FWHM analysis of pressure drop oscillations for lowest and highest heat flux (7.27 and 12.52kW/m2) 132

Figure 6-9: FWHM values for resolved peaks during flashing at different heat flux for mass flow rate 133

Figure 6-10: FWHM values for resolved peaks during flashing at different heat flux for pressure drop 134

Figure 6-11: FWHM values for resolved peaks during flashing at different heat flux for void fraction 134

Figure 6-12: Summary of characteristic two-phase mass flow rates measured during tank volume sensitivity studies (80%, 70% and 60% tank volume) 137

Figure 6-13: Measured mass flow rate, pressure drop and void fraction during two-phase (flashing) under the effect of accelerated tank depletion. 140

Figure 6-14: Instantaneous velocity surface plot and flow field for isothermal dual-jets 143

Figure 6-15: Regions along the geometric centerline velocity decay of parallel dual-jets 143

Figure 6-16: Effect of Δ**Thc** across both jets on the streamwise centerline velocity decay 145

Figure 6-17: Thermal mixing along the geometric centerline for non-isothermal dual-jets 146

Figure 6-18: Streamwise velocity and temperature profiles for non-isothermal ($\Delta \mathbf{T} = \mathbf{50K}$) and iso-velocity (2.3 m/s) dual-jets. Point "A" represents the merge point, "B" represents the completion of momentum mixing while "C" represents the peak thermal mixing.....147

Figure 6-19: Spanwise temperature profile across the flow field at different elevations for $\Delta \mathbf{T} = \mathbf{50K}$ **and Vratio** $= \mathbf{1}$ 148

Figure 6-20: Velocity field plots for different velocity ratios at $\Delta \boldsymbol{T} = \mathbf{10}\boldsymbol{K}$ showing the different merge points (a) $\mathbf{Uc/Uh} = \mathbf{0.5}$ (b) $\mathbf{Uc/Uh} = \mathbf{0.7}$ (c) $\mathbf{Uc/Uh} = \mathbf{1}$ 149

Figure 6-21: Influence of velocity ratios on non-isothermal field ($\Delta \mathbf{T} = \mathbf{10K}$) 150

Figure 6-22: Instantaneous velocity field for isothermal (773K) and iso-velocity (2.3m/s) dual jets for S/D =2, 5 and 7 respectively 151

Figure 6-23: Influence of jet-spacing on turbulent mixing of two parallel jets at T=773K and U=2.3m/s 152

Figure 6-24: Correlation between jet-spacing and onset of mixing for two isothermal (773K) and iso-velocity (2.3m/s) jets. 152

LIST OF TABLES

Table 1-1: Countries with the largest percentage of nuclear power for electricity production (NEI, 2013) 2

Table 1-2: PIRT for normal operation and off-normal events in the RCCS of the HTGR (*extracted from the NGNP roadmap NUREG/CR/6944*).....8

Table 1-3 : Some Gaps of relevance to Sodium Fast Reactor Technology as identified by PIRT.....9

Table 2-1: Summary of scaled quantities for OSU-MASLWR 19

Table 2-2: Summary of scaled quantities for PANDA test Facility.....20

Table 2-3: Summary of scaled quantities (PUMA) 22

Table 2-4: Summary of scaled quantities (PASCAL Facility).....27

Table 3-1: Summarizing the PIRT of relevance to RCCS (*Extracted from NUREG/CR/6944*).....32

Table 3-2: Developed and Developing RCCS designs in HTGRs.....36

Table 3-3: Summary of scaled quantities for UW Test Facility 47

Table 3-4: Summary of Scaled Values 48

Table 3-5 : Technical features of different insulation materials.....58

Table 3-6: Bubble diameter and bubble rise velocity from bench-top separate effect test with RBI Instrument.....69

Table 3-7: Void fraction verification in the RCCS test facility 69

Table 3-8: Summary of instrumentation and measuring parameters with uncertainties.....74

Table 4-1: Test Matrix: Single phase steady-state experiments 82

Table 4-2: Two-phase test matrix.....86

Table 5-1: Some research gaps with high level importance to the safety of SCFR [Denman et.al (2012)] 89

Table 5-2: Literature summary of numerical investigation of thermal stripping phenomena in a Sodium-Cooled Fast Reactor 94

Table 5-3: Literature summary of experimental investigation of thermal stripping phenomena focused on a Sodium Fast Reactor 95

Table 5-4: Some recent and past SFRs 97

Table 5-5: Characteristic average flow outlet conditions at the core exit of a prototype SFR....97

Table 5-6: Areas of application, strengths and weaknesses of various RANS based models....103

Table 5-7: Numerical representation of different core outlet flow conditions in a SFR....119

Table 6-1: Summary of key system parameters for two –phase baseline condition and repeatability 126

Table 6-2: Scaled decay heat load from the RPV, corresponding heat flux and heating rate for each power scheme 126

Table 6-3: Average dynamic system measurements in the flashing region 128

Table 6-4: Corresponding FWHM values for pressure drop (ΔP) peaks in Figure 6-8.....132

Table 6-5: FWHM values for five pressure drop peaks for 9.29 and 10.9 kWm2 ...135

Table 6-6: Average dynamic system measurements in the two-phase flashing regions 138

ACRONYMS AND ABBREVIATIONS

AM&S	Advanced Modeling and Simulation
ANL	Argonne National Laboratory
APEX	Advanced Plant Experimental Facility
APR	Advanced Power Reactor
BWR	Boiling Water Reactor
CAES	Center for Advanced Energy Studies
CFD	Computational Fluid Dynamics
CSAU	Code Scalability, Applicability and Uncertainty
DAQ	Data Acquisition System
DBA	Design Basis Accident
DNS	Direct Numerical Simulation
EBR	Experimental Breeder Reactor
EPCC	Equipment Protection Cooling Circuit
ESBWR	Economic Simplified Boiling Water Reactor
EU	European Union
FOM	Figures of Merit
FWHM	Full Width Half Maximum
GA	General Atomics
GCFR	Gas-cooled Fast Reactor
Gen	Generation of Nuclear Reactor Designs
GIF	Generation IV Forum

HTS	Heat Transport System
HXG	Heat Exchanger
IHX	Intermediate Heat Exchanger
INL	Idaho National Laboratory
ITF	Integral Test Facility
JSFR	Japanese Sodium Fast Reactor
LDV	Laser Doppler Velocimetry
LES	Large Eddy Simulation
LFR	Lead Fast Reactor
LMFR	Liquid Metal Fast Reactor
LOCA	Loss of Coolant Accident
LOFC	Loss of Forced Cooling
LOFT	Loss of Fluid Test
LOOP	Loss of Onsite Power
LRSFM	Low Reynolds number Turbulence Stress Heat Flux Equation
LWR	Light Water Reactor
MASLWR	Multi-Application Small Light Water Reactor
MHTGR	Modular High Temperature Gas-Cooled Reactor
MSR	Molten Salt Reactor
NC	Natural Circulation
NEI	Nuclear Energy Institute
NEUP	Nuclear Energy University Program

NGNP	Next Generation Nuclear Plant
NI	National Instrument
NSTF	Natural Shutdown Test Facility
OECD	Organization of Economic Cooperation and Development
OSU	Oregon State University
PAFS	Passive Auxiliary Feed-water System
PANDA	Passive Decay Heat Removal Assembly
PC	Personal Computer
PCCS	Passive Containment Cooling System
PCCT	Passive Containment Cooling Tank
PIRT	Phenomena Identification and Ranking Table
PUMA	Purdue University Multi-Dimensional Assembly
R&D	Research and Development
RAM	Random Access Memory
RANS	Reynolds Averaged Navier Stokes
RCCS	Reactor Cavity Cooling System
RELAP	Reactor Excursion and Leak Analysis Program
ROSA	Rig of Safety Assembly
RPV	Reactor Pressure Vessel
RSM	Reynolds Stress Model
RTD	Resistance Temperature Detection
SBWR	Simplified Boiling Water Reactor

SCS	Shutdown Cooling System
SCWR	Super-Critical Water-cooled Reactor
SET	Separate Effect Test
SFR	Sodium Fast Reactor
TC	Thermocouple
UDV	Ultrasonic Doppler Velocimetry
UIS	Upper Instrumentation Structure
US DOE	United States Department of Energy
US NRC	United States Nuclear Regulatory Commission
UW	University of Wisconsin
V&V	Verification and Validation
VHTR	Very High Temperature Reactor
WNA	World Nuclear Association

NOMENCLATURE

A	Cross-sectional area of pipe (m^2)
A_i	Interfacial area (m^2)
C_p	Specific heat capacity ($\frac{J}{kg.K}$)
D	Riser diameter (m)
d	Pipe diameter (m)
d_b	Bubble diameter (mm)
d_h	Hydraulic diameter (m)
E	Energy (J)
f	Friction factor
f_{int}	Interference frequency (Hz)
g	Gravitational force ($\frac{m}{s^2}$)
G	Production term of the turbulent kinetic energy
h	Heat transfer co-efficient ($\frac{W}{m^2.K}$)
ΔH	Latent heat of vaporization ($kJ.kg^{-1}$)
I	Turbulence intensity (%)
k	Turbulent kinetic energy ($\frac{J}{kg}$)
K	Orifice co-efficient
l	Characteristic length (m)
L_e	Entrance length (m)
$\dot{m}$	Fluid mass flow rate ($\frac{kg}{s}$)
n	Refractive index of material

$n_{1,2}$	Refractive index of material
p	Pressure (Pa)
P	Pitch (m)
P_o	Reactor power before shutdown (MW)
P_s	Reactor power after shutdown (MW)
Q	Power input (kW)
Q_g	Volumetric flow rate of gas ($\frac{\mathrm{m}^3}{\mathrm{s}}$)
q''	Heat flux ($\frac{\mathrm{kW}}{\mathrm{m}^2}$)
s	Spacing between nozzles (m)
S_K	Secondary source term
t	Time(s)
t_{aq}	Acquisition time (s)
t_f	Time of flight (s)
t_o	Reactor operation time (days)
t_s	Time past shutdown (days)
T	Temperature (K)
T_{sat}	Saturation temperature (K)
ΔT	Relative temperature difference (K)
U	Fluid velocity ($\frac{\mathrm{m}}{\mathrm{s}}$)
u	Dimensionless velocity
U_b	Bubble rise velocity (mm/s)
u'	Root mean square of turbulent velocity (m/s)
V_g	Superficial gas velocity ($\frac{\mathrm{m}}{\mathrm{s}}$)

w	Width of a surface (m)
Y_m	Contribution of fluctuating dilation to overall dissipation rate

GREEK SYMBOLS

α	Void fraction (%)
β	Volumetric thermal expansion co-efficient (K^{-1})
C_{μ}	Turbulence modeling constant
$C_{1\varepsilon}$	Turbulence modeling constant
$C_{2\varepsilon}$	Turbulence modeling constant
ε	Turbulent dissipation rate ($\frac{\mathrm{J}}{kgs}$)
η	Kolmogorov scale
γ	Thermal diffusivity ($\frac{\mathrm{m}^2}{\mathrm{s}}$)
ϑ	Kinematic viscosity ($\frac{\mathrm{m}^2}{\mathrm{s}}$)
μ	Dynamic viscosity ($\frac{\mathrm{kg}}{\mathrm{ms}}$)
θ	Non-dimensional temperature
θ_i	Incident angle (°)
θ_r	Refractive angle (°)
θ_c	Critical angle (°)
φ	Scaled quantity between prototype and model
ρ	Fluid density ($\frac{\mathrm{kg}}{\mathrm{m}^3}$)
$\Delta\rho$	Density difference ($\frac{\mathrm{kg}}{\mathrm{m}^3}$)
σ_{ε}	Turbulent Prandtl number for dissipation rate
σ_K	Turbulent Prandtl number for kinetic energy
τ_i	Time interval (s)

SUBSCRIPTS

b	Bubble
c	Cold fluid
cav	Heated cavity of the reactor cavity cooling system
con	Convection heat transfer
f	Liquid phase
g	Gas phase
h	Hot fluid
i	Refers to a specific section (heated section)
in	Inlet
m	Model
o	Reference value of a quantity
out	Outlet
p	Prototype
r	Characteristic variable
rad	Radiation heat transfer
rpv	Reactor pressure vessel
R	Ratio of a scaled quantity φ between model and prototype
sub	Sub-cooling
w	Water

DIMENSIONLESS QUANTITIES

Fi	Friction number (relates frictional to inertia forces)
Fr	Froude number (relates fluid inertia to gravitational head)
Gr	Grashoff number (relates buoyancy to viscous forces on a fluid)
Pe	Peclet number (relates heat convection to conduction)
Pr	Prandtl number (relates momentum to thermal diffusivity)
Ra	Raleigh number (relates gravity to thermal diffusivity)
Re	Reynolds number (relates inertia to viscous forces)
Ri	Richardson number (relates buoyancy to viscous forces)
St	Stanton number (relates heat transferred to fluid to thermal capacity of fluid)

CHAPTER 1: INTRODUCTION

The much anticipated nuclear energy re-naissance over the past decade following the Three mile Island (March 28th 1979) and Chernobyl (April 26th 1986) accidents in the USA and the Soviet Union respectively, was mostly driven by increasing cost of fossil fuels, the need to reduce greenhouse gas emission, increasing global population, and depleting oil reserves. Loss of coolant accidents and other component failures during the two major disasters also accelerated the need to enhance the safety features of existing and future nuclear reactors in order to prevent a recurrence.

The nuclear renaissance has, however, suffered several setbacks within the past few years following decreasing cost of natural gas and competitive cost of coal, thereby not making nuclear economically viable and price competitive. Other contributive factors include increasing non-proliferation concerns, shortage of manpower and most especially the recent Fukushima Dai-chi nuclear accident (March 11th 2011). This has slowed the expansion of current nuclear plant projects and led to the cancellation of planned expansions in countries such as Germany, Spain, Italy and Belgium.

The global energy demand, dwindling oil and gas reserves, climate change concerns, in-sufficient throughput from alternative energy sources such as wind and solar still make nuclear energy the most viable and reliable option (WNA, 2012). Nuclear power currently constitutes approximately 75% and 20% of the energy mix in France and the United States respectively. Table 1-1 shows ten countries with largest percentage share of nuclear power for electricity production.

Table 1-1: Countries with the largest percentage of nuclear power for electricity production (NEI, 2013)

Country	Percent (%)
France	77.7
Slovakia	54.0
Belgium	54.0
Ukraine	47.2
Hungary	43.3
Slovenia	41.7
Switzerland	40.9
Sweden	39.6
Korea Rep.	34.6
Armenia	33.2
Czech Rep.	33.0
Bulgaria	32.6
Finland	31.6

To ensure that nuclear power remains a key component of the US energy mix and to re-assure the public of the safety of nuclear technology, the U.S Department of Energy (DOE) in year 2002 started the Generation IV (Gen-IV) International forum. This initiative is tasked with the development of reactor systems with advanced safety features. The Gen-IV initiative was jointly supported by ten countries (Argentina, Brazil, Canada, France, Japan, South Korea, South Africa, Switzerland, USA and UK) [GIF (2002)]. The aims of the forum were to:

1. Develop advanced nuclear reactor systems with significant improvements over current Gen-II, III and III+ designs in terms of safety and reliability, economic competitiveness, waste minimization, sustainability and proliferation resistance.
2. To see to the deployment of different Gen-IV reactor designs by the year 2030.

With design modifications and addition of safety features, the nuclear industry is transitioning from the early Gen-I reactor types in the 1950's to the anticipated Gen-IV reactors due for deployment around 2030 as shown in Figure 1-1.

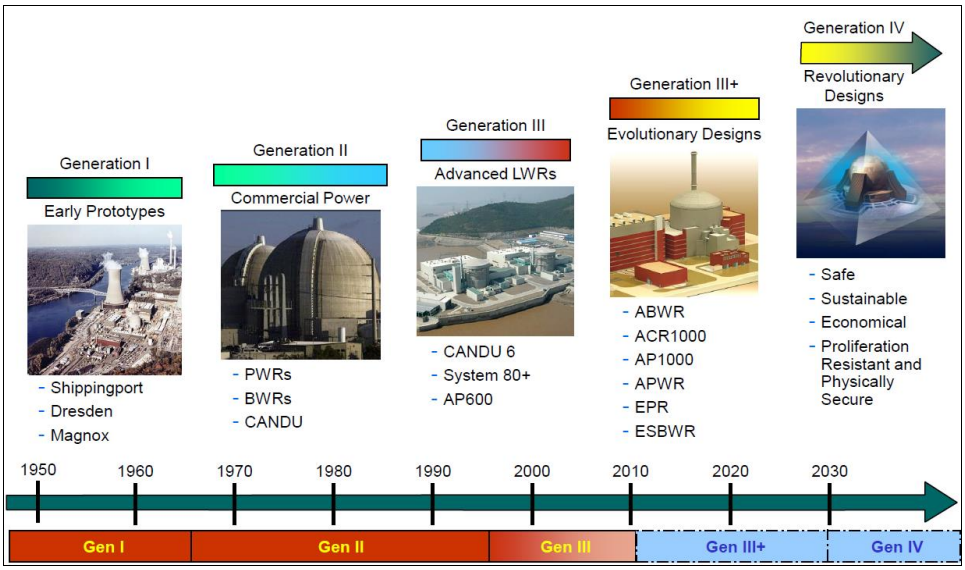

Figure 1-1: Gen-IV Nuclear Systems Roadmap

Six different reactor concepts have been identified to have technical viability and commercial potential based on the Gen-IV criteria. They include the Very High Temperature Reactor (VHTR), Gas-cooled Fast Reactor (GCFR), Sodium Fast Reactor (SFR), Molten Salt Reactor (MSR), Super-Critical Water-cooled Reactor (SCWR) and the Lead Fast reactor (LFR). The VHTR and SCWR employ thermal neutron spectrum while the GCFR, SFR and LFR employ a fast neutron spectrum in order to attain a high utilization of nuclear materials through recycling. The sixth type, MSR uses a circulating liquid fuel mixture which also provides flexibility in terms of nuclear

material recycling. Figure 1-2 shows a graphical representation of the six reactor types described above.

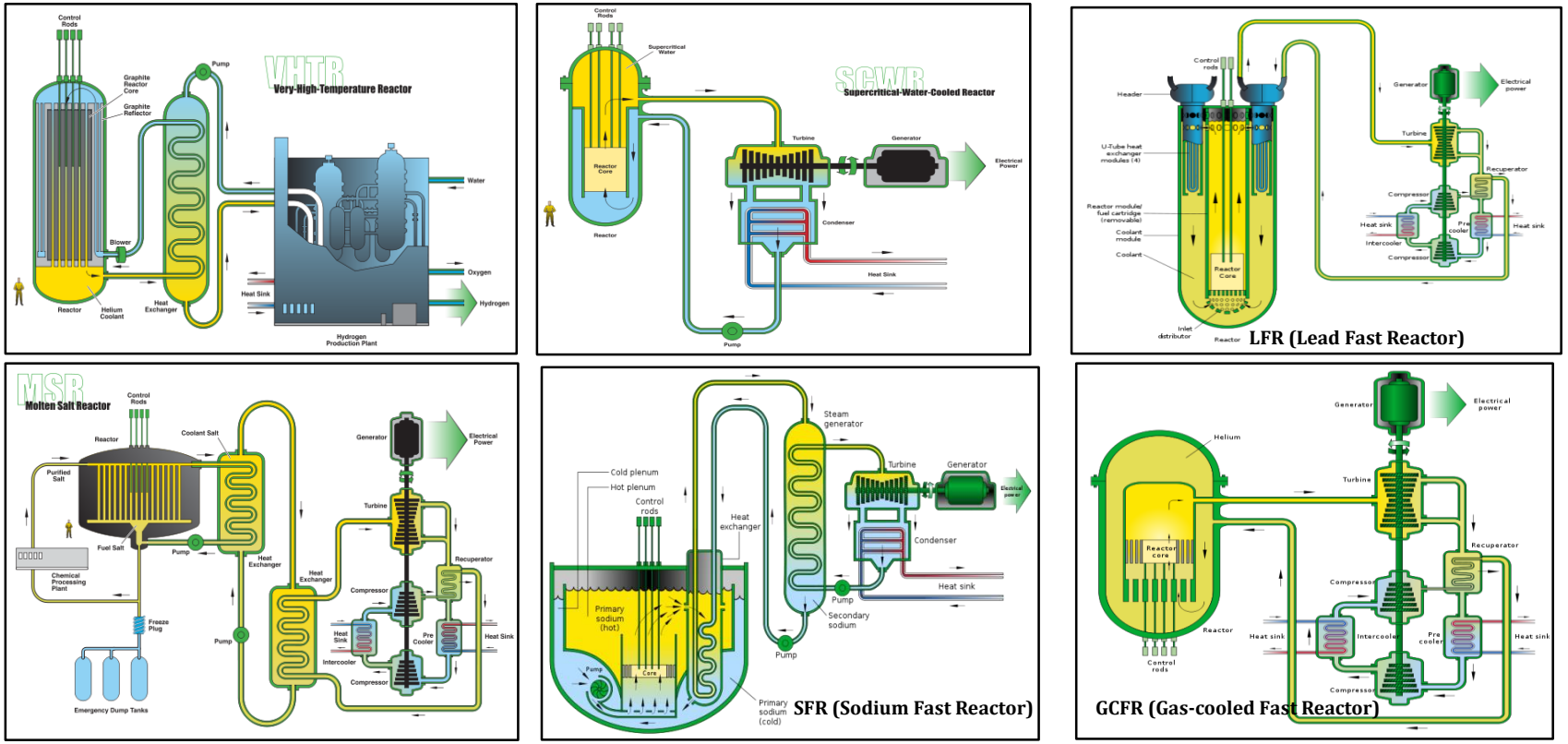

Figure 1-2: Six innovative designs under the Gen-IV Initiative

The Very High Temperature Reactor (VHTR), often referred to as the High Temperature Gas-cooled Reactor (HTGR), is one of the leading concepts in the US. With high operating temperatures, it has the capability of supplying process heat to chemical industry and can be coupled to a hydrogen generating plant to support the anticipated hydrogen economy (NGNP, 2009). Another feature of the HTGR is the inherent passive safety system which removes residual heat from the Reactor Pressure Vessel (RPV) in the event of an accident through natural circulation heat transfer. Although, some of the Gen III+ LWR technology (AP 1000 and ESBWR) reactors are designed with natural circulation passive safety systems such as the passive containment cooling system (PCCS), the HTGR natural circulation heat removal system is through the Reactor Cavity Cooling System (RCCS). Full description is provided in Chapter 3.

Another concept of interest to the US DOE is the development of Sodium Fast Reactor (SFR). The SFR has a compact high power density core relative to conventional light water reactors (LWR) and hence has the capability of producing more power for the same size of reactor. In addition, since the chain reaction is sustained with fast neutrons, it facilitates the transmutation of minor actinides and hence has a potential to reduce waste and extended utilization of fuel resources leading to a closed fuel cycle. To make the SFR concept more economically viable, several components such as the Intermediate Heat Exchanger (IHX) and the Upper Instrumentation Structure (UIS) and Pump are co-located in the reactor vessel.

As part of safety requirements prior to design certification and licensing, a Phenomena, Identification and Ranking Table (PIRT) was developed for each potential

reactor concept by a panel of experts assembled by the DOE. The PIRT is developed to identify and characterize the various phenomena that are expected during normal and off-normal conditions of the reactor system and those that can control the plant transient response. These phenomena are ranked based on safety response importance, the level of knowledge of such phenomenon by the panel or the scientific community. The natural circulation heat transfer in the RCCS of the HTGR and the thermal-striping phenomena in the upper plenum of the SFR were identified to be of high importance with low knowledge. Tables 1-2 and 1-3 show a summary of PIRT for HTGR and SFR, respectively.

Table 1-2: PIRT for normal operation and off-normal events in the RCCS of the HTGR (*extracted from the NGNP roadmap NUREG/CR/6944*)

Scenario	Upper Plenum	Core	RCCS	Lower Plenum
Normal operation	i. Flow distribution ii. Pressure drop	i. Reactivity feedback behavior ii. Core configuration (bypass) iii. Pressure drop iv. Heat transfer v. Flow distribution vi. Power distribution	i Heat transfer at operational conditions ii Natural circulation in cavity	i Flow distribution ii Heat transfer iii Thermal striping iv Jet behavior
DCC	i. Mixing and stratification ii. Hot plumes iii. Thermal resistance of structures	i Thermal radiation and conduction of heat across the core ii Axial heat conduction and radiation iii Natural circulation in the reactor pressure vessel iv Air and water ingress v Potential fission product transport vi Power distribution vii Core configuration viii Decay heat ix Flow distribution x Material properties xi Pressure drop	i Laminar-turbulent transition flow ii Forced-natural mixed convection flow iii Heat transfer—radiation and convection in duct	i Thermal mixing and stratification ii Flow distribution iii Air ingress
PCC	i. Mixing and stratification ii. Hot plumes iii. Thermal resistance of structures	i Thermal radiation and conduction of heat across the core ii Axial heat conduction and radiation iii Natural circulation in the reactor pressure vessel iv Power distribution v Core configuration vi Decay heat vii Flow distribution viii Material properties ix Pressure drop	i Laminar-turbulent transition flow ii Forced-natural mixed convection flow iii Heat transfer—radiation and convection in duct	i Thermal mixing and stratification ii Flow distribution

Table 1-3 : Some Gaps of relevance to Sodium Fast Reactor Technology as identified by PIRT

Gap	Importance to Safety	State of Knowledge
Steady State Intact Fuel and Fuel Changes	High	Medium
Transition to Natural Convective Cooling, Sodium Stratification	High	Medium
Thermal Response of Structures, Thermal Striping	High	Medium
Decay Heat Rejection, Radiation Heat Transfer from Vessels	High	Medium
Power Conversion Cycle, S-CO2 Accident Analysis	High	Low
Fuel Transient Behavior	Medium	Low
Sever Core Damage, Metal Fuel Motion, Dispersal and Morphology	High	Medium

To investigate important safety features in both the HTGR and SFR reactor concepts as identified in the PIRTs above, detailed experiments as well as advanced modeling and simulation (AM&S) will be required. It is, however, not economically viable to build a full-scale mock-up of the conceptual reactor for experimental purpose prior to certification and licensing. To evaluate the behavior and performance of the HTGR-RCCS and to improve the long-term safety of the SFR, this research proposes, develops and demonstrates the applicability of a top-down and bottom-up scaling approach in designing two different thermal-hydraulic systems i.e. an integral and a separate effect test, using a scaled experiment and AM&S tools such as CFD and traditional thermal-hydraulics and system analysis codes.

1.1. Motivation

Within the past four decades, large and small scale experiments to investigate key safety systems in advanced nuclear plant designs have been performed since it is not economically viable to build a full-scale nuclear reactor for experimental purposes. The high construction and operational costs associated with these experiments led to the development and utilization of finite element and system codes to model and simulate engineered safety systems under different operational conditions. In recent years, CFD as a 'localized tool' has emerged alongside system codes; they are jointly being used to guide the modeling, simulations and design of various next generation reactor designs. The role of experiments can however not be overemphasized as there are several instances where the codes need to be benchmarked using experimental data, i.e., verified and validated (V&V).

As part of the design certification and safety review requirements of the US NRC, detailed experimental and computational investigations need to be performed in scaled integral and separate effect test facilities. Separate effect tests are traditionally not often scaled. Detailed scaling relations however need to be established between conceptual reactor designs and scaled experiments to address the anticipated thermal-hydraulic performance metrics of concern to nuclear power plants under both steady-state or off-normal conditions as explicitly anticipated by the designer , for example design basis accident (DBA).

To improve the safety and economics of existing fleet of nuclear reactors, i.e. mostly LWRs (Generation II and III) and advanced reactor designs (Gen III, III+ and IV), scaled

integral and separate effect experimental test facilities (ITFs and SETs) have been built to study the engineered feasibility, predict thermal-hydraulic behavior and performance under normal and hypothetical accidents and to generate a database for code development and assessment.

In as much as data-sets are generated from these test facilities, the ability to correlate the data to the codes to scale-up/down processes and phenomena to full plant conditions with confidence remains an open issue. This is because the capability of a code to predict steady and/or transient phenomena in a scaled facility does not automatically translate on average into its ability to reproduce the same transient quantitatively in the full plant scenario. The top-down scaling analysis with respect to the thermal-hydraulics of prototype nuclear systems often does not provide details at the non-integral level because local phenomena is seldom scaled. Detailed analysis of existing scaling methodologies and approaches will be useful for better prediction of ITFs and SETs performance and for more accurate evaluation of full-scale reactor system performance.

CHAPTER 2: LITERATURE REVIEW

It is not economically viable to conduct full-scale mock-up experiments; therefore, complex engineering system such as a full-scale reactor can be scaled into reduced levels of complexity: integral and separate effect tests. Both tests involve different levels of physics coupling. Figure 2-1 gives a hierarchical structure of the scaling approach for complex nuclear system thermal-hydraulics.

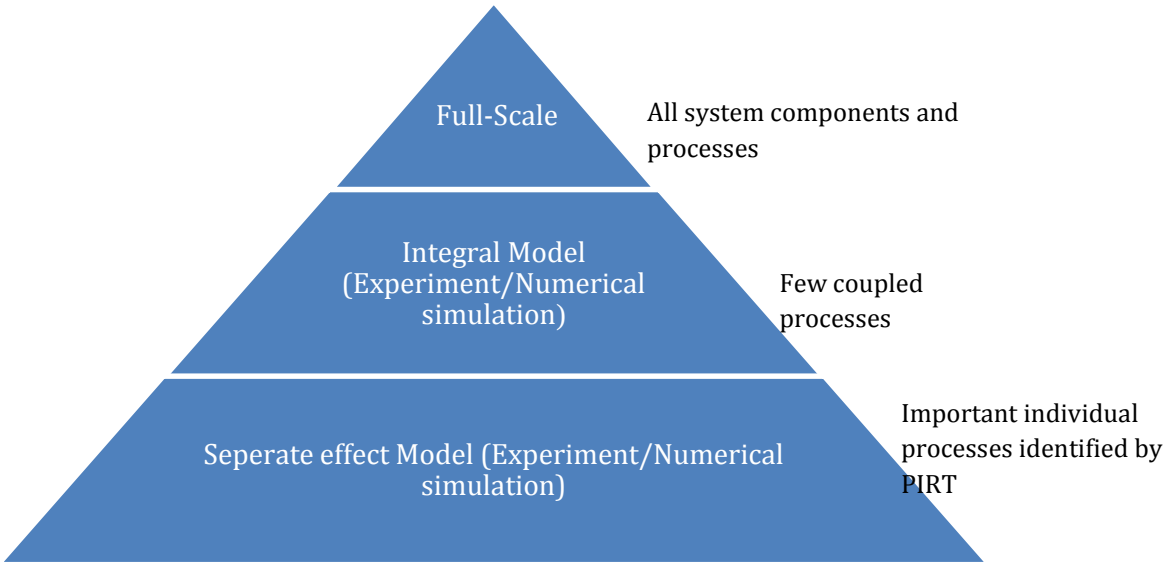

Figure 2-1: Schematic of hierarchical scaling approach for complex systems [adapted from Zuber (1991)]

2.1. Scaling Analysis

Scaling analysis describes the algebraic based, phenomenological analysis of a physical system in terms of its conservation, constitutive and empirical correlations. This scientific design technique is widely used to simplify and rank processes based on cumulative knowledge gained; thus simpler equations for describing these processes

can often be used. With focus on thermal-hydraulics in reactor systems, the primary purpose of performing scaling analysis is to develop a homologous relationship between a prototype and an experiment [Ransom et.al, 1998].

By non-dimensionalizing the various forms of basic conservation equations of mass, momentum and energy, scaling analysis represents (as a model) the characteristics of a real-life system by approximating and contrasting the orders of magnitude (OM) of the terms in the conservation equations. When conservation equations are ill-posed for a physical phenomenon, i.e., do not have a unique solution, constitutive and empirical models may also be needed to give a more accurate description of the system and to close the system mathematically. This provides insight into the behavior of the system, the response times and the variations, i.e. increase or decrease in the system state variables (e.g. temperature, energy and pressure).

All scaling techniques have similar conceptual procedures. Ransom et al. (1998) identifies two classical non-dimensionalization techniques as the empirical and analytical approach.

2.1.1. Empirical Approach

This is a traditional scaling technique that is based on order of magnitude analysis or dimensional homogeneity. Though, not based on the laws of physics, it has been found useful in establishing similarity between two or more physical quantities. Based on physical dimensions such as length, time, mass and absolute temperature representing a system, the sets of equations may be used to evaluate the performance

of a system. An example is the Buckingham Pi theorem which establishes a relationship between the number of physical dimensions and independent quantities (thermo-physical quantities) in a given expression or phenomena. Though it generates sets of dimensionless parameters of relevance to a system, it however does not rank the non-dimensional parameters in order of importance and does not cover all phenomena such as mixing. In addition, it is possible to omit (in error) some important parameters in the model. Typically, it is assumed that similitude is achieved between a conceptual design and a model if all or as many as feasible dimensionless parameters are preserved. With this traditional approach, Ransom et.al (1998) confirms that there is a high likelihood of omitting some important parameters. For example, it does not take into account the dynamics of turbulent and multi-phase flows.

2.1.2. Analytical Approach

The analytical scaling approach has extensively been developed and utilized in the design of several thermal-hydraulic facilities [Ransom et.al (1998), Ishii et.al. (1984), and Zuber (1991). Important steps relevant to the analytical approach are:

1. Problem formulation: write out the governing equations representing the process or system including the initial and boundary conditions. Graphical representation were applicable could be useful.
2. Identify the characteristic reference parameters and use them to scale the dependent and independent variables and differential expressions.

3. Substitute for scaled parameters into the governing equations. This produces some dimensionless groups as coefficients of the various terms of the differential expression.
4. Dynamic similarity is preserved if the dimensionless parameters have same value in both the conceptual system and the model.

This procedure is only straight-forward for idealized systems. For more complex systems, integral methods will need to be applied in order to understand larger scale phenomena in terms of integral dimensionless parameters. Extensive development work has been reported by Ishii and Kataoka (1984) and Ishii and Jones (1976) to preserve geometric, kinematic and dynamic similarity between two or more physical systems or processes.

Two broad categories that govern the analytical scaling approach are the top-down and bottom-up scaling methods.

2.1.3. Top-Down Scaling

The Top-down scaling approach is also referred to as integral system scaling, system level scaling or global scaling approach. This methodology develops and establishes sets of similarity criteria at the system level by relating the interaction between the different components of a reactor system [Blandford and Peterson (2009)].

System idealization at this level is based on integral methods by converting the partial differential equations of the governing transport equations to ordinary

differential equations. In addition to preserving the integral response functions, this scaling methodology also preserves the mass and energy across different flow boundaries and control volumes in the reactor system. A major challenge with this scaling approach is that though it provides a good understanding of the performance of the overall system response, there is a tendency that some local spatial details will be lost due to the integration or averaging effects.

2.1.4. Bottom-up Scaling

Often referred to as local scaling approach, this methodology establishes sets of similarity criteria for the dynamic interaction of key local phenomena or dominant processes in a system. These processes or phenomena include but not limited to heat transfer, natural convection, flashing, phase distribution and mixing. To further simplify this approach and resolve some of the open issues associated with it, Zuber et.al (2001) developed a fractional scaling methodology based on identification of dominant processes in the Phenomena Identification and Ranking Table (PIRT) process. Wilson et.al (1998) also emphasized the significance of the PIRT process in scaling analysis on code development and validation for key phenomena and dominant processes based on the importance to systems of relevance and expert knowledge.

Sets of scaling criteria to guide the engineering design of thermal-hydraulic test facilities have been derived by Ishii and Kataoka (1984), Kocamustagullari and Ishii (1983), Zuber (1991). These scaling methodologies are herein referred to and described as Ishii's methodology and Zuber methodology.

2.2. Integral Test Facilities (ITF)

Integral test facilities are often geometrically scaled-down experimental facilities designed and built to resolve some of the existing or anticipated challenges in conceptual reactor designs. Over the years, data obtained from these facilities has been used to benchmark several developed system codes for reactor safety evaluation. ITF design incorporates the two scaling approaches (global and local) as explained above. Over the past three decades, following the Three Mile Island and Chernobyl accidents, several experimental programs were conducted in many countries all over the world to investigate some of the design basis accidents. First of this kind was the full-scale heavy water moderated R4 (140 MWe) Marviken reactor in Sweden in 1960 as shown in Figure 2-2. It was originally built for power generation and plutonium production. However due to political obstacles and unexpected design challenges, the reactor was never fueled and hence never operated. It was instead converted into a large scale test facility to study reactor behavior under accident conditions.

Figure 2-2: External view of the full-scale R4 Marviken Power Plant

While most of the facilities were designed for LWR technology, results and data obtained from experiments performed have guided and supported development and assessment of system codes. With only few ITFs currently in operation, the need for more experimental facilities to perform tests unique to innovative designs cannot be over emphasized. Some of the existing ITFs include:

2.2.1. Multi-Application Small Light Water Reactor (MASLWR):

Jointly designed and developed by Idaho National Laboratory (INL) and Oregon State University (OSU) in the United States, the MASLWR is a scaled-down small

modular pressurized water reactor design. MASLWR was designed to investigate the natural circulation heat removal capability of a conceptual design from the reactor core under steady state and transient operating conditions [Reyes and King (2003) and Mascari et.al, 2012]. Table 2-1 summarizes the scaled quantities, and side view of the test facility is provided in Figure 2-3.

Table 2-1: Summary of scaled quantities for OSU-MASLWR

Quantities	**Scaling ratio**	**Basis**
Length	1:3	Height
Volume	1:254.7	Power
Time	1:1	Kinematics
Area	1:82.2	Power

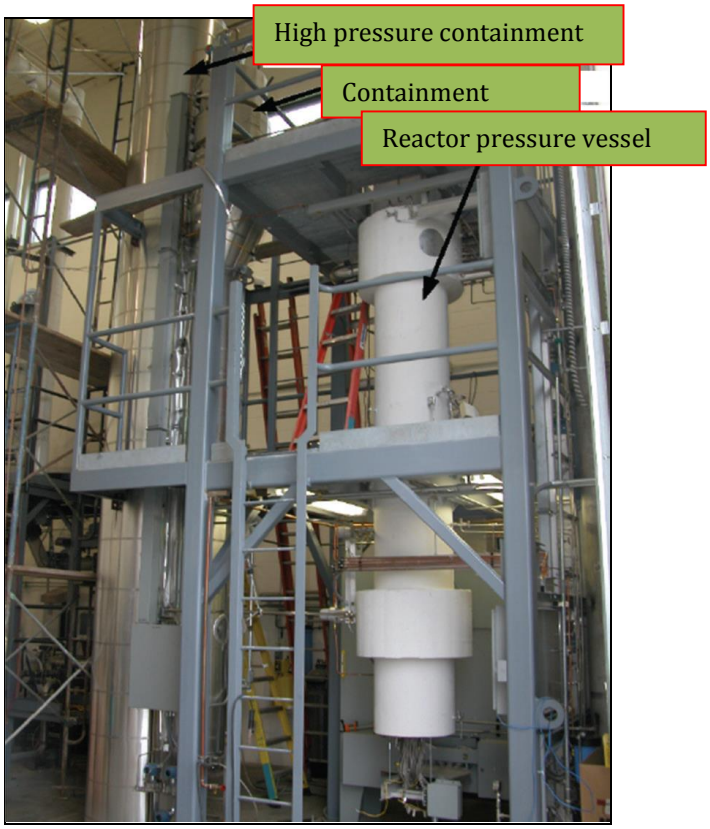

Figure 2-3: Side view of OSU-MASLWR Test Facility

2.2.2. Passive decay heat removal Assembly (PANDA)

Jointly sponsored by the European Union (EU) and Organization of Economic Co-operation and Development (OECD) and the Swiss utilities, the PANDA test facility was built by Paul Scherrer Institute in Switzerland. The PANDA thermal-hydraulic facility was scaled based on the SBWR reference design and was developed to investigate key safety systems of importance to existing and advanced BWRs. Table 2-2 summarizes the scaled quantities. Test performed included investigating natural circulation and flashing induced instabilities, the performance of the passive core cooling system and to simulate the long-term phase of the SBWR LOCA transient. In addition, several separate effect tests addressing thermal stratification, condensation and mixing were also performed [Yadigaroglu, (1996), Paladino and Dreier, 2012]. Figure 2-4 shows an internal view of the PANDA test facility.

Table 2-2: Summary of scaled quantities for PANDA test Facility

Quantities	Scaling ratio	Basis
Length	1:1	Height
Volume	1:40	Power
Power	1:40	Power
Mass flow rate	1:40	Area
Heated area	1:40	Power

Figure 2-4: Internal view of the PANDA Test Facility

2.2.3. Purdue University Multi-Dimensional Integral Test Assembly (PUMA)

PUMA is a scaled model of the simplified boiling water reactor (SBWR) design. The facility was built under the auspices of the US NRC to investigate the performance of the SBWR passive safety systems during parallel operations and also to provide integral test data for assessment and development of the RELAP5 thermal-hydraulic code. Built in 1997, the PUMA facility is currently the only BWR test facility in existence in the USA. Figure 2-5 shows a top-down view of the PUMA facility. Scaled based on the top-down and bottom-up scaling approach, the integral facility comprises of all the unique engineered safety systems and all thermal-hydraulic components of the SBWR.

Ishii et.al, (1998), Ishii and Kataoka (1984), Ishii and Kocamustafaogullari (1983) and Ishii et.al, (1998) all detail the sets of scaling laws used for building the PUMA facility and their applicability for similar facilities. Table 2-3 highlights the scaled quantities for the PUMA test facility.

Table 2-3: Summary of scaled quantities (PUMA)

Parameters	**Ratio**	**Basis**
Length	¼	Height
Time scale	½	Kinematics
Velocity	½	Dynamics
Volume	1/400	Power
Aspect ratio	5/2	Power
Power	1/200	Power
Flow area	1/100	Power & velocity
Mass Flow	1/200	Area & velocity

Ishii's integral scaling approach comprises of three levels as follows: (a) integral responses function scaling, (b) Mass and energy inventory and boundary flow scaling and, (c) local phenomena scaling. The first two levels are essential to the dynamic interactions between several components while the third level was a local or bottom-up scaling approach. In solving the system conservation equations, Ishii expressed the solutions in terms of transfer functions between variables. Based on these, eight different dimensionless groups were identified as being necessary to be preserved under both single and two phase conditions as shown in Figure 2-6.

Figure 2-5: Top-down view of the PUMA Test Facility

Some other ITFs in existence to investigate the thermal-hydraulic behavior and technical feasibility of various in-core reactor designs include the Rig of Safety Assembly (ROSA), Loss of Fluid Test (LOFT) facility, Toshiba Innovative Germinate Test Loop for Reactor Safety System (TIGER), and Advanced Plant Experimental (APEX) test facility. Experimental data obtained from series of tests performed in these test facilities has supported development of thermal-hydraulic codes, e.g. RELAP5 used to analyze reactor thermal-hydraulic behavior during both normal and transient scenarios. Excerpts from literature however show that several problems plague ITFs. This includes inability to accurately simulate or predict the thermal-hydraulic behavior in all components and processes taking place within the reactor system due to the high number of components involved. Therefore, accessing detailed information from all components is not trivial. Inconsistency in scaling analysis or inability to completely

satisfy all scaling requirements remains a challenge. Confirmatory tests are more specific and high fidelity experimental data could contain phenomenological information representative of a real reactor system.

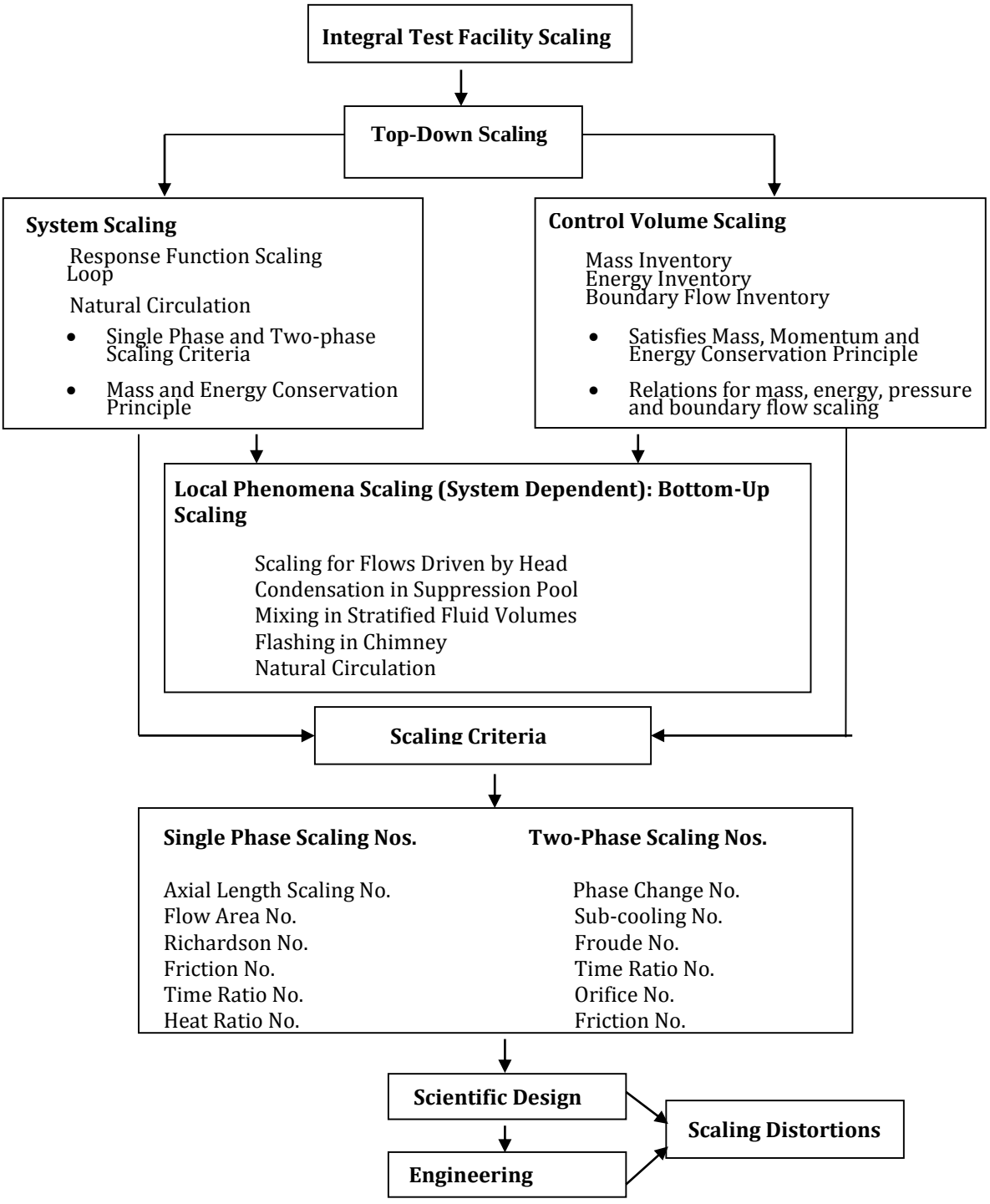

Figure 2-6: Integrated scaling approach for integral and separate effect thermal-hydraulic tests for nuclear systems design

2.3. Separate Effect Tests (SETs)

Separate effect tests (SETs) play a significant role in understanding some important phenomena of relevance to existing and innovative reactor designs. This includes but not limited to condensation, temperature distribution, buoyancy effects, mixing, flashing flows and liquid carry-over. An example of a large separate effects test is the PASCAL facility in Korea.

2.3.1. PAFS Condensation Heat Removal Assessment Loop (PASCAL)

As part of the advanced safety features of the Korean advanced power reactor (APR), the passive auxiliary feed-water system(PAFS) is designed to provide cooling to the steam generators secondary side and ultimately remove decay heat from the reactor core through natural circulation during accident transients. One of the separate effects tests performed in the PASCAL facility was to experimentally investigate the steam condensation inside the passive condensation cooling tank (PCCT) and natural circulation in the PAFS. Thermal-hydraulic parameters such as the local and overall heat transfer coefficients, fluid and wall temperatures and PCCT temperature distribution was used to evaluate the condensation heat transfer Kang et.al (2012).

Table 2-4: Summary of scaled quantities (PASCAL Facility)

Quantities	Scaling ratio
PCCT height	1:1
PCCT length	1:2
PCCT width	1:120
PCCT pressure	1:1
Steam pressure	1:1
Steam flow rate	1:240
Elevation from SG level	1:1

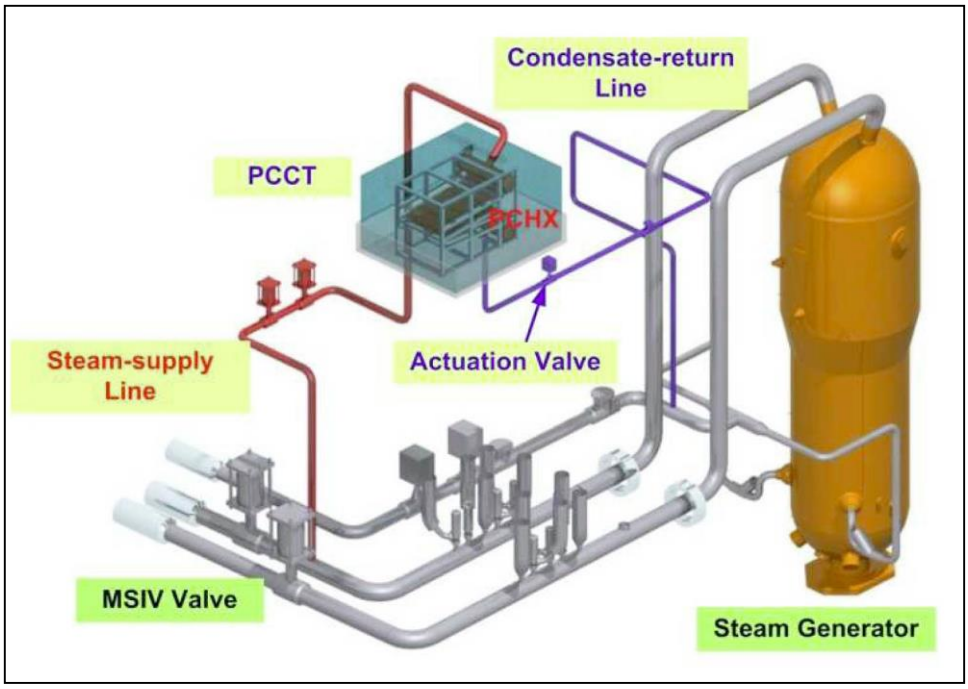

Figure 2-7: Schematic diagram of the Korean Advanced Power Reactor passive auxiliary feed-water system

Similar condensation heat transfer separate effect tests were performed on the passive containment cooling system (PCCS) of the PUMA integral test facility following a Loss of Coolant Accident (LOCA) conditions.

2.4. Research Objectives

This research work is motivated by the need to enhance the safety of advanced reactor systems. Additional significance is the need to obtain a more consistent and uniform mode of integration used in describing system behavior in both integral and separate effect tests facilities and also improves the similitude of important processes in full-scale, integral and separate effect tests as related to nuclear systems. The objective of this research is therefore to ***develop an approach*** that can be used to:

- Integrate scaling methods for the design and thermal-hydraulics of a scaled integral passive cooling system, and separate effect thermal-jet mixing using the top-down and bottom-up scaling approach respectively. This is for consistency and of relevance to understanding the detailed spatial, temporal and energetic scales that relate phenomena to a system in both prototypes and models.
- Use CFD as part of a bottom-up scaling approach to optimize the design of the upper plenum of the SFR against thermal-striping phenomena through modeling of turbulent mixing.
- Experimentally and computationally investigate linearity and non-linearity in two different thermal-hydraulic convective flows at integral and separate effect scales.

To guide this research work and support code V&V and UQ requirements of the US DOE for issues of technical concern to next generation nuclear reactor concepts, two aforementioned DOE projects: “Experimental Studies of NGNP Reactor Cavity Cooling System with Water” and “Data Collection Methods for Validation of Advanced Multi-Resolution Reactor Simulations” are used as case studies to substantiate the

methodology. Natural circulation heat transfer in the reactor cavity cooling system of the NGNP and turbulent mixing in the upper plenum represent two different characteristic convective flows of relevance to two different nuclear reactor designs. Figure 2-8 gives a graphical illustration relevance and relationship between both phenomena.

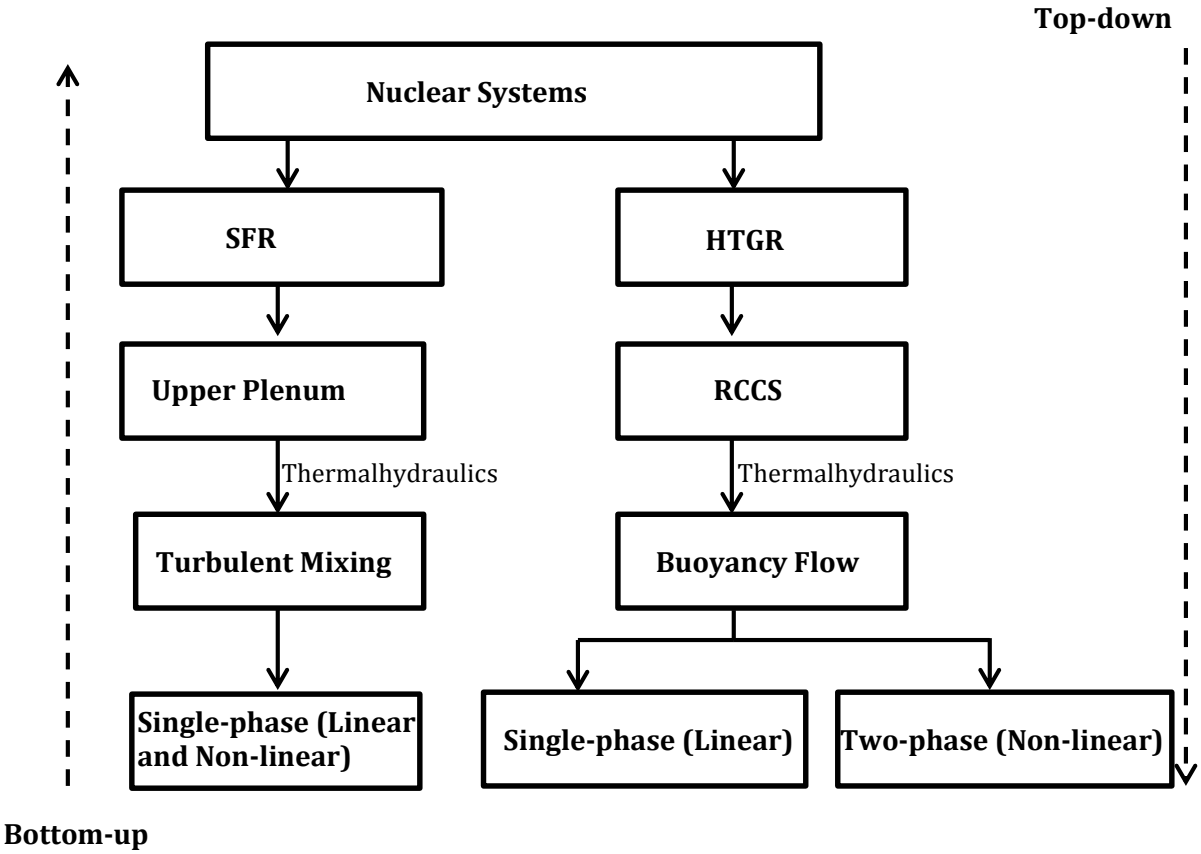

Figure 2-8: Relevance of scaling to thermal-hydraulic flows in two different nuclear systems

CHAPTER 3: NGNP-VHTR CONCEPT- REACTOR CAVITY COOLING SYSTEM

The Next Generation Nuclear Plant (NGNP) is the US DOE's generation IV version of the VHTR. The VHTR technology is also generically referred to as High Temperature Gas Cooled Reactor (HTGR); it is helium-cooled and has a graphite moderated core. With design inlet and outlet temperatures of approximately 325°C and 750°C respectively, it has a higher efficiency steam cycle, potential of being coupled to a nearby hydrogen production plant using supplied process heat for in addition to electricity. Another advantage of the HTGR is its inherent safety features which include passive decay heat removal system. Figure 3-1 shows a schematic of the proposed HTGR. Another inherent safety feature of the HTGR is the TRISO (tri-isotropic) coated fuel particles which provide additional protection and retention of fission products because of the graphite matrix and concentric layers of materials.

The DOE NGNP technology readiness level roadmap recognizes that three HTGR designs, one each by AREVA, Westinghouse and General Atomics (GA), are under consideration in the USA (INL, 2009). Focus of the scaled water-cooled reactor cavity cooling system (RCCS) used for the purpose of this research is based on the GA design as funded under the US DOE's Nuclear Energy University Programs contract number 193K340.

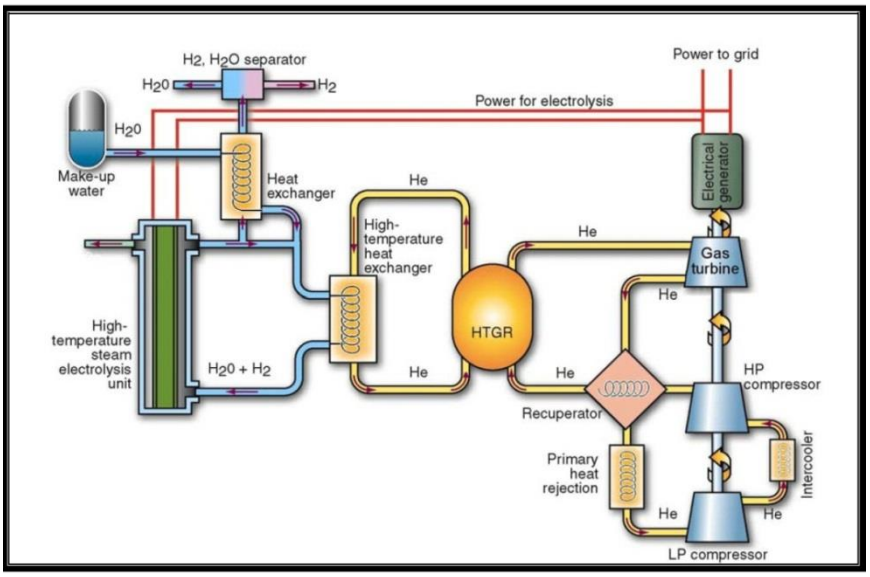

Figure 3-1: Schematic Diagram of the Proposed HTGR (NUREG/CR/6944)

As regards to safety and licensing, a joint document, "Phenomena Identification and Ranking Table" (PIRT), was developed by groups of technical experts to address the following: (i). Identify and prioritize safety related issues of importance to the HTGR. (ii). Identify gaps based on past and existing knowledge and (iii). Develop research and development (R&D) roadmap(s) to fill the identified gaps. This has facilitated experimental and computational efforts to investigate and thereby to establish a better understanding of some identified, high-priority safety issues. One of such components of importance to the safety of the HTGR during off-normal operations is the decay heat removal capability of the RCCS. As noted in Table 3-1, key RCCS thermal-hydraulic phenomena such as radiative heat transfer (from reactor pressure vessel surface of given emissivity to the RCCS) and performance of the RCCS are dependent on the configuration (thus scaling) and accompanying phenomena.

Table 3-1: Summarizing the PIRT of relevance to RCCS (*Extracted from NUREG/CR/6944*)

Component	Phenomena	Importance	Knowledge Level	Rationale
Vessel	Vessel and RCCS Panel emissivity (general LOFC) {Radiant heat transfer from vessel to RCCS affects heat transfer process at accident temperatures}	H	M[c]	FOM—vessel integrity—maintains cool-able geometry; limit vessel temperature—Change in inner surface vessel emissivity based on degraded environment; T^4 (radiant) heat transfer dominates (85–90%) in LOFC transients; and scoping calculations: large temperature differences between vessel and RCCS reduce emissivity importance.
				– In-service steel vessel emissivity's are fairly well known. – Emissivity's not well known during accidents as a function of time, dust on surface, optical transparency, etc., as a result of disturbances from a depressurization. – Knowledge of inner emissivity 0.5–>0.3, change nature of surface coating; e.g., from loss of oxide film.
				– Emissivities are fairly well known for steel, once oxidized (in air cavity).
				– Complex geometries involved—difficult to calculate for transient cases, especially in upper head region with control rods (standpipes) in between vessel and RCCS.
Vessel	Reactor vessel cavity air circulation and heat transfer {Affects upper cavity heating}	H	L	FOM—vessel and vessel support integrity—Affects RCCS performance; skewed (toward top) heat distribution; generation of hotspots.

3.1. Reactor Cavity Cooling System (RCCS)

3.1.1. Description

The RCCS is designed to remove decay heat from the reactor pressure vessel (RPV) of a nuclear reactor during both normal and off-normal scenarios (NGNP, 2008). Heat rejected from the RPV is transferred by thermal radiation from the RPV surface, conduction from the support structures and natural convection from the surrounding air to the RCCS riser tubes.

During normal plant operations, the RCCS operates in active mode with equipment protection cooling circuit (EPCC) pumps circulating water through the standpipes. This serves as a backup heat removal system to the heat transport system (HTS). During planned shutdown for maintenance or re-fueling, the HTS or shutdown cooling systems (SCS) are used for providing cooling. Apart from removing the residual heat rejected from the RPV, the RCCS also serves as a protective layer for the concrete walls as it forms a curtain around the reactor cavity and prevents degradation of the concrete structure by keeping the surface temperatures within safety limits (~300°C).

Following a loss-of-forced-circulation (LOFC) transient, i.e. failure of the EPCC pumps, the RCCS operation transitions from active to passive mode. While in the passive mode, the density difference between the fluid within the heated section and the storage tank initiates buoyancy driven circulatory flow. Cooler water descends through the downcomer and replaces the displaced warm water rising in the heated section. Figure 3-2 and 3-3 illustrate the flow paths of the RCCS during active and passive modes of operation.

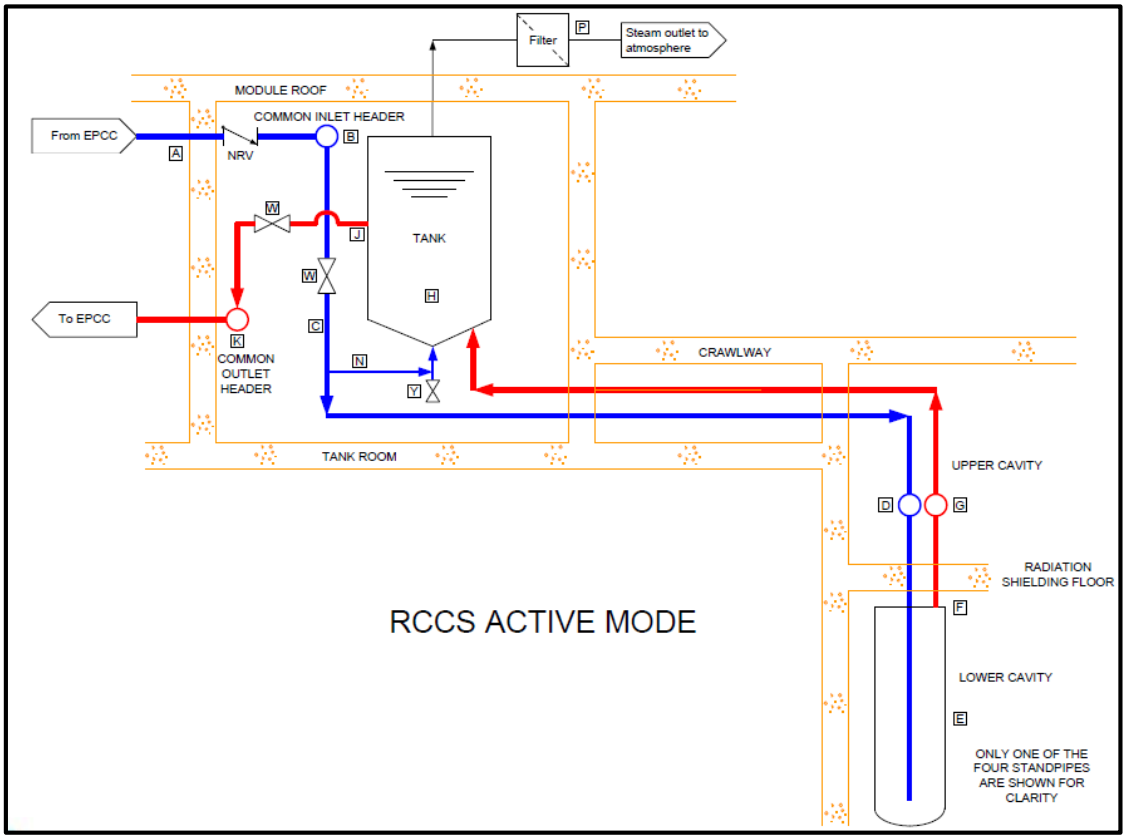

Figure 3-2: Flow path of the water in the RCCS during active mode of operation (NGNP, 2008)

As earlier described, the EPCC circulates water through the standpipes during normal operating conditions, i.e., active mode. Residual heat is transported to the water in the standpipes and dissipated through the main heat sink, i.e., tank, as shown in Figure 3-2. Also, the non-return valve located between the EPCC and the RCCS inlet header in Figure 3-2 prevents the header from emptying, if the EPCC feed pipe ruptures.

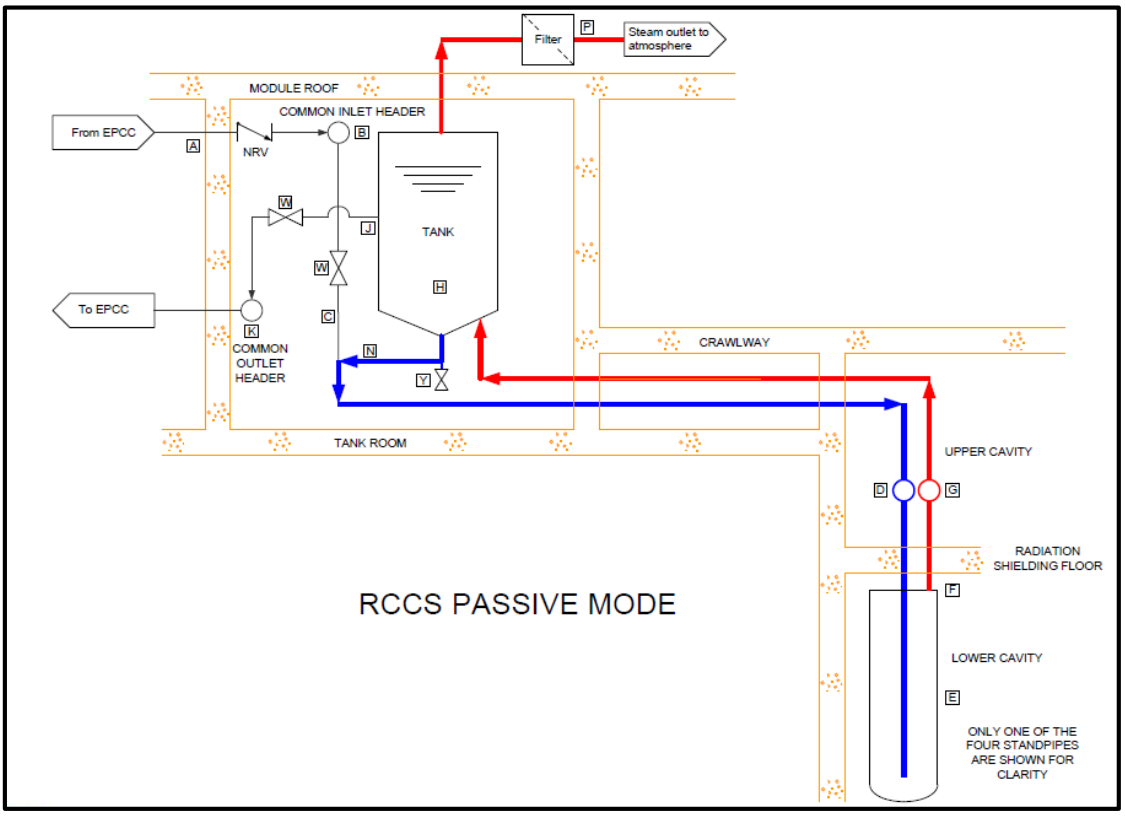

Figure 3-3: Flow path of the water in the RCCS during passive mode of operation (NGNP, 2008)

The three proposed NGNP-HTGR designs (AREVA, Westinghouse and GA) all adopt the RCCS configuration. Using water as the working cooling fluid, all three designs have water storage tanks serving as the heat sink and located above the RPV with connections to vertically positioned risers (NGNP, 2009). The GA design however incorporates the possibility of using air as the cooling fluid as an alternative to water thereby replacing the storage tanks with large air intake and exhaust ducts. A schematic in Figure 3-4 shows the general layout of the RCCS. Table 3-2 summarizes RCCS designs proposed in developed and developing HTGRs. It should be mentioned

that scaling analysis for either an air or water-cooled buoyancy-driven RCCS is important to determine any safety in design.

Table 3-2: Developed and Developing RCCS designs in HTGRs

Reactor	RCCS Coolant	Heat Transfer Mechanism
HTTR (Japan)	Water	Forced convection
HTR-10 (China)	Water	Natural convection
PBMR (South Africa)	Water	Natural convection
GT-MHR (Russia)	Air	Natural convection
MHTGR (USA)	Air	Natural convection
NGNP-HTGR (USA)	Water	Natural convection

3.1.2. Prototype (Conceptual Design) Description

The prototype MHTGR-water-cooled RCCS is a conceptual design based off a full-scale GA-MHTGR reactor design with a modular core power of 350 MWt (125 MWe). Going off a ½-scale air RCCS natural convection shutdown test facility (NSTF) at Argonne National Laboratory (ANL) and as reported by Tzanos and Farmer (2006), the air ducts in the air-cooled GA-RCCS were replaced with 2" inner diameter water riser tubes maintaining the same riser pitch[1] to diameter (P/D) ratio of four in the reactor cavity, i.e., ratio of the geometric pitch of two risers to the diameter of the riser..

A total of 227 water standpipes, i.e. riser tubes, form a curtain along the concrete walls. All 227 standpipes are connected through banks of hot and cold headers at the top and bottom respectively to a total of 8 water storage tanks (independent A and B trains for redundancy) which serve as a heat sink located above the reactor vessel. Providing cooling to the reactor cavity under both steady-state and transient scenarios,

[1] Pitch here is the distance between centerline of two risers

the standpipes transfer heat rejected from the RPV. The tank has an opening at the top and is hence maintained at atmospheric pressure. A particle filter is placed at the top opening to prevent the system from contamination.

A down-comer is connected to the bottom of each tank and it centrally distributes the coolant through sets of cold headers in the lower plenum into the riser tubes. As part of the inherent safety features, flow into and out of each tank is distributed into and collected from alternating riser tubes (A and B trains). To assure redundancy, following a loss of inventory or water supply into one of the storage tanks, adjoining riser tubes will be functional rather than lose an array of riser tubes. Figures 3-4, 3-5 and 3-6 illustrate different configurations of the RCCS system, redundant trains, and flow paths.

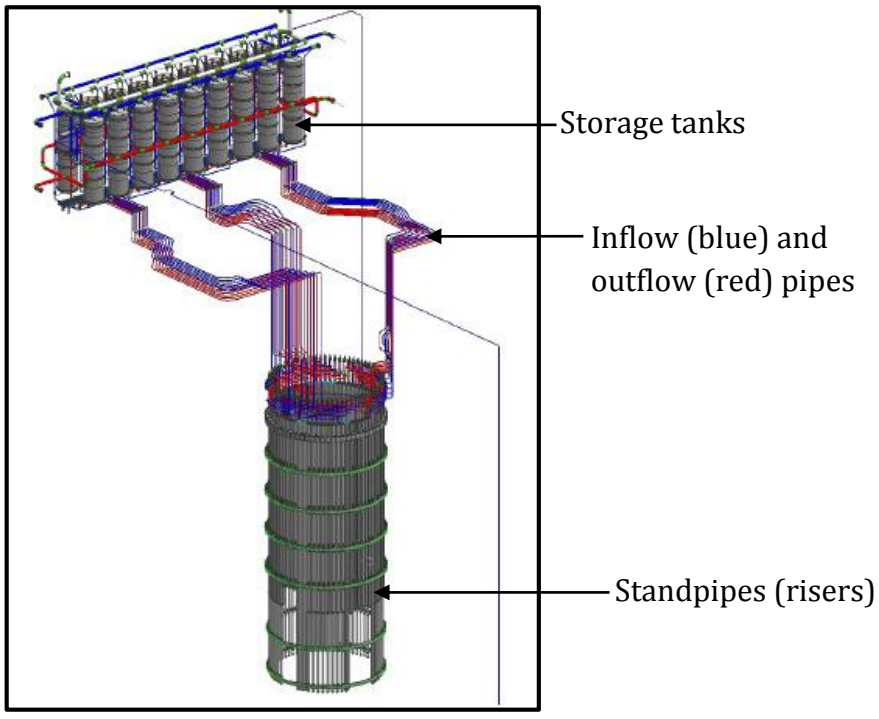

Figure 3-4: General arrangement of Water-Cooled RCCS components (NGNP, 2008)

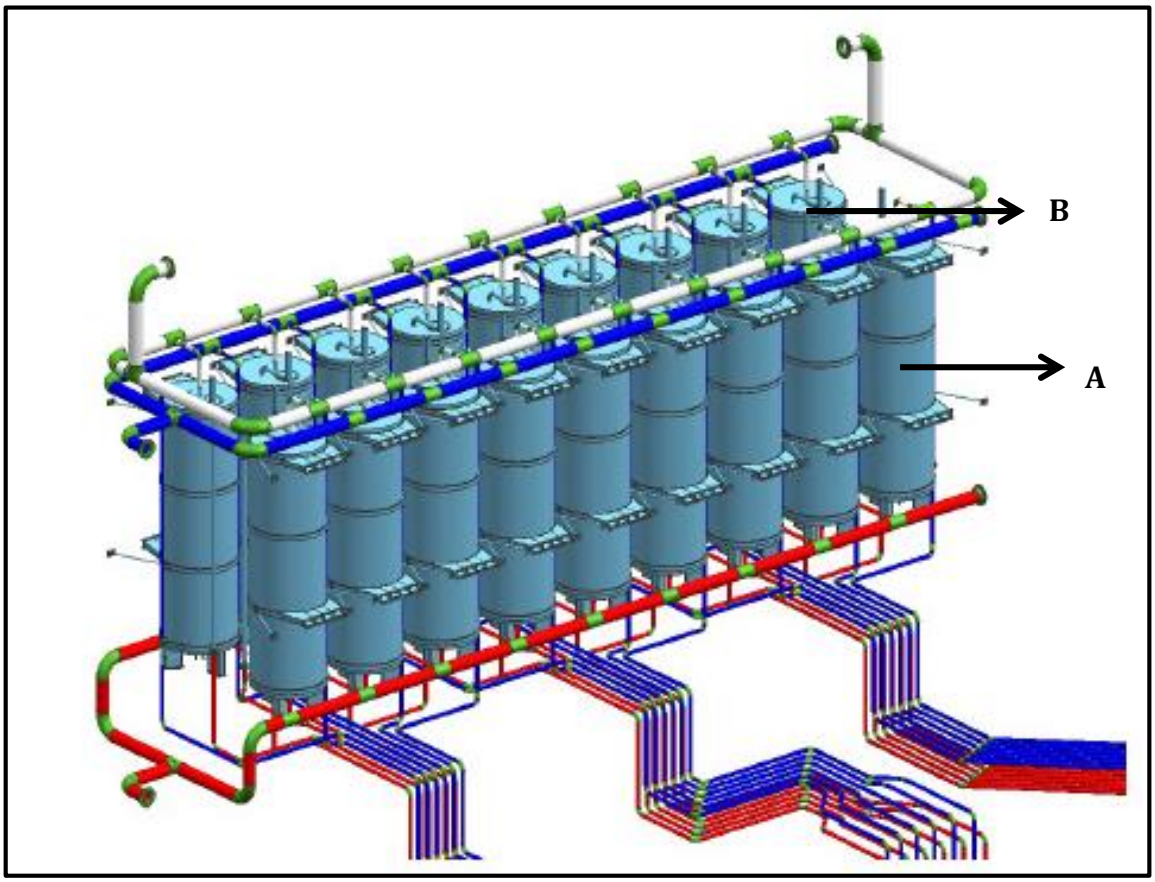

Figure 3-5: Arrangement of A and B trains of water storage tanks, overhead headers for steam release, water inlet to the tank and outlet through the downcomer and piping network for sub-cooled and hot fluid (NGNP, 2008)

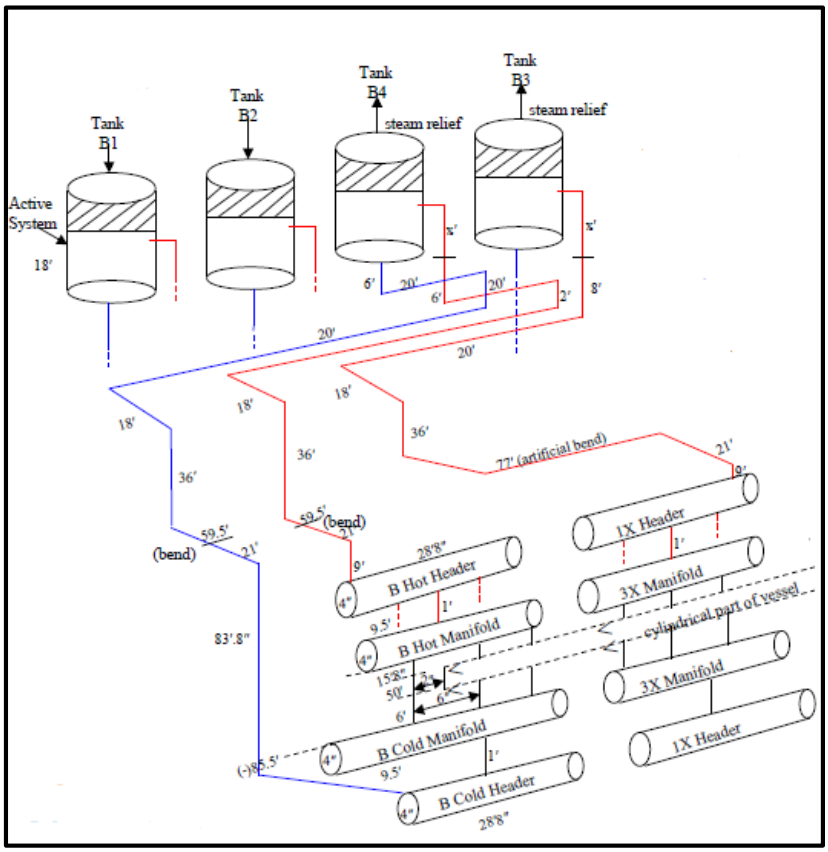

Figure 3-6: Drawing of the pipe network for a Water RCCS System Configuration

In figures 3-4, 3-5 and 3-6, the blue piping represents the cold line while the red piping represents the hot fluid line to the heat sink. Steam relief lines are connected to the storage tanks, hence making the atmosphere the ultimate heat sink.

Normal Operations

The RCCS heat removal mechanism during normal operating conditions is in the active mode, i.e. forced convection. This involves the use of cooling pumps to drive the fluid flow through the cooling pipes in order to absorb decay heat within the reactor

cavity. The water exits the risers at the top through a header and passes into the overhead storage tank.

Off-Normal Operation:

Following a design basis accident scenario such as loss-of-on-site-power (LOOP), it is anticipated that there will be a loss-of-forced-cooling (LOFC), i.e. failure of active mode. The RCCS hence transitions from the active to the passive mode of operation without human intervention. It is a key safety requirement by the NRC to ensure systems such as the RCCS provide sufficient cooling for at least 72 hours after the transient. A decay heat curve as a function of time for thermal reactors is obtained from Ragheb (2013) and represented by Equation 3-1[2]. The decay heat generation is graphically shown in Figure 3-7.

$$\boldsymbol{P_s = P_o 6.48 * 10^{-3}[(t_s{}^{-0.2} - (t_s + t_o)^{-0.2}]} \qquad 3\text{-}1$$

where P_o and $P_s$are the reactor powers before and after shutdown respectively, t_s is the corresponding time past shutdown and t_o is the reactor operation time in days. Figure 3-7 also shows the RCCS heat removal rate as is expected to match the heat generation rate following a transient. At about 100 hours, the core temperature peaks at approximately 1307℃. Hence, the overall heat removal rate exceeds the heat generation rate beyond this point.

[2] Based on the assumption that the reactor operation time $\boldsymbol{t_o}$ is one year after shutdown

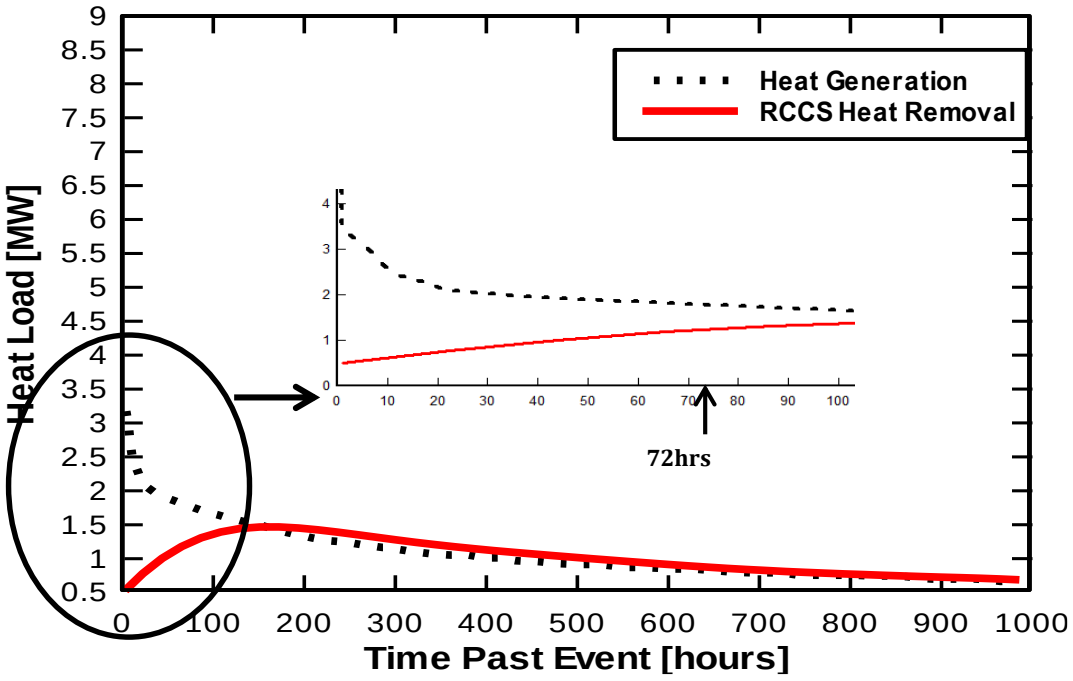

Figure 3-7: Reactor power and RCCS heat removal following a design basis accident [HTGR-86-024]

At elevated water temperatures during the off-normal operating conditions, it is anticipated that the water will reach saturation. Hence the on-set of steam flashing at high elevation (as the standpipes can be as long as 21m in height), initiation of boiling, propagation of the two-phase flow into storage tank and release of generated steam to the atmosphere. US NRC requires that sufficient passive cooling capacity be made available for decay heat removal for at least 72hours.

While during normal operation, convective flow via pumps can compensate for a give system scaling, under natural circulation the thermal-hydraulic performance and scaling thereof is critical in meeting safety requirements. That is, the riser, storage tank, header, chimney, and downcomer have to be scaled with confidence.

3.2. Scaling Approach

As part of the scientific design preceding the engineering design of a scaled test facility, detailed scaling analysis was performed to represent the major thermal-hydraulic processes, “integral and local phenomena”, that will occur in the water-cooled RCCS of the prototype plant. With the components of the RCCS designed to be operational under both single and two-phase flow conditions, a set of scaling parameters (geometric, kinematic and dynamic) were developed to accommodate both phase conditions.

Because of the need to preserve the integral response functions, control volume and boundary flows, a two-level scaling approach was used for the design of the UW test facility. This approach is based on the conservation principles and preserves geometric, kinematic and dynamics similarities between a prototype and model across steady-state and transient conditions in the thermal-hydraulic system. First level involved application of integral scaling parameters to preserve the geometric similarity between the natural circulation loop of the model and the prototype. Second level includes the derivation of sets of similarity groups to describe the underlying physics of natural circulation in the reactor cavity and risers.

3.2.1. Scaling Methodology (UW-RCCS Test Facility)

As a proof of concept, evaluation of the thermal-hydraulic behavior and demonstration of the viability of the water-cooled RCCS, a ¼-scale test facility was designed and built at the University of Wisconsin-Madison under the US DOE NEUP

programs. The UW scaled test facility is designed to show similarity in both the dynamic and kinematic behavior of the full scale design under normal and postulated accident conditions. Hence, experiments performed in the test facility were intended to validate or invalidate the scaling laws. Using scaling studies carried out at Argonne National Laboratory (ANL) as reported by Tzanos and Farmer (2006) for the Natural Convection Shutdown Test Facility (NSTF) as a reference, a set of scaling laws were derived to describe key processes of importance to the design and operation of the prototype design. This included derivation of both geometrical and physical similarity groups.

Since the designed RCCS is gravity-driven, the hydrostatic head is the essential driving force. In the design of similar natural circulation systems, Ishii and Jones (1976) emphasized that full-height need not be preserved as long as key dynamics and kinematics are reproduced. A reduced-height scaling was therefore proposed and was successfully tested in the design of PUMA.

Using the reduce-height, full-pressure scaling as the reference approach, the basis of the reduced length scale is justified by limited space resources as discussed later in this chapter.

Dynamic similarities between the prototype and model can be preserved in the sense that similar sequence of events will be predicted even if length scales are not kept the same. The time scale is however expected to be shorter in a reduced length test facility. For a scaled model, Ishii and Jones (1976) reports that this time scale will be shifted by a factor of,

$$t_R = \frac{l_R}{u_R} \qquad 3\text{-}2$$

where l and u are lengths and velocity and the subscript 'R' represents the ratio between the model (subscript 'm') and prototype (subscript 'p') for a scaled quantity φ.

$$\text{Where: } \varphi_R = \frac{\varphi_{model}}{\varphi_{prototype}} = \frac{\varphi_m}{\varphi_p} \qquad 3\text{-}3$$

In order to represent the dynamics of the driving head for natural circulation flow, Ishii and Kataoka (1984) suggests that the ratio of the length scale in the heated section of the prototype and model be kept at unity i.e.

$$\left[\frac{l_i}{l_o}\right]_R = 1 \qquad 3\text{-}4$$

However if Equation 3-4 is not obtainable, the total non-dimensional length to area ratio i.e. Equation 3-5 should be preserved in order to simulate the fluid transient time over the entire loop.

$$\left[\sum_i \frac{L_i}{A_i}\right]_R = 1 \qquad 3\text{-}5$$

For two-phase natural circulation flow conditions, obtaining the similarity parameters is much more complex. Similarity parameters are derived by non-dimensionalizing the transfer functions obtained from the one-dimensional drift flux model and the perturbation method as developed by Ishii and Zuber (1970) and Tzanos and Farmer (2006).

In order to preserve the key thermal-hydraulic behavior and phenomena, a detailed scaling study was developed based on Ishii and Kataoka (1984) and Tzanos and Farmer (2006) to guide the engineering design of a scaled ¼ RCCS facility.

Based on the reduced-height scaling, an axial length scale $l_R = {}^{1}/_{4}$ was decided by the project team based on space constraint in the high bay of the thermal-hydraulic laboratory at the University of Wisconsin-Madison. Using water as the working fluid preserves the fluid-fluid scaling and hence represents coupled effects in the system.

Taking the heated section as the reference point denoted by subscript o, the temperature rise between scales was preserved i.e.,$\Delta T_{o,R} = 1$, where

$$\Delta T_o = \frac{Q_o}{U_o A_o \rho_o C_p} \qquad 3\text{-}6$$

where $\Delta T_o = (T_{out} - T_{in})$

Recall $Q = m\dot{C_p}\Delta T$ and m =ρUA; thus,

The scaled quantity ratio is $\frac{\Delta T_m}{\Delta T_p} = \frac{Q_{o,m}/Q_{o,p}}{U_{o,m}/U_{o,p} \; A_{o,m}/A_{o,p}}$

Therefore $\Delta T_R \approx \frac{Q_{o,R}}{U_{o,R}\, A_{o,R}} = 1$ 3-7

The cross-section area was also preserved i.e. $A_{o,R} = \frac{A_{o,m}}{A_{o,p}} = 1$ 3-8

Therefore,

$\frac{U_{o,m}}{U_{o,p}} \approx \frac{Q_{o,m}}{Q_{o,p}}$ Thus, $U_{o,R} \approx Q_{o,R}$ 3-9

Assuming the ratio of the bubbles inertia to gravitational head is preserved, i.e., Fr= $\frac{u_o^2\rho}{g l_o \Delta\rho}$, this reduces the similarity relationship between the prototype and model velocities to

$$U_{o,R} \approx \sqrt{l_R} \qquad 3\text{-}10$$

From Equations 3-9 and 3-10,

$$Q_{o,R} \approx U_{o,R} \approx \sqrt{l_R} \qquad 3\text{-}11$$

The power transferred from the rectangular surface, i.e. RPV is represented by;

$$Q_{o,R} = q''_R w_R l_R \qquad 3\text{-}12$$

With $w_R = 1,$ and $Q_{o,R} \approx \sqrt{l_R}$

It implies that

$$\sqrt{l_R} = q''_R l_R \qquad 3\text{-}13$$

Re-writing equation 3-13

$$q''_R \approx 1/\sqrt{l_R} \qquad 3\text{-}14$$

Thus

$$q''_m = 2q''_p \qquad 3\text{-}15$$

A summary of scaled quantities based on derived scaling parameters above is given in Table 3-3.

Table 3-3: Summary of scaled quantities for UW Test Facility

Parameter	Notation	Scaled Ratio
Axial length scale	l_R	0.25
Radial scale	$A_{o,R}$	1
Power	$Q_{o,R} \approx \sqrt{l_R}$	0.5
Heat flux	$q''_R \approx 1/\sqrt{l_R}$	2
Velocity	$U_{o,R} \approx \sqrt{l_R}$	0.5
Temperature difference	ΔT_R	1

Applying the scaled quantities, Table 3-3 provides values obtained based on the design parameters of the prototype.

A sample calculation will be for the scaling of the full scale decay heat power of 1.5 MW corresponding to 227 riser tubes.

Prototype (decay heat load): $Q_{o,p}$ =1.5 MW ~ 227 risers

$Q_{o,R}$ = 0.5 (from scaling derivation above and tabulated in Table 3-3)

For the scaled model with 3 risers, equivalent full scale power $Q_{o,p}$ is 18.82 kW

From Equation 3-3, $Q_{o,R} = \frac{Q_{o,m}}{Q_{o,p}}$

Therefore, the scaled model power $Q_{o,m}$ is 9.91 kW.

Summary of other scaled parameters are shown in Table 3-4.

Table 3-4: Summary of Scaled Values

Parameters	Prototype	Model
Height of riser tube(m)	19.8	4.95
Diameter of riser tube(cm)	2.5	2.5
Tank height(m)	5.49	1.63
Tank diameter (m)	2.74	0.82
Steady state power off RPV(kW)	700	4.63
Transient heat load off RPV	1.5 MW	9.91 kW
Heat flux during transient (kW/m^2)	10	20

3.2.2. Similarity Parameters:

Using simplified balanced equations of one-dimensional conservation laws of mass momentum and energy, a set of non-dimensional groups are formulated to guide the scaling analysis of the UW RCCS natural circulation loop. Deriving similarity parameters, it was assumed the fluid in the riser tubes was Boussinesq-incompressible[3] in the single phase with exception to the gravitational term in the integral momentum equation (i.e., the gravity term is sufficient enough to cause a difference specific weight). The basis for the application of Boussinesq approximation assumption is that the RCCS working fluid (water) is incompressible and there is negligible density change with temperature variation. The buoyancy force is yet the driving force for motion. The approximation further helps in the derivation of the important dimensionless parameters.

A set of dimensionless variables that will be used in non-dimensionalizing the conservation equations are first defined by the relations as follows:

$$u_i = \frac{U_i}{U_r} \qquad 3\text{-}16$$

[3] Illustrates a relationship between the temperature and flow fields

$$u_o = \frac{U_o}{U_r} \quad 3\text{-}17$$

$$u = \frac{U}{U_r} \quad 3\text{-}18$$

$$\theta = \frac{(T - T_o)}{(T_r - T_o)} \quad 3\text{-}19$$

$$l_i = \frac{L_i}{L_r} \quad 3\text{-}20$$

$$d_i = \frac{D_i}{L_r} \quad 3\text{-}21$$

$$z = \frac{Z}{L_r} \quad 3\text{-}22$$

Subscripts *i*, *o* and *r* denote the *i*th section (the heated section being the reference point), the reference value of a quantity (e.g. temperature, pressure) within the heated section relative to the thermal-hydraulic state of the entire loop and the characteristic variable of the reference quantity respectively. The reference parameters are best deduced under steady state conditions. The dimensionless form of the conservation equations can then be expressed as:

Continuity equation:

$$u_i = \frac{A_o}{A_i} u_o \quad 3\text{-}23$$

The integral momentum equation for the standpipes section of the RCCS test loop can be written as:

$$p_{in} + \int_0^{L_h} (\rho g dL)_d = p_{out} + \int_0^{L_h} (\rho g dL)_u + \frac{f_i \rho_i U_i^2 L_i}{2 D_i} + \frac{K_i \rho_i U_i^2}{2} \quad 3\text{-}24$$

The left and right integral in Equation 3-24 represents the gravitational head of the cold leg in the standpipe and the hot leg above the heated section respectively. The fourth and fifth terms on the right side represent the frictional pressure drop and other pressure losses in the ith component. Figure 3-8 provides a sketch that illustrates the cold and hot legs along the vertical length of the risers before the fluid enters the heated section and the above the heated sections respectively. Here, we assume that the density variations are small (in single phase) and the spatial pressure variation is negligible.

Introducing the Boussinesq approximation, we have;

$$\rho(T) = \rho_o - \rho_o\beta(T - T_o) \qquad 3\text{-}25$$

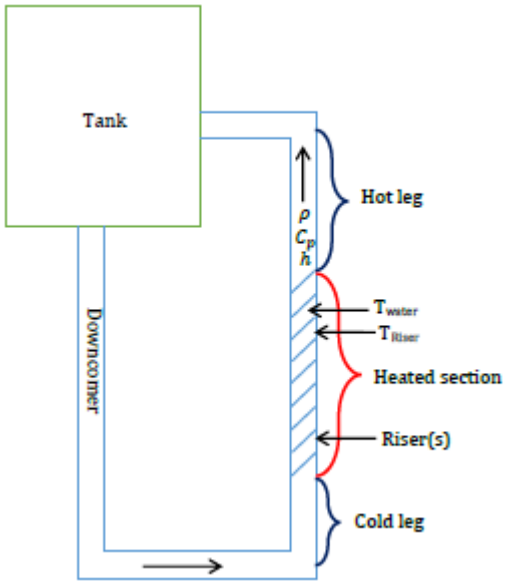

Figure 3-8: Sketch illustrates the cold and hot legs described in the integral momentum equation above.

Substituting the non-dimensional temperature into Equation 3-25 gives;

$$\rho(\theta) = \rho_o - \rho_o\beta\theta(T_r - T_o) \qquad 3\text{-}26$$

Substitution of Equation 3-26 into 3-24, the integral momentum equation between the inlet and outlet regions of the heated section can be re-written as:

$$p_{in} - p_{out} - \rho_o g\beta(T_r - T_o)\int_0^{L_h}(\theta dL)_d = \frac{f_i\rho_i U_i^2 L_i}{2D_i} + \frac{K_i\rho_i U_i^2}{2} - \rho_o g\beta(T_r - T_o)\int_0^{L_h}(\theta dL)_u \qquad 3\text{-}27$$

Substituting the non-dimensional variables for L, L_i and U_i into Equation 3-27 and dividing through by $\rho_o U_r^2$ gives,

$$\frac{\Delta p}{\rho_o U_r^2.} - \frac{\rho_o g\beta(T_r - T_o)}{\rho_o U_r^2}L_r\int_0^{l_h}(\theta dl)_d = \frac{f_i\rho_i u_i^2 U_r^2 l_i L_r}{\rho_o U_r^2.2d_i L_r} + \frac{K_i\rho_i u_i^2 U_r^2}{2.\rho_o U_r^2} - \frac{\rho_o g\beta(T_r - T_o)}{\rho_o U_r^2}L_r\int_0^{l_h}(\theta dl)_u \qquad 3\text{-}28$$

Cancelling out like terms, the second term outside the integral on the left side and third term outside the integral on the right side in Equation 3-28 represent a dimensionless scaling π group i.e. Richardson number Ri, defined as

$$Ri \equiv \frac{g\beta(T_r - T_o)L_r}{U_r^2} = \frac{buoyancy\ forces}{inertia\ forces} \qquad 3\text{-}29$$

Re-arranging Equation 3-28 yields,

$$\frac{\Delta p}{\rho_o U_r^2.} - Ri\left[\int_0^{l_h}(\theta dl)_d - \int_0^{l_h}(\theta dl)_u\right] = \frac{1}{2\rho_o}\left[\frac{f_i\rho_i u_i^2 l_i}{d_i} + K_i\rho_i u_i^2\right] \qquad 3\text{-}30$$

But from continuity equation, $u_i = \frac{A_o}{A_i}u_o$

Equation 3-30 therefore becomes,

$$\frac{\Delta p}{\rho_o U_r^2.} - Ri\left[\int_0^{l_h}(\theta dl)_d - \int_0^{l_h}(\theta dl)_u\right] = \frac{u_o^2}{2\rho_o}\left(\frac{A_o}{A_i}\right)^2\left[\frac{f_i\rho_i l_i}{d_i} + K_i\rho_i\right] \qquad 3\text{-}31$$

The overall integral momentum equation for all the *i*th components is hence given as,

$$\frac{\Delta p}{\rho_o U_r^2} - Ri\left[\int_0^{l_h}(\theta dl)_d - \int_0^{l_h}(\theta dl)_u\right] = \frac{u_o^2}{2\rho_o}\sum\left\{\left[\frac{f_i \rho_i l_i}{d_i} + K_i \rho_i\right]\left(\frac{A_o}{A_i}\right)^2\right\} \quad 3\text{-}32$$

From Equation 3-32, the friction number $Fi=\sum_i(\frac{fl}{d} + K)_i$ can be obtained from the term on the RHS.

Fluid energy equation at steady-state for water in the riser tube:

$$\rho C_p U_i \frac{dT}{dZ} = \frac{4h}{D}(T_{riser} - T_{water}) \quad 3\text{-}33$$

Substituting the non-dimensional parameters, the non-dimensional form of the fluid energy equation is given as,

$$u_o \frac{A_o}{A_i}\frac{d\theta_{water}}{dz} = \frac{4hL_r}{\rho C_p U_r D_{pipe}}(\theta_{riser} - \theta_{water}) \quad 3\text{-}34$$

From the fluid energy equation, we can establish a relationship between the wall and axial convection terms. This represents the modified Stanton number *St* as

$$St = \frac{4hL_r}{\rho C_p U_r D} = \frac{heat\ transferred\ to\ the\ fluid}{thermal\ capacity\ of\ the\ fluid} \quad 3\text{-}35$$

(a) Processes and Phenomena

Heat Transfer: Preliminary CFD simulation results indicated that the significant heat transfer mechanism is via radiative and convective modes of heat transfer from the RPV wall to the surrounding air cavity and riser tubes (Albiston, 2011). Developing scaling relations between the prototype and the model, a set of similarity parameters are established to account for the single phase flow conditions. The total heat transfer is composed of convective and radiative heat transfer and is defined as

$$Q(t) \approx \underbrace{A_c h_{cav}\left(T_{rpv} - T_{riser}\right)}_{\text{Convection}} + \underbrace{A_{rad}\varepsilon\sigma(T_{rpv}^4 - T_{riser}^4)}_{\text{Radiation}} \qquad 3\text{-}36$$

Scaling analysis of the local processes is within the bounds of the set criteria of the integral system scaling used for the geometry. The scaled parameters derived above were used to guide the design and construction of the ¼ scale water-cooled UW test facility as described in the next section.

3.3. Scaled Water-cooled RCCS Test Facility

3.3.1. Facility Description:

In response to the design requirements of the prototype RCCS, the ¼ axially scaled RCCS test facility was jointly designed by University of Wisconsin-Madison and University of Idaho-Idaho Falls using the scaling parameters derived in section 3.2. To simulate the decay heat rejected from the RPV, a bank of 34 radiant heaters within an enclosed cavity represent the heat flux off a 5° wedge from the RPV to the concrete wall of the full-scale design as shown in Figure 3-9.

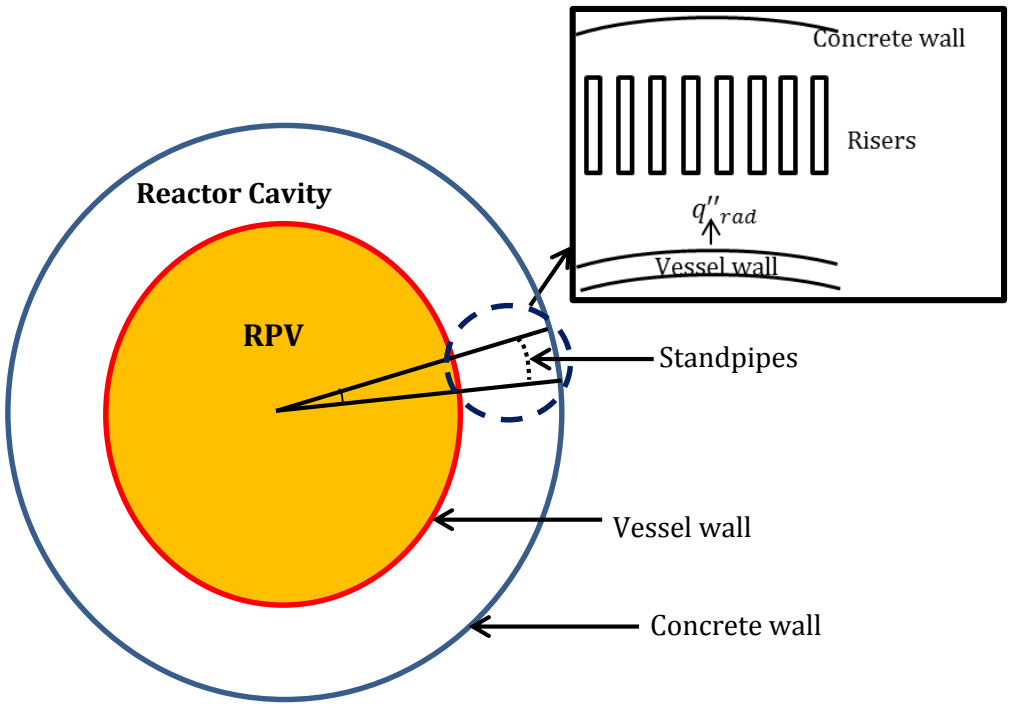

Figure 3-9: 5˚ wedges from the RPV to the concrete wall (*inse*t: risers lining the walls of concrete wall)

The proximity of the heaters to the risers in the test facility was as a result of CFD parametric studies. The goal was to achieve uniform heat distribution and minimize heat loss to the environment.

Of the 227 riser tubes in the prototype, 3 riser tubes were designed for in the model RCCS, representing a 5° sectorial cut from the RPV. The scaled test facility was built in the high bay of the Thermal-hydraulic Laboratory of the Department of Mechanical Engineering at the University of Wisconsin-Madison. The entire test facility stands at 7.6m (25ft) in height. This consists of a 320 gallon (1200 L) storage tank, a down-comer connecting the storage tank to the bottom of three 4.95m (16.2ft) length riser tubes; 3m (10ft) of the riser tubes is heated by two banks of 34 radiant heaters

(manufactured by Mellen Heater Company). The heaters are wound on flat ceramic plates, each measuring 12” x 6” x 0.75” and with a capacity of 1,250 W and maximum temperature of 1,100℃. The three riser tubes are connected through manifolds at the top and bottom and have fins welded perpendicular to each riser within the heated section, i.e. 3m length. The fins surface enhances heat transfer and ensures there is no thermal radiation line of sight between the RPV and the concrete wall behind the finned riser tubes. An illustration of the scaled test facility is shown in Figure 3-10 while Figure 3-11 shows details of the heated cavity.

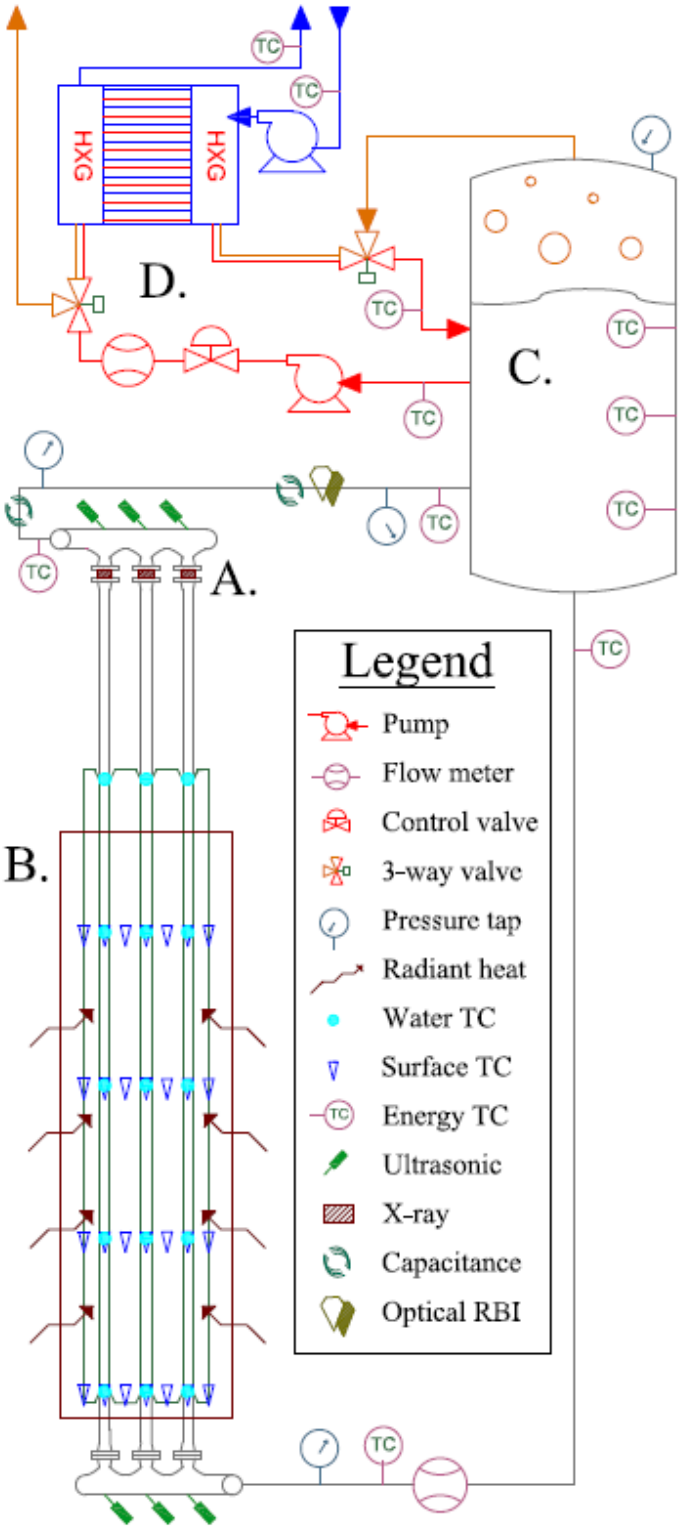

Figure 3-10: Schematic of a Scaled Water-Cooled RCCS at the University of Wisconsin-Madison [*Lisowski et.al, 2014*]

(a)

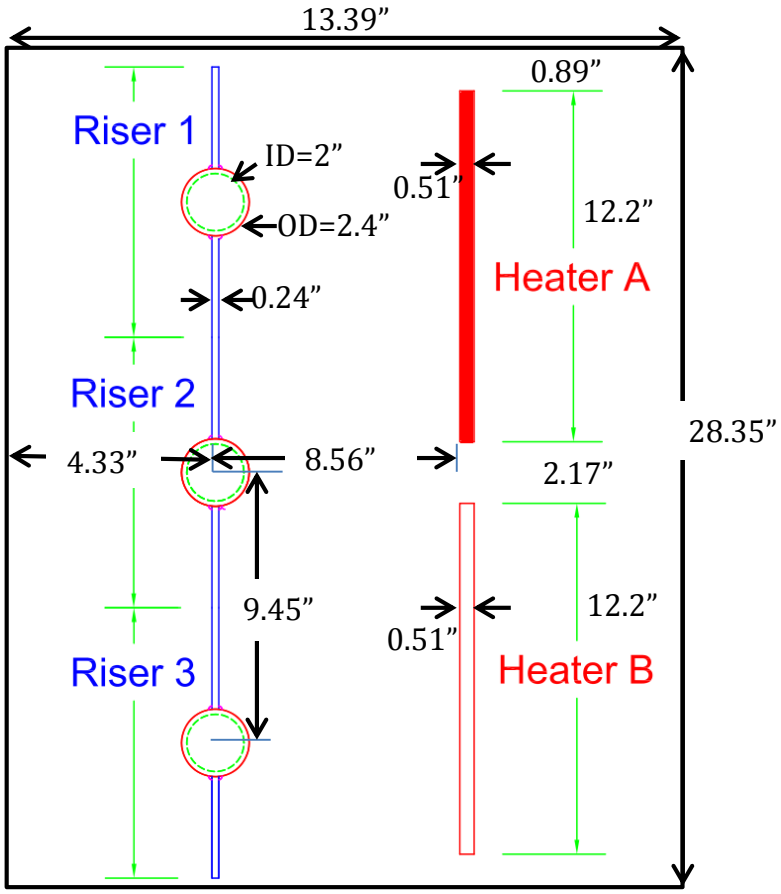

(b)

Figure 3-11: (a) Plan view of heated cavity **(b)** Diagram of heater, pipe and fin configuration within the heated cavity

3.3.2. Thermal Insulation

The entire pipe network, including the storage tank were thermally insulated in order to minimize heat loss to the surrounding and to be able to evaluate the heat removal performance of the RCCS. A combination of K-flex, Pyrogel, Zirca-18 and Microtherm insulation materials were used based on the low thermal conductivity, judgment and consideration of areas with anticipated high, medium and low temperatures regions. Table 3-5 highlights key features of different insulation materials and their positioning along the test facility.

Table 3-5 : Technical features of different insulation materials

	K-flex	**1" block micro-therm**	**2" Zircal-18**	**0.25" Pyrogel – XT**
Thermal Conductivity (W/mK)	0.036	0.015 – 0.034	0.07(@ 200C) - 0.1(@ 600C)	0.02 – 0.089
Operating temperature range (°C)	-45 – 104	-170 – 1000	1100	-40 - 650
Location within the test facility	Storage tank and all piping outside heated cavity	Adjacent to radiant heaters	Behind radiant heaters	Rear cavity (behind riser tubes)
Advantages	Widely used for commercial and industrial HVAC applications due to high insulation performance and low cost	Low thermal conductivity at very high temperatures, remains stable at high temperatures	High temperature tolerance, high insulation performance and ideal for fireproofing and heat processing applications	Flexible insulation material for high temperature applications, low thermal conductivity

Figure 3-12 gives an overview of the entire test facility and also highlights some key areas.

Figure 3-12: (a) Facility overview (b)Heated cavity (c) Well insulated overhead water tank and upper header (d) Lower header and three riser tubes

3.3.3. Instrumentation

To account for dynamic changes of state variables (P, T, V, E), sensors and process control devices are positioned at key locations along the test loop to detect and measure these variables. Numerous thermocouples are used to obtain temperature measurement in order to characterize thermal energy content and distribution. Additional instrumentation to measure volumetric flow rate needed to quantify the injection fluxes, differential pressure for measuring the changes in water level, gas space pressure transmitters and phase sensors to guide in determining the thermodynamic state of the steam and voids in the storage tank in two-phase are all discussed in this section.

3.3.3.1. Thermocouples

Variations in temperature along the test section on both structural surface (pipes, fins and tank) and bulk flow (inside pipe and air cavity) as a result of energy transferred from the heaters were measured using Type-K Omega thermocouples (TC) junctions. A total of 64 thermocouples were used. Surface measurement thermocouples are 20 gauge Type-K TCs (*model no.: HH-K-20-50*) while bulk fluid thermocouples are $1/8^{th}$ in diameter and 12 inches long Type-K Inconel TCs (*model no.: HKMQIN-125G-12*). The TCs are capable of detecting temperatures as high as 1250°C. Figure 3-13 shows example of welded TCs for surface and bulk fluid temperature measurements.

(a)

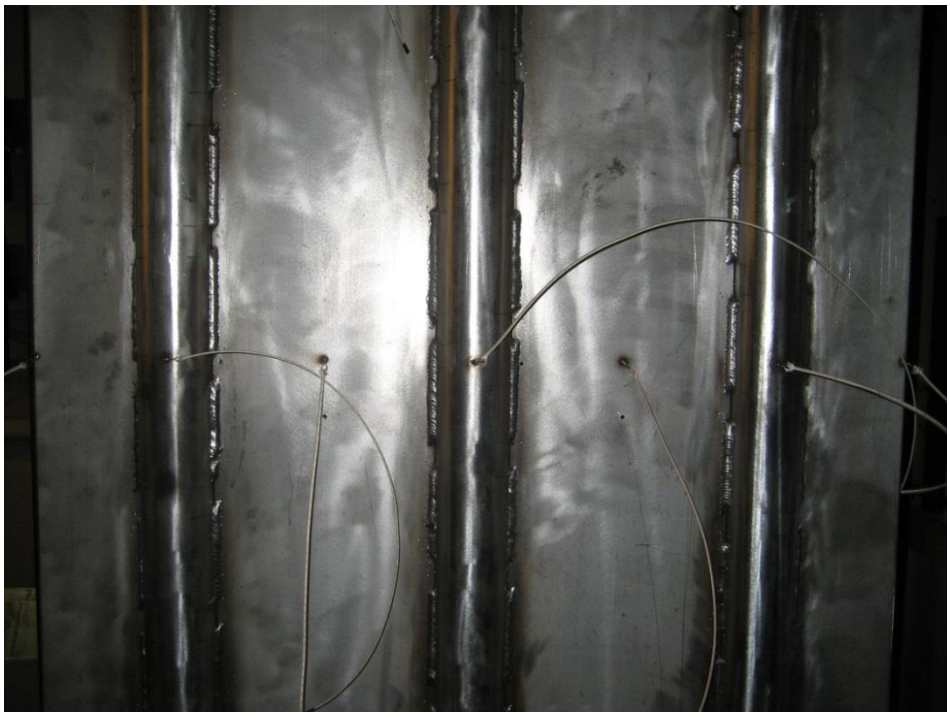

(b)

Figure 3-13 : (a) Thermocouple welds to riser tube surface and attached fins. (b) Thermocouple welds to capture bulk flow temperature at the lower header.

Calibration Procedure

For accuracy of measurements, each TC was calibrated with high precision Platinum Resistance Temperature Detector (P-RTD), Model no. 5624. Uncertainty associated with the TCs was reduced from a factory accuracy of ± 1.1℃ to ± 0.2℃ after using the P-RTD.

3.3.3.2. Optical Phase Sensor (RBI)

Manufactured by *RBI Instrumentation* in France, the optical probe is capable of providing accurate measurements of void fraction, bubble diameter, bubble rise velocity, and interfacial area (RBI, 2012).

Key components of the RBI optical device include:

(a) A double sapphire-tip optical fiber probe: Designed with a prism configuration, the optical probe is used for phase detection based on the discrete changes in refractive index of two phases i.e. Snell's Descartes law of refraction. Each of the two sapphire tips measure $25\mu m$ in diameter and both are 500 μm apart.

(b) An Opto-electronic unit: Connected directly to the double-tip optical fibers, the Opto-electronic unit receives the feedback response and integrates the phase indicator functions of the emitted light using a thresholding operation method.

(c) Data acquisition box: The data acquisition box collects and converts the analog signals into TTL signals which are then amplified and transformed into output signals of **0V** and **5V** corresponding to water and air accordingly.

Figures 3-14 and 3-15b highlight the components of the optical phase sensor and the phase indicating function for signal processing.

(a) 

(b) 

(c) 

Figure 3-14: Components of RBI two-phase flow optical instrumentation.(a) Dual-tip phase sensor probe with 0.5mm sapphire fibers (b)Opto-electronic unit and (c) data acquisition box

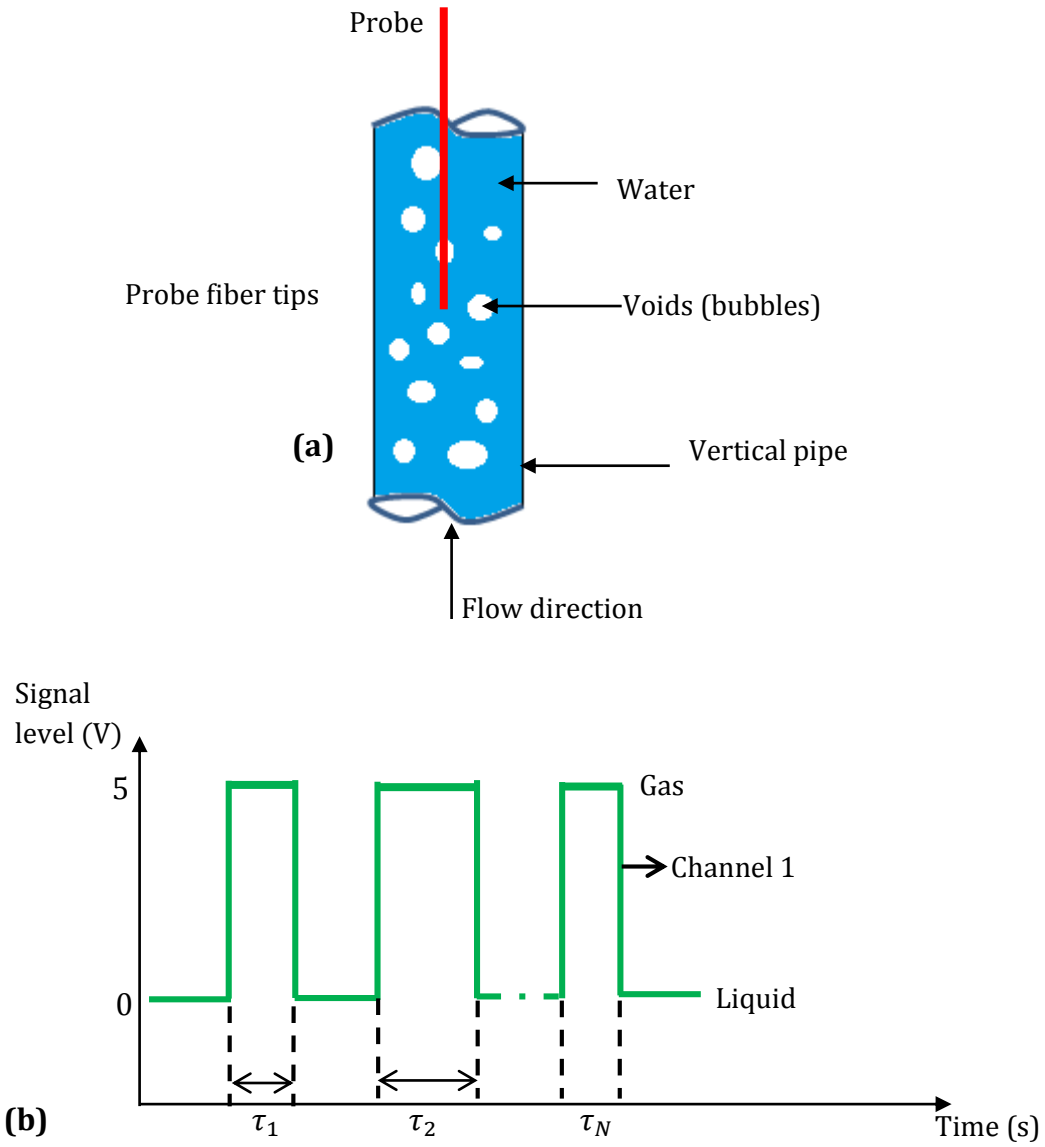

Figure 3-15: (a) Schematic of probe positioning in a vertical pipe section (b) Phase indicating function for the gas and liquid phase from individual channels.

To observe and capture changes in hydrodynamics conditions in two phase flow regime, a double sapphire tip intrusive optical probe shown in Figure 3-13(a) was used. Using statistical methods, represented by Equations 3-41 to 3-44, local measurements such as void fraction (α), bubble rise velocity (V_b), bubble diameter

(d_b) and interfacial area (A_i) at superficial gas velocities can be computed and analyzed.

$$\alpha = \frac{1}{t_{aq}} \sum_{i=1}^{n} \tau_i \quad 3.41$$

$$U_b = \frac{d}{t_f} \quad 3.42$$

$$A_i = \frac{4 f_{int}}{U_b} \quad 3.43$$

$$d_b = \frac{6\alpha}{A_i} \quad 3.44$$

where t_{aq} (s) is the active acquisition time, d is the length scale between sapphire tip1 and tip2 specified as $500\mu m$, t_f is the average transit time of bubble from sapphire tip1 to tip2, and d_b representing the bubble diameter is Sauter mean diameter, i.e. diameter of the bubble whose volume/surface ratio is the same as that calculated for all bubbles observed during the test. f_{int} is the interference frequency defined as the ratio of number of bubbles acquired to total acquisition time t_{aq}.

Operating Principle:

The double tip optical probe is vertically positioned opposite the direction of flow as shown in Figure 3-14a. Under two-phase flow conditions, i.e. water and air, the intrusive double tip probe penetrates the bubbles. A fraction of incident light beams strike the walls of the fiber (refractive index n_1=1.762) at a 45 degree angle. At a

critical angle θ_c when no light is transmitted or refracted into the surrounding medium, the refraction angle must be 90 degree normal to the surface.

$n_1 \sin\theta_i = n_2 \sin\theta_r$ (Snell's Descartes law of refraction)

where n_1, n_2 are the refractive indices of the incident material and surrounding medium respectively and θ_i, θ_r are the incident and refractive or reflective angles respectively. The critical angle $\theta_c = sin^{-1}\left(\frac{n_2}{n_1}\right)$ for air and water are then calculated as 34.6° and 49° respectively. Therefore, when the ray of light strikes the interface of the sapphire fiber ($n_1 = 1.762$) and air ($n_2 = 1.0$), the light is completely reflected back into the Opto-electronic unit i.e. $\theta_i > \theta_c$while at the boundary of the fiber and water ($n_2 = 1.33$), a fraction of the incident light is refracted i.e. $\theta_i < \theta_c$.

Capable of operating under high temperature and pressures, the choice of the point measurement optical device is premised on short response times and small dimensions of contact areas and designed to have minimal flow intrusiveness. This makes it a suitable detector for phase changes compared to resistive and capacitive probes.

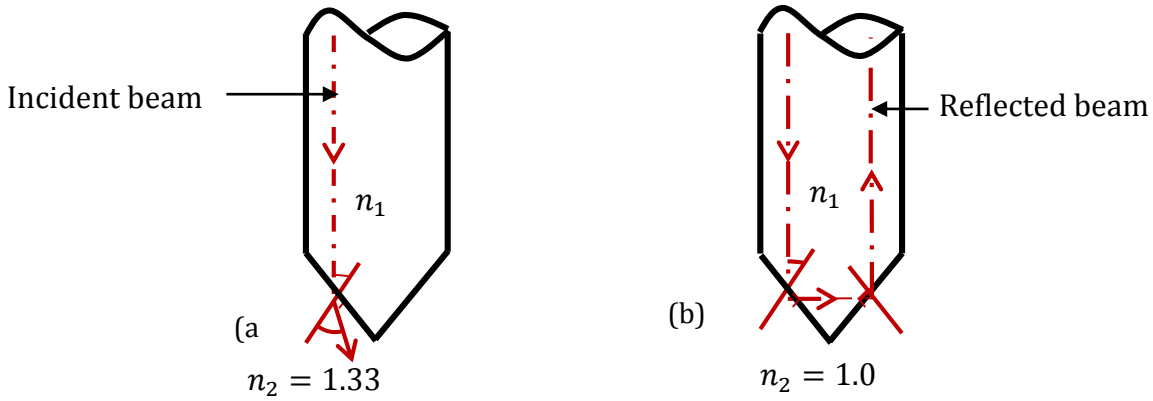

Figure 3-16: Graphical description of the operating principle of the two phase optical probe

Calibration Procedure

Built to specification, the distance between both fiber tips is $500\mu m$. Prior to the commencement of its use and full scale utilization, the spatial location of each fiber was defined and the phase indicators (0V and 5V) were set. Acquisition parameters were defined in the manufacturer provided ISO software. These parameters include the distance between tips, mode of acquisition, and acquisition termination criteria (acquisition time or number of bubbles encountered). A separate effect test was then carried using a 1" acrylic tube with stagnant water. The optical probe was fixed at the top of the column perpendicular to the flow direction as shown in Figure 3-12a. Injecting compressed air through a diffuser with known flow rate from the bottom of the test column, air bubbles were generated and flowed in the direction of the optical probe.

Local measurements of the void fraction, bubble velocity and bubble diameter were computed and analyzed. The actual bubble rise velocity obtained using the RBI probe

was theoretically compared to correlations in Comolet (1979). Visualization studies were also performed to determine the average bubble diameter and compared with RBI obtained bubble diameter. Results from the bench-top separate effect tests showed less that 2% difference as detailed in Table 3-7.

$$U_b = \sqrt{0.52gd_b + 2.14\,\frac{\sigma_t}{\rho_w d_b}} \quad (0.8\text{mm} < d_b < 10\text{mm}) \qquad 3\text{-}51$$

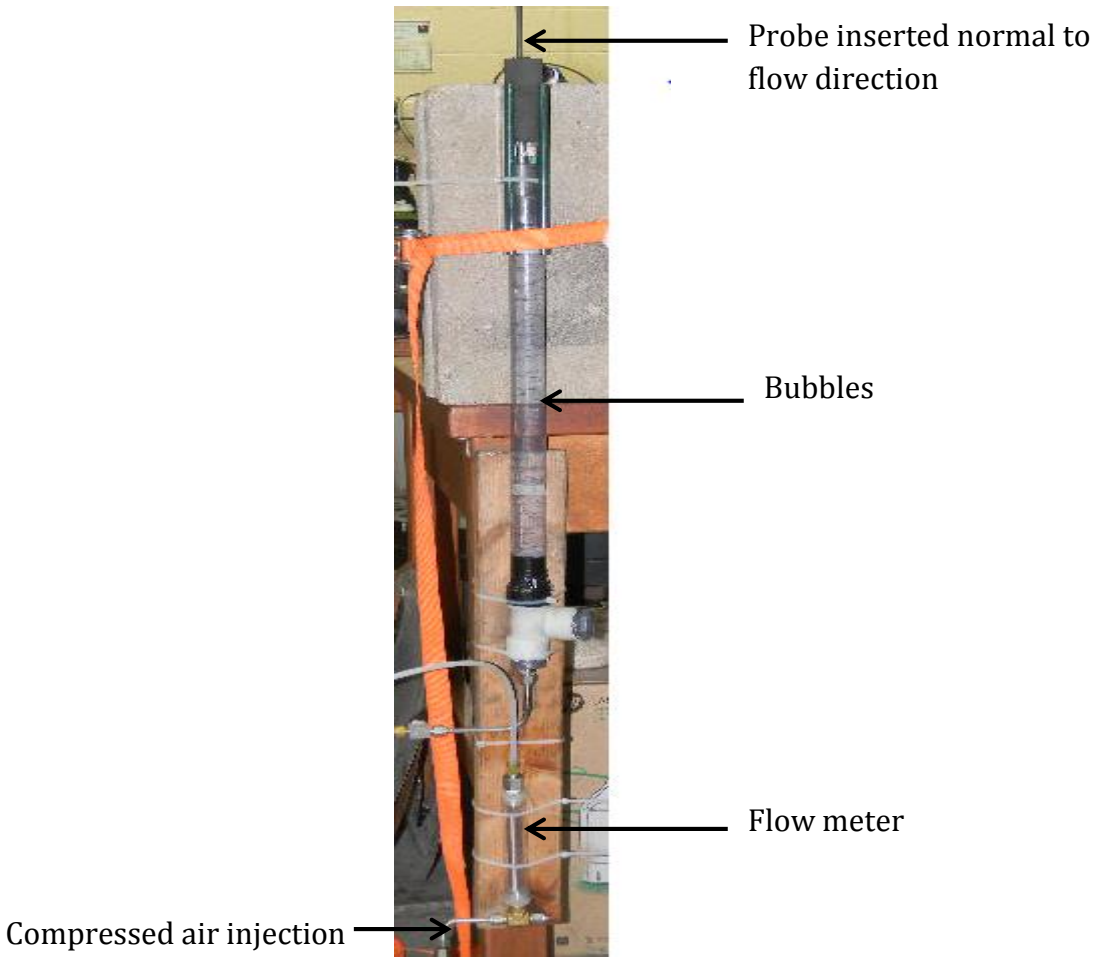

Figure 3-17: Bench-top separate effect test of optical sensor probe i.e. RBI

Table 3-6: Bubble diameter and bubble rise velocity from bench-top separate effect test with RBI Instrument

Q (ml/min)	Average predicted d_b (mm)	Average RBI d_b (mm)	Average predicted U_b (m/s)	Average RBI U_b (m/s)	Acquisition time (s)
30	3.0	3.13	0.26	0.29	500
45	3.2	3.53	0.25	0.32	500

A second verification test was performed in the RCCS test facility. The RBI probe was in the vertical section close to the tank inlet as shown in Figure 3-18. Similar to the bench-top test, compressed air was injected from the bottom (lower header). Visualization studies could not be performed since there were no viewing points along the facility piping. However, with known volumetric flow rates, void fractions were calculated. Table 3-8 details the result from the second verification test in the RCCS test facility.

Table 3-7: Void fraction verification in the RCCS test facility

Q_g (L/min)	Calculated average void fraction[4] α (%)	RBI measured average α (%)
4	2.3	2.31
8	4.7	4.74

Figure 3-18 shows the signal visualization interface for the RBI-ISO software after data acquisition.

[4] $V_g = \frac{\alpha}{1-\alpha} 0.35(gd)^{1/2}$ where $Q = V_g/A$ (*Whalley, 1987*)

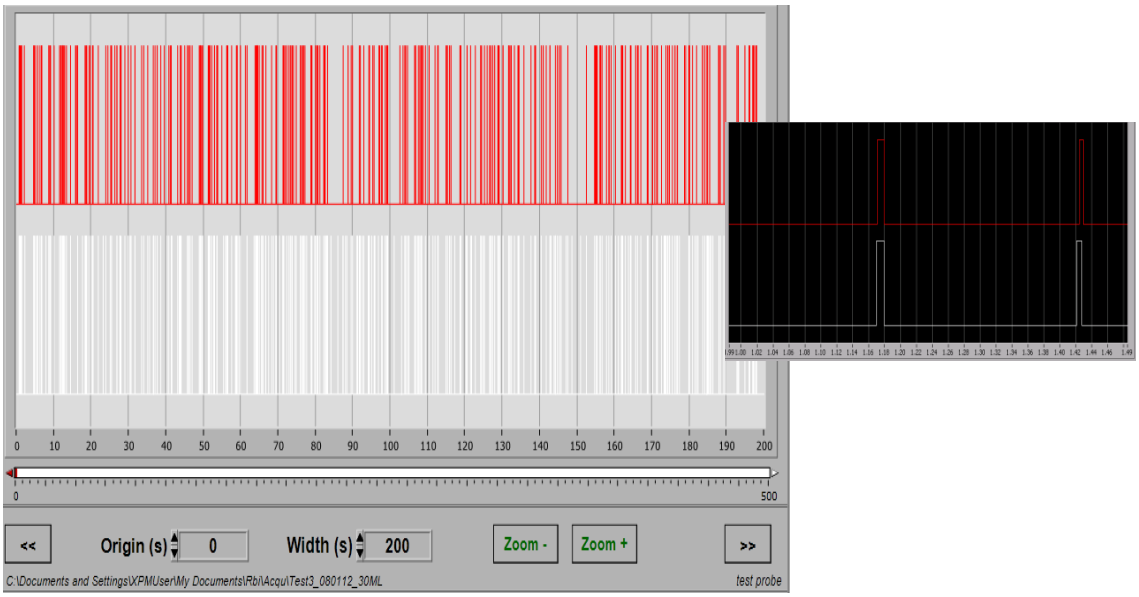

Figure 3-18: Signal visualization interface. (*Inset: zoomed signals*)

Measurements:

Following the completion of the verification separate effect tests, it was discovered that data acquisition using the ISO software was limited to creating a single output file with single thermal-hydraulic information (bubble size etc.) over the lifetime of the test without creating a time history. To account for changes in flow regimes over the course of the integral tests, multiple acquisitions were carried out and results averaged over multiple 10 second periods. Acquisition over a short time frame also prevented a buffer overflow software problem that was initially encountered over extended run-time. A MATLAB script was then written to combine the hundreds of multiple 10s files and post-process accordingly to create a time history and transition regimes. Data from each optical fiber was sampled at about 10 kHz.

The positioning of the optical probe in the test facility was technically guided by our judgment of expected two-phase flow region and a vertical section within the UW natural circulation loop as shown in Figure 3-19.

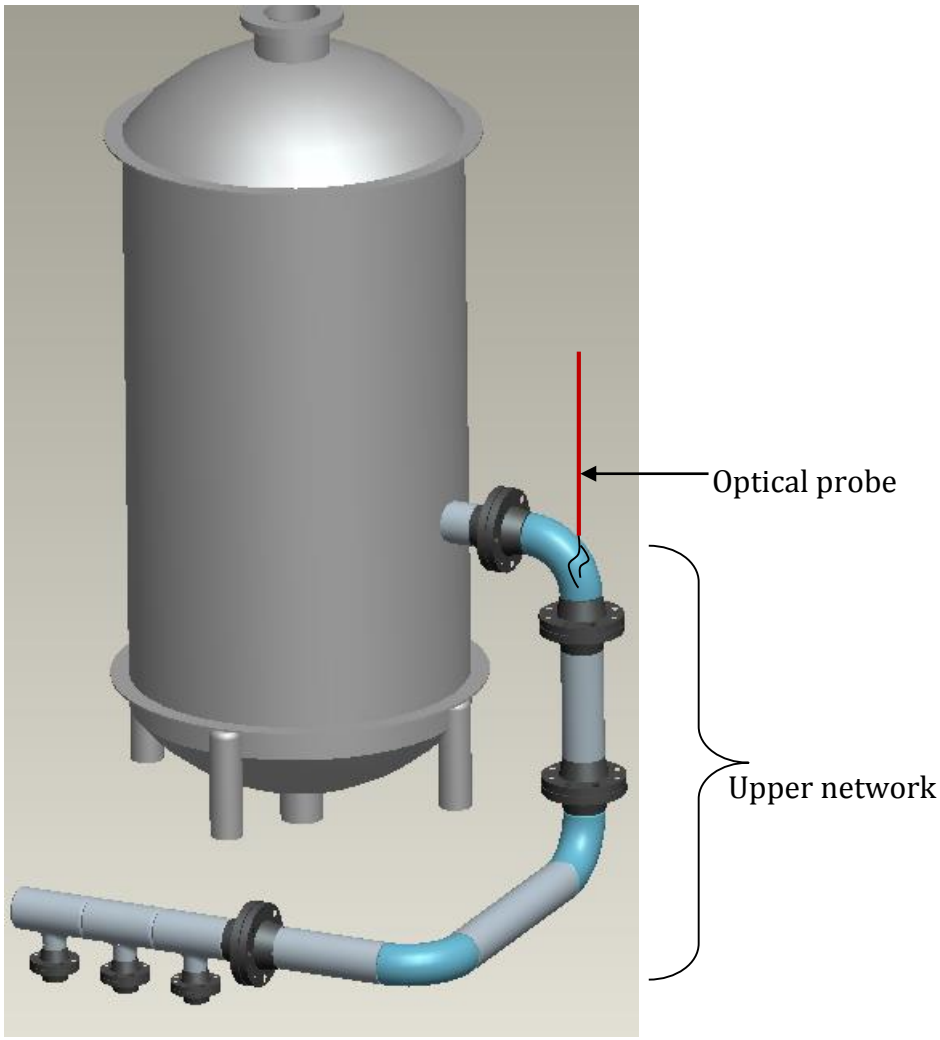

Figure 3-19: RBI Probe vertically fixed normal to direction of flow in the upper network

In addition to data from other thermal-hydraulic processes, key physical parameters such as local void fraction α and bubble rise velocity will guide our

understanding of the integrated system behavior and determination of flow distribution under two-phase flow conditions. Increasing void fraction could have significant changes on the dynamics of the system and affect the heat transfer characteristics. Using the optical probe, we can also deduce the liquid and superficial gas velocities.

3.3.3.3. Magnetic Flow Meter

Injection fluxes were measured with two 3'' magnetic flow meter (*model: Opti-flux 1000, C-RK20-C006*) located at the loop inlet (i.e. bottom of the test-section between the lower network and the lower header) and a 0.5" magnetic flow meter located on the secondary loop along the HXG network to measure flow rate during steady state operations. The 3" magnetic flow meter was manufactured by Flocat (Krone) while the 0.5" flow meter was manufactured by Rosemount. The operations of the magnetic flow meters are coupled with two signal converters (*model no: C-RK75-A004* and *model no*: *8712C* respectively). The signal converter for the 3" magnetic flow meter has a set range of$\pm$ 600 L/min. Both flow meters only have the ability to measure flow rates of 80% of the maximum set-point range. Table 3-9 summarizes the instrumentations and the associated uncertainties in measurement.

(a)

(b)

Figure 3-20 : (a): Magnetic flow meter and signal converter (b): Showing the location of the magnetic flow meter

The positions of all instruments described above are summarized in Table 3-8.

Table 3-8: Summary of instrumentation and measuring parameters with uncertainties

Instrumentation	Parameter	Location	Uncertainty
Type K Omega Thermocouples	Temperature	Fluid Centerline	± 0.2℃
Type K Omega Thermocouples	Temperature	Structure surface	± 1.1℃
Flocat 3" Magnetic flow Meter	System Flow Rate	Loop inlet	$\pm 0.2\% + 1\text{mm/s}$
Rosemount 0.5" Magnetic flow meter	Hot leg flow rate	HXG loop	$\pm 0.5\%$
Differential Pressure Transmitter	Pressure drop	Between upper header outlet and tank inlet	<0.2%
RBI Optical phase sensor	Void fraction	Vertical section in Chimney	<0.5%

3.3.4. Data Acquisition System

A National Instrument Data Acquisition System (NI-DAQ) is being used. A modularly configured NI chassis hardware (*model: SCXI-1000*) has 4 expansion card slots to which all the instrumentation devices are connected. Two analogue input cards (*model: SCXI-1102*) allow 32 TCs to be scanned per card for a maximum channel count of 64. An analogue output module (*model: SCXI-1124*) and digital SSR module (*model: SCXI-1163R*) are used for the Eurotherm power controllers (*model: TE10P*) control signal and digital relay respectively.

The NI-DAQ is controlled from a PC via a PCI card (*model: PCI-6221*). This allows data to be sent and stored in the PC memory. Communication through the PCI card and the NI hardware is through ASCII strings. LabVIEW software is installed and programmed on the PC to output data file containing all required measurements. Because the NI-DAQ is equipped with cold junction compensation, it can precisely and simultaneously measure TC readings within the response time of the TC.

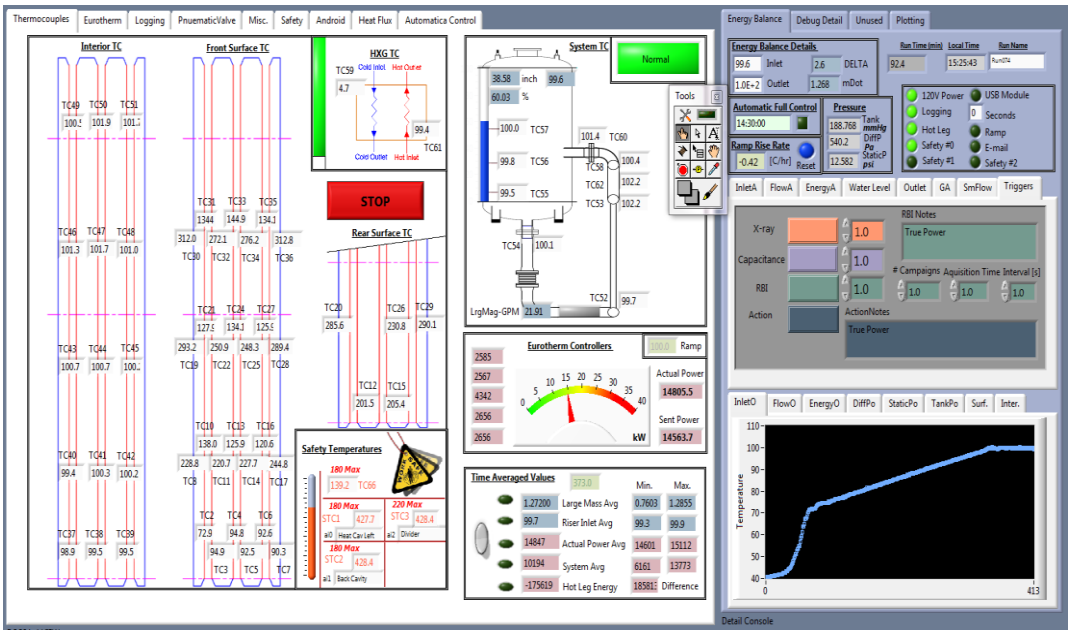

Figure 3-21: Screenshot of programmed LabVIEW software interface on PC showing details on TCs along the test loop

Experimental data obtained from installed instruments will be used to validate the system code model and also the derived scaling laws. This represents a significant part of the integrated scaling methodology.

3.3.5. Modeling and Simulation (RELAP5)

To support thermal-hydraulic and system analysis code assessment (V&V and UQ) efforts and licensing process, RELAP5-MOD 3.5 is used to validate the design and evaluate the thermal-hydraulic performance of the water-cooled RCCS. RELAP5 is here also used as a computational integral (system) scale modeling and simulation tool and forms a part of the scaling methodology development. This is a consistent approach as that used by Ransom and Ishii. RELAP5/MOD3.5 is a computer code mostly used for

the thermal-hydraulic analysis of transients and small-break type accidents in LWRs. This version of the code was obtained from Innovative Systems Software (ISS). It has advanced architecture which improves computational speed and increases its capability to simulate more detailed plant models and transients, improved thermo-physical properties and integrated uncertainty analysis.

The RCCS is modeled as a stand-alone integral test without any other reactor component. A detailed input deck was developed to model and simulate a wide range of thermal-hydraulic conditions under both normal and off-normal, single and two-phase flow conditions as will be discussed in Chapter 4. A RELAP5 nodalization diagram representing the ¼-scaled RCCS test facility is shown in Figure 3-22. This nodalization diagram was used to guide the development of the FORTRAN based input deck. The RELAP5 model was developed based on the scaled parameters for the scaled RCCS.

Each nodalized volume (component) and pipe as shown in the figure was estimated to have same dimensions as the ¼-scaled experimental RCCS loop and the RELAP5 model was used to validate the scaling parameters and assess the code scale-up-scale-down capability.

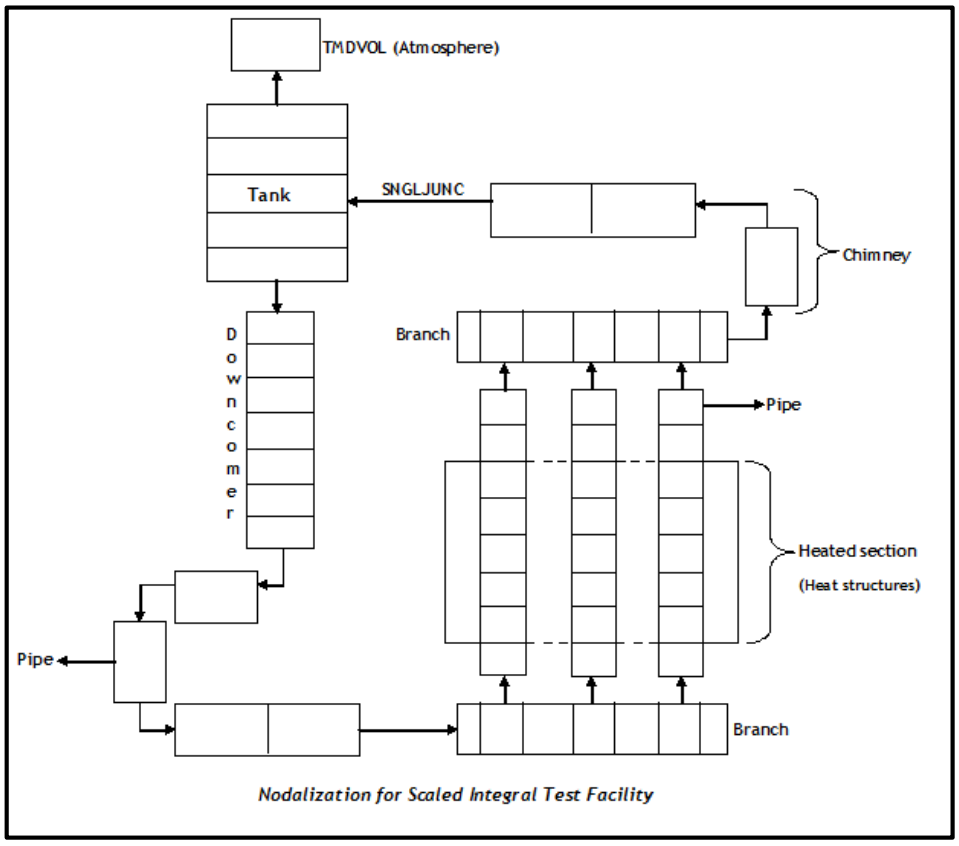

Figure 3-22: Nodalization diagram for UW ¼ scaled water-cooled Reactor Cavity Cooling System (RCCS)

CHAPTER 4: RCCS EXPERIMENTAL PROCEDURE

4.1. Overview: Established Experimental Procedure

Depending on the conditions of the experiment and parameters to be investigated, the desired tank volume (inventory) is attained either by filling up or draining. Also, the desired power is set and detailed start-up notes are taken. With a running integrated Lab-VIEW program on a personal computer (PC), all instrumentation, working status and necessary flow parameters can be monitored and recorded as the experiment progresses. The discussion below briefly outlines the experimental method and sequence of operation that was adopted for a typical test.

(i) Set the specific experiment desired power on the Eurotherm tab of the Lab-VIEW program.

(ii) Record initial system conditions (temperature and storage tank volume) and a short description of the experiment in the specified window on the “Logging tab” of the Lab-VIEW program and also specify the run number e.g. Run011. Hit the write button to create a “.csv” file in the experiment directory.

(iii) Enable the 120V power switch mounted on the wall. This sends power to the Eurotherm controllers.

(iv) Enable the five Eurotherm controllers. This automatically turns on the 34 radiant heaters.

(v) Enable the power ramp up button in the Eurotherm tab. All experiments are ramped up over a 60 minute period to the total desired power specified in "1". This gradual increase in power is to prevent damage to the heaters and the controllers.

(vi) If steady state single phase test is performed, the HXG is turned on once the bulk fluid temperature reaches steady state criteria of 30°C (*see section 4.1.1 for full HXG operation*). The system is then maintained at steady state for approximately 4 hours once a 30°C inlet temperature condition is reached. For transient two phase test, a HXG is used as a condenser only after saturation temperature is reached (*see section 4.1.2*). The system is maintained for approximately 4 hours after the onset of flashing.

(vii) On completion of each test, the power is gradually ramped down over a period of 6-10minutes. This is to prevent thermal shock on the radiant heaters.

(viii) Data recorded from all acquisition devices i.e. .csv file can then be analyzed.

4.1.1. Single Phase – Steady-State Tests

As representative of the full-scale design, RCCS inlet temperatures were constantly maintained at 30°C and at the prototypic steady state power of **750 kW**. This corresponds to a scaled down steady state power of **4.63 kW** for the UW test facility. Under this steady state conditions, effect of three parameters were investigated. This included power variation in scaled increments i.e. 4.63, 7.27, 9.91 and 12.55 kW, power shaping representative of a skewed heat flux following the loss of a heater bank and change in coolant inventory level, following depletion in overhead storage tank as a result of evaporation.

To keep the system under steady state conditions, a pump is used to draw water out of the overhead storage tank at a constant flow rate into a hot leg of a flat plate type heat exchanger (HXG). A return cooled water line from the HXG cold leg is then lowered into a diffuser (for uniform distribution) through an opening at the top of the tank. At some threshold point, the energy removed through the heat exchanger operations equals the energy in the system. Figure 4-1 shows a schematic of the single phase steady state operation.

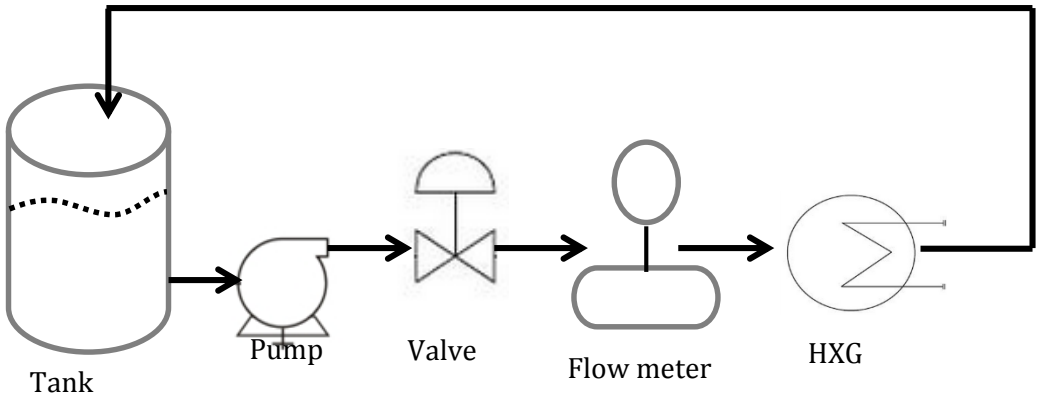

Figure 4-1: Schematic of single phase steady-state operation

The thermal-hydraulic behavior of the RCCS loop under steady state conditions was then characterized by the system mass flow rate, energy balance, and inlet and outlet system temperatures and heat loss to the surroundings. Comprehensive single phase steady state analysis observing the effect of varying decay heat, linear and cosine power shaping had previous been investigated and reported by Albiston (2011). Summarizing Albiston's single phase steady state results, it was shown that key system performance parameters were linear with increasing decay heat (see Figure 4-2). It

was also shown that the power shaping had no effect on the overall system performance.

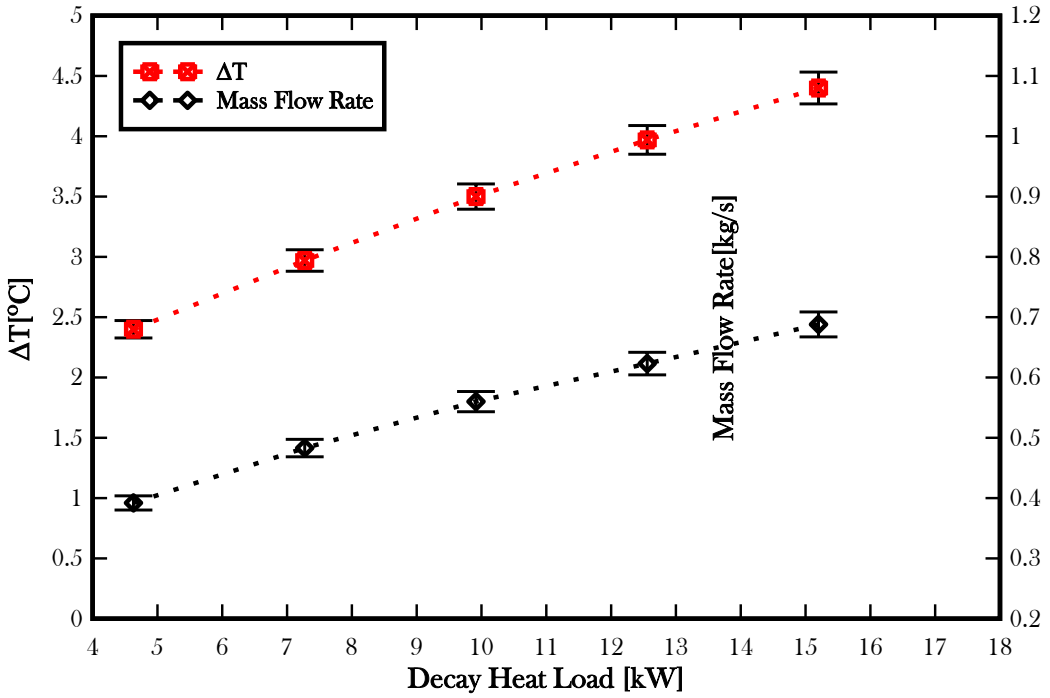

Figure 4-2: Temperature difference across the natural circulation loop and average mass flow rate at 4.63, 7.27, 9.91, 12.55 and 15.19 kW decay heat loads during single phase steady-state operations.

We performed additional single phase steady-state runs to validate earlier results and also to become more familiar with the operations in preparation for transient experiments. For consistency and to have a basis for comparison, 80% storage tank volume and decay heat load of 9.91 kW was set as the baseline condition. To ensure that the system thermal-hydraulic behavior could be repeated under same conditions, a replica test of the baseline conditions was performed. Table 4-1 details the single phase steady state tests that were performed.

Table 4-1: Test Matrix: Single phase steady-state experiments

Run No.	Decay Heat (kW)	Inlet Temp (℃)	Outlet Temp (℃)	Δ*T* (℃)	Mass flow rate (kg/s)	Heat loss[5](kW)	Steady state duration (min)	Rationale
036	9.91	29.44	32.94	3.5	0.56	1.65	61	Baseline condition, investigate the effect of decay heat variation
037	9.91	30.07	33.49	3.42	0.58	1.61	120	Repeatability
039	12.55	30.54	34.53	3.99	0.63	2.04	100	Investigate effect of decay heat variation
041	7.27	29.65	32.54	2.89	0.49	1.32	39	Investigate effect of decay heat variation

4.1.2. Two-Phase Transient Tests

In the sudden event of an accident (D-LOFC), it is assumed that the reactor is immediately shutdown and hence the decay heat load from the RPV begins to rise from the prototypic steady state heat load of **750 kW**, varies during the transient event and peaks at about **1.5 MW**. Slight modifications were made to the single phase operation. Rather than running water through the HXG for steady state operation, the valve at the tank outlet is closed and the HXG is hence isolated. A steam line from a 1.5" opening at the top of the tank, is then connected to the hot leg of the HXG. Figure 4.3 shows a schematic of a typical two-phase transient operation. With continuous heat addition to the system, the fluid remains in single phase until the riser tube surface temperatures are high enough to initiate nucleate boiling (excess temperature 4-30℃). This indicates the transition phase leading to boiling at fluid saturation temperatures. Accelerated

[5] Energy balance (heat loss) calculations for single and two-phase tests are detailed in Appendix C

increase in the steam temperature (>30℃) initiates the start of the condensation operation. A cold leg representing the condensed liquid line is then channeled into a 151 L (40 gallon) tank. This was useful in performing mass balance analysis. The system was kept under two-phase boiling conditions for approximately 4 hours until the power is gradually ramped-down, indicating the end of each experiment.

Initial two phase scoping tests were performed with start-up inlet temperature ($T_{in} = 22$℃) and power (12.55 kW) and showed that it took on average 15 hours to reach saturation at a temperature rise rate of 5.18℃/hour. With an additional 4-5 hours to observe the thermal-hydraulic two-phase behavior, a total of about 20 hours was required. Tests were therefore split over two consecutive days. On day 1, the water temperature was raised from room temperature (22℃) to approximately 70℃, after which the ramp-down process as earlier described is initiated. On day 2, it is expected that the bulk fluid temperature is lowered by a few degrees (5℃ on average) due to minimized heat loss to the surroundings with adequate thermal insulation. Tests therefore started on day 2 with average bulk temperature of 65℃ $\pm$ 5℃. Due to thermal stratification, it took a few hours of continuous heating for the system to reach thermal equilibrium.

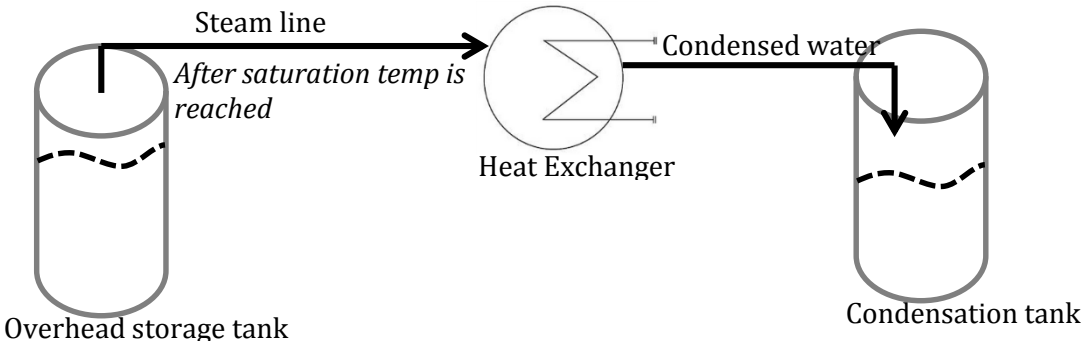

Figure 4-3: Schematic of two-phase operation after saturation temperature is reached.

Investigated system parameters include,

(i). The influence and individual contribution of different scaled decay heat loads (9.91, 12.55, 15.19, 17.84 and 20.49 kW) to the thermal-hydraulic behavior of the RCCS. These represent heat removal (power scheme) of the RCCS during transition from normal to peak off-normal condition.

(ii). The influence and effect of different coolant inventories (80%, 70%, 60%, 50% volume) in the overhead storage tank on the thermal-hydraulic behavior and performance of the system. These represent a change in coolant volume as evaporation and dry-out occurs during two-phase boiling conditions.

(iii). Investigate system behavior and performance under prototypic conditions i.e. transition from steady state to off-normal condition. This incorporates all the residual heat load schemes in (i) and also inventory depletion.

(iv). The different coolant inventories in (ii) were also coupled in an accelerated depletion test. These represent the combined effect of storage tank volume change on the thermal-hydraulic behavior of the system.

(v). Influence of increased system pressure on the thermal-hydraulic behavior under two-phase conditions. This was investigated to understand the effect of pressure on dynamic two-phase flow oscillations.

(vi). Influence of positioning of an inlet orifice plate on the two-phase system behavior. An inlet orifice plate was needed to preserve the temperature difference across the heated section as earlier described in chapter 3 (scaling section).

4.1.2.1. Two-phase Baseline Conditions

Following the initial scoping tests at 12.55 kW, it was observed that the dynamic behavior of the system was sensitive to a variety of parameters including decay heat rate and volume of water in the tank. It was therefore decided that a set of consistent initial conditions be maintained as a basis for comparison with different variables and also to guide our ability to repeat the same tests under same conditions. Baseline conditions were an initial 80% $\pm$ 1% (corresponding to 960 Litres and 52.5" of water) storage tank volume, 15.19 kW decay heat load, a day 2 average bulk temperature of 65℃ $\pm$ 5℃ prior to start of test. Test procedures (i-viii) highlighted in section 4.1 was also strictly followed.

To validate the baseline scenario and to ensure that the thermal-hydraulic behavior of the system is repeatable under same initial and boundary conditions, a repeat of the baseline test was performed.

Based on the set of system parameters to be investigated and the baseline condition criteria set, a comprehensive two-phase test matrix as provided in Table 4-2 was developed. A more detailed test matrix representing all tests performed is available in *Appendix C*. Results from tests performed are provided in Chapter 6.

Table 4-2: Two-phase test matrix

No. of Runs	**Run #**	**Power (kW)**	**Heat flux (kW/m^2)**	**Tank Vol. (%)**	**Rationale**
1	52	15.19	9.29	80	Baseline condition for varying power and tank inventory depletion. Two-phase regime observed for only 4 hours
2	58	15.19	9.29	80	Repeatability: baseline condition
3	50	15.19	9.29	60	Inventory depletion i.e. boil-off
4	51	15.19	9.29	70	
5	54	12.55	7.27	80	Decay heat load variation
6	59	17.84	10.9	80	
7	61	20.49	12.52	80	
8	55	15.19	9.29	80	Inventory depletion from 80-50% .Reduced time-scale with depletion at 1L/min (accelerated drain)
9	63	15.19	9.29	50	Inventory depletion coupled with accelerated draining
10	60	15.19	9.29	80	Increased pressure (10 psi)
11	66	15.19	9.29	80% Orifice (0.9)	Designed and Installed 0.9" orifice plate to match prototypic steady state $\Delta T=11.5^{\circ}C$ and at baseline conditions.
12	68	Variable	7.27 – 12.52	80% Orifice (0.9")	Prototypic: Transition from steady state to transient scenario (*Time=28hrs)*
13	74	15.19	9.29	80	Complete tank drain (inventory dropped below tank inlet)

CHAPTER 5: MIXING IN UPPER PLENUM OF ADVANCED FAST REACTORS

A second thermal-hydraulic flow of relevance to this research is the mixing phenomena in the upper plenum of a prototypic Sodium Fast Reactor (SFR) or Liquid Metal Fast Breeder Reactor (LMFBR). These reactors operate on a fast energy neutron spectrum to sustain the fission chain reaction. As the LMFBR name implies, the core of the fast reactor is designed to breed more fuel (Pu-239) through neutron absorption of U-238, hence minimal moderation is desirable to sustain the fast fission. With low neutron absorption cross-section and good heat transfer characteristics, sodium is the employed as the coolant of choice and thus, the SFR is of research interest as one of the revolutionary reactor designs under the Gen-IV initiative. Using sodium coolant, the reactor is designed to operate at high power density with a compact core in contrast to light water reactors (LWR). SFRs also promote a closed fuel cycle with the potential ability to efficiently manage actinides and the significant extended use of fuel resources. Another advantage of using sodium (Na) as a coolant is the fact that the reactor does not need to be pressurized because sodium's boiling point ($902℃/1175K$) is higher than the reactor's design operating temperature which ranges between 500℃ (773K) and 550℃ (823K).

Drawbacks to using sodium include its high exothermic reaction reactivity with water, and in air environment. This does not compromise the integrity of the reactor's operation as appropriate design measures to prevent such reactions have been incorporated into the conceptual designs following incidences recorded in the BN-600

(1981, 1990, 1993 and 1994) and Monju (1985). One of the identified research gaps in the SFR PIRT analysis that is "high" in importance with respect to the safety of the pool type SFR is the "thermal striping" phenomena (Bruning (1982), Denman et.al, 2012) as shown in Table 5-1. Thermal striping is the random temperature fluctuation that occurs at fluid-structure interface due to incomplete mixing of fluid streams at different temperatures. As a result, accumulated thermal stresses could cause fatigue on the structures and hence lead to eventual failure of the structures or components.

Thermal striping phenomenon is a potential safety concern to the long term operation of a SFR due to the thermal stresses accumulated on structures and components from the impingement of poorly mixed streams of coolant flow from the reactor core. Thermal striping occurs at different locations in the reactor assembly but mainly at the interface of the core cover plate and upper instrumentation structure (UIS) above the reactor core in the upper plenum (Kimura et.al (2007), Tenchine (2010)). Figure 5-1 illustrates the region most susceptible to thermal striping phenomena. It should be noted that in the pool-type SFR, economic viability leads to the design basis and co-location of several components such as the UIS, intermediate heat exchanger (IHX) and pumps within the reactor vessel. However, the more components are placed within the vessel, the more coolant is displaced. This will hence lead to an increase in core outlet velocity (to maintain cooling) which in-turn increases the chances of thermal-striping because there is shorter length scale and time for mixing between multiple streams exiting the core.

Table 5-1: Some research gaps with high level importance to the safety of SCFR [Denman et.al (2012)]

Research Gap	Importance to Safety Within Category	State of Knowledge
Transition to Nat. Convective Cooling, Sodium stratification	H	M
Thermal Response of Structures, Thermal Striping	**H**	**M**
Decay Heat Rejection, Radiation Heat Transfer from Vessels	H	M

Furthermore, as demonstration SFRs (EBR-I, EBR-II, Phenix, Superphenix, Monju and Joyo) were built without a notable integral test facility, the equivalent scaling analysis are not readily available in the public domain. Moreover, the thermally un-mixed flow in the upper plenum can impact the design of the SFR pool, the IHX, and coolant pump. Thus thermal striping is a key scaling consideration in the design of the SFR pool.

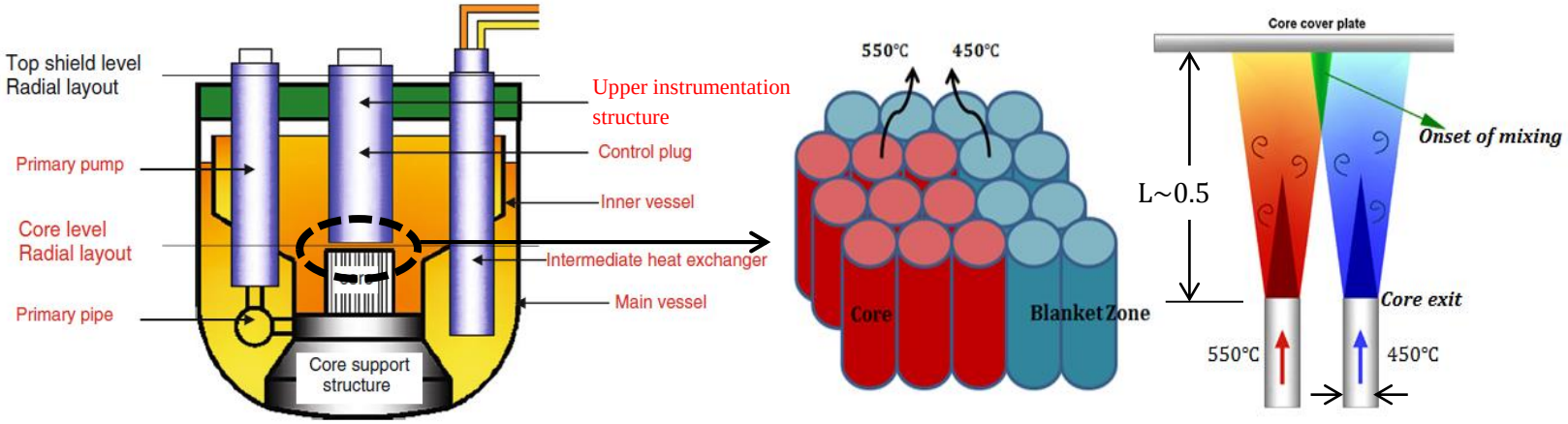

(a) (b) (c)

Figure 5-1: Schematic of (a) a pool type JSFR (b) core fuel and blanket zone highlighting core exit conditions and (c) core exit mixing between a fuel zone and blanket zone channels

The turbulent thermal mixing of core exiting streams (from multiple coolant assemblies) is represented as thermal-hydraulic jet flow at different velocities and temperatures. Several authors have reported both experimental and numerical investigations using single (as reference) and multiple jet configurations. This is to have a basic understanding of both the thermal-hydraulics and fluid-structure interaction of the thermal striping phenomena and the effect of temperature fluctuations on structures.

A review of some existing literature on experimental and numerical investigation of jet mixing was performed in order to guide our understanding and to support our numerical approach.

Flow of simple single jet (planar, axisymmetric, buoyant, and isothermal) has been analytically, computationally and experimentally documented. These are understood to be reference flows in that the (idealized) jet flow has well defined characteristics. Tokuhiro (1999) experimentally investigated flow through a single, planar nozzle with equivalent hydraulic diameter, $0.0358m$, nozzle at isothermal conditions using water as the working fluid and Ultrasound and Laser Doppler Velocimetries (UDV and LDV) for velocity measurements. Based on the centerline velocity decay along the axial coordinate and the jet half-radius, i.e. width of the jet when the velocity is half of the maximum, the thermal-hydraulic flow development close to the nozzle exit, and developed flow regions were characterized. Tokuhiro's experimental result of the centerline velocity decay was in good agreement with correlations of some gas jets as reported in Tokuhiro (1999). Differences in radial jet spread were attributed to the

short entrance length of the nozzle piping and existence of a non-homogenous flow at the nozzle exit of the experimental facility as built. This isothermal single jet work serves as a reference to confirm that UDV measurements can be used to characterize jet flows.

Tanaka (1974) and Elbanna et.al (1983) experimentally investigated the turbulent mixing of dual parallel jets at the same velocity (iso-velocity). The authors characterized the velocity flow field in the axial direction into three distinct regions: (i.) the converging region which refers to the region between the core exit and the merge point of the inner shear layers, (ii) merging region describing the region between the merge point of the inner shear layers to the point where the centerline velocity is maximum along the jets axis, and (iii) combining region which depicts a fully developed flow region beyond the merging region. Beyond this region, the dual jets approach self-similarity as observed in an idealized single jet.

Thermal mixing of three parallel (planar) jets in ordinary fluids was also experimentally studied by Tokuhiro and Kimura (1999) in the same facility described above for single jet. The flow was on average symmetric with respect to the central jet. The authors investigated the effect of varying temperatures, i.e. ΔT= 5°C and 10°C, and velocity ratios of U_c/U_h = 0.5, 0.7 and 1 between the jets using two UVP transducers. The effect of relative velocity difference between both jets was shown to delay the onset of mixing while temperature fluctuations at ΔT= 5°C and 10°C were insignificant on the velocity flow field. The delay of the onset of mixing impacts the scaling of the

length above the core to bottom of the UIS (as an example) over which a given level of thermal mixing can occur.

Kimura et.al (2002) further numerically investigated the temperature fluctuations and thermal mixing in the triple jets experiments performed by Tokuhiro and Kimura (1999). Kimura and co-workers used a standard k- ε model, direct numerical simulation (DNS), and low Reynolds number turbulence stress and heat flux equation (LRSFM) models. The standard k- ε and LRSFM model simulations predicted higher magnitude temperature fluctuations than experimentally reported by Tokuhiro and Kimura (1999), while the jet mixing was well-predicted by the DNS model. The DNS predictions of flow variables (velocity and temperature) are numerically resolved as functions of spatio-temporal scales and hence enhance the predictive capabilities of physical world problems.

Summary of numerical and experimental thermal-hydraulic studies is given in Table 5-2 and 5-3 respectively.

Table 5-2: Literature summary of numerical investigation of thermal stripping phenomena in a Sodium-Cooled Fast Reactor

Author	Jets	Turbulence models	Discretization Schemes	$Ri(10^{-2})$	$Re(10^{4})$
Anderson and Spall (2001)	2	k-epsilon and RSM[6]	Convection terms: QUICK Viscous terms: Second order central differencing Pressure coupling: SIMPLEC	25	0.6
Nishimura et.al (2000)	3	LRSFM k-epsilon	Diffusion term: Second order central difference Convection term: skew upwind	0.2	1.5
Kimura et.al	3	k-epsilon	Convection term: skew upwind Diffusion term: Second order Central diff.	0.63	2.29
Kimura et.al	3	DNS	convective term: third order upwind	0.63	2.29
Jung and Yoo (2012)	3	LES Model; K-l, and Smagorinsky - Lily	Convection term: Monotone advection and reconstruction scheme (MARS)	0.2	1.5
Choi and Kim	3	Two-layer model, V2-f Model, k-omega SST	Unsteady term: second order backward scheme; Convection term: second order HLPA scheme	0.022	1.87
Chandran et.al (2011)	10	RSM	Unsteady term: Second order central differencing	___	2

[6] RSM: Reynolds Stress Model

Table 5-3: Literature summary of experimental investigation of thermal stripping phenomena focused on a Sodium Fast Reactor

Author	Fluid	Velocity ratios	S/D	Delta T(℃)	Jet Type	Jet(s)	Data range(Z/D)	Parameters Investigated
Tokuhiro (1999)	Water	0.5m/s, 1m/s, 2m/s	___	0	Planar	1	0 - 15	Velocity (flow characterization)
Tokuhiro and Kimura (1999)	Water	1,0.7,0.5	3.5	5,10	Quasi-planar	3	0 - 27	U,U',T
Nishimura et.al (2000)	Water	1	3.5	5	Quasi - planar	3	15	Convective mixing and temperature fluctuations
Kimura et.al (2002)	Water	1	3.5	5	Planar	3	5, 7.5	Temperature fluctuations
Choi and Kim (2007)	Air	1	2.5	24	Planar	3	3.2 –35	Temperature fluctuations

With reference to published works in Tables 5-2 and 5-3, several experimental and numerical models were developed to reproduce similar conditions in the upper plenum. In all, emphasis has been put on basic understanding of the thermal-hydraulics of the mixing phenomenon and its effect on structural mechanics. Structural models have only been able to predict instantaneous effect of temperature fluctuations on structures. Models are also been developed for creep-fatigue damage correlations to help predict the extent of thermal stress on structures. In addition, the impact of the lack of complete thermal mixing on a scaled design of the SFR has not been

Identifying the local and global parameters that influence thermal and momentum mixing in the upper plenum of a SFR, an attempt is made to develop numerical models to guide the design of a SFR using a bottom-up scaling approach and CFD as a design

tool. A correlation has been developed using a variation of scales to guide the understanding of non-linear, single phase thermal-hydraulics. This is an original contribution towards designing separate effect and integral test experiments to investigate the thermal-mixing between multiple streams.

The United States' first fast reactor, i.e. Experimental Breeder Reactor (EBR I) was operational from 1951 to 1963. A second breeder reactor i.e. EBR II was operational from 1964 to 1994. Table 5-4 highlights some other recent or past operating research and demonstration SFRs across the world. There is currently no conceptual advanced SFR design in the USA under the Gen-IV initiative. On the other hand, Japan, India, Russia and France do have prototype designs even though the long term thermal response of the structures and materials remain unknown. Owing to the economics and a compact reactor vessel, all existing conceptual designs have a short length scale between the reactor core exit and the UIS or core plate ($\sim$ 1m). Typical design characteristics of the Japanese Sodium Fast Reactor (JSFR) were used as a reference prototype design for the purpose of this research because the demonstration SFR is planned to be built in Japan. Flow conditions at the core exit of the SFR are in the turbulent regime ($Re \sim 5 \times 10^4$) . Characteristic outlet parameters are summarized in Table 5-5.

Table 5-4: Some recent and past SFRs

Facility	Operation period	Country
Phenix	1973 – 2009	France
Super Phenix	1985 – 1996	France
FBTR	1985 - present	India
PFR	1984 – 1994	United Kingdom
BN-600	1981 – present	Russia

Table 5-5: Characteristic average flow outlet conditions at the core exit of a prototype SFR

Parameter	Values
Outlet temperature (K)	773
Outlet velocity(m/s)	2.3 - 5
Inner diameter of flow channel(mm)	6.5

5.1. Turbulence Modeling

5.1.1. Overview:

Since the flow out the core is turbulent, with average Re_D as high as 50,000, a brief description of turbulence modeling is given in this section as a summary and to guide the numerical modeling and simulations that follows. Detailed turbulence fundamentals and modeling can be found respectively in Tennekes and Lumley (2000) and Rodi (2000).

Turbulence as characterized by random and chaotic motion of fluid flow is prevalent in many engineering applications. This includes flows around airplanes, ships and submarines, mixing of fuel and air in engines, and smoke out of a chimney amongst many other applications.

Turbulent flow has the ability to transport energy and mix fluid momentum more effectively compared to laminar flows [Osborne, (1983)]. Turbulence is traditionally

described by high Re, which relates the dynamics of the flow with specific characteristic length scales often defined by the geometry. In general, Re is defined by $\frac{\rho UL}{\mu}$ (ratio of inertial to viscous forces) where ρ, U and L are the density, characteristic velocity and length scales of the flow and μ is the dynamic viscosity of the fluid. Figure 5-2 illustrates the chaotic nature of turbulence and is characterized by different scales (eddies).

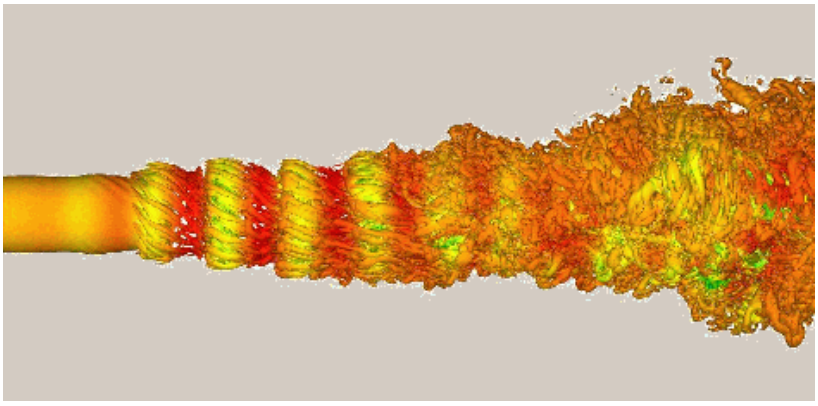

Figure 5-2: Turbulent flow from a planar nozzle [www.ifd.mavt.ethz.ch]]

Modeling turbulence is often a challenge because the fluid velocity field is three dimensional and time dependent. It also spans across a large length and time-scales and the eddies increases with increasing Re [Rodi, (2000)]. These small and large scales of motion can be represented by Navier-Stoke equations and can be numerically solved with the right sets of initial and boundary conditions, in recent time, accessible Computational Fluid Dynamics (CFD). CFD modeling is a physics-based approach to solving and analyzing flow problems using numerical techniques and algorithms. It is

widely used in understanding and predicting increasingly complex thermal-hydraulic flow phenomena including turbulent flows.

This chapter describes the approach used to predict the turbulent mixing in the upper plenum of a Sodium Fast Reactor (SFR) using a CFD package with contained turbulence models. Models were developed and incorporated into the proposed methodology of using CFD as a tool to guide the understanding of thermal-striping phenomena in the upper plenum of a SFR. As earlier noted, the lack of thermal mixing, influences the scaled design of the pool-type SFR and its in-pool components.

Governing Equations:

The equations governing the distribution of the mean - flow quantities are derived from the conservation laws of mass, momentum and energy. For incompressible flows, these equations can be written using tensor notation as follows:

Continuity Equation:

$$\frac{\partial U_i}{\partial x_i} = 0 \qquad 5.1$$

Navier-Stokes Equations:

$$\frac{\partial U_i}{\partial x_t} = U_j \frac{\partial U_i}{\partial x_j} = -\frac{1}{\rho_r}\frac{\partial P}{\partial x_i} + \frac{\partial}{\partial x_j}\left(\vartheta \frac{\partial U_i}{\partial x_j} - \overline{u_\iota u_\jmath}\right) + g_i \frac{\rho - \rho_r}{\rho_r} \qquad 5.2$$

Energy Equations:

[7] Influence of density on the buoyancy term in the Boussinesq equation

$$\frac{\partial \phi}{\partial t} + U_i \frac{\partial \phi}{\partial x_i} = \frac{\partial}{\partial x_i} \left(\gamma \frac{\partial \phi}{\partial x_i} - \overline{u_i \varphi}\right) \quad 5.3$$

where U_i is the instantaneous velocity component in the x_i direction, P is the instantaneous pressure, ρ_r is the reference density, ϕ is a scalar quantity, γ is the thermal diffusivity and the overbars indicate time-averaged values.

5.1.2. Turbulence Models:

To understand the dynamics of the turbulent flow, models have been developed based on the transport equations. These include Direct Numerical Simulation (DNS), Large Eddy Simulation (LES) and Reynolds-Averaged Navier Stokes (RANS) turbulence models. Brief description of each of these models is given below.

Direct Numerical Simulations (DNS):

The DNS is a three dimensional time-dependent solution of the Navier-Stokes and continuity equations. With the right sets of initial and boundary conditions, the DNS model solves the convective and diffusive transport terms in the Navier Stokes equation for a given flow problem. In principle, DNS gives numerically-accurate solutions for exact equations of motion and hence solution to the turbulence problem. DNS is currently the most descriptive and accurate computational modeling approach for flow realization. It however requires high computational resources and cost, and thus inaccessible for many numerical engineering institutions. By solving all the spatial and temporal scales of the fluid turbulent motion, the smallest turbulent length and time scales (Kolmogorov scale) can hence be resolved (Tennekes and Lumley, 2000). The Kolmogorov scale "η" can be described using equation 5.4. This therefore means

that the computational domain i.e. grid, must be very fine in order to resolve the smallest eddies of the order "η".

$$\eta = (\frac{\vartheta^3}{\varepsilon})^{\frac{1}{4}} \qquad 5.4$$

Large Eddy Simulations (LES):

Also developed based on the Navier Stokes equations, the LES model only explicitly computes the large scale turbulent eddies with high accuracy while only modeling the effect of the Kolmogorov scale. LES is based on the assumption that the large turbulent eddies are mostly directly influenced by the boundary conditions and transport most of the Reynolds stresses. Hence the need to explicitly compute large turbulent eddies. On the other hand, small eddies contribute less to Reynolds stress because they are weaker and hence assumed to be less critical. A thresholding method is used to filter spatial and temporal scales into resolved $\overline{U(x,t)}$ and a residual $u'(x,t)$ velocity components. Hence, separating the large and small scales eddies. In terms of computational resources, the fact that the smallest scales are not computed in details makes it less expensive than the cost of modeling with DNS.

Reynolds Averaged Navier-Stokes (RANS) Models:

These models are developed based on averaged forms of the Navier-Stokes equation. Inability to resolve the non-linear Reynolds stress term leaves a closure problem. The RANS models decompose the velocity field $\tilde{u}_i$ into its mean $\overline{U}$ and fluctuating u_i components. The pressure and stress terms are also decomposed. These

models are widely used in engineering modeling and simulations because they are less computationally expensive compared to DNS and LES based simulations. Because the transport terms are averaged, they are also not as accurate as the DNS and LES models. Examples of the RANS based models are standard $k-\varepsilon$, Realizable $k-\varepsilon$, standard $k-\omega$ and SST $k-\omega$ turbulence models.

Graphical comparison of flow realization from different numerical approaches, in contrast to a color representation of thermocouple data is shown in Figure 5-3 for three vertical jets in a water test facility.

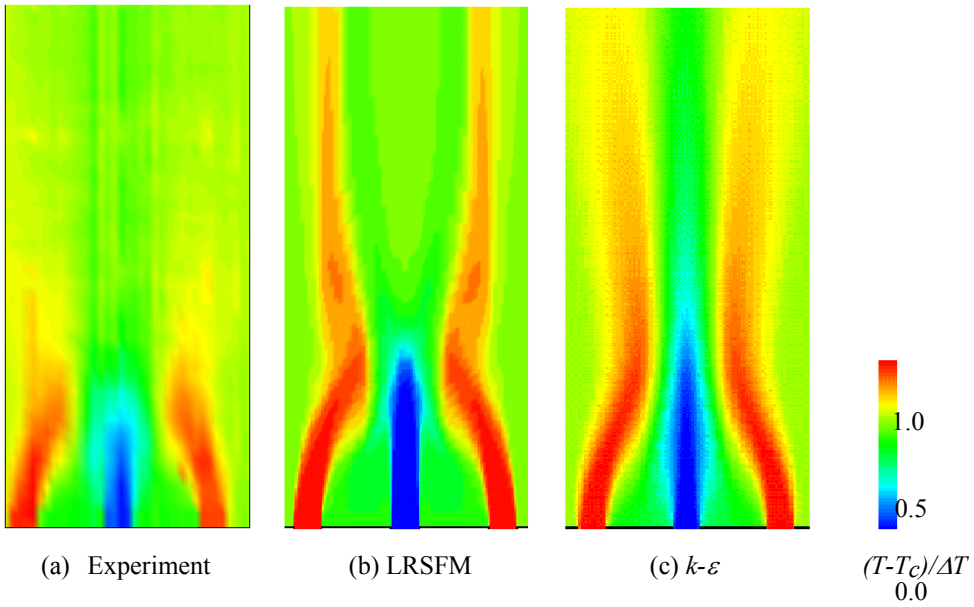

Figure 5-3: Flow realization of the axial normalized temperature field for triple jet fluid interaction in a water test facility, computed from Experiment, Low Reynolds number turbulence stress and heat flux equation models (LRSFM) and RANS based k-ε based models [Kimura et.al]. A cold jet is sandwiched between two hot jets.

To guide the modeling, simulation and design of a pool-type SFR and to support code verification and validation, an evaluation of numerical models was carried out based on the pros and cons mentioned above, ability to model turbulent mixing with high level of accuracy in comparison to experimental data, and availability of computing resources. COMSOL Multiphysics, a finite element based numerical code was used to guide the design process. This code was selected because availability and knowledgeable technical support. One of the limitations of the code is the availability of only two RANS based closure models ($k-\varepsilon$ and $k-\omega$ turbulence models). However, they are the most often used because of their versatility and the existence of a large user base. The research was however not to study the suitability of different turbulence models but rather to study the impact of scaling thermal jet mixing on the pool-type SFR design. Table 5-6 details the strengths and weaknesses of both RANS based models.

Table 5-6: Areas of application, strengths and weaknesses of various RANS based models

RANS Model	Advantages	Disadvantages
Standard K-ε (2 eqn.)	Robust, economical, reasonably accurate; long accumulated performance data. Good prediction for free shear flows and swirling flows	Mediocre results for complex flows with severe pressure gradients, strong streamline curvature, swirl and rotation. Predicts that round jets spread 15% faster than planar jets whereas in reality they spread 15% slower.
Standard k –ω (2 eqn.)	Gives good prediction for near wall treatment (wall-bounded B.L) and low Re flow problems. Can be used for transition flows	Subjected to limitations due to isotropic eddy viscosity assumption. Under predicts severe adverse pressure gradient flows. Over predicts under existence of flow separation.

To establish an initial understanding of turbulent flow and mixing between multiple jet streams, the **k-ε** turbulence model was used. To achieve higher order accuracy in simulation, high performance computing capabilities were needed[8]. In the absence of such, all simulations were performed on a PC (Quad-Core AMD 2.00 GHz processors and 8.0GB RAM) using a two-dimensional, two-jet model.

5.1.2.1. K-ε Turbulence Model:

The **k-ε** two-equation RANS-based turbulence model incorporates solutions from the turbulent kinetic energy "k", and dissipation rate "ε "transport equations from which the turbulent length scale "L" and turbulent velocity "U" can be computed. The turbulent intensity[9] "I" is the ratio of the root mean square of the turbulent velocity to the mean velocity. Thus,

$$k = \frac{3}{2}(UI)^2 \qquad 5.5$$

$$\varepsilon = \frac{C_\mu^{3/4} k^{3/2}}{0.075L} \qquad 5.6$$

Both equations 5.5. and 5.6 determine the energy and scale of the turbulence and account for convection and diffusion of turbulent energy in the flow stream.

The equations which comprise the complete **k-ε** model are:

$$\vartheta_t = C_\mu \frac{k^2}{\varepsilon} \qquad 5.7$$

---

[8] Restricted access to Idaho national Laboratory's (INL) High Performance Computing facilities

[9] $I=\frac{u'}{U}$

$$\frac{\partial}{\partial t}(\rho k) + \frac{\partial}{\partial t}(\rho k u_j) = \frac{\partial}{\partial x_j}\left[\left(\mu + \frac{\mu_t}{\sigma_k}\right)\frac{\partial k}{\partial x_j}\right] + G - \rho\varepsilon - Y_M + S_k \quad 5.8$$

$$\underbrace{\frac{\partial}{\partial t}(\rho\varepsilon)}_{\text{Rate of change}} + \underbrace{\frac{\partial}{\partial t}(\rho\varepsilon u_j)}_{\text{Convective transport}} = \underbrace{\frac{\partial}{\partial x_j}\left[\left(\mu + \frac{\mu_t}{\sigma_\varepsilon}\right)\frac{\partial \varepsilon}{\partial x_j}\right]}_{\text{Diffusion}} + \underbrace{\rho C_1 S\varepsilon}_{\text{Generation}} - \underbrace{\rho C_2 \frac{\varepsilon^2}{k+\sqrt{\vartheta\varepsilon}}}_{\text{Destruction}} + \underbrace{C_{1\varepsilon}\frac{\varepsilon}{k}C_{2\varepsilon}G_b}_{\text{Buoyancy}} \quad 5.9$$

where ϑ_t is the eddy viscosity term. $C_\mu = 0.09$, $C_{1\varepsilon} = 1.44$, $C_{2\varepsilon} = 1.92$, $\sigma_k = 1$, $\sigma_\varepsilon = 1.3$ are all empirical constants deduced from legacy experiments [Rodi (2000)] and found applicable to turbulent shear flows.

5.2. Benchmark Studies: Model Description

To support high fidelity temporal and spatial data for code development and assessment, numerical models were developed to simulate the momentum and heat transfer transport in single and two jet streams. A single jet was used because it is well documented analytically, computationally and experimentally. Thus, to verify the predictive capabilities of COMSOL Multiphysics, single-jet water based experimental results reported by Tokuhiro (1999) and dual-jets water scoping tests performed at the University of Idaho were used to validate the thermo-fluid simulations.

5.2.1. Single-Jet Benchmark:

Initial and boundary conditions reported by Tokuhiro (1999) for a single water jet experiment vertically injected into a pool were used to validate the k-ε turbulence models. This study was part of a triple-jet study of thermal mixing for the Japanese SFR. Figure 5-4 shows the schematic of the geometry used for the single jet model.

Boundary Conditions:

A two-dimensional single nozzle measuring, 0.02 x 0.169m^2, and an equivalent hydraulic diameter d_h of 0.03576m was used. The width and height of the test section are 0.4 and 0.95m respectively. Inlet boundary condition for velocity was 0.5 m/s and an isothermal condition was maintained for the inlet and pool temperatures at 293K. The corresponding Reynolds number Re_{d_h} is 1.79 x10^4. An entrance length "L_e"of 0.45 was added to the duct to ensure a fully- developed turbulent flow was obtained at the jet exit (see Equation 5.10). Walls of the test-section were set as stationary walls with no slip conditions, assumed to be insulated and with logarithmic wall functions. The logarithmic wall function assumes that there is no near wall effect on the flow field. The outlet boundary condition for the flow field was set as pressure, no viscous stress because it's numerically stable and controls the pressure level along the entire boundary that is exiting into an infinite environment. The specified outlet boundary condition for the heat transfer field was convective flux. This option was used because neither temperature not heat flux was known at the outlet boundary. Moreso, convective heat transfer is active in the system.

$$\mathrm{L_e} = 4.4\mathrm{D}_h\mathrm{Re}^{\frac{1}{6}} \qquad 5.10$$

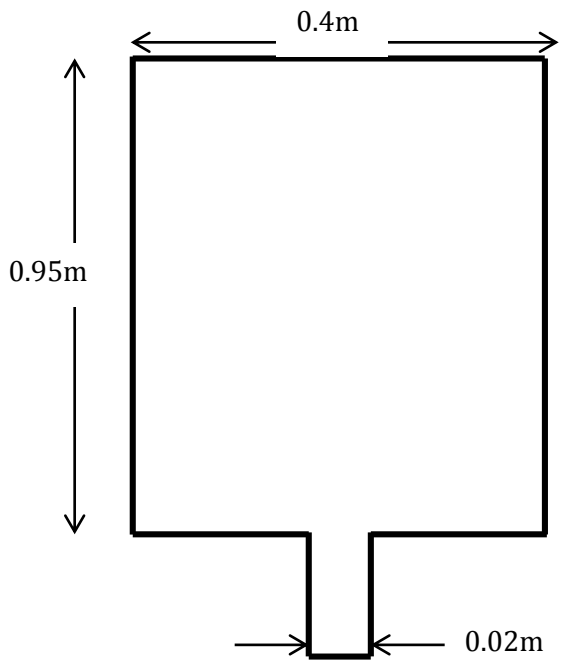

Figure 5-4: Schematic of vertical planar jet used for numerical simulation benchmark

The turbulence intensity "I" at the jet exit was calculated as 4.7 percent using Equation 5.11[10].

$$I = 0.16 Re_{d_h}^{-\frac{1}{8}} \qquad 5.11$$

Numerical Method:

The k-ε turbulence model was employed for closure approximations. All calculations were performed using COMSOL Multiphysics v.3.5 on Quad-Core AMD 2.00 GHz processors and 8.0GB RAM. The flow field was discretized using a structured grid and the pressure-velocity coupling was based on SIMPLE algorithm. Mesh size sensitivity studies was first performed on the fluid domain to investigate the optimum

[10] The equation represent calculation of turbulence intensity and is only applicable to fully developed pipe flows (http://www.cfd-online.com/Wiki/Turbulence_intensity)

mesh size and ensure that key physics were qualitatively captured in reasonable computing time. The grid size study for the single jet benchmark was for 4, 6, 8 and 10 elements per D. This corresponds to 15560, 35010, 62240 and 97250 elements in total across the entire test section.

The difference in simulation results between 35010 and 97250 grids was calculated to be less than 2%. A grid size with 35010 mesh elements was therefore considered to be sufficient enough to capture the physics at the region of interest and was hence used as a reference. Figure 5-5 displays the velocity field comparison plots of the mesh sensitivity studies performed on the single jet benchmark. Figure 5-6 shows a structured mesh representing the grid system of choice with 35010 elements and velocity contour plot for the benchmark simulation. An iterative tolerance level of 10^{-6} was set as a convergence criteria for continuity, energy, momentum, k and ε in the benchmark simulations and all other simulations henceforth. Model constants used are as described in section 5.1.3. The velocity profile at the nozzle exit of the single jet as shown in Figure 5-7 verifies a homogenous and fully developed flow.

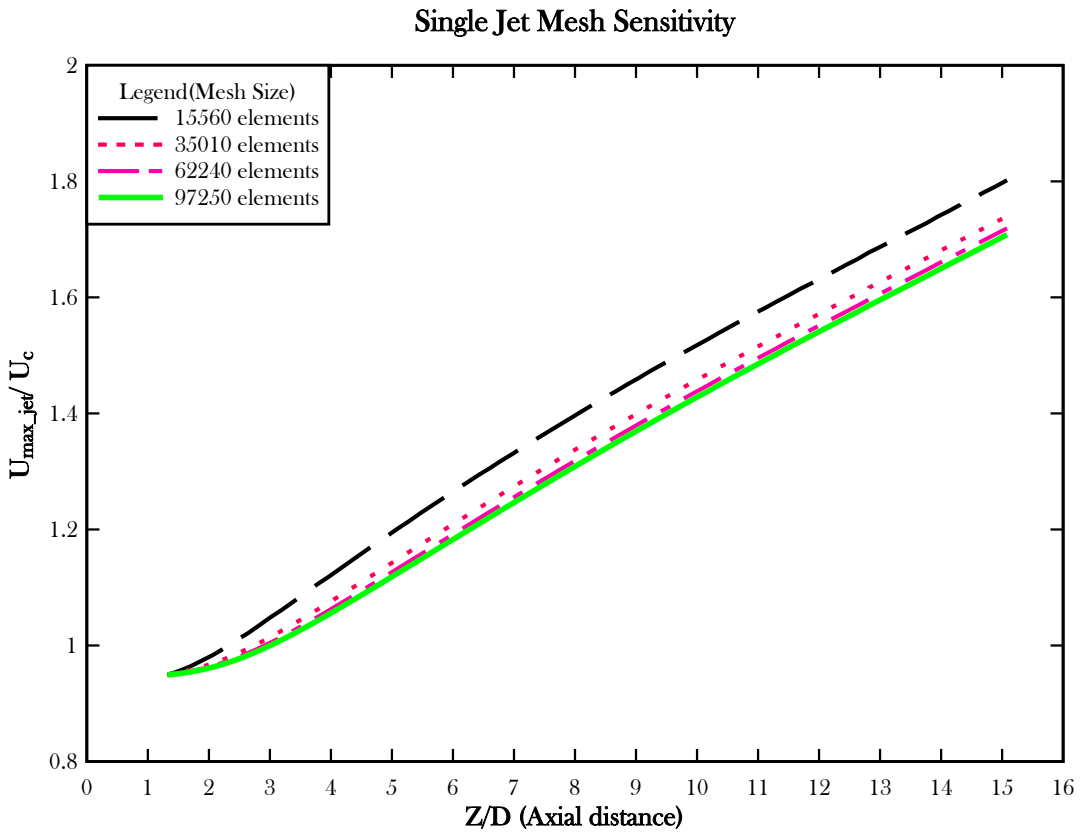

Figure 5-5: Sensitivity study based on grid size for single jet numerical simulations

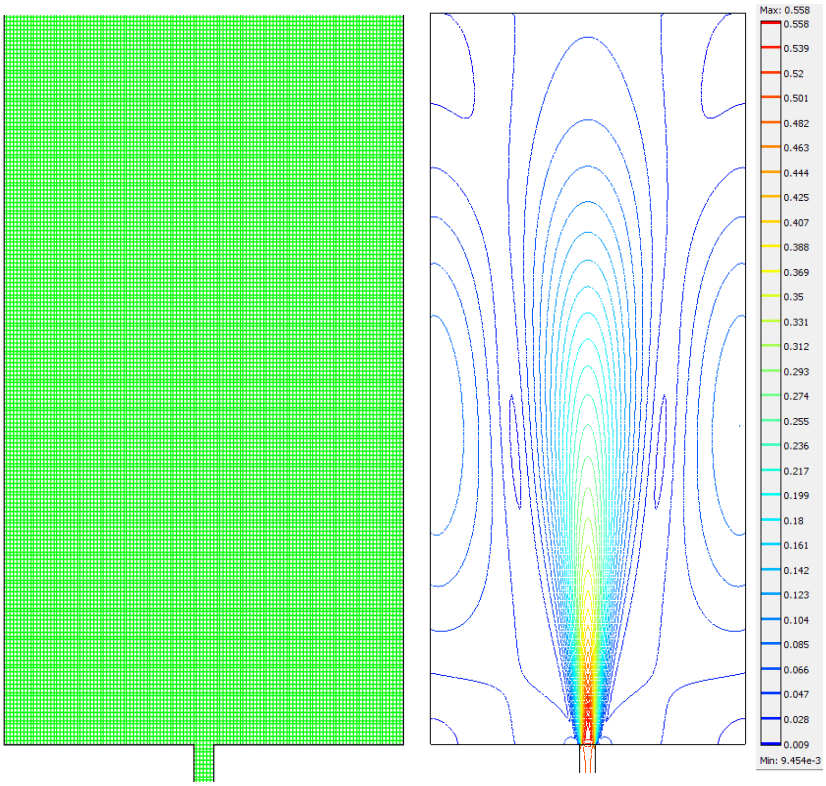

Figure 5-6: Discretization of the fluid domain with 32010 elements and contour plot of the velocity field

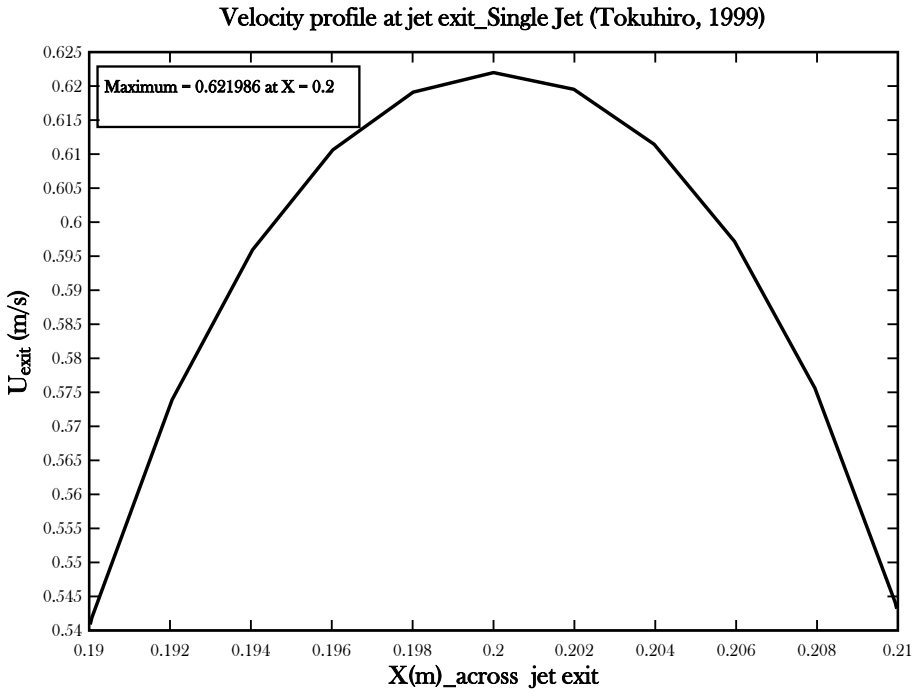

Figure 5-7: Fully developed turbulent flow: Jet exit velocity profile

To verify the accuracy and validity of the CFD simulations, comparisons of the centerline velocity decay and the jet half-radius relative to that reported by Tokuhiro (1999) were performed and thus as characteristic of jet behavior. This was used to benchmark the numerical simulations and validate the capability of COMSOL Multiphysics to predict the momentum mixing and thermal-hydraulic behavior of a jet. Figures 5-8 and 5-9 show the single jet verification and validation profiles for centerline stream-wise velocity distribution and the jet-half radius.

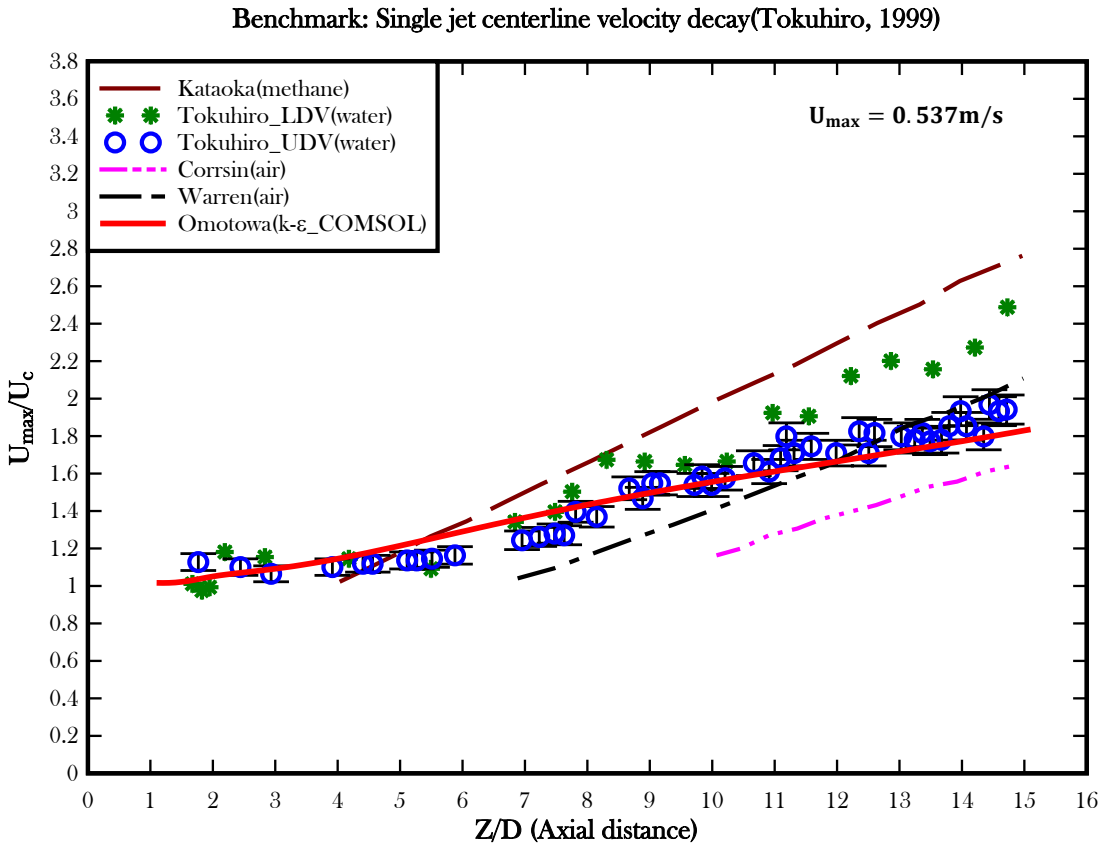

Figure 5-8: Benchmark series: Numerical and experimental comparison of centerline velocity decay in a single jet

The slope of the COMSOL simulation in Figure 5-8 is of the same order of magnitude as the UDV experimental data and falls within 4% uncertainty bounds of the experimental results. It should also be noted that Tokuhiro (1999) test-section had a short entrance length and hence the flow was not fully developed prior to been entrained into the pool.

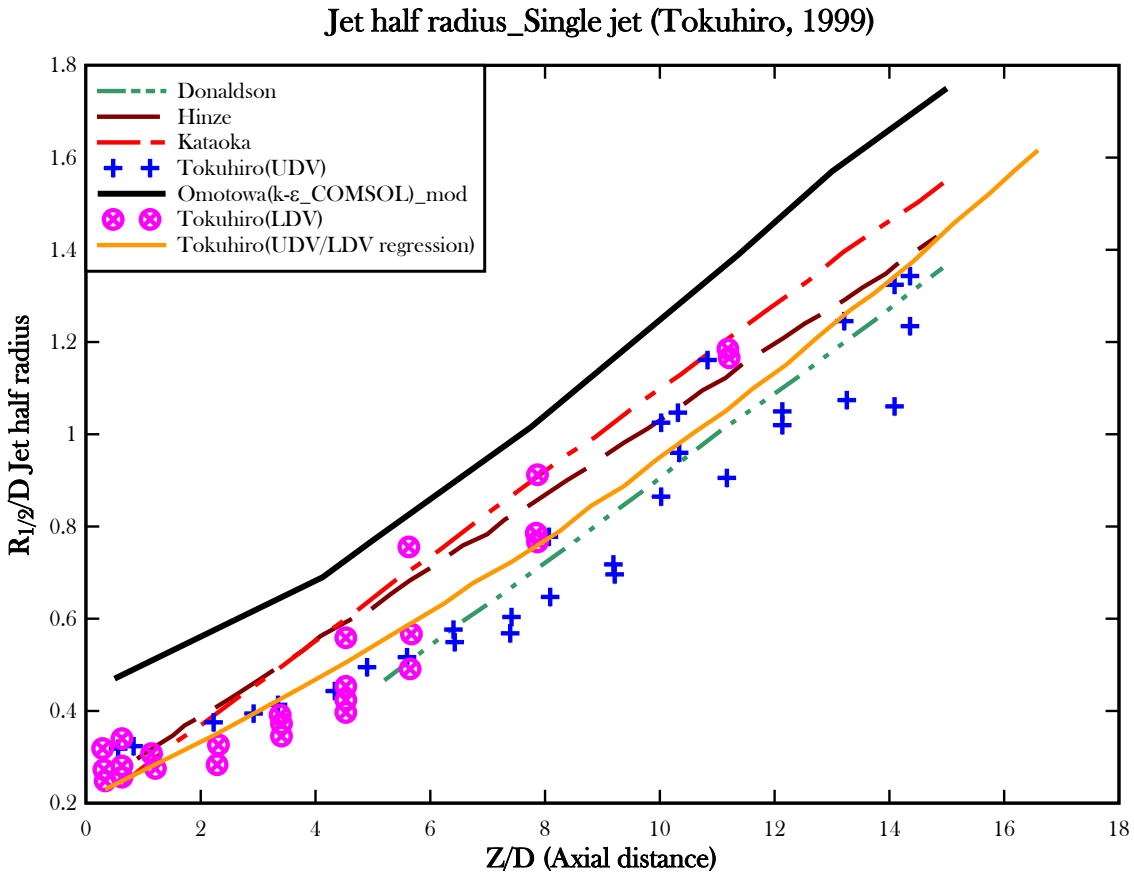

Figure 5-9: Benchmark series: Numerical and experimental comparison of jet-half radius in a single jet

Based on Figure 5-9, it is evident that the numerical simulation over-predicts the jet spread when compared to Tokuhiro (1999) experimental data. This is attributed to the

high value of artificial crosswind diffusion, i.e. stabilization technique used to dampen flow oscillations and stabilize the thermal diffusion equations at corners and across boundary layers by introducing diffusion orthogonal to the streamline direction**.** By these, the boundary layer is smooth out and hence easy to resolve on the mesh in the computational domain. The local element size contributes to the determination of the stabilization tuning parameter. The most predominant effect of the crosswind diffusion is along the entrance region (pipe walls, corners and boundary layers).

Rodi (2000) reports that over-prediction up to 30% is expected in the jet spread when using k- ε turbulence model and hence recommends a modification of the C_{μ} , $C_{2\varepsilon}$ constants. The jet width however has a linear trend similar to other plots and also the slope is of the same order of magnitude.

5.2.2. Two-Jet benchmark:

A second benchmark was performed using dual-jet water experiments performed at the University of Idaho. This was part of initial scoping tests that were performed to support the high fidelity data collection in a sodium test loop currently under construction at the Center for Advanced Energy Studies (CAES) Idaho Falls. Tests were performed at room temperature and velocity measurements were obtained using UDV, an identical technique to the single jet benchmark measurement.

Boundary Conditions

A simple two-dimensional test-section representing the test geometry at the University of Idaho was developed because of limited computational resources. The 2D

test-section measures 0.260 x 0.158 m^2 and the nozzle dimensions are 0.172m in length and 0.00635m in width. Using an approximate nozzle exit velocity of 0.5 m/s, the simulation was performed at room temperature with water as the working fluid. Wall and outlet boundary conditions were maintained similar to the single jet benchmark scenario. Figure 5-10 displays the 2D geometry used to validate the predictive capability of COMSOL. Figure 5-11 illustrates the benchmark comparison of the numerical and experimental results for two-jets.

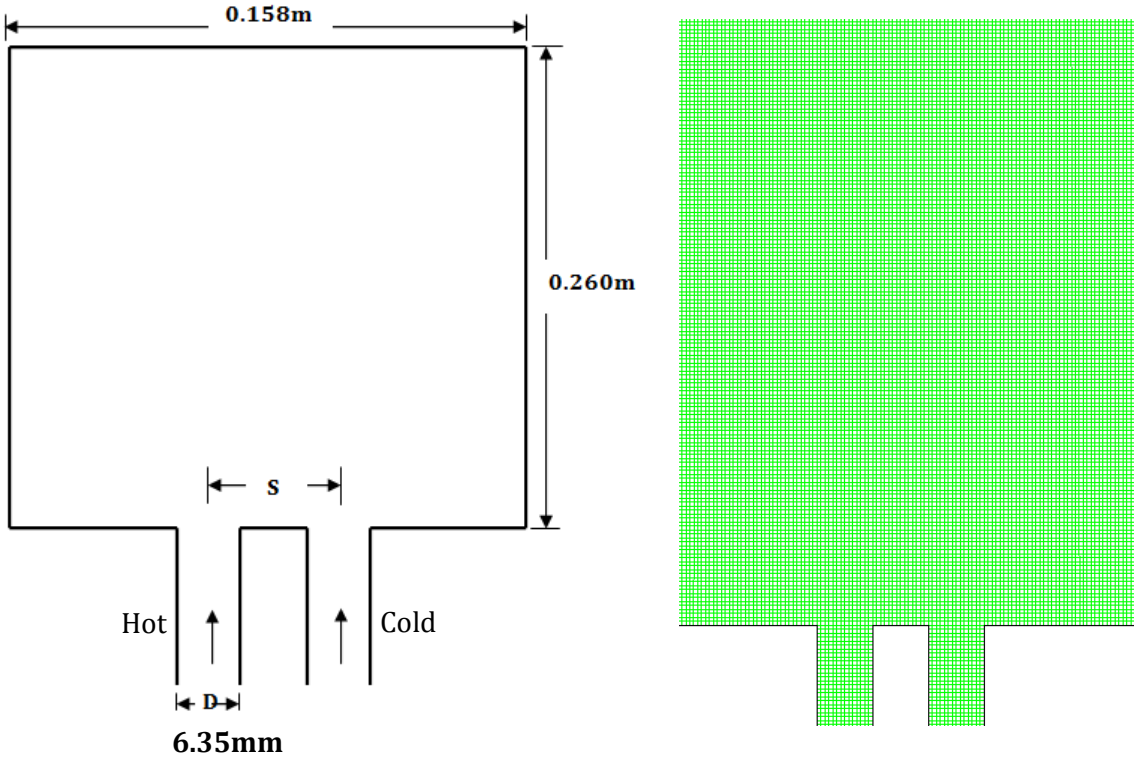

Figure 5-10: 2-D geometry and grid system used to validate dual-jet numerical simulations

A grid sensitivity study was also performed for a dual jet scenario for verification of the grid independence of the results. After varying the number of elements across every D (4, 6, 7, 8 and 10), the peak difference in results obtained for 68202 (8

elements per D) elements and 106 832 (10 elements per D) elements was calculated to be less than 3%. A uniform grid corresponding to 68202 elements was therefore used as a reference for the dual-jet thermofluid simulation. Steady-state blind simulations were then performed and validated with preliminary experimental water test data as shown in Figure 5-11. The figure compares the decay rate of the jet centerline velocity which is a parameter used to characterize the mixing level of the jet. From the figure, the region 3.5<Z/D<14 corresponds to the convective mixing regime. The plateau represents the point where both jets become self-similar and beyond that little or no mixing is obtained. More discussion of the jet centerline behavior is provided in the results section.

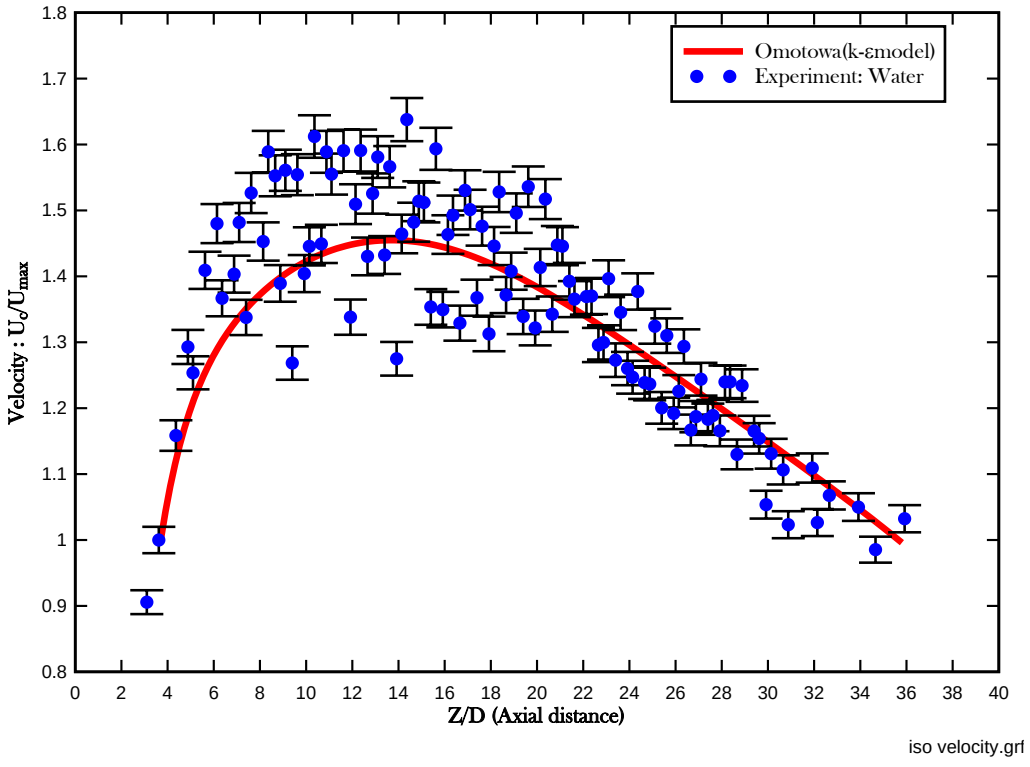

Figure 5-11: Benchmark series: Numerical and experimental comparison of centerline velocity decay for two-jets.

Since a good agreement was obtained in benchmark cases highlighted above (single and two-jets), there was within the limitations of the turbulence model and simple set-up of the scoping experiments, confidence in the ability of COMSOL to adequately predict the thermal-hydraulic behavior of single and multiple jets in both near and far field regions. Further refinement would aid in understanding of both computational and experimental uncertainties.

An obvious fact from both benchmarks is that the jet streamwise velocity decays as the jet spread (transversely) increases along the axial distance from the jet axis.

5.3. Scaling Approach

The design of separate effect thermo-fluid experiments such as the turbulent mixing are often based on preservation of common dimensionless parameters such as Re_D , Pr, and Pe, where,

$$\mathrm{Re_D} = \frac{\mathrm{UD}}{\vartheta} \text{ (inertia to viscous forces)} \qquad 5.12$$

$$\mathrm{Pr} = \frac{\vartheta}{\alpha} \text{ (momentum to thermal diffusivity)} \qquad 5.13$$

$$\mathrm{Pe} = \frac{\mathrm{UD}}{\alpha} = \mathrm{Re_D Pr} \text{ (thermal energy convection to conduction)} \qquad 5.14$$

While the scaling parameters[11] (equations 5.12 to 5.14) do describe the global characteristic of the turbulence induced mixing, they do not provide any information about the local turbulence characteristics. In addition, they do not correlate the

[11] Traditional global dimensionless parameters used to characterize liquid metal thermal-hydraulic flows. The parameters also guide in the integration of separate effect tests to integral and full-scale conditions.

associated length and time scales of the thermal-hydraulics to the energy transport within the system.

In order to achieve similitude in separate effect and integral turbulent mixing in large volumes, detailed consideration needs to be given to transport mechanism, geometric, kinematic and dynamic similarities.

The relative impact of scaling on the thermal-hydraulic mixing phenomena is therefore analyzed. For a pool-type SFR design, the associated scales of relevance to the impingement of the unmixed streams to the interface of components, include the vertical length-scale (~0.5m) between the core exit and the UIS and the lateral length-scale between the core exit and the IHX, pump or hot leg pipe (see Figure 5-12).

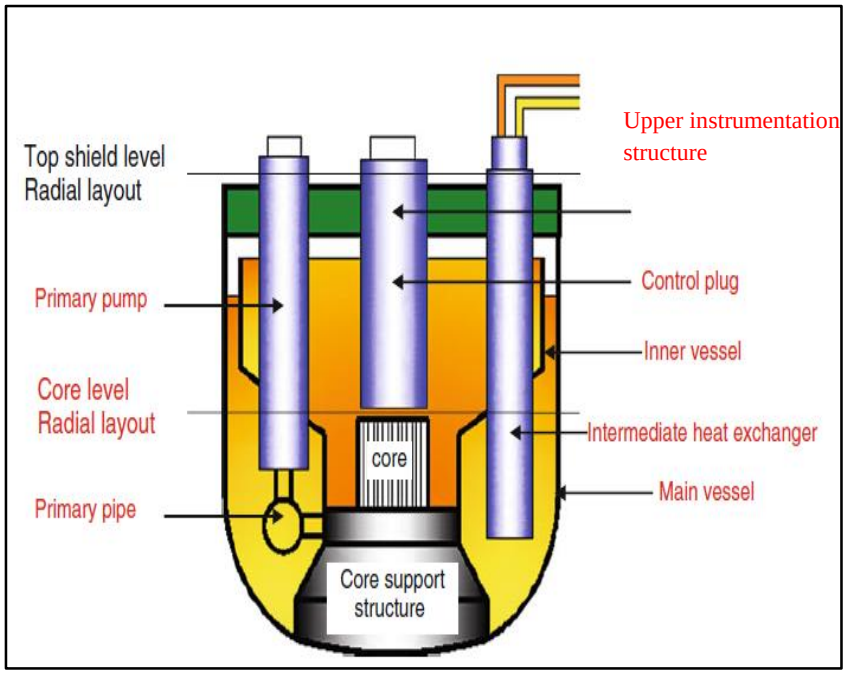

Figure 5-12: Schematic of the in-vessel components in a pool-type SFR configuration

Based on existing advanced SFR designs, the average core out-let velocity and temperatures are 2.3 m/s to 5 m/s and 500°C (773K) respectively. Also, temperature difference at the exit of core sub-assemblies could be as high as 60°C. With reference to current SFR designs, co-location of several large internal components into the reactor vessel displaces the coolant. Hence, less inventory of sodium and a resulting increase in nominal flow through the high power density core. High core exit velocities also pose additional surface gas entrainment safety challenges as wake regions develop at the free surface around the components. Such entrainment into the core has a potential to impact the kinetics of the reactor operations.

Given the above considerations, CFD is used as a tool to evaluate the impact of scaling on the pool-type SFR design and provide insight into the mixing phenomena. The lack of thermal mixing impacts the scaled design of the SFR pool and its in-pool, col-located components. Identified length scales include: the jet diameter '*d*', the spacing between multiple jets '*s*', and the axial distance between the core exit and the upper core structures '*h*', e.g. UIS. Parametric studies are also performed to evaluate the impact of kinematic ratios at core exits into the upper plenum pool. To understand the dynamics of the transport mechanism and quantification of the convective mixing in the upper plenum, a test matrix (see Table 5-7) representing different core outlet flow conditions was modeled and simulated using COMSOL CFD with liquid sodium as the working fluid.

Table 5-7: Numerical representation of different core outlet flow conditions in a SFR

		Temperature Difference (ΔT) Between Dual Jets (K)							
		0	**5**	**10**	**20**	**30**	**40**	**50**	**60**
Velocity Ratio (V_c/V_h)*	**0.1**	**X**	**X**	**X**	**X**	**X**	**X**	**X**	**X**
	0.3	**X**	**X**	**X**	**X**	**X**	**X**	**X**	**X**
	0.5	**X**	**X**	**X**	**X**	**X**	**X**	**X**	**X**
	0.7	**X**	**X**	**X**	**X**	**X**	**X**	**X**	**X**
	1	**X**	**X**	**X**	**X**	**X**	**X**	**X**	**X**

*

V_c *and* V_h are velocities of cold and hot jet representing fuel and blanket zones respectively

where temperature of the hot jet 'T_h' is kept constant at 773K representative of the fuel-subassembly outlet condition and temperature of the cold jet 'T_c' representing blanket-zone subassembly temperature is varied accordingly.

In summary, parametric studies has been performed to reveal the relative impact poorly mixed streams to the scaling and design of the SFR pool and in-pool, co-located components such as IHX, UIS, and pump.

CHAPTER 6: RESULTS and DISCUSSION

Evaluation of the integral two-phase thermal-hydraulic behavior and performance of the scaled-down water-cooled RCCS was based on system mass flow rate, pressure drop, static pressure, tank pressure, and bulk fluid and solid surface temperature measurements at different locations. Numerical thermal-hydraulic analysis of the separate effect turbulent mixing in the upper plenum of an SFR was based on parametric scaling studies and evaluation of momentum and thermal mixing. This chapter therefore provides results obtained from the investigated system parameters highlighted in sections 4.1.2 and 5.2.2 respectively.

6.1. Experimental Thermal-Hydraulic Analysis of a Scaled RCCS

Results of the thermal-hydraulic analysis of the scaled integral natural circulation RCCS test facility under off-normal two-phase flow conditions are presented. Here, emphasis is on the characterization of the two-phase dynamic behavior during storage tank volume and heat flux sensitivity studies. Using the baseline conditions (see section 4.1.2.1) as a reference, Figure 6-1 displays inlet and outlet fluid temperature, mass flow rate, pressure drop data over the full-time history of an experiment. It should be noted that local sensors were not available to investigate the boiling point elevation or depression effects in details since the integral effects were the primary scope of work. Hence the spatial-temporal flashing flow phenomenon driving the circulation was of primary interest.

6.1.1. Baseline Conditions (80% tank volume, 15.19 kW decay power)

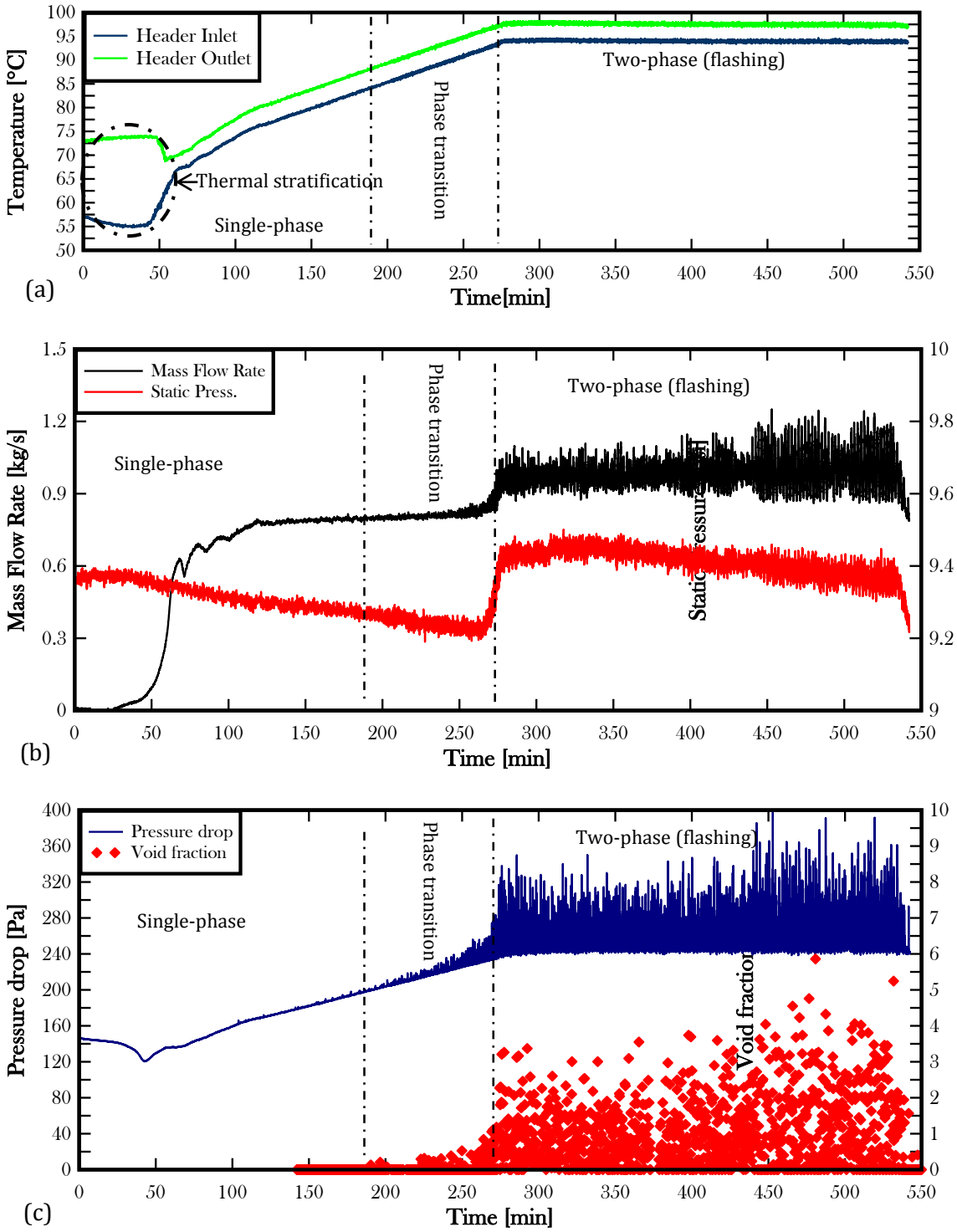

Figure 6-1: Full time history of (a) inlet and outlet temperature (b) mass flow rate and (c) pressure drop data, under baseline conditions (15.19 kW heat load and 80% tank volume)

Figure 6-1 is representative of system description on day 2 of a two-phase test as earlier described in Chapter 4. All system parameters are coupled. As seen in Figure 6-1(a), at the start of the test on day 2, the fluid in the system is thermally stratified. Hence the bulk of the fluid in the upper section of the test loop is at an average temperature of 73°C while the lower section is at 58°C. As the system is gradually heated up during the 1 hour ramp-up phase, a density difference induces flow which leads to the rise in system mass flow rate ($\dot{m} = \rho UA$) after about *t=25 minutes* into the test. The induced flow initiates thermal mixing in the storage tank and hence the bulk fluid temperature tends towards thermal equilibrium after *t=60 minutes*.

With continuous heat addition to the system, the header inlet and outlet temperatures increase. Increase in mass flow rate (Figure 6-1b) is proportional to an increase in pressure drop (Figure 6-1c), and as the water level gradually decreases due to evaporation (*t=35 to 270 minutes*), there is a corresponding gradual decrease in hydrostatic head (see Figure 6-1b). After *t=190 minutes*, with an outlet temperature of about 90°C, low magnitude perturbations are observed in the pressure drop and bubbles are detected by the optical phase sensor located in the chimney between the upper header and the tank inlet. These indicates the onset of nucleate boiling and phase transition region (*t=190 to 270 minutes*). The nucleate boiling regime is characterized with the formation and release of small bubbles from their corresponding nucleation sites along the risers. An evidence of the nucleate boiling and transition regime, the pipe surface temperature in the upper heated section, is 20°C to 40°C in excess of the saturation temperature. At *t=270 minutes*, the header outlet

temperature reaches saturation temperature 98.9℃ (boiling point of water at approximately 1000ft elevation above sea level). The onset of flashing leads to a sudden rise in all system parameters in Figure 6-1(a-c). Increase in the magnitude of voids translates to frequent oscillations in flow rate and pressure drop (Figure 6-1b and 6-1c) because of the order of magnitude change in density ($\rho_l/\rho_v \sim 10^3$).

The flashing flow phase is sustained between *t=270* to *545 minutes*, beyond which the power is ramped down. Hence, indicating the end of the test. The flow behavior within the flashing phase exhibit dynamic oscillations. Figure 6-2 highlights distinct oscillatory patterns within the boiling regime of Figure 6-1.

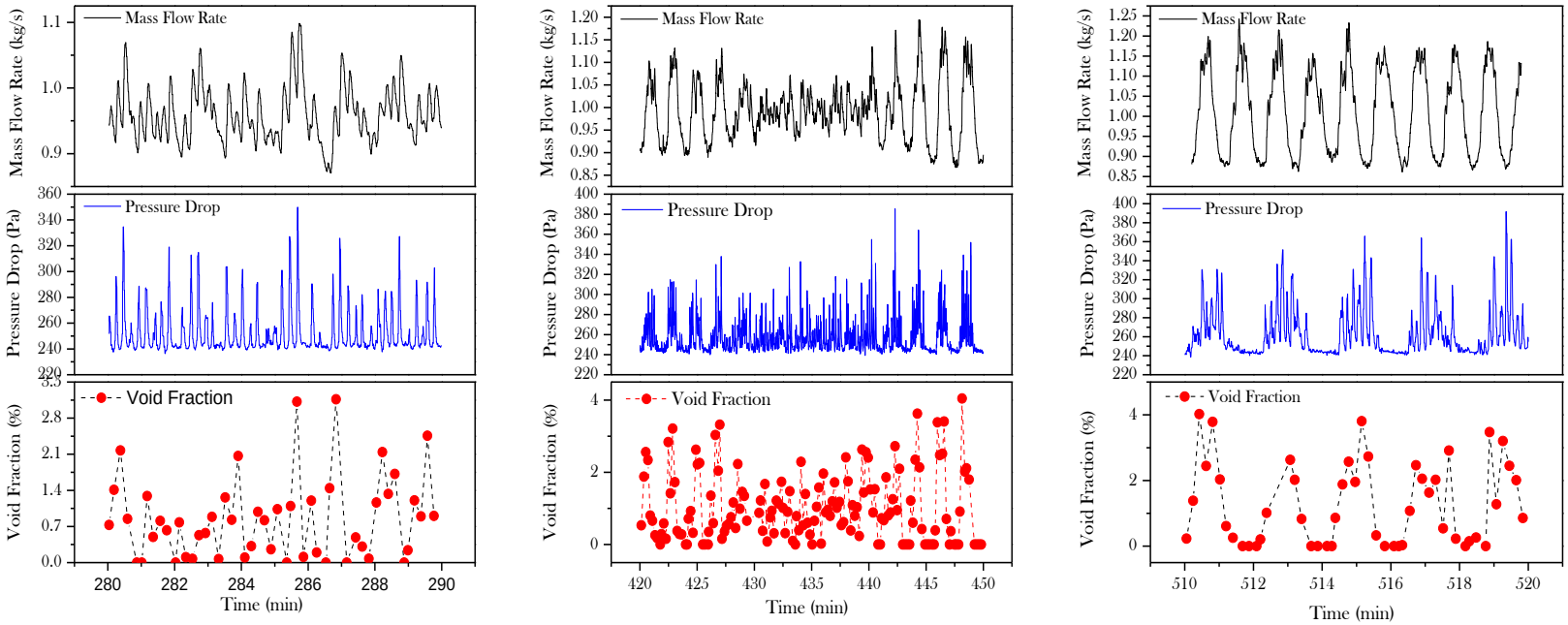

Figure 6-2: Three distinct oscillatory modes (a) t=280 to 290 minutes (b) 420 to 450 minutes (c) 510 to 520 minutes, representing mass flow rate, pressure drop and void fraction data during flashing of the baseline scenario test (15.19 kW, 80% tank volume)

Table 6-1 summarizes key system parameters for two-phase test at baseline conditions as earlier described in section 4.1.2.1.

A repeatability test was also performed using same initial conditions (80% tank volume, 15.19 kW heat load) as the baseline scenario. Figure 6-2 shows a comparison of system mass flow rate between the transition and two-phase boiling regime. A summary of key system parameters during two-phase boiling for the baseline condition and the repeat test (Run052 and 058) is provided in Table 6-2.

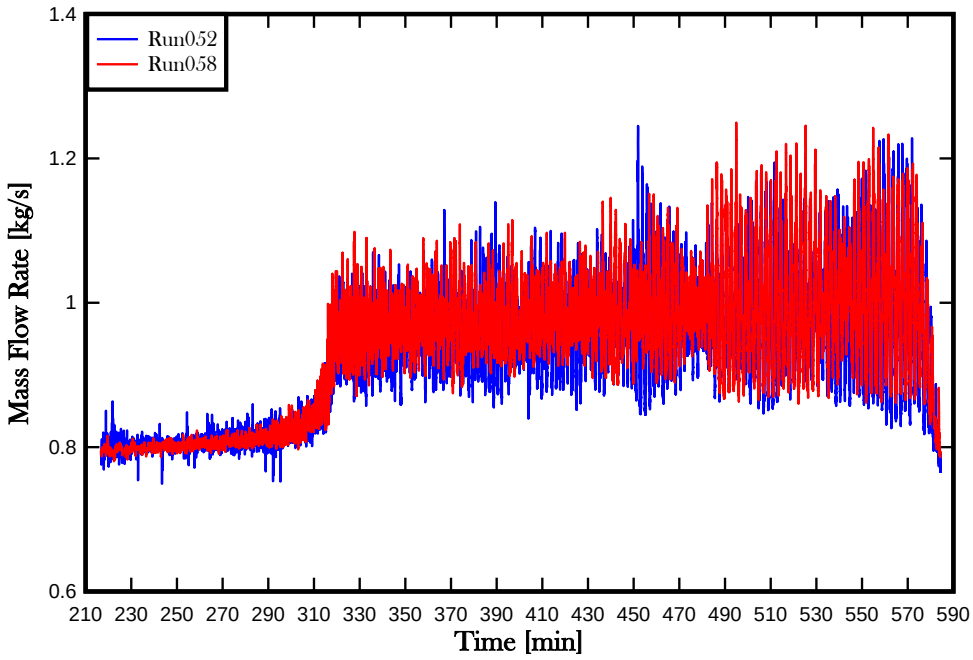

Figure 6-3: Comparison of system mass flow rate during two-phase regime under baseline conditions and repeat tests

Table 6-1: Summary of key system parameters for two –phase baseline condition and repeatability

Parameter	Run 058	Run 052	% difference
Heat flux (kW/m^2)	9.29	9.29	-
Mean ΔT (°C)	3.04	2.9	4.6
Mean $\dot{m}$ (kg/s)	0.986	0.971	1.5
Mean ΔP (Pa)	255.84	256.97	0.4
Mean α (%)	0.91	0.95	4.4
Mean head (psi)	9.41	9.44	0.3

6.1.2. Influence and Effect of Varying Decay Heat Load

Influence and individual contribution of different scaled decay heat loads (12.55, 15.19, 17.84 and 20.49 kW) to the thermal-hydraulic behavior of the RCCS are presented in this section. Similar procedure as the baseline conditions were kept and initial storage tank volume for all power tests were at 80% (52.5" $\pm$ 0.5"). Table 6-2 summarizes variation in decay heat loads, corresponding heat flux, and heating rate.

Table 6-2: Scaled decay heat load from the RPV, corresponding heat flux and heating rate for each power scheme

Scaled decay heat load (kW)	Heat flux (kW/m^2)	Heating rate (°C/min)
12.55	7.67	0.084
15.19	9.29	0.112
17.84	10.90	0.157
20.49	12.52	0.173

All tests were also sustained for approximately 4 hours after the onset of two-phase boiling. It was observed that there are dynamic changes in two-phase behavior with different energy input. Using the characteristic mass flow rate as basis for comparison, Figure 6-4 shows the magnitude of oscillations recorded for different heat flux. Other

Figures are reported in Appendix C. Table 6-3 gives a synopsis of the average of measured flow parameters in the boiling region.

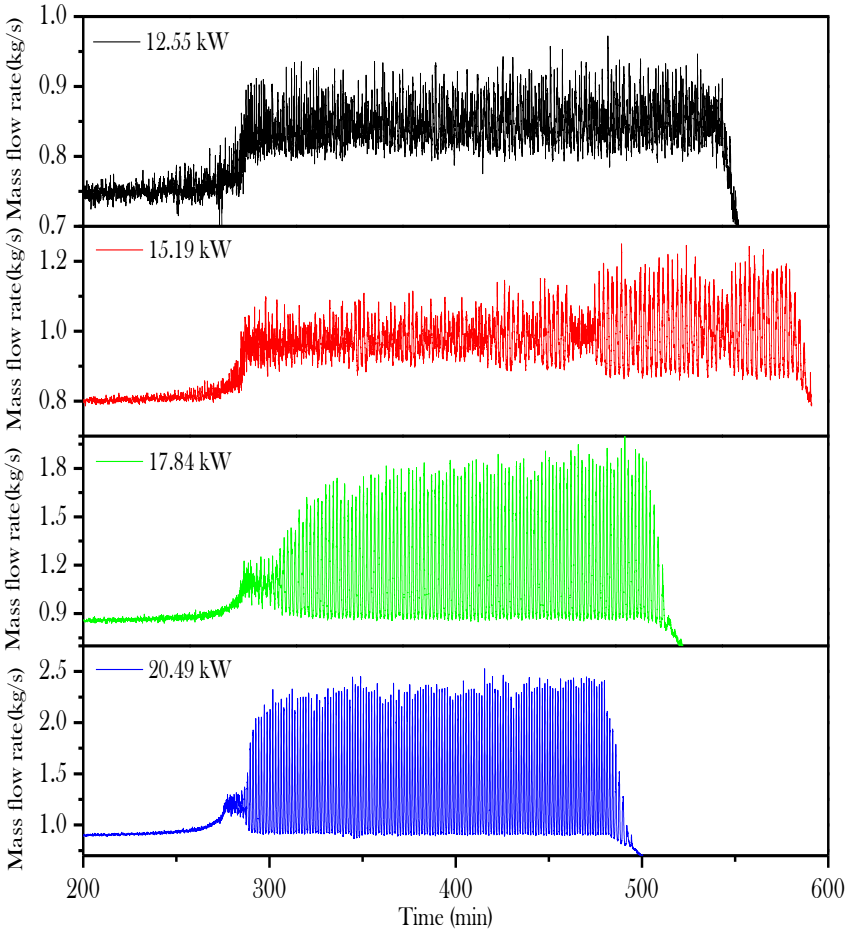

Figure 6-4: Summary of characteristic two-phase (flashing) mass flow rates during 12.55 kW, 15.19 kW, 17.84 kW and 20.49 kW tests

Table 6-3: Average dynamic system measurements in the flashing region

Heat flux (kW/m^2)	Mass Flow (kg/s)		Press. Drop (Pa)		Void Fraction (%)		Period (s)
	Mean	σ	Mean	σ	Mean	σ	___
7.67	0.85	0.03	245.37	9.36	0.92	0.47	297.4
9.29	0.99	0.07	256.62	18	1.18	0.94	126
10.9	1.16	0.31	292.94	70.81	2.89	4.07	103.2
12.52	1.33	0.45	327.48	117.13	5.49	8.15	84.6

Taking a closer look at the oscillatory behavior for each test in Figure 6-4, it was found that flow measurements corresponding to low input heat flux ($7.67\ kW/m^2$) showed a rather charateristic chaotic and random oscillatory behavior. With an increase in heat flux, the oscillatory behavior became more periodic. Test performed at $9.29\ kW/m^2$ exhibit a combination of chaotic (random) and periodic oscillatory behavior with the flow oscillations increasing in amplitude and dampening in a cyclic pattern in increments of 20, 32, 48 minutes until a more periodic behavior is established (see Figure 6-5).

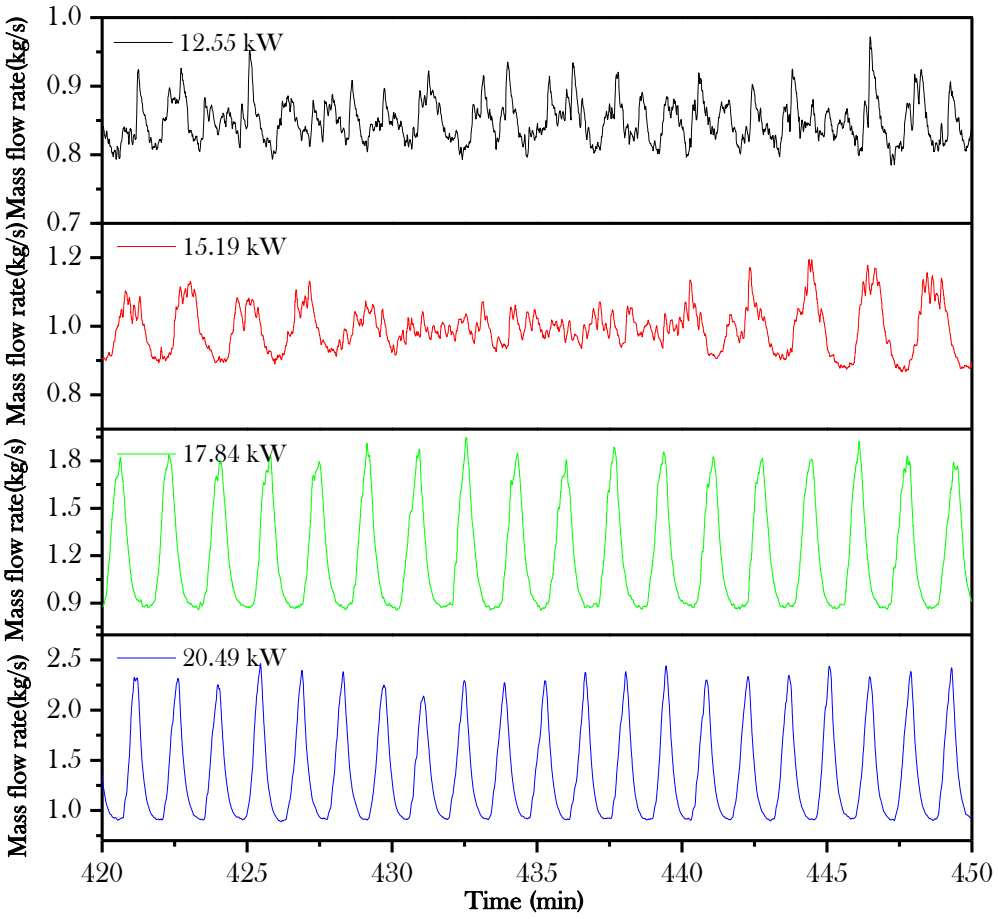

Figure 6-5: Mass flow rate oscillatory behavior over a 30 minute window 2.5 hours into the flashing phase.

At 17.84 kW (10.9 kW/m^2), a periodic behavior is sustained 15 minutes after the onset of boiling while tests performed at 20.49 kW (12.52 kW/m^2) showed a sustained periodic oscillatory pattern 10 minutes after the onset of boiling. Figure 6-6 shows a plot of the average period of oscillations during the two-phase boiling region for each test and also indicates that with increasing decay heat flux, the period becomes much smaller and hence the frequency is higher.

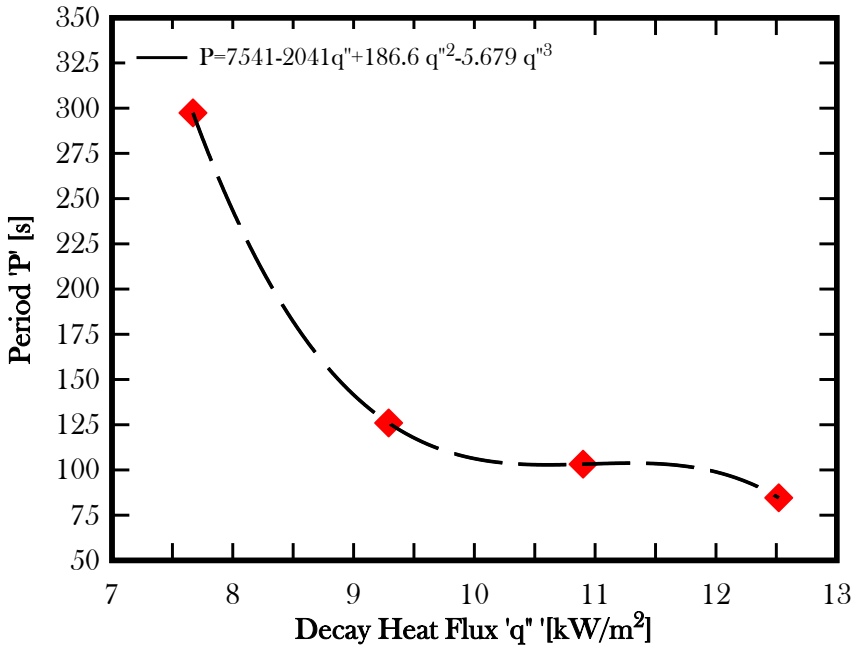

Figure 6-6: Average period of oscillations for 7.27, 9.29, 10.9 and 12.52$\frac{\mathbf{kW}}{\mathbf{m^2}}$ tests

Since the flashing front is occurring above the heated section, it was found necessary to understand the dynamics and flow mechanism downstream. Statistical analysis (full-width-at-half-maximum) was then used to analyze the random and periodic oscillatory behavior observed in the mass flow rate, pressure drop, and void-fraction results of each experiment within the boiling regimes.

The full width at half maximum (FWHM) describes the 'peakedness' of the oscillatory behavior and the two-phase flow mechanism, given that the phenomena is periodic and gives a good estimate of the standard deviation of each signal. Multiple samples (approximately 20 samples) of oscillatory behavior were taken from the instant when the oscillations are deemed established after the onset of boiling, 20

samples were also taken approximately two hours into boiling and another 20 samples taken within the last hour of each power scheme experimental test. All resolved peaks were fitted using a Gaussian model of the form in Equation 6-1 and Figure 6-7.

$$\mathbf{y = y_o + \frac{Ae^{-\frac{4\ln(2)(x-x_c)}{\omega^2}}}{\omega\sqrt{\frac{\pi}{4\ln(2)}}}} \qquad \text{0-1}$$

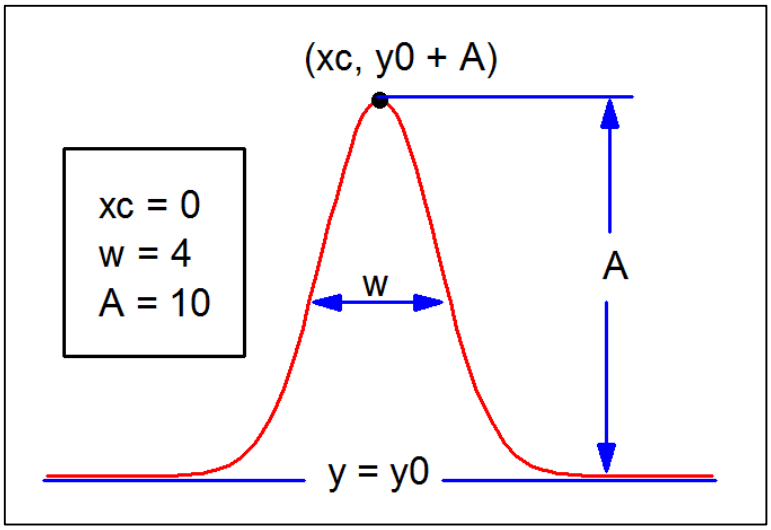

Figure 6-7: Components of the FWHM statistical analysis with a normal distribution

where y_o is the baseline offset, A is the total area under the curve from the baseline, x_o is the center of the peak and ω is the width of the peak at half height.

Since the lowest heat flux (7.27 kW/m^2) exhibits more random oscillations in the early stages of flashing, the peaks were carefully analyzed. Examples of curve fitting and FWHM analysis for the lowest and highest heat flux test are shown below in Figure 6-8 and corresponding peak values in Table 6-4. This represents the most random and periodic sets of oscillatory behavior. Similar analysis for the mid heat fluxes (9.29 and 10.9 KW/m^2) are detailed in Table 6-5.

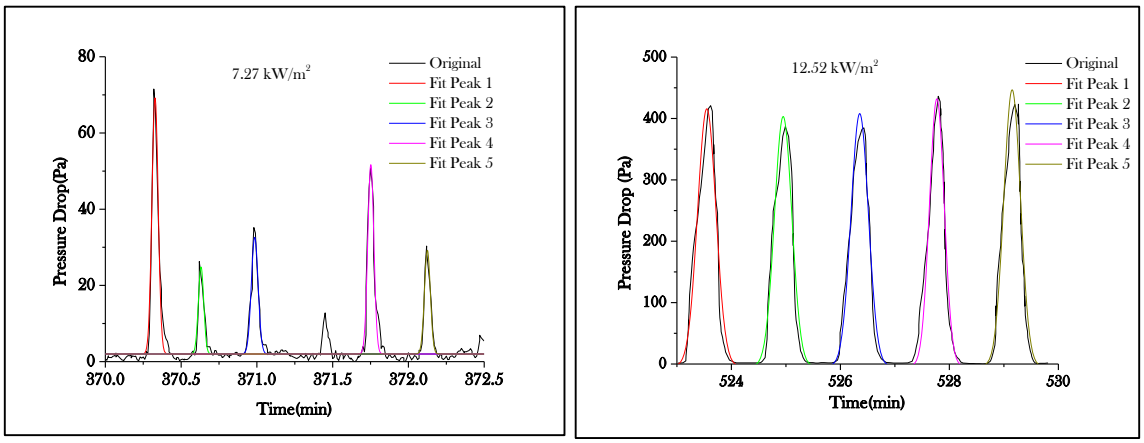

Figure 6-8: FWHM analysis of pressure drop oscillations for lowest and highest heat flux (7.27 and 12.52$\frac{kW}{m^2}$)

Table 6-4: Corresponding FWHM values for pressure drop (ΔP) peaks in Figure 6-8.

		7.27 kW/m^2		**12.52 kW/m^2**	
		Value	Standard Error	Value	Standard Error
Peak 1	y0(Pa)	2.00916	0.15233	-3.6723	4.08123
	x_c(min)	370.328	5.09E-04	523.548	0.00399
	A(Pa)	3.44639	0.07484	176.867	5.09131
	w(min)	**0.04819**	0.00117	**0.39616**	0.01084
Peak 2	y0(Pa)	2.00916	0.15233	-3.6723	4.08123
	x_c(min)	370.631	0.00134	524.95	0.004
	A(Pa)	1.00896	0.0684	162.162	4.90479
	w(min)	**0.04154**	0.00329	**0.37445**	0.01128
Peak 3	y0(Pa)	2.00916	0.15233	-3.6723	4.08123
	x_c(min)	370.986	0.00109	526.354	0.00422
	A(Pa)	1.70146	0.07464	164.646	5.08314
	w(min)	**0.05226**	0.00269	**0.37582**	0.01281
Peak 4	y0(Pa)	2.00916	0.15233	-3.6723	4.08123
	x_c(min)	371.752	6.22E-04	527.77	0.00305
	A(Pa)	2.49164	0.06955	147.87	4.10128
	w(min)	**0.04712**	0.00154	**0.31886**	0.00949
Peak 5	y0(Pa)	2.00916	0.15233	-3.6723	4.08123
	x_c(min)	372.125	0.00125	529.152	0.0033
	A(Pa)	1.31309	0.0739	173.616	4.58308
	w(min)	**0.04533**	0.00282	**0.36221**	0.00957

It can be deduced from Table 6-4, that there is an order of magnitude change in the width ω at full height when comparing the random oscillations at lowest heat flux input 7.27 kW/m^2, to the more periodic oscillations at highest heat flux input of 12.52 kW/m^2. FWHM analysis of the full spectrum of oscillations for all the different heat flux tests was performed and corresponding results are provided in Figures 6-9, 6-10 and 6-11.

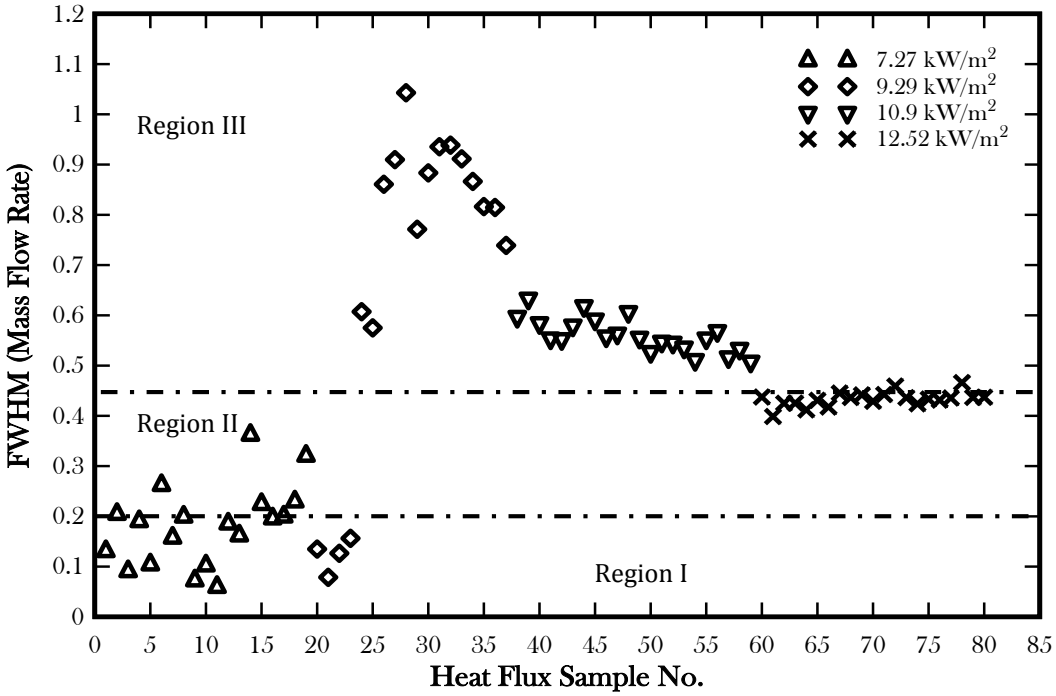

Figure 6-9: FWHM values for resolved peaks during flashing at different heat flux for mass flow rate

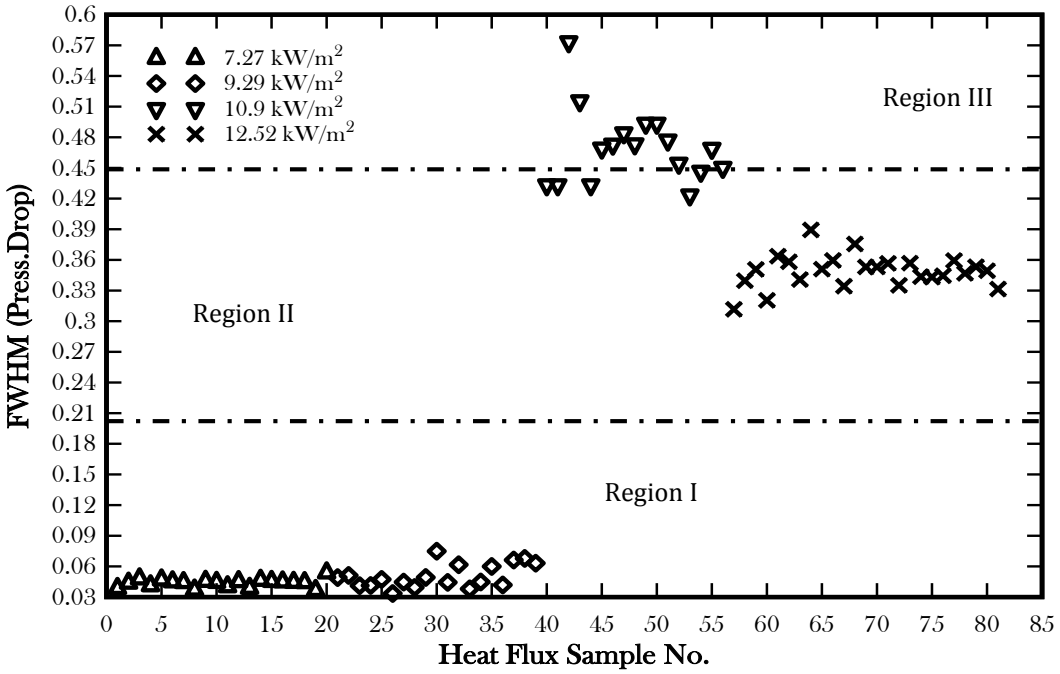

Figure 6-10: FWHM values for resolved peaks during flashing at different heat flux for pressure drop

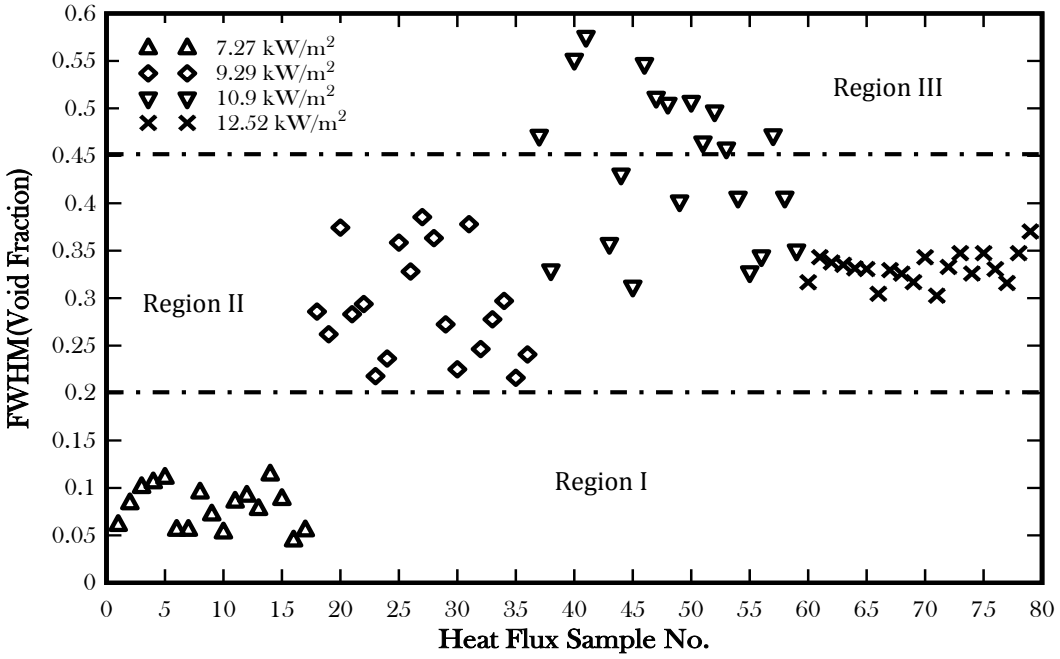

Figure 6-11: FWHM values for resolved peaks during flashing at different heat flux for void fraction

Table 6-5: FWHM values for five pressure drop peaks for 9.29 and 10.9 $\mathbf{kW/m^2}$

	9.29 kW/m^2		10.9 kW/m^2	
	w(min)	x_c(min)	w(min)	x_c(min)
Peak 1	0.0402	523.526	0.5449	542.289
Peak 2	0.0439	524.416	0.4262	544.075
Peak 3	0.0395	524.521	0.3703	545.569
Peak 4	0.0614	524.685	0.3888	547.462
Peak 5	0.0601	525.054	0.3163	548.762

From Figures 6-9, 6-10 and 6-11, three distinct regions can be identified. The tight coupling of the heat transfer with the circulation flow dynamics does not make resolving the results a trivial matter. Moreso, the configuration (i.e. geometry) and scaling is indeed a contributing factor to the complexity of this natural circulation test loop. At the onset of flashing, the temperature of the fluid in the chimney is constrained because of the phase change. However, because of the intermittent voiding and orders of magnitude change in density ($\rho_l/\rho_v \sim 10^3$) with heat (energy) input, there will be an increase in momentum injection into the storage tank. Due to the large volume of the tank relative to the rest of the loop, it has the capacity to accommodate the injection of momentum and thermal energy. This explains region I in Figures 6-9, 6-10 and 6-11, where the tank capacity is dominant over the flashing phenomena.

At a higher heat flux ($9.29\,kW/m^2$), more of the liquid flashes, hence a competing effect between the frequency of the flashing flow and the constraint from the natural frequency of the tank first and then the downcomer emerges. This coupled effect is reflected by the system mass flow rate since the measurement is recorded below the downcomer. This also explains why the FWHM for the mass flow rate (see Figure 6-9)

shows some high values as compared to pressure drop (see Figure 6-10) and void fraction (see Figure 6-11). Since two fundamental oscillatory modes were earlier identified (see Figure 6-5) for tests performed at 7.27 and 9.29 kW/m^2, the transitioning between regions I, II and III is expected. With increasing heat flux (10.29 and 12.52 kW/m^2) to the system, a higher fraction of the liquid is expected to flash. The dominant frequency of the flashing flow then begins to drive the entire loop since the liquid in the tank also approaches saturation temperature similar to the flashing flow. Thus, from lower to higher energy input into the system, at the point of flashing flow initiation, the upper header, the storage tank and the downcomer dimensions (length, cross-sectional area, volume) all come into play in the changing frequency signature as measured by G, ΔP and α. Scaling of these sections is thus important in understanding the thermal-hydraulic phenomena. Here we have used the FWHM to characterize the oscillatory behavior. This method is simpler than a full blown fluid-structure analysis that is seemingly complex.

6.1.3. Influence and Effect of Varying Storage Tank Inventory

The sensitivity of the RCCS test loop to changes in volume of water in the storage tank was also investigated. Sensitivity studies were performed with initial storage tank water volumes of 80% (960 L), 70% (840 L), and 60% (720 L). Heat input for all the tests were maintained at 15.19 kW (9.29kW/m^2). Aside from the change in initial conditions, start-up and other two-phase tests procedures remained the same as earlier described. Once again, the characteristic system mass flow rate was used as basis for comparison. The magnitude of two-phase system wide oscillations is provided

in Figure 6-12. Figures representing all other system parameters are given in Appendix C. Mass and energy balance calculations for all tests during two-phase (flashing phase) were also performed. Summary of average dynamic system parameters measured is also provided in Table 6-5.

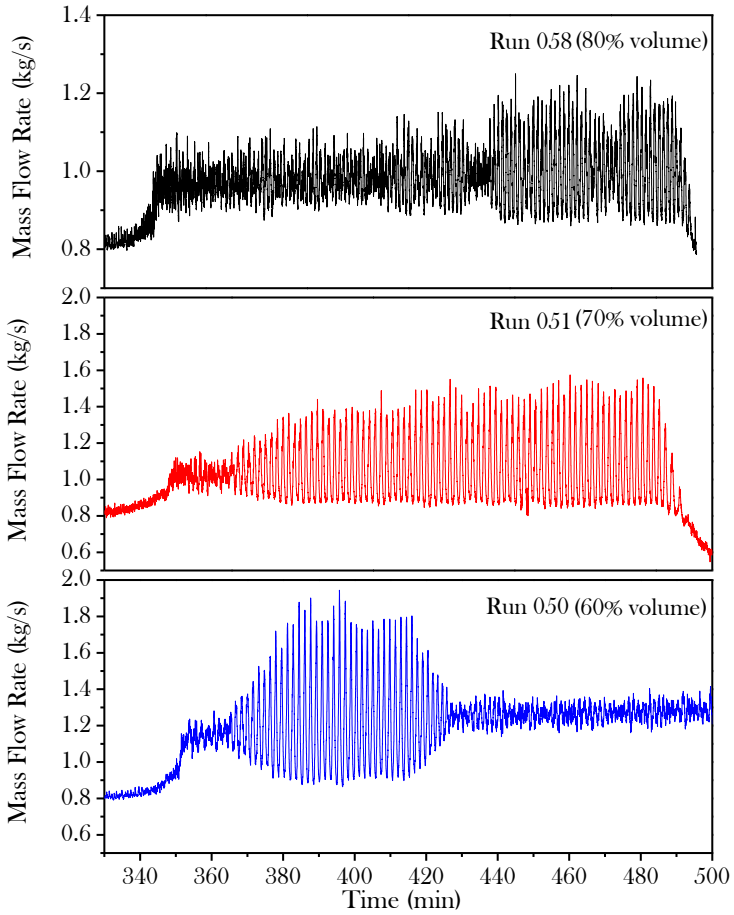

Figure 6-12: Summary of characteristic two-phase mass flow rates measured during tank volume sensitivity studies (80%, 70% and 60% tank volume)

Table 6-6: Average dynamic system measurements in the two-phase flashing regions

Tank Vol.		Flow Rate (kg/s)		Press. Drop (Pa)		Void Frac. (%)		Condensation
%	Litres	Mean	σ	Mean	σ	Mean	σ	Volume (gal)
80	960	0.99	0.07	256.62	18	1.18	0.94	18.2
70	840	1.06	0.176	273.48	37.9	3.40	2.22	13.5
60	720	1.24	0.164	306.60	61.5	4.90	4.21	22.5

Critical observation of the oscillatory behavior for each test in Figure 6-12, shows that dynamic system responses are different. It should be remembered that all tests were performed at same heat flux (9.29 kW/m^2). Initially, a comparison of the three cases in Figure 6-12 looks as if the time-scale is compressed with reduction in inventory. However, the thermal-hydraulic is not that simple as there is circulatory flow of liquid within the RCCS test loop.

At 80% tank volume (960 L), the system under two-phase flashing, exhibits a combination of chaotic (random) and periodic flow oscillations with the flow oscillations increasing in amplitude and dampening in a cyclic pattern in increments of 20, 32, 48 minutes until a more periodic behavior is established. Two-phase flow oscillations (*t=330 to 500 minutes*) at 70% tank volume (840L), shows a more periodic oscillatory behavior approximately t=20 minutes after the onset of flashing. The amplitude of flow oscillations gradually increased as the test progressed recording minimum and maximum flow rates corresponding to 0.8 and 1.57 kg/s respectively. Flow oscillations for two-phase (flashing) tests (*t=351 to 510 minutes*) performed at 60% tank volume (720L), shows a rather more interesting periodic oscillatory

behavior. The amplitude of oscillations gradually increase after the onset of flashing (*t=351 minutes*), peaks at 1.94 kg/s (*t=395.7 minutes*) and then the oscillations gradually dampen out until a more randomly oscillates between 1.14 and 1.42 kg/s. The oscillations however show a tendency to increase towards the end of the test. With reference to Figure 6-12, the dynamics of the flashing phenomena is a contribution of phase change due to heat addition from the heated section and a decrease in hydrostatic head along the vertical section of the chimney. Again, both these factors are scaling dependent within the context of integral loop design.

6.1.4. Influence and Effect of Accelerated Tank Depletion

Starting at the baseline conditions, i.e. 9.29 kW/m^2 and initial 960 L (80%) of water in the storage tank, this test was designed to simulate the RCCS behavior while it gradually undergoes inventory depletion due to evaporation over extended operating hours without replenishing storage tank inventory. Based on the average condensation rate (4.16 gal/hr.) recorded from the baseline condition tests, it is estimated to take approximately 23 hours under saturation for the storage tank level to reach 50%. An accelerated drain system was therefore introduced. A drain line was connected from the overhead storage tank inlet through a flow meter and a heat exchanger into a standalone tank. Hot fluid was gradually collected at a variable flow rate of ~ 0.25 – 0.4 gal/min. With the accelerated tank drain system, it took approximately 4.5 hours after saturation to reach the 50% desired level in the overhead storage tank. This corresponds to a $1/5^{th}$ shift in the timescale of operation. This test is also expected to give an integrated system behavior of sensitivity to the varying storage tank inventory

(80%, 70%, 60%) reported in Section 6.3. On completion of the accelerated tank drain test, approximately 85.5 gals (representing 33.8% of original tank inventory) of water was collected as a result of draining and condensation. Figure 6-13 shows the characteristic response of measured parameters.

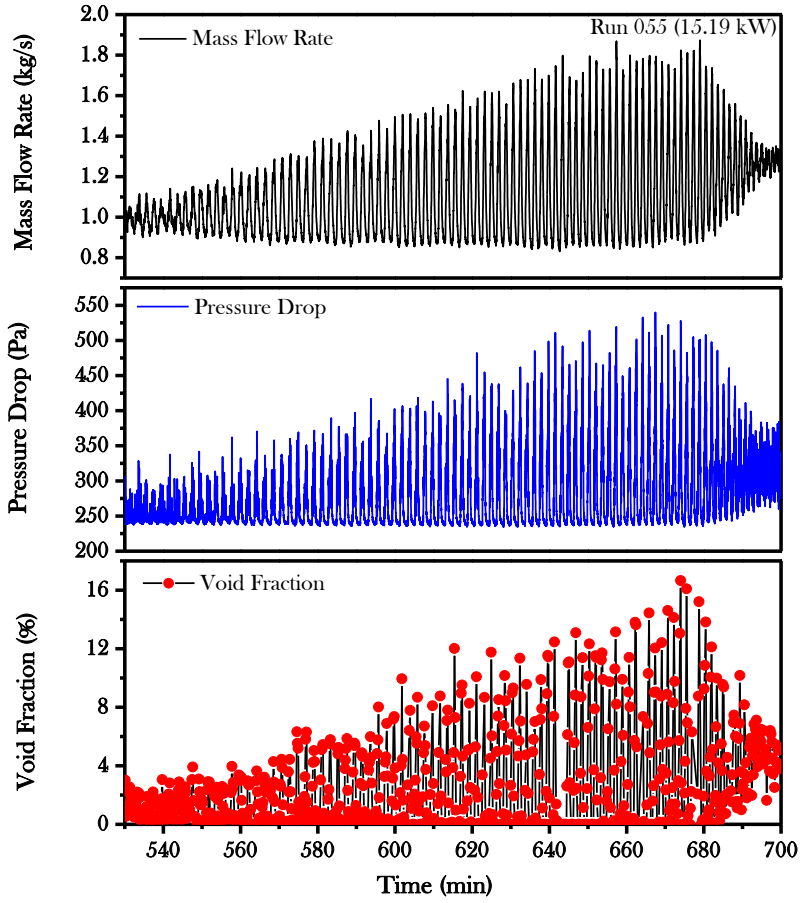

Figure 6-13: Measured mass flow rate, pressure drop and void fraction during two-phase (flashing) under the effect of accelerated tank depletion.

The oscillations in the flashing two-phase regime as shown in Figure 6-13 represents a tight coupling of flashing in the chimney due to the heat addition from the core (heated

section) and the decreasing hydrostatic head. This coupled effect can be attributed to the standard phase change due to heat addition and also the rate of phase change due to decrease in hydrostatic head.

Figure 6-13 displays an increasing magnitude of periodic oscillations from the onset of flashing (*t=530 minutes*) as the tank volume was gradually depleted (accelerated drain and loss due to vaporization). Though the amplitude of the oscillations increased with time, the crests of the oscillations were similar until t=630 minutes. Beyond this point, the amplitude of the periodic oscillations gradually decrease and eventually dampen (*t>695 minutes*). At this point in time, the water level is approaching the tank inlet and the flashing front is moving down the chimney towards the horizontal section (upper network). Hence, the phase sensor probe could no longer detect the void formation.

The dynamic behavior once again showed the coupling of the thermal-hydraulics across loop segments (storage tank, downcomer, interaction between standpipes, chimney), scaling of the initial flow conditions, and also the impact of scaling different sub-systems, e.g. length of heated section.

6.2. Numerical Thermal-hydraulic Analysis of Turbulent Mixing in SFR

Modeling and simulation of thermal mixing for an anticipated SFR core outlet thermal-hydraulics configuration with COMSOL Multiphysics has been computationally investigated as a separate effect test. Considerations have been given for the inclusion of additional scales (geometric and kinematic) other than the global dynamic

similarities (Re and Pe) in order to have a good representation of the convective mixing in small and large scale designs.

6.2.1. Baseline Thermo-fluid Simulation: Iso-velocity and Iso-thermal

A baseline thermo-fluid simulation with sodium is representative of similar velocities (2.3 m/s) and temperatures (773K) across both jets. This gives a basis for thermal-hydraulic comparison for the parametric studies at different flow conditions as highlighted in Table 5.7. Maintaining the same nozzle diameter (D=6.35mm) and geometric ½ axial length-scale ($l = 0.5$) of a full-scale upper plenum, the equivalent $\mathrm{Re_D}$ and Pe are $5.2 * 10^4$ and $2.29 * 10^2$ respectively. Figure 6-14 shows the instantaneous velocity surface field for the steady-state simulation and also the representation of the idealized lateral velocity profile . Figure 6-15 displays the streamwise velocity decay along the geometric centerline from a representative simulation.

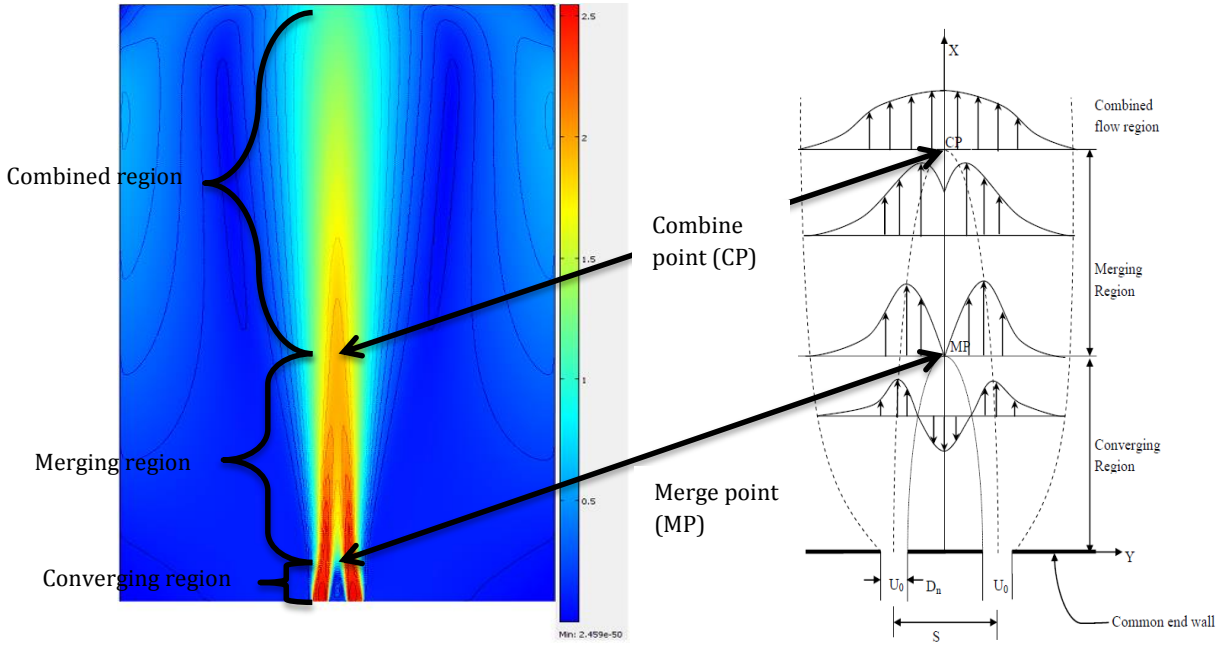

Figure 6-14: Instantaneous velocity surface plot and flow field for isothermal dual-jets

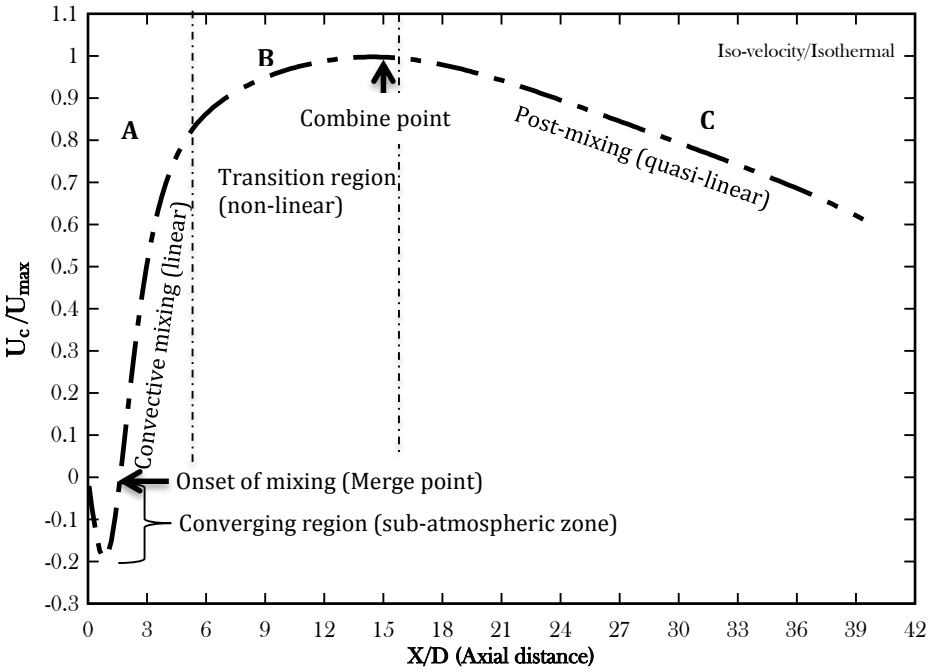

Figure 6-15: Regions along the geometric centerline velocity decay of parallel dual-jets

In Figure 6-15, the axial distance and velocity along the geometric centerline were non-dimensionalized by using the jet diameter and maximum centerline velocity respectively. Comparing the flow pattern in Figures 6-14 and 6-15, there is an equal entrainment rate (2.3m/s) across both jets. This creates a sub-atmospheric region with reverse flow near the entrance region between both jets. This explains the converging region (negative velocity) between $0 < \frac{X}{D} < 1.6$. At $\frac{X}{D}$= 1.6, the velocity along the geometric centerline is zero and the inner shear layers of both jets begin to merge, i.e. merge point. This represents the onset of mixing between both streams. The merging region ($1.6 < \frac{X}{D} < 14.2$) is where the most convective mixing takes place. This peaks at the combine point ($\frac{X}{D} = 14.2$) which equally represents the maximum velocity along the geometric centerline. At $\frac{X}{D} > 14.2$ (post-mixing region), the dual-jets gradually become self-similar (acting like single jet). However, any existing ΔT between the jet gradually dissipates as transverse heat transfer takes place.

6.2.2. Effect of Temperature on Sodium Turbulent Mixing

The velocity field was kept the same but the temperature difference at the inlet across both jets was varied ($5K < \Delta T_{hc} < 50K$) because besides velocity, the two streams are expected to be at different temperatures. Though the temperature difference between multiple jets at the exit of different sub-assemblies could be as high as 150K, the thermo-fluid simulations were limited to $\Delta T_{hc} < 50K$ mainly because up to $\Delta T_{hc} = 50K$, no significant thermal effect was observed on the velocity field (see

Figure 6-16). Figure 6-16 shows the geometric centerline velocity decay for several iso-velocity but non-isothermal thermo-fluid simulations.

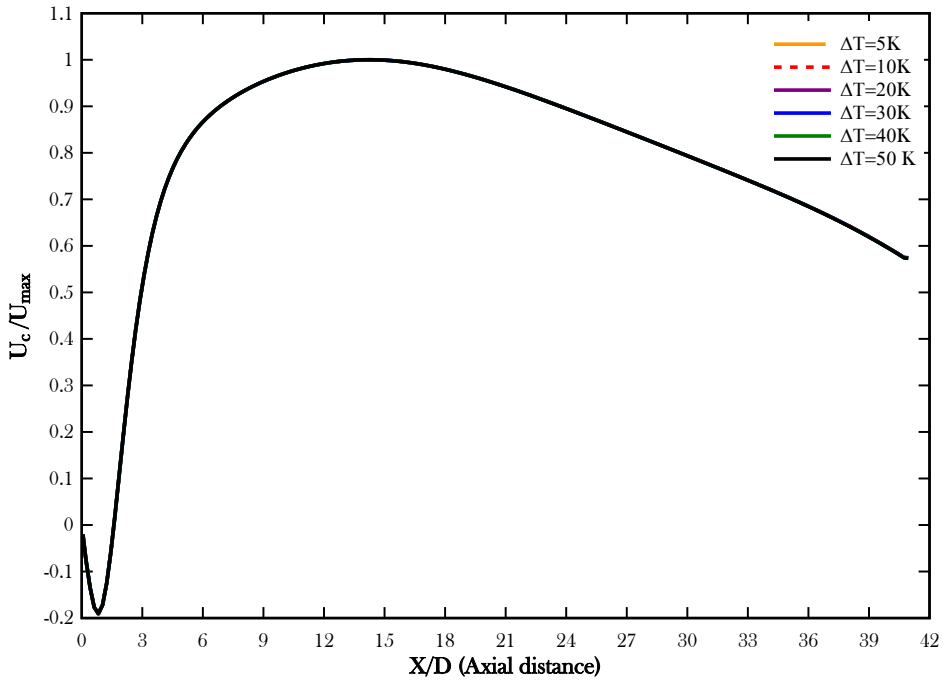

Figure 6-16: Effect of ΔT_{hc} across both jets on the streamwise centerline velocity decay

In Figure 6-16, no noticeable difference (less than 0.5%) was observed as a result of temperature difference (ΔT_{hc}) on the convective mixing regime ($1.6 < \frac{X}{D} < 14.2$) because all the centerline profiles over-lay each other. It hence shows that the jet flow is momentum or inertially-controlled and buoyancy effects are negligible. The momentum dominated analysis was further confirmed with the Richardson number (Ri) ranging between $1.70 \times 10^{-5} < Ri < 1.69 \times 10^{-4}$.

Figure 6-17 illustrates the centerline thermal mixing for different ΔT_{hc}. The centerline thermal field profile for $5K < \Delta T_{hc} < 50K$ shows that a homogenous mixture was not obtained even at 5K.

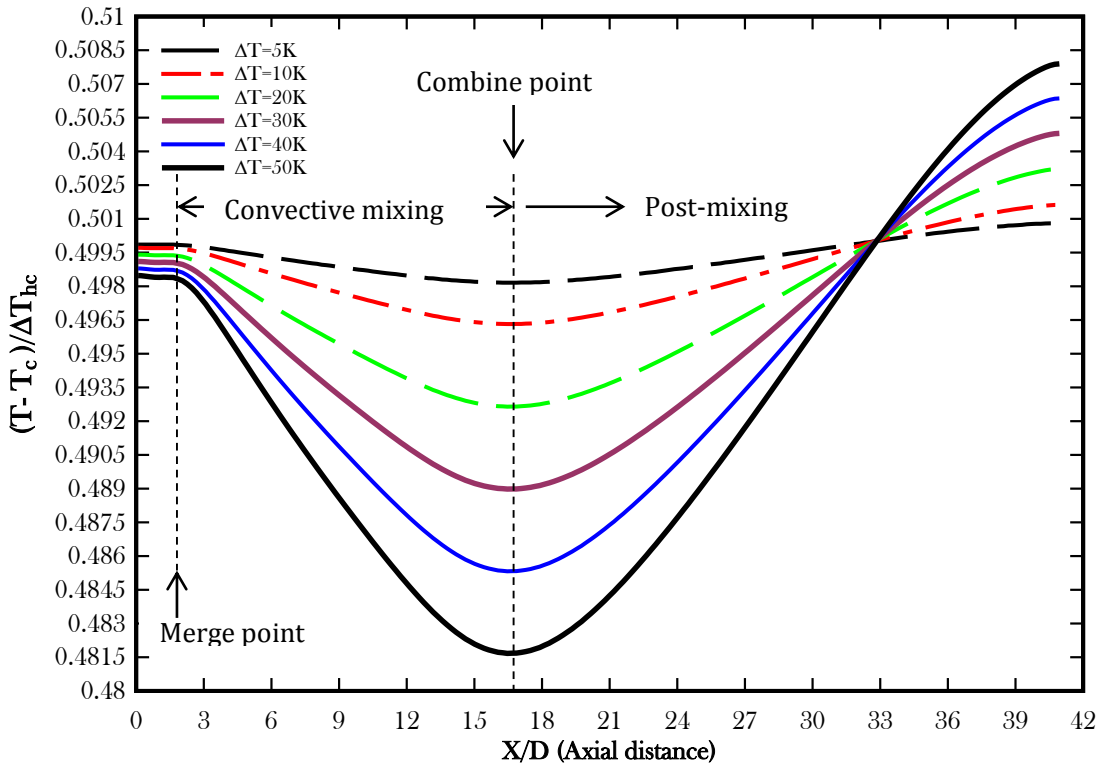

Figure 6-17: Thermal mixing along the geometric centerline for non-isothermal dual-jets

On the y-axis of Figure 6-17, the difference between the instantaneous temperature and the temperature of the cold jet is non-dimensionalized by the temperature difference between hot and cold jet. From Figure 6-17, the onset of thermal mixing corresponds with the onset of momentum mixing at $\frac{X}{D}$~1.6. There is however a slight shift in the combine point at $\frac{X}{D}$~ 16.8 as compared to $\frac{X}{D}$~14.2 for the velocity field. Beyond $\frac{X}{D}$~16.8, the convective mixing is small compared to the

transverse heat transfer after the jets merge. Hence, the temperature gradually increases beyond $\frac{X}{D}$~16.8. Since temperature is a scalar, thermal mixing is facilitated by mixing of the transverse momentum. However, transverse momentum is smaller than its axial counterpart. Hence, there is a slight spatial lag that corresponds to the minimal point of thermal mixing relative to momentum mixing.

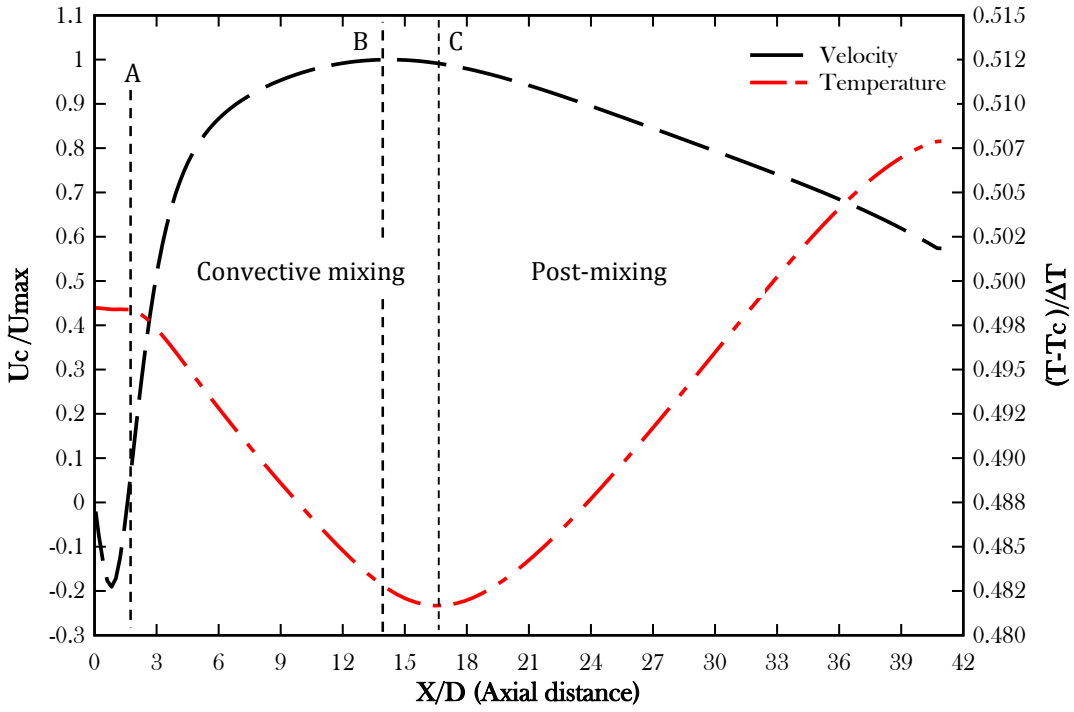

Figure 6-18: Streamwise velocity and temperature profiles for non-isothermal ($\Delta T = 50K$) and iso-velocity (2.3 m/s) dual-jets. Point "A" represents the merge point, "B" represents the completion of momentum mixing while "C" represents the peak thermal mixing

Figure 6-18 incorporates an element of Figure 6-16 and Figure 6-17, and gives a comparison of the geometric centerline of the thermal and velocity fields. From Figure 6-18, it can be deduced that thermal mixing and momentum mixing are both initiated at same merge point ($\frac{X}{D}$~1.6). However, it is observed that the peak momentum

mixing occurs at $\frac{X}{D}\sim 14.2$ while peak thermal mixing is essentially achieved further downstream at $\frac{X}{D}\sim 16.8$.

Figures 6-19 shows the prediction of the temperature field across the test loop at different axial locations along the flow field. As it would be expected, the temperature gradient is highest close to the jet exit (X/D=1.6) and gradually decreases downstream (X/D=41) after to thermal mixing and radial dissipation.

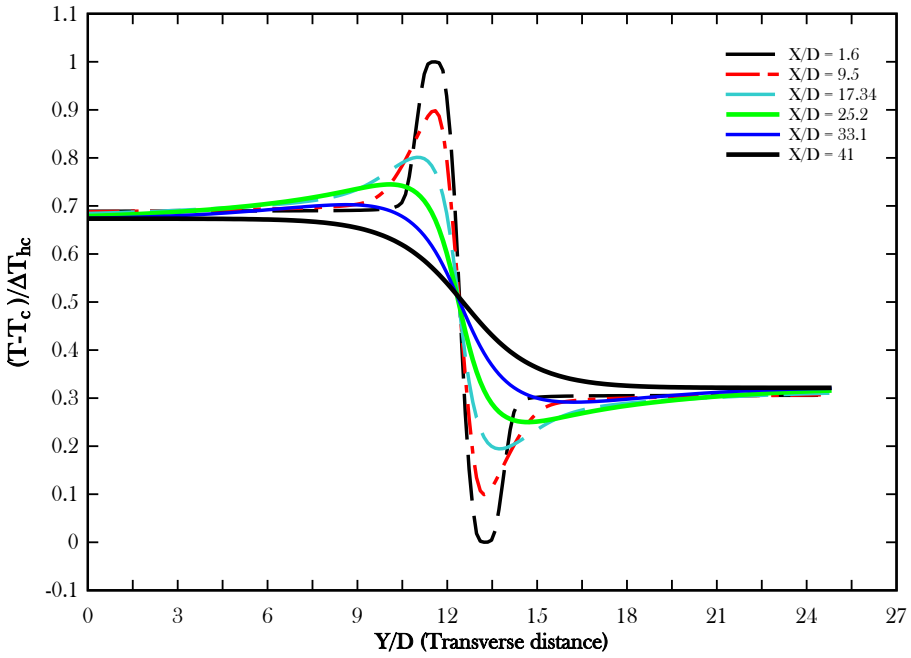

Figure 6-19: Spanwise temperature profile across the flow field at different elevations for $\Delta T = 50K$ and $Vratio = 1$

6.2.4. Effect of Velocity Ratios on Thermal Field

Convective mixing was also quantified under scenarios where the core exit velocities in different core sub-assemblies varied. Based on the matrix in Table 5-7,

simulations were performed for velocity ratios $0.1 < \frac{U_c}{U_h} < 1$. For non-isothermal jets (ΔT_{hc}=10K), Figure 6-21 shows the velocity contour plots for $\frac{U_c}{U_h} = 0.3, 0.5$ and 1.

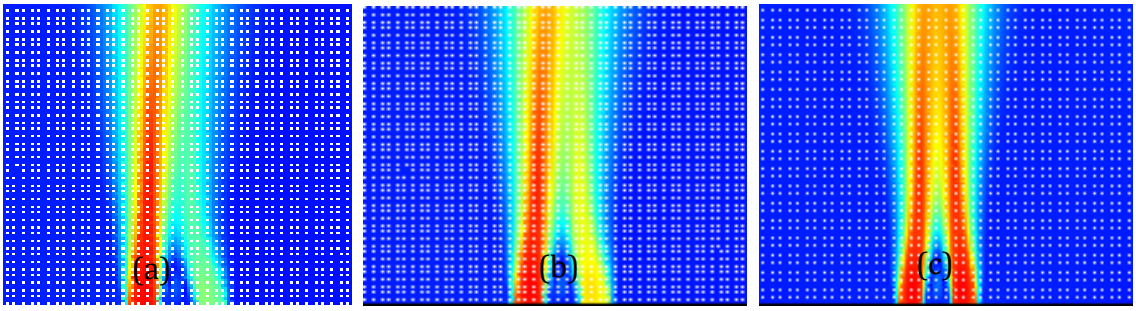

Figure 6-20: Velocity field plots for different velocity ratios at $\Delta \boldsymbol{T} = \boldsymbol{10K}$ showing the different merge points (a) $\frac{\mathbf{U_c}}{\mathbf{U_h}} = \mathbf{0.5}$ (b) $\frac{\mathbf{U_c}}{\mathbf{U_h}} = \mathbf{0.7}$ (c) $\frac{\mathbf{U_c}}{\mathbf{U_h}} = \mathbf{1}$

Figure 6-20 therefore shows a slightly modified flow trajectory for different jet velocity ratios. It is observed that the lower velocity jet (right jet) merges with the higher velocity jet (left jet) slightly closer to the jet entrance. This is largely due to the higher entrainment rate of the surrounding fluid by the higher velocity jet. Figure 6-21 shows the centerline temperature for the different velocity ratios and reveals the effect of velocity ratios across the jet streams on thermal mixing.

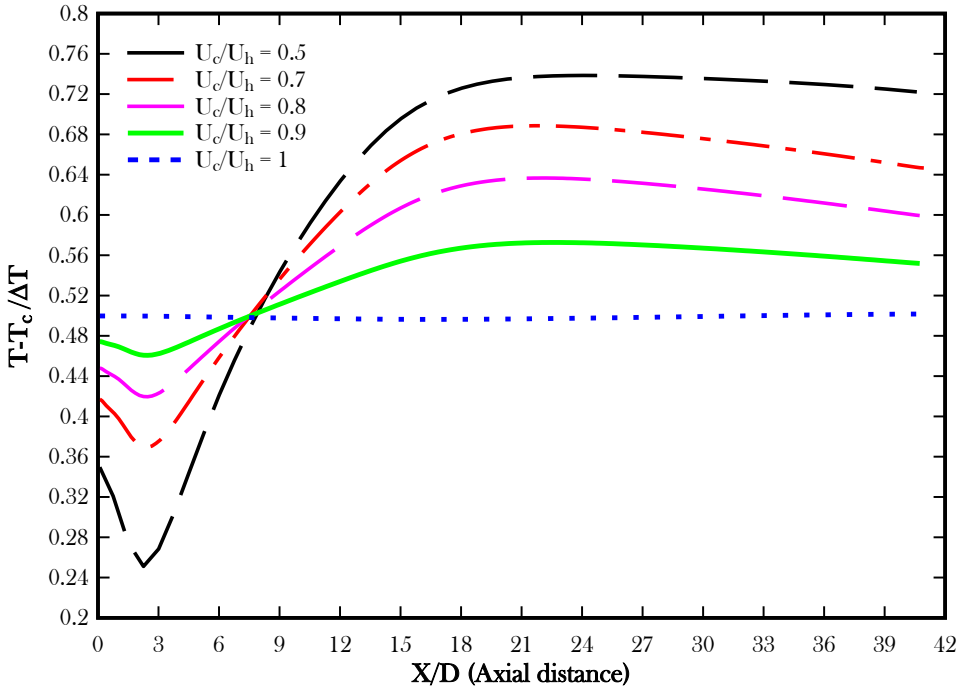

Figure 6-21: Influence of velocity ratios on non-isothermal field ($\Delta \mathbf{T} = \mathbf{10K}$)

Though with lower velocity ratios, the onset of mixing occurs earlier, Figure 6-21 shows that $\frac{\mathbf{U_c}}{\mathbf{U_h}} < \mathbf{1}$ are not favorable to turbulent mixing between the two jets. An explanation for this is because a much lower pressure zone is established due to different entrainment rates between the jets with $\frac{\mathbf{U_c}}{\mathbf{U_h}} < \mathbf{1}$ as compared to $\frac{\mathbf{U_c}}{\mathbf{U_h}} = \mathbf{1}$. As a result, the respective jets are entrained in a non-symmetric manner. Hence the mixing rate at the onset of mixing is lower and less thermal mixing is achieved.

6.2.5. Effect of Jet Spacing

Studies to investigate an optimum jet spacing that will be most appropriate to enhance turbulent mixing were performed. For the dual jet under review, Figure 6-22 highlights the onset of mixing (merge point) in the instantaneous surface velocity field plots for S/D =2, 5 and 7.

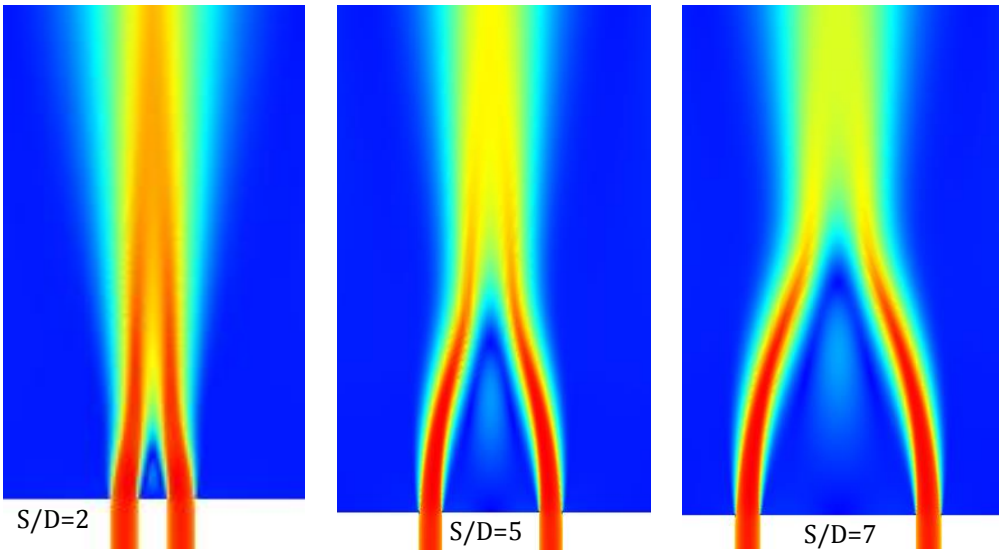

Figure 6-22: Instantaneous velocity field for isothermal (773K) and iso-velocity (2.3m/s) dual jets for S/D =2, 5 and 7 respectively

Comparative plots of the centerline velocity decay for each of the jet-spacing thermo-fluid simulations (S/D=2, 3, 5 and 7) are shown in Figure 6-23. A visible shift further downstream of the onset of mixing is noticeable with increasing spacing between both jets (see Figure 6-23). Based on the results from Figure 6-23, Figure 6-24 establishes a correlation that relates the jet-spacing to the onset of mixing for two parallel jets.

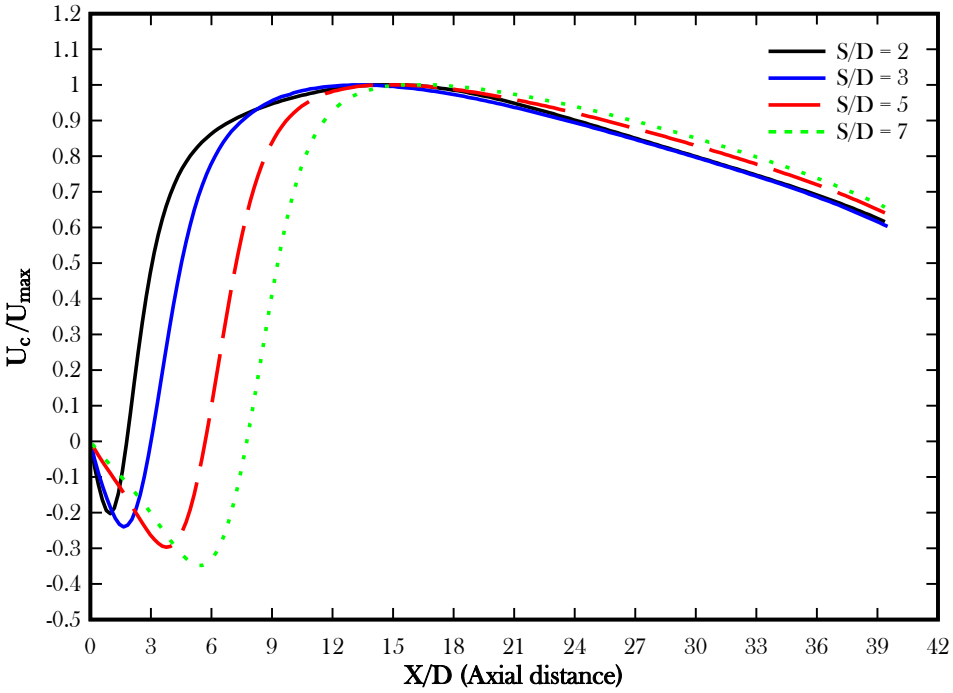

Figure 6-23: Influence of jet-spacing on turbulent mixing of two parallel jets at T=773K and U=2.3m/s

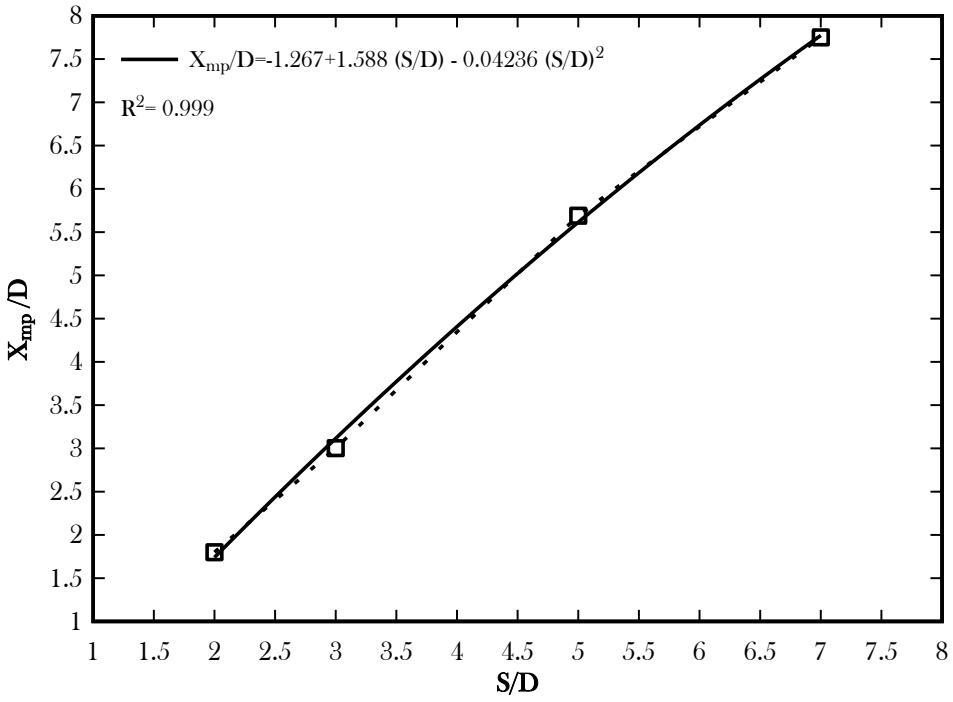

Figure 6-24: Correlation between jet-spacing and onset of mixing for two isothermal (773K) and iso-velocity (2.3m/s) jets.

Figures 6-23 and 6-24 therefore show that at some threshold spacing between both jets, less and almost no mixing will be achieved. Hence, each of the jets will essentially behave as a single-jet. For an optimized turbulent mixing system, the S/D=2 facilitates the most thermal mixing. Lack of thermal mixing beyond the core exit therefore has significant impact on the scaling of the SFR pool (height and width), and major in-pool components (UIS, IHX and pump). For the design of larger scale or integral test facility, there will be need to simulate the realized lack of thermal mixing and its scaling impact on IHX and pump performance.

CHAPTER 7: CONCLUSIONS

This thesis research work focused on the scaling methodology and thermal-hydraulic analysis of two safety systems of relevance respectively to the Next Generation High Temperature Gas-cooled Reactor (HTGR) and advanced Sodium Fast Reactors (SFR). The analysis include two-phase and single phase thermal-hydraulic flows in the reactor cavity cooling system of the HTGR and in the upper plenum of the SFR have been experimentally and computationally investigated. The scaling methodology integrates separate effects and integral tests, and uses both experimental and computational tools to fulfill top-down and bottom-up scaling methods. These are seen as original contributions.

6.3. Thermal-hydraulic Performance of the Reactor Cavity Cooling System

An integrated scaling approach based on Ishii's scaling methodology was utilized to guide the design of a ¼-scaled RCCS test facility at the University of Wisconsin-Madison. Scaling laws for the test facility have been validated under both single and two-phase conditions using RELAP5. Single phase, steady-state experimental tests performed further validated derived scaling laws and showed linearity in system wide parameters. It has also been shown that the RCCS is capable of removing the decay heat from the RPV of the HTGR under forced circulation during normal operating conditions.

Passive cooling (natural-circulation) capability of the RCCS has been investigated under off-normal operating conditions such as in LOFC. Parametric and sensitivity studies to investigate the influence of scaling system inventory and varying heat flux input on RCCS decay heat removal capability were also performed. These parameters (P, T, ΔP, G, α) have been used to characterize system behavior and evaluate system performance at saturation conditions (two-phase flashing). Observed two-phase flow oscillations as recorded using a range of instruments have been analyzed using a demonstrated Full Width-at-Half Maximum (FWHM) statistical method. The FWHM characterized the flashing-induced oscillatory system and facilitated understanding of the coupling of loop segments of the RCCS. It was established that at low heat flux (7.67 kW/m^2) and approximately 80% tank inventory, the flow oscillations were more random and chaotic in nature. Gradual increase in heat flux from 7.67 kW/m^2 to 12.52 kW/m^2 however showed increasing periodicity. FWHM analysis shows that there is a tight coupling between the RCCS sub-systems, and the scaling dependent transient thermal-hydraulics. Hence, with increasing heat input from the RPV (heated section); the dynamics of the flashing phenomena is constrained by the phase change in the chimney above the heated core and this changes the thermalhydraulics as defined by the given scales.

Also, an increase in vapor generation leads foremost to an increase in momentum injection into the storage tank. Because the tank storage capacity (volume) is approximately of a 10:1 ratio relative to the rest of the entire natural circulation loop, it has the capacity to accommodate the momentum and thermal energy input. At

a higher heat flux (10.9 and 12.52kW/m^2), the flashing phenomena intensifies and hence, the dynamic interaction, notably the natural frequencies of liquid in the tank and downcomer change. At some threshold heat flux, the energy transfer reaches a condition such that the tank bulk temperature approaches the phase change temperature. Hence the flashing phenomenon begins to drive oscillatory flow under natural circulation in the loop.

Similar analysis was performed for the storage tank inventory sensitivity studies. Here, the flashing phenomenon is a coupled effect of the heat addition into the standpipes and additional phase change due to hydrostatic head change. The qualitative analysis of the two-phase dynamics also shows a tight coupling of the four regions within the natural circulation loop (tank, downcomer, standpipes and chimney), the inertial and thermal effect into the tank, and the natural frequency of the downcomer. Regardless of the initial tank volume, 80%, 70% or 60%, momentum and heat injection to the tank continues during the two-phase flashing phase. There is however a longer time-scale associated with establishing an overall circulatory flow at 80% than at 60%. Once the water level falls below the tank inlet as is the case of the 60% volume test and the reduced inventory tests, there is no more momentum injection into the system. The interaction is therefore only between the tank, downcomer and standpipes. The only system response hence becomes due to the hydrostatic head change.

The relative volumes of the four regions (tank, downcomer, standpipes and chimney) will need to be scaled in order to account for the momentum and heat

injection that translates into dynamic character of the loop. Since the key expectation of the RCCS loop is to provide passive-cooling for approximately 72 hours before any inventory replenishing, the following will be recommended to support design of the full-scale RCCS. The ratios of the volumes, length-scales and cross-sectional area of each region should be varied and a parametric study using RELAP5 will need to be performed. This should provide insight into the different stages of the flashing phenomena, the associated time-scales and also the linked impact of scaling on the overall RCCS performance. It will be expected that increasing the cross-sectional area of the downcomer, the time-scale for establishing the overall circulatory flow will be shorter. Also, increasing the cross-sectional area of the chimney will require a longer time-scale to build the flashing flow momentum in the chimney prior to injection into the tank. In addition, a larger cross-sectional area chimney will further help disperse the momentum and energy more radially. Incorporating a larger cross-sectional area for the downcomer and chimney will promote the overall circulatory flow and limit the over-pressurization of the gas-space in the tank, boil-off and inventory loss. This further indicates the impact of scaling the sub-systems in the RCCS on the thermalhydraulics of the entire system.

6.4. Modeling of Turbulent Mixing in Upper Plenum of Sodium Fast Reactors

CFD has been used as a tool to establish a computational separate effects understanding of the geometric, kinematic and dynamic scales of relevance to turbulent thermal-jet mixing in the upper plenum of a prototypic SFR. Enhanced

turbulent mixing is important in order to prevent poorly mixed coolant streams out of the SFR core and its thermal-cyclic load deposition on in-vessel structures and components. The cyclic effect is undesirable because it can cause thermal fatigue and eventual failure of the components. The extent of thermal mixing or lack thereof above the core impacts the scaling of the SFR pool and functions of major in-vessel components such as the IHX.

The predictive capabilities of COMSOL Multi-physics was first explored and verified using experimentally obtained single and two-jet water-based UVP data under isothermal conditions. COMSOL CFD, even with a limited k-ε turbulence model showed results within the same order of magnitude and accuracy as the validation experimental data.

To enhance mixing of coolant streams beyond the core exit, parametric studies (length, velocity and temperature) were performed to investigate the phenomenological driving mechanism, effect of relative scales and how they influence mixing in the upper plenum.

It can be concluded that under current configuration and operating conditions of advanced SFRs, thermal mixing is momentum driven and it's difficult to prevent both lateral and transverse thermal striping from occurring. Design (thus scaling) modification will therefore be required to distort the jet flow and enhance mixing, either with baffles or skirts. One therefore needs to change the momentum of the jets (distribution of the axial to radial momentum). Also most mixing is achieved when the

spacing between the jets is kept at an optimized minimum (2D) because the farther apart the jets, the less mixing is achievable.

With respect to the pool-type SFR and under current configurations, the most susceptible components to thermal striping are the vertically positioned UIS above the core and also the lower portions of the laterally positioned IHX. This therefore shows that the relative importance of mixing to the geometry. In addition, co-location of multiple components, e.g. IHX and primary pump into the vessel further displaces the sodium inventory in the upper plenum pool. Hence the flow rate through the SFR has to correspondingly increase. High outlet velocity translates to shorter residence time for streams to mix and potentially further exacerbate thermal striping. Also, high outlet velocity has a potential to initiate gas entrainment into the coolant from the free surfaces. This is another unacceptable safety issue because it poses a safety challenge to the performance of the SFR.

Extrapolating the CFD results with respect to the pool-type SFR, geometric, kinematic and dynamic scales represent the length scale between the core exit and in-pool components and also between coolant channels of the un-mixed streams, variation of velocity (momentum) ratios, and the forces that influence the mixing phenomena all have an impact and hence emphasize the importance of scaling the SFR pool and its co-located components. These conclusions in composite provide design and scaling guidelines (geometric, kinematic and dynamic) for an integral pool-type test facility, as well as a full-scale pool-type SFR. Scaling of separate effects test should therefore be consistently integrated into the integral scaling via use of both

experimental and computational methods, since due to prohibitive resource constraints (cost), one or both may not necessarily be experimentally realized. In addition, scaling of the SFR pool, IHX and pump positions should not be strictly based on preserving the global scaling metrics (e.g Re and Pe) because they do not describe the local phenomena.

REFERENCES:

Ahmad S.Y., "Fluid to fluid modeling of critical heat flux: a compensated distortion model," J. Heat Mass Transfer, 16, 641-662 (1973)

Albiston M., "Experimental and CFD Studies of Single Phase Heat Transfer in Water Reactor Cavity Cooling System for NGNP" Master's degree thesis (2011)

Bejan A., "Convection Heat Transfer", 3rd ed., New Jersey, John Wiley & Sons (2004)

Blandford E.D. and Peterson P.F., "Global Scaling Analysis for the Pebble Bed Advanced High Temperature Reactor," Proc. 13th International Tropical Meeting on Nuclear Reactor Thermal Hydraulics (NURETH-13), Kanazawa City, Ishikawa Prefecture, Japan, 2009

Bruning J.E., "LMFBR Thermal-Striping Evaluation", Electric Power Research Institute
(EPRI), Research Project Report 1704-11, NP-2672, 1982

Chandran R.K., Banerjee I., Padmakumar G., and Reddy K.S, "Investigation of Thermal Striping in Prototype Fast Breeder Reactor Using Ten-Jet Water Model", Journal of Heat Transfer Engineering, vol.32, 5, p.369-383 (2011)

http://www.cfd-online.com/Wiki/Turbulence_intensity [accessed 01/09/2014]

Corradini M., Private communication, University of Wisconsin-Madison, (2012)

Denman M., LaChance J., Sofu T., Flanagan G., Wigeland R., and Bari R., "Sodium Fast Reactor Safety and Licensing Research Plan – Volume I", Technical Report, Sandia National Laboratory, SAND2012-4260 (2012)

Elbanna H., Gahin S., and Rashed M.I., "Investigation of two plane parallel jets," AIAA Journal, 21, 7, p. 986-990 (1983)

Generation IV Int. Forum (GIF) "A Technical Roadmap for Generation IV Nuclear Energy Systems" US DOE Nuclear Energy Research Advisory Committee, GIF-002-00, (2002)

http://ctr.stanford.edu/gallery.html [last accessed 05/05/2013]

IAEA, "Current Status and Future Development of Modular High Temperature Gas-Cooled Reactor Technology" IAEA-TECDOC-1198 (2001)

IAEA, "Heat Transport and Afterheat Removal for Gas-Cooled Reactors under Accident Conditions," IAEA-TECDOC-1163, Vienna (2000)

Incropera F., DeWitt D.P., Bergman T.L., Lavine A.S., "Fundamentals of Heat and Mass Transfer, 6th ed., New Jersey, John Wiley & Sons (2007)

Innovative Systems Software, "RELAP/SCDAPSIM, Input Manual: MOD 3.4, 3.5 & 4.0" (2012)

Ishii M. and Jones O., "Derivation and Application of Scaling Criteria for Two-Phase Flows," Two-Phase Flows and Heat Transfer, Proc. NATO Advanced Study Institute, Vol. 1, p. 163 (1976)

Ishii M. and Kataoka I., "Scaling Criteria for LWR's under Single Phase and Two-Phase Natural Circulation," Technical Report, CONF-820962-4

Ishii M. and Kataoka I., "Scaling Laws for Thermal-hydraulic System Under Single Phase and Two-Phase Natural Circulation," *Nuclear Engineering and Design*, vol. 81, p. 411-425, (1984)

Ishii M. and Zuber N., "Thermally induced flow instabilities in two-phase mixtures," 4th Int. Heat Transfer Conf., Paris, B5.11 (1970)

Ishii M., Revankar S.T. and Viskanta R., " Scientific Design of Purdue University Multi-dimensional Integral Test Assembly (PUMA) for GE SBWR", NUREG/CR/6309, Technical Report, US NRC (1996)

Ishii M., Revankar S.T., Leonardi T., Dowlati A., Bertodano M., Babelli I., Wang W., Pokharna H., Ransom V.H., Viskanta R., Han J.T., " The Three-level Scaling Approach with the Application to the Purdue University Multi-Dimensional Integral Test Assembly (PUMA)", *Nuclear Engineering and Design*, 186, 177-211, (1998)

Jung J., and Yoo J., "Analysis of Unsteady Turbulent Triple Jet Flow with Temperature Difference", Journal of Nuclear Science and Technology, vol.41, 9, p.931-942 (2004)

Kang K., Kim S., Bae B., Cho Y., Park Y., and Yun B., "Separate and Integral Effect Tests for Validation of Cooling and Operational Performance of the APR Passive Auxiliary Feedwater System", Nuclear Engineering and Technology, 44, 597-610, (2012)

Kimura, N., Miyakoshi, H. and Kamide, H., "Experimental investigation on transfer characteristics of temperature fluctuation from liquid sodium to wall in parallel triple-jet", International Journal of Heat and Mass Transfer, (2007), 50, 2024–2036

Kimura N., Nishimura M., and Kamide H., "Study of convective mixing for thermal striping phenomena (experimental analyses on mixing process in parallel triple jet and comparison of numerical methods)," JSME international Journal Series B45 (2002)

Kocamustafaogullari G. and Ishii M., "Scaling Criteria for Two-Phase Flow Natural and Forced Convection Loop and their Application to Conceptual 2 x 4 Simulation Loop Design", NUREG/CR-3420, ANL-83-61, 1983

Leyer S. and Wich M., "The Integral Test Facility Karlstein," Hindawi Publishing Corporation, 2012, 439374.

Lisowski D., Omotowa O., Muci M., Tokuhiro A., Anderson M. and Corradini M., "Influences of boil-off on the behavior of a two-phase natural circulation loop", International Journal of Multi-phase Flow, (2014), 60, 135-148

Lisowski D., Albiston M., Scherrer R., Haskin T., Tokuhiro A., Anderson M. and Corradini M., "Experimental Studies of NGNP Reactor Cavity Cooling System with Water", Proc. of ICAPP11, 11116 (2011)

Lucas Pitso, "NGNP Technology Development Road Mapping Report: Reactor Cavity Cooling System", NGNP-CTF MTECH-TDRM-016, Westinghouse LLC (2008)

Mascari F., Vella G., Woods G. and D' Auria F., "Analyses of the OSU-MASLWR Experimental Test Facility," Hindawi Publishing Corporation, 2012 528241

Masoni, P., Bianchini, G., Billing, P. F., Botti, S., Cattadori, G., Fitch, J. R., and Silveri, R., "Tests on Full-Scale Prototypical Passive Containment Condenser for SBWR's Application," ICONE-3, Vol. 2, 1023, Kyoto, Japan, April (1995)

Mishima K. and Ishii M., "Flow Regime Transition Criteria Consistent with Two-Fluid Model for Vertical Two-Phase Flow", NUREG/CR-3338, ANL-83-42, 1983

Next Generation Nuclear Plant (NGNP) Phenomena Identification and Ranking Tables (PIRTs), NUREG/CR-6944,Vol.1

Next Generation Nuclear Plant (NGNP) Project Technology Development Roadmaps: "The Technical Path Forward for 750-800°C Reactor Outlet Temperature", Technical Report, INL/EXT-09-16598, August (2009)

Next Generation Nuclear Plant (NGNP) Project Technology Development Roadmaps: "The Technical Path Forward", INL/EXT-08-15148, January (2008)

NGNP Point Design – Results of the Initial Neutronic and Thermal- Hydraulic Assessments during FY-03," Idaho National Engineering and Environmental Laboratory, INEEL/EXT-03-00870 Rev. 1, September 2003.

NGNP Research and Development Status, Technical Report, INL/EXT-10-19259, August (2010)

Nuclear Energy Institute (NEI) website: http://www.nei.org/resourcesandstats/nuclear_statistics/worldstatistics [last accessed on April 20, 2013]

Ogawa M. and Nishihara T., "Present Status of Energy in Japan and HTTR Project", Nuclear Engineering and Design, vol.233, Issues 1-3, pp.5-10 (2004)

Paladino D. and Dreier J., "PANDA: A Multipurpose Integral Test Facility for LWR Safety Investigations," Hindawi Publishing Corporation, 2012

Park G., Cho Y. and Cho H., "Assessment of a New Design for a Reactor Cavity Cooling System in a Very High Temperature Gas-Cooled Reactor", Nuclear Engineering and Technology, vol.38, pp. 45-60 (2006)

Ragheb M., "Decay Heat Generation in Fission Reactors", Lecture notes (Ch. 8), University of Illinois, Urbana-Champaign, (2013)

Ransom V.H., Wang W. and Ishii M., " Use of an ideal scaled model for scaling evaluation," Nuclear Engineering Design, 186, 135-148, (1998)

Reyes J.N and King J., "Scaling Analysis for the OSU Integral Test Facility", OSU-NE-2003-01, (2003)

Rodi Wolfgang, "Turbulence Models and Their Applications in Hydraulics – A State of the Art Review", International Association for Hydraulic Research, Delft, Netherlands, (1980)

Talaia M., "Terminal Velocity of a Bubble Rise in a Liquid Column", World Academy of Science, Engineering and Technology, 28, 264-268 (2007)

Tanaka E., "The interference of two-dimensional parallel jets (1st report, experiments on combined flow of dual jet)," Bulletin JSME, 17, 109, p. 920-927 (1974)

Tenchine, D., "Some thermal hydraulic challenges in sodium cooled fast reactors", Nuclear Engineering and Design, (2010), vol.240, 1195-1217

Tennekes, H and Lumley, J.L, "A First Course in Turbulence", Cambridge, MA, MIT Press (1972)

Title 10, Energy, Code of Federal Regulations, Part 50, Office of Federal Register, National Archives and Records Administration, Available through Superintendent of Documents, US Government Printing Office, Washington DC, 20402 (2004)

Tokuhiro A. and Kimura N., "An Experimental Investigation on Thermal Striping: Mixing Phenomena of a Vertical Non-buoyant Jet with Two Adjacent Buoyant Jets as Measured by Ultrasound Doppler Velocimetries," Nuclear Engineering and Design, 188, 1, p.49, (1999)

Tokuhiro A., Private communication, University of Idaho- Idaho Falls, (2010-2012)

Tokuhiro A.T., "Experimental Investigation of a Vertical Planar Jet by Ultrasound and Laser Doppler Velocimetries", Journal of Nuclear Science and Technology, vol.36, 6, p.540-548 (1999)

Tom W., Private communication, Argonne National Laboratory, (2010)

Tzanos C.P. and Farmer M.T., "Feasibility study for use of the Natural Convection Shutdown Heat Removal Test Facility (NSTF) for Initial VHTR Water-Cooled RCCS Shutdown", Technical Report, Argonne National Laboratory, ANL-GenIV-079, (2006)

US Department of Energy, "Preliminary Safety Information Document for the Standard MHTGR" DOE/ HTGR-86-024, Vol.1 (1992)

Van Staden M.P., "Analysis of Effectiveness of Cavity Cooling System", *Proc. of 2nd International Tropical Meeting on High Temperature Reactor Technology*, C20, Beijing, China (2009)

Wallis G.B., "One-dimensional Two-phase Flow", McGraw-Hill Book Company, NY (1969)

Weirs, V.G., Mousseau K.C., Johnson R.W., Lee H., Oberkampf W.L., Smith B., Fort J., and Rider W.J. "Nuclear Energy- Knowledge Base for Advanced Modeling and Simulation (NE-KAMS) Code Verification and Validation Data Standards and Requirements: Fluid Dynamics", INL/EXT-11-23419, Version1 (2011)

Whalley P.B, "Boiling, Condensation, and Gas-Liquid Flow", Clarendon Press, Oxford, p.21-25, (1987)

Wilson G.E, and Boyack B.E., "The role of PIRT process in experiments, code development and code applications associated with reactor safety analysis, Nuclear Engineering and Design, 186, 23-37 (1998)

World Nuclear Association (WNA) website: http://worldnuclear.org/info/Economic-Aspects/Energy-Security/#.UYBW1bXbONY [last accessed on April 20, 2013]

Yadigaroglu G. and Zeller M., "Fluid to fluid scaling for a gravity and flashing driven natural circulation loop," Nuclear Engineering and Design, 151, 49-64 (1994)

Yadigaroglu G., "Derivation of General Scaling Criteria for BWR Containment Tests", 4th Int. Conf. on Nuclear Engineering, ICONE-4, New Orleans, March 10-14 (1996)

Zuber N., "The effects of complexities, of simplicity and of scaling in thermal-hydraulics", *Nuclear Engineering and Design*, 204, 1-27 (2001)

Zuber N., Appendix D: "Hierarchical Two-Tiered Scaling Analysis, An Integrated Structure and Methodology for Severe Accident Technical Issue Resolution, US Nuclear Regulatory Commission, Washington DC, NUREG/CR-5809 (1991)

APPENDIX A

NEUP-09-202 PROPOSAL

This is a condensed version of the project proposal, including only the description of the work. It does not include the budget, schedule, location capabilities, or Principal Investigators' qualifications.

Experimental Studies of NGNP Reactor Cavity Cooling System with Water

TECHNICAL WORK SCOPE: G4M-1 – Generation IV Methods – Pre-application #09-202

PROPOSED SCOPE DESCRIPTION

Technical Objectives

Our team proposes to investigate the flow behavior that can occur in the Reactor Cavity Cooling System (RCCS) with a water coolant under the passive cooling-mode of operation. We will conduct separate-effects tests and develop associated scaling analyses, and provide system-level phenomenological and computational models that describe key flow phenomena during RCCS operation, from forced to natural circulation, single-phase flow and two-phase flow and flashing.

Task 1: Conduct separate-effects, single-phase flow experiments and develop associate scaling analysis with comparison to system-level computational modeling (Task 3) for the RCCS standpipe design. The RCCS under accident conditions transitions from forced to natural convection cooling in the standpipe and piping. These tests will measure global flow behavior and local flow velocities, as well as develop instrumentation for use in the larger scale NSTF tests. This will provide a proper flow distribution among standpipes for decay heat removal.

Task 2: Conduct separate-effects experiments for the RCCS standpipe design as two-phase flashing occurs and flow develops. As natural circulation cooling continues without an ultimate heat sink, water will heat up to temperatures approaching the saturation temperature within the system. Two-phase flashing and flow will begin. Our focus is to develop a phenomenological model from these tests that will describe the flashing and flow stability phenomena. In addition, one could determine the efficiency of phase separation in the RCCS storage tank as the two-phase flashing phenomena ensues and the storage tank vents the steam produced.

Task 3: Develop a system-level computational model that will describe the overall RCCS behavior as it transitions from forced flow to natural circulation and eventual two-phase flow in the passive cooling-mode of operation. This modeling can then be used to in conjunction with Tasks 1 and 2 to test the phenomenological models developed as a function of scale.

Importance and relevance of proposed work:

The RCCS is a key safety system that is important to the overall design of the Next Generation Nuclear Plant (NGNP). The RCCS is to be designed for NGNP and developed under the auspices of the Department of Energy (DOE) Generation IV (GENIV) program. The water-cooled option for the RCCS design is currently part of the anticipated design for the Pebble Bed Modular Reactor (PBMR), and an option for the Prismatic Modular Reactor (PMR). Our team will conduct separate-effects tests that are applicable to the RCCS, in support of the Natural-convection Shutdown heat-removal Test Facility (NSTF) that is planned to test the RCCS

operation. With our geometrical scaling approach we can empirically check the relevant scaling laws for the system, develop key phenomenological models, and use modeling to verify the overall behavior of the water-cooled RCCS for the NGNP design in a passive cooling-mode of operation. Our goals are to: (a) develop scaling laws for transition from forced to natural convective flows in the standpipe and piping for single-phase flow; (b) provide phenomenological models for two-phase flashing and flows, as well as phase separation and liquid carryover, respectively, in the storage tank, and (c) develop a system-level computational model for the passive cooling-mode of operation.

Technical Approach and Task Description

Rationale: The confinement building that surrounds the NGNP, a gas-cooled thermal-spectrum reactor, is part of a safety strategy of defense-in-depth in the siting of the NGNP. The RCCS is a key safety system that is important to the NGNP safety case being incorporated in the overall design. The RCCS will be one of the new safety systems specifically designed for the NGNP, developed under the auspices of the DOE GENIV program. The confinement building with RCCS operation, which encloses the Reactor Pressure Vessel (RPV) must accommodate limiting design basis accidents and successfully remove core decay heat, as well as any long-term heat of reaction from graphite oxidation. Some RCCS designs use water as the working fluid and operate in a passive mode during accidents, providing heat transport from the cavity and confinement building to the surroundings using natural circulation throughout the accident. During accident conditions, when all AC power is lost, the RCCS can operate in a passive cooling-mode that removes heat radiated or naturally convected from the metal RPV wall through the cavity atmosphere to the inner boundary of the RCCS facing the vessel. The RCCS is located within the reactor cavity surrounding the RPV and is a key system affording decay heat transport by water-cooling to the ultimate heat sink.

We propose to examine specific thermal-hydraulic issues that will allow the RCCS to successfully accomplish this safety function under the passive cooling-mode with natural circulation. This work will be coordinated with the integral Natural-convection Shutdown-heat-removal Test Facility (NSTF) for the NGNP project, which will provide near prototypical scale RCCS testing. This RCCS design with water-cooling has advanced enough in detailed design to allow a prototypic facility to be built at the NSTF at Argonne National Laboratory. The RCCS is composed of a water-cooled standpipe array, which surrounds the RPV. The vessel with the surrounding RCCS standpipe array is situated within the concrete reactor cavity structure (Figure A.1).

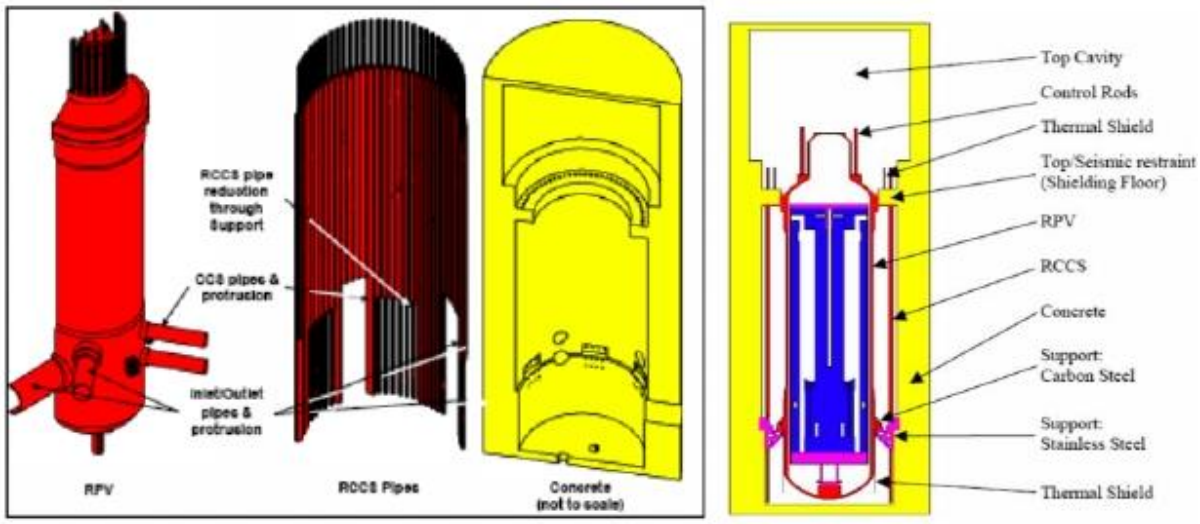

Figure A.1 Overall picture of the NGNP RPV, RCCS pipes and Reactor Cavity configuration

The RCCS steel standpipes consists of ~60 oval tubes (15 groups of 4) [1-4]. The major heat transfer area of the standpipe is ~20 m in height, with ~40 m to the top of the water storage tanks connected by network piping that provides the water supply and return. Water flows from the storage tanks through network piping manifolds, whereupon it is distributed to the downcomers inside the oval tubes (Figure A.2). Water then flows up through the RCCS tubes and returns to the storage tanks. Under normal operation, forced convection pumping to heat exchangers cools the water in the RCCS system, returning it to the tanks. These water-filled storage tanks are appropriately sized to provide passive heat removal without forced cooling for over three days. This is accomplished without forced flow by allowing for boil-off and steaming of the storage tank water during the emergency decay heat removal mode. Vaporization occurs if storage tank cooling is lost. During off-normal conditions (Figure A.2), forced convection water-cooling in the RCCS is presumed to be lost, as well as the ultimate heat sink outside the containment. In this case, water is passively drawn from an open line located at the bottom of the header tank. This line is orificed so that flow bypass during normal operations is small, but large enough to provide adequate flow during passive operations to remove NGNP decay heat while at acceptable fuel temperatures. In the passive operating mode, water flows by natural convection from the bottom of the supply tank to the standpipe downcomer, and returns up through the standpipe and the normal pathway to the top of the storage tanks. After the water reaches saturation and boiling commences, the two-phase flow passes up through the manifold piping with water separation and steam is vented via pressure relief in the storage tanks.

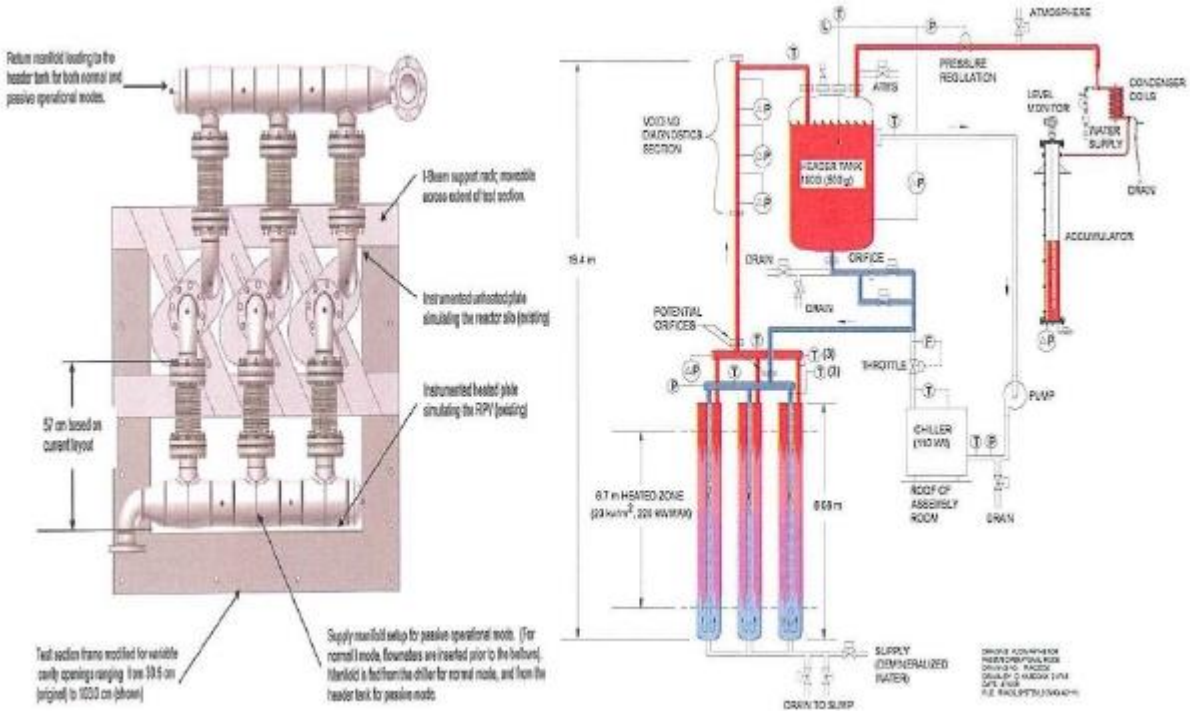

Figure A.2 Top-view of Standpipe group, and RCCS operation in the passive cooling mode

It is this passive cooling-mode of operation that we seek to better understand, as the RCCS transitions from forced flow to natural circulation as single-phase flow and eventually reaches saturation conditions in the RCCS storage tank with two-phase flashing occurring.

Scaling Analysis, Transition to Steady Natural Convection and Two-Phase Flow:
Transition from forced to natural convective flow, and related flow stagnation and thermal stratification in single and two-phase natural circulation loops have been experimentally studied in scaled thermal-hydraulic test facilities using various codes [5-9]; e.g., Integral Test Facilities - OSU APEX-CE, Purdue PUMA, ROSA-LSTF, LOFT and codes such as CATHARE, RELAP5, TRAC. For the RCCS during off-normal conditions, when forced convective water-cooling is lost, the time required to re-establish natural convective flow is key to having confidence in its operation. Ishii and Kataoka [6] proposed general scaling criteria for LWRs under single- and two-phase natural circulation. They reported that the general time scale, tR(atio), would be shifted with respect to phenomena by a ratio of the characteristic length scales of the model and prototype, lR=lm/lp, and the ratio of the characteristic velocity scales of the same, vR=vm/vp. The heat transfer analysis was characterized by traditional correlations for forced and natural convection for specific flow configurations, under the tacit assumption that the ratio, Gr/Re2, characterizes convective flow over the other (Gr/Re2<1 indicates forced). In fact, in terms of phenomenological time scales, Gr/Re2 represents the ratio of the 'harmonic' mean of the convective and momentum-based time scales, to the square of the time scale associated with buoyancy; that is, [tc*tm/tb2]. But, Bejan [7] proposed different scaling to be (Ra1/4/Re1/2Pr1/3), while for heat transfer, it is (NuRe1/2Pr1/3). If this were the case, the corresponding time-scale ratio would be more complex, [tc6 * tm/tb6 * tH 3]1/12, where tH is the characteristic time for thermal diffusivity. What seems certain from Reyes and Nishimura [8,9] is that transitional flows can often take on the order of 1000-3000 secs (water) and 500 secs (Na), respectively, in scaled facility thermal-hydraulics. Here the

order of magnitude difference in Pr-number between water and Na appears consistent. Otherwise, studies on transition from forced to natural convective flows in simple geometries are few. We anticipate that in the present separate-effects test in a single standpipe, the time scale will be shorter because of the shortened configuration. This will be confirmed in transient to steady-state tests.

Thus, our objective in the design of the single-phase and the two-phase experiments is to develop an experimental facility that can be of similar size so that cross-comparisons of data under the same geometry can be empirically made with minimal distortions. In addition, we want the two facilities to be appropriately scaled to the NSTF facility. Let us first consider our overall geometric scaling approach as described in Table A.1.

Table A.1 Proposed Geometrical Scaling for RCCS Two-phase Flow Experiments

Parameter	RCCS Scale	NSTF Scale	Proposed Task 1 & 2
Water Standpipe Header	4	3	1
Standpipe Diameter	25cm	25cm	25cm
Standpipe Length	20 m	8m	4m
Total Elevation	40 m	16 m	8 m (Task 2 only)
Facility Scale	Real	1:1 Radial 1:2 Vertical	1:1 Radial 1:2 Vertical
Peak Wall Heat Flux	3 - 5 kW/m2	3 - 5 kW/m2 *1.4	3-5 kW/m2 * 2

We propose to use water at ambient conditions in a single standpipe configuration that is one-half the vertical size of the NSTF experimental facility; as the NSTF is about one-half the vertical size of the actual RCCS design. The lateral scaling will be full scale as in the NSTF. This scaling approach has two major advantages. First, it replicates the scaling approach taken in the NSTF and is thus, faithful to the overall system-level scaling that underlies the NSTF design for the standpipe region. Second, this approach to scaling will allow us to empirically scale the phenomena we are observing the same quantitative amount 'down-in-scale' as the NSTF would need to 'scale-up'. Thus, we can afford an empirical as well as model comparison for the single-phase and two-phase phenomena we observe.

Task 1- Separate-effects tests for RCCS standpipe with single-phase natural circulation: We will conduct separate-effects experiments with the following objectives. Overall we will conduct single-phase convective flow experiments and develop associate scaling analysis with comparison to system-level computational modeling (Task 3) for the RCCS standpipe design. Under accident conditions the RCCS transitions from forced to natural convection cooling in the standpipe and piping. One of the Co-PIs will investigate three-dimensional (3D) natural convection heat transfer and flow in the anticipated RCCS standpipe configuration. These tests will measure global flow behavior and local flow velocities, as well as develop instrumentation for use in the larger scale NSTF RCCS tests. The RCCS standpipe is an oval-shaped, tall enclosure with a heat flux (3-5 W/m2) along the one lengthwise, exposed side of the standpipe [1-3], due to convective and radiation heat transfer from the reactor vessel to the exposed wall of the standpipe. The back of the standpipe in the anticipated NGNP faces the concrete reactor pit. The standpipe itself has a centrally-located inlet at the top (thus defining an annular, internal flow configuration) and outlet located along one side at the top. Under 'passive' mode of operation, the flow of water from a 'header tank' is directed downward through the center channel and at the bottom reverses direction upward to flow along the (heated) outer

periphery (annulus) of the standpipe. The geometric scaling of the NSTF is full-scale in diameter and half height relative to the NGNP. For similitude to the NGNP, a vessel wall peak heat flux factor of 1.4 is used, corresponding to a Rayleigh number range of 0.84x1011 ≤ Ra ≤ 1.0x1012 (Table A.1) [1-3].

Under these objectives, the proposed separate -effects test section will be 1:1 in cross-sectional area, but a further ½-scale in height. For consistency, both test sections for Tasks 1 and 2 will be the same 4 m height. The corresponding Ra-number range will be ~1.05 x1010 ≤ Ra ≤ 1.25x1011, and the vessel wall peak heat flux will be increased further within the bounds of a desired single-phase natural convection to increase the upper limit of the Ra-number. This range of the Ra-number corresponds to the upper laminar, to transition to turbulent natural convection range. In that the cross-
sectional aspect ratio is much smaller than the vertical aspect ratio, also that the imposed heat flux can be non-uniform, and finally that the central pipe defines an annular internal flow configuration (Figure A.3), the natural convective flow will be 3D. Thus, we need to quantify both velocity and temperature fields.

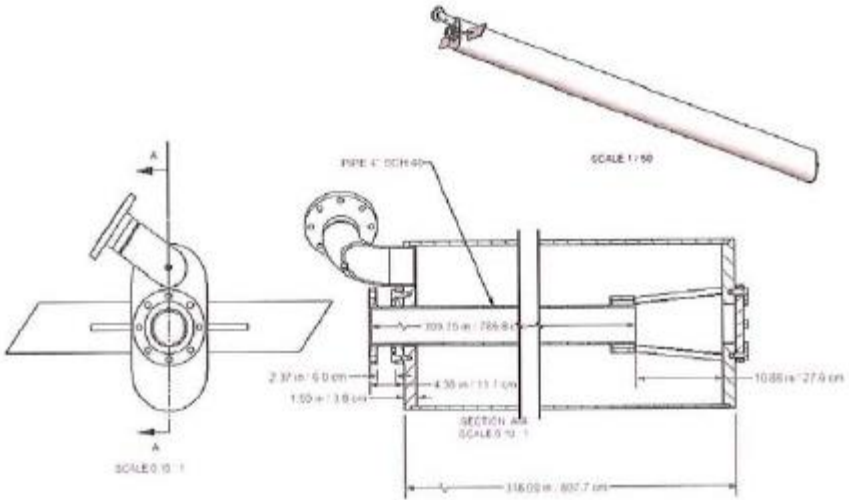

Figure A.3 Schematic of Standpipe Facility for Single-Phase Natural Circulation Tests

Velocity field measurements: The principle of ultrasound Doppler velocimetry (UDV) is explained with the aid of Figure A.4. In brief, an ultrasound (US) transducer (tdx) positioned non-invasively or invasively emits a cylindrically-shaped burst of US-waves into the flow field of interest (measuring line). The non-invasive configuration shows use of an US-gel to acoustically "couple" the tdx to the pipe wall. The characteristic acoustic velocity in the medium defines the medium itself (i.e. fluid/liquid). A fraction of the emitted waves are reflected from reflectants (tracer particles) moving with the flow. A single transducer (or multiple transducers with a multiplexer), is subsequently switched to the receive mode and measures both the time-of-flight (t) and the Doppler shift (*fD*), including the sign of the shift, at the instant of echo reception. The Doppler shift provides information to deduce the velocity. By closely matching the density of the reflectant with that of the test media, one can assume 'no-slip' between particle and carrier liquid. Plastic particles, 10-100□□m, are well suited for use as reflectants. UDV thus generates a velocity profile of the velocity component *along* the US beam in time; a time-averaged profile can be determined over 128 points (channels) over 1024 profiles in time (per probe). As the channels are over-sampled, we gain spatial-temporal

information of the flow. The device was co-developed by Takeda et al. [10], and they have extensively documented the applications of the device for liquids. Tokuhiro [11] used the device to verify flow of liquid jets and in buoyant driven flows. The Co-Principal Investigator, Co-PI, will develop a measurement configuration of up to 20 probes for Task 1 that can be equally used at the NSTF.

Temperature field measurements: Temperature measurements will be taken using conventional thermocouples linked to a PC-based data acquisition system. Both the interior and exterior surface temperatures of the standpipe, as well as the bulk (liquid) temperature of the heat transfer medium, will be taken The bulk temperature will be taken using a movable thermocouple 'tree' probe to characterize the axial, radial and peripheral distribution in heat transfer. Select heat flux sensors will quantify the imposed heat flux on the standpipe's exterior.

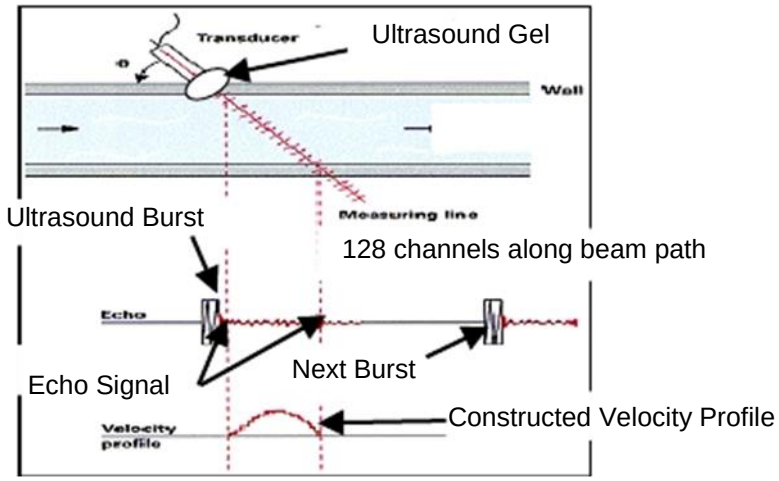

Figure A.4 Principle of Ultrasound Doppler velocimetry as applied to pipe-flow

Task 2 - Separate-effects tests for the RCCS standpipe with two-phase flashing and flow: For the RCCS passive cooling-mode operation, it is assumed that forced flow cooling of water in the storage tanks will not be available, and the flow path will be modified Figure A.2 with natural circulation, single-phase flow transitioning to two-phase, flashing flow into the storage tank with steam venting. We propose to investigate this two-phase mode of natural circulation by building a scaled RCCS standpipe and piping to a scaled storage tank. Our objective is to develop a test facility that can be of similar size to the single-phase, natural convection apparatus used in Task 1, and appropriately scaled to the NSTF facility (Table A.1).

We propose to use water at ambient conditions in a single standpipe configuration that is one-half the vertical size of the NSTF experiments, which are about one-half the vertical size of the actual RCCS design. The lateral scaling will be full scale as in the NSTF. This scaling approach has two major advantages; we are faithful to the NSTF approach, and we can observe phenomena 'down-in-scale'. This ability can provide for direct empirical observations of any unexpected scaling effects. The schematic of our proposed test facility is shown in Figure A.5.

The facility will consist of radiant heaters to deliver a heat flux representative of that expected from the reactor vessel to the RCCS standpipe surface (approximately 5 kW/m2). There will be a single standpipe (4m in height made of steel alloy similar to the RCCS) with a diameter of actual size (~25cm). The radiant heater, standpipe and its downcomer will be housed in a shielded enclosure to maximize direct heating of the standpipe from the heater. The outlet of the standpipe will be up to 4m in length and directed to the inlet of the storage tank, where any flashing two-phase flow will be discharged. The storage tank will be 1m in diameter. The storage tank will be outfitted with pressure relief to a condenser to keep the system at a fixed pressure similar to that in the passive cooling-mode for the actual RCCS.

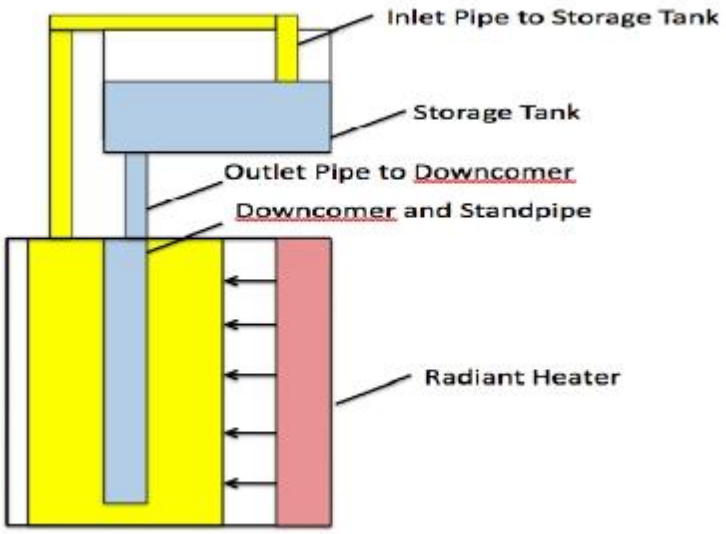

Figure A.5 Schematic Picture of Standpipe Facility for Two-Phase Flashing Flow Tests

As far as we are aware, there is no detailed design information and no available analysis for this reference water-cooled RCCS design. For the purposes of our proposed work, we expect that during the transient time for water heat up to saturation conditions, boiling in the standpipes is not significant, and that the two-phase flow in the pipes above the RCCS heated section will be first observed as a flashing phenomena. To verify this expected behavior, we will construct the facility with observation ports on the backside of the standpipe (away from the radiant heater), along its outlet piping, and in the storage tank below the water surface. The test variables in the experimental program will be the heat flux to the standpipe (Table A.1), the frictional losses embodied in the network piping from the standpipe to the storage tank and back to the downcomer (composed of the pipe length, diameter and loss coefficient – fL/D), and the operating pressure (1-2 bar). The experiments will examine the two-phase flashing flow, its onset, oscillatory period, and developing flow regimes as a function of these variables.

Both the interior and exterior surface temperatures of the standpipe, as well as the bulk (liquid) temperature of the heat transfer medium, will be taken The bulk temperature will be taken using a movable thermocouple 'tree' probe to characterize the axial, radial and peripheral distribution in the heat transfer. Special heat flux sensors will quantify the imposed

heat flux on the standpipe's exterior. We expect to develop a two-phase flow stability map based on traditional stability parameters to characterize the two-phase flow behavior; i.e., a dimensionless sub-cooling parameter and a dimensionless input power parameter.

Task 3: System-level computational model to describe the overall RCCS behavior
Pretest predictions of the RCCS test facility standpipe behavior from forced flow to natural circulation will be computed using system-level computer programs. This scenario can be calculated using the RELAP-3D computer program [12, 13]. The transition from single-phase, forced flow to natural circulation, as well as the transition from single-phase to two-phase natural circulation, will be simulated using RELAP-3D. These simulations will provide the needed overall system conditions for comparison between the experimental scales for Task 1 and 2 and the NSTF facility scale and prototypic NGNP scale. In addition, the two-phase flashing and phase separation correlations in the code will be reviewed and assessed compared to data. These correlations will be compared with other codes' correlations, such as the French CATHARE thermal Hydraulic system code. The correlations will be refined utilizing the proposed test results. Post-test predictions will be performed.

References:

1. R. V. Vilim and E. E. Feldman, "Scalability of the Natural Convection Shutdown Heat Removal Test Facility (NSTF) Data to VHTR/NGNP RCCS Designs", ANL-GenIV-049, Argonne National Laboratory Report, June 2005.
2. C. Tzanos, "CFD Analysis for the Applicability of the Natural Convection Shutdown Heat Removal test Facility (NSTF) for the simulation of the VHTR RCCS", ANL-GenIV-055, Argonne National Laboratory Report, Sept. 2005.
3. M. T. Farmer, et. al., "Natural Convection Shutdown Heat Removal Test Facility (NSTF) Evaluation for Generating Additional Reactor Cavity Cooling System (RCCS) Data", ANL-GenIV-058, Argonne National Laboratory Report, Sept. 2005.
4. M. P. Van Staden, "Analysis of Effectiveness of Cavity Cooling System", Proceedings of the HTR2004 Conference, Paper 20, Beijing, China, Sept. 2004.
5. J. Kobayashi, A. Tokuhiro, H. Kamide, H. Ohshima and Y. Ieda, An experimental investigation on penetration of buoyancy-driven cold liquid into a vertical channel with hot, forced-flow, Nucl. Eng. Des., 177, 91-104, 1997.
6. M. Ishii and I. Kataoka, Scaling criteria for LWR's under single-phase and two-phase natural circulation, CONF-820962-4, DE83 007721, ANL, Joint NRC/ANS Mtg. Basic Thermal Hydraulic Mechanism in LWR Analysis, Bethesda, MD, Sep 1982.
7. A. Bejan, Convection Heat Transfer, 3rd ed., John Wiley & Sons, Hoboken, NJ, ISBN0-471-27159-0, m 2004,
8. J. N. Reyes, Jr., Flow stagnation and thermal stratification in single and two-phase natural circulation loops, IAEA TECDOC Natural Circulation Working Mtg., ANNEX 15, Jun 25-29, 2007 (www.iaea.or.at/OurWork/ST/NE/NENP/NPTDS/Downloads/TECDOC_NC_WM/Annex15.doc)
9. M. Nishimura, H. Ohshima, H. Kamide, Fast reactor core thermal-hydraulic analysis during transition from forced to natural circulation, IAEA-TECDOC—1157, Vienna, 27-31 July 1998.
10. Y. Takeda, et al., Relevant UVP-related publications are at URL: http://www.met-flow.com/
11. A. T. Tokuhiro, Experimental investigation of a vertical planar jet by ultrasound and laser doppler velocimetry, Atomic Energy Soc. Japan, J. Nucl. Sci. Technol., 36[6], 1999.

12. The RELAP5-3D© Code Development Team, "*RELAP5-3D© Code Manual Volume I: Code Structure, System Models, And Solution Methods,*" INEEL-EXT-98-00834, Revision 2.3, Idaho National Laboratory, April 2005.
13. The RELAP5-3D© Code Development Team, "*RELAP5-3D© Code Manual Volume IV: Models and Correlation,*" INEEL-EXT-98-00834, Rev 2.3, Idaho National Laboratory, April 2005.

APPENDIX B

NEUP-09-321 PROPOSAL

09-321, Data Collection Methods for Validation of Advanced Multi-Resolution Fast Reactor Simulations

Technical Work Scope Identification: AFCI Regulatory and Safety, Models, codes and data to address fast reactor safety, AFG-2

PROPOSED SCOPE DESCRIPTION

Technical Objectives

Our team proposes to provide initial data to support the development of the advanced tools, develop methods for the reduction and characterization of the very large data sets generated using the high-resolution measurement methods, develop methods for time correlation of fluid dynamic and heat transfer data from high-resolution measurements, identify new technologies to facilitate high-resolution measurements at Peclet numbers for liquid-metal cooled fast reactor (LMFR) systems, and develop initial best practices to guide the development of rigorous validation, verification and benchmarking requirements for the advanced codes. We have identified the following tasks:

Task 1. Learn current status of work PI3's institution; define PI1's and PI2's specific scope of work to support and broaden DOE laboratory's computational and experimental efforts and separately investigate related instrumentation, scaling and data analysis issues.
Task 2. PI1, 2 will design and construct small-scale separate effects thermal fluid mechanics test section that will yield thermal mixing data. Test sections and auxiliary loop components should be adaptable to the existing DOE laboratory sodium loop for 'system' testing options.
Task 3. PI1, 2 will define and conduct thermal mixing experiments that are similar but broaden and encompass the parameter-space covered by PI3's computational study.
Task 4. PI3 will lead computational simulations of these experiments using LES and RANS methodologies developed by the fast reactor modeling and simulation 'team' at PI3's institution. PI3 will simulate near-to-exact experimental conditions defined by PI1 and PI2; further generate spatio-temporally averaged data from simulations to 'match' experimental measurement methods.
Task 5. PI1, 2 and 3 will jointly validate and verify to the extent possible the experimental results against the computational simulations. The team will also quantify the associated uncertainties.

IMPORTANCE and RELEVANCE of PROPOSED SCOPE OF WORK (SOW)

New methods are needed for the collection, reduction, characterization and the comparison of experimental validation data to support the development, deployment and application of advanced multi-scale or multi-resolution thermofluid simulation tools. The proposed project scope will include the design and construction of two new separate effects facilities relevant to advanced fast reactor design and safety, qualification of new instrumentation methods, development of high-performance computing solutions for data management and analysis, and development of best practices for validation of the advanced multi-resolution thermofluids simulation tools. These efforts will seek to leverage recent developments in instrumentation for fluid dynamics and heat transfer measurements, availability of massively parallel computing resources and participants' collective experience in the design of validation experiments for liquid metal cooled systems and advanced reactors.
In legacy experiments for validation of nuclear simulation tools, data collection has largely focused on measuring integral behavior over large control volumes. This approach allows the use of sparse instrumentation largely based on thermocouple, dynamic pressure, or single point bulk velocity measurements. Experiments of this type are scaled based on the familiar dimensionless scaling parameters such as the Reynolds, Prandtl, or Grashof numbers. While these dimensionless parameters describe the characteristic turbulence effects in the system, they do not provide any information about the turbulence spectrum.

The inclusion of high-resolution computational fluid dynamics codes as part of the

thermofluid simulation suite clearly requires that data be collected at high spatial densities and high frame rates. However, simply applying high-resolution measurement methods to experiments scaled (or as separate effects) for validation of correlation based system design tools may not be sufficient if experiments are not designed to provide a characteristic turbulence length scales and shear stresses in addition to average field values.

In legacy validation experience, the limited state space considered in the experimental program restricted the applicability of the legacy codes to a very limited subset of the design state space. The broader applicability of the computational fluid dynamics tools will allow the multi-resolution thermofluids simulation tools to be applied to a much broader design state space, extending opportunities for significant improvements in efficiency, safety, and economic performance.

The proposed effort will provide additional 'modern' data to support the development of the advanced tools, develop methods for the reduction and characterization of the very large data sets generated using the high-resolution measurement methods, develop methods for time correlation of fluid dynamic and heat transfer data from high-resolution measurements, identify new technologies and surrogate materials to facilitate high-resolution measurements at Peclet numbers for fast reactor systems, and develop initial best practices to guide the development of rigorous validation, verification and benchmarking requirements for the advanced codes

TECHNICAL APPROACH and TASK DESCRIPTION

Rationale: Computational fluid dynamics (CFD) codes are increasingly relied upon for design, performance, and safety analysis of anticipated engineered systems. As computing power and availability increase, these codes are being used to predict physical phenomena on ever more refined spatiotemporal scales. As reliance upon these tools grows, it becomes critical to ensure that they do indeed describe the physical world to an acceptable level of accuracy. Validation and verification (V&V) of high resolution models of physical systems requires, however, comparisons with similarly finer-scaled experimental data. This, in turn, necessitates the use of 'modern' instrumentation and measurement techniques.

Many of the DOE laboratories are engaged in an effort to generate high resolution experimental data for the V&V of CFD tools used to predict fluid flow and heat transfer phenomena in advanced nuclear systems. The proposed work will be performed by a team of two universities and a specific DOE laboratory with both universities in close proximity to two additional DOE laboratories. The team plans to broaden a data base that can be applied towards code V&V specifically for liquid-metal based systems such as a sodium-cooled reactor. The team has a unique expertise base in both experimental and computational studies of liquid metal systems which includes fluid dynamics experiments using mercury, sodium, molten salts, water and gas as working fluids. The 'high' spatiotemporal nature of the data generally means enormous amounts of data. Thus the experimental (counterpart) challenge is the development and demonstration of spatiotemporal data generation, management and processing techniques and strategies. The proposed scope of work (SOW) facilitates comparisons between simulation tool predictions and the validation data. The three-year effort will focus on three primary objectives as follows; to:

- design and construction of two liquid-metal thermal-hydraulic (LM TH) separate effects experimental facilities at two universities, similar in scope, size (order of

magnitude) and specifications to an existing DOE laboratory facility. Initial study on dual (parallel) jet, thermal mixing phenomena.

- Identify and qualify advanced instrumentation for use in liquid metal coolants that provide higher-resolution spatio-temporal flow field data required for V&V, UQ and data management and standardization; also establish an accessible database. The databases will consist of large, time-correlated measurement data that characterize similar liquid-metal thermal-hydraulics in LMFRs.
- Investigate, model and simulate thermal mixing of dual jets as a separate effects experiment and computationally, at additional scales of relevance to SFR flows. The CFD study will essentially dictate the prototypic condition of the experiments; in addition, results of the simulation will be 'tuned' to spatio-temporal scales that 'match' the corresponding measurement of the convective field.

In terms of a generalized task, **Task 1** will consist of surveying the current state of knowledge work PI3's institution; define PI1's and PI2's specific SOW to support PI3 and finalize design of the separate effects experiments. The team will broaden DOE's computational and experimental efforts via development of instrumentation that will yield spatio-temporal velocimetric and thermometric data.

The selected reference (benchmark) thermal-hydraulic phenomena will be the thermal mixing of two, side-by-side, jets at similar to dissimilar velocities and temperatures. This has configuration has been selected for the following general and specific considerations:

1) Understanding the thermal mixing of convectively dissimilar LM streams is key to SFR issues such as thermal striping and flow in plena.

2) Flow of the simpler single jet (planar, axisymmetric, buoyant, isothermal) are well documented analytically, computationally and experimentally

3) Thermal mixing of a triple-jet configuration in ordinary and low Pr-number fluids has been studied by Kimura and co-workers both experimentally and computationally. These studies are fairly recent, well-documented and the database is (likely) available. The flow is 'on average' symmetric with respect to the central jet.

4) Thermal mixing of a dual-jet provides relevant complexity and an opportunity to investigate turbulence modeling, RANS, as well as LES and DNS approaches.

Computational simulations using commercial CFD codes and an advanced DOE lab developed code will completed prior to the finalization of the experimental design to identify potential flow instabilities that would limit the applicability of the data, aid in defining the state space for the test matrix, and assist in focusing the location and resolution of the instrumentation. Blind simulations of the final test geometry will also be completed as an initial validation of the applicability of the tools to the thermal mixing into larger plena of the generic SFR design.

SEPARATE EFFECTS TEST FACILITIES and VELOCIMETRY

As noted, since isothermal and buoyant single-jets are well-documented and the thermal mixing of three parallel jets for both ordinary and low Pr-number fluids has been studied by Kimura, Nishimura and co-workers both experimentally and computationally, we plan to design and construct a separate effects test facility, initially configured to study two parallel jets with different velocities and temperature. A separate effects facility will be constructed at each participating university. In the current effort we will use two low Pr-number fluids, mercury (Hg) and sodium (Na); the former, since it is the fluid of choice at a major DOE facility in proximity to PI2. Further, though toxic, its oxidation reaction does not pose a physical hazard and can be controlled and monitored by documented means. Lastly using both Hg and

Na provides a means to investigate and compare the convective flow and heat transfer differences in LMs due to approximate order of magnitude difference in Pr-number (~0.025 for Hg vs. 0.005 for Na); that is, an evaluation of both experimental and computational sensitivity and 'resolution' to small relative influences in thermal-physical properties.

The set-up will be similar in layout to an existing DOE laboratory sodium facility so that a common reference is maintained for the present and future collaborations; in fact, if possible connecting flanges and piping will be identical so that we create an option to exchange and share components amongst all three facilities. Thus inside a suitable confining volume with an auxiliary system similar to the existing DOE facility, we will design and configure two parallel jets, very similar to the triple-jet t arrangement shown in Figure 1 by Kimura et al. In fact, a very similar ultrasonic Doppler velocimeter will be used in our experiments in both sodium and mercury. In both liquid sodium and mercury, we will focus on generating spatio-temporal convective heat transfer data for detailed validation of turbulence dissipation and wall treatment models. Some point verification permanent magnet velocimetry probe measurements will also be conducted. A brief note on the principle of ultrasonic Doppler velocimetry is noted below.

PI1 - Task 2 and 3, Separate Effects Facility and Thermal Mixing of Two-Jets

Each university participant will design and construct a separate effects test facility, respectively planned for low Pr-number fluids, sodium and mercury. Other than the test section which will be specific to the proposed SOW, each university will adopt an auxiliary system (pump, tanks, fittings, piping, valves, etc.) to the extent possible that takes the DOE laboratory's system as the reference facility. We propose this so that the three institutions can 'exchange' components and test sections under the present and future collaborations. Details of the DOE lab facility are in the NERI Annual Report and depicted in Figure 2. The test section will consist of outer and inner enclosures with the 'annular' space serving as the return overflow to the auxiliary system (see Fig. 1a). The two streams will be pre-conditioned via differential heating (resistance) and cooling (via liquid to gas heat exchanger) and differential electromagnetic (EM) pumping conditions. Per Kimura et al. we will also maintain the option to heat one stream relative to the other which we will keep at the bulk loop temperature. In order compare results, the temperature difference and velocity ratio between the heated (h) and unheated (c) jets will initially be, $\Delta Thc=5°C$, 10°C and $R=(Vcold,exit/Vhot,exit)=1.0$ (isovelocity), 0.7, 0.5 respectively. The corresponding typical Reynolds number will be $Re_D=1.8$ x 104, where D is the hydraulic diameter of the exit nozzle. Velocity measurement of single-jet and dual-jet arrangement will be taken by ultrasound Doppler velocimetry (UDV) while temperature data will be taken using a vertically traversed thermocouple array and a UD-thermometry (UDT) method reported by Hayashida et al. and currently under development by one of the PIs. Since UDV may be the only means by which higher fidelity spatiotemporal measurement can be obtained in LMs, we provide a short introduction below.

The separate effects test facility will be collaboratively designed and constructed by PI1 and PI2, in consultation with PI3 and PI4. Two identical (or nearly identical) enclosures and test sections will be constructed using the best available and cost-effective practices available to the team. In particular, PI4 will provide expert knowledge of the design and construction methods of the DOE facility as well as on the auxiliary system components. This close-knit collaboration will assure a measure of QA and QC with respect to each facility and test sections, but take advantage of the regional 'best practices' that may exist where the team members are located.

PI1 and PI2, Ultrasonic Doppler Velocimetry

The principle of ultrasound Doppler velocimetry (UDV) is described the aid of Figure 3. In brief, an ultrasound (US) transducer (tdx) positioned in- or ex-situ emits a cylindrically shaped burst of US-waves into the flow field of interest (measuring line). The ex-situ configuration shows use of an US-gel to acoustically "couple" the tdx to the pipe wall. The characteristic acoustic velocity in the medium defines the medium itself (i.e. fluid/liquid). A fraction of the emitted waves are reflected from reflectants (tracer particles) moving with the flow. Single (or multiple transducers with a multiplexer), is then switched to the receive mode and measures both the time-of-flight and the Doppler shift, including the sign of the shift, at the instant of echo reception. The Doppler shift is related to velocity. By closely matching the density of the reflectant with that of the test media, one can assume 'no-slip' between particle and carrier liquid. Particles, 10- 100μm, are well suited for use as reflectants. UDV thus generates a velocity profile of the component *along* the US beam in time; a time-averaged profile can be determined over 128 points (channels) over 1024 profiles in time (per probe). As the channels are over-sampled, we gain spatial-temporal information of the flow. The UDV was co-developed by Takeda and coworkers; a representative reference is given. PI1, 2 and 3 have experience with UDV.

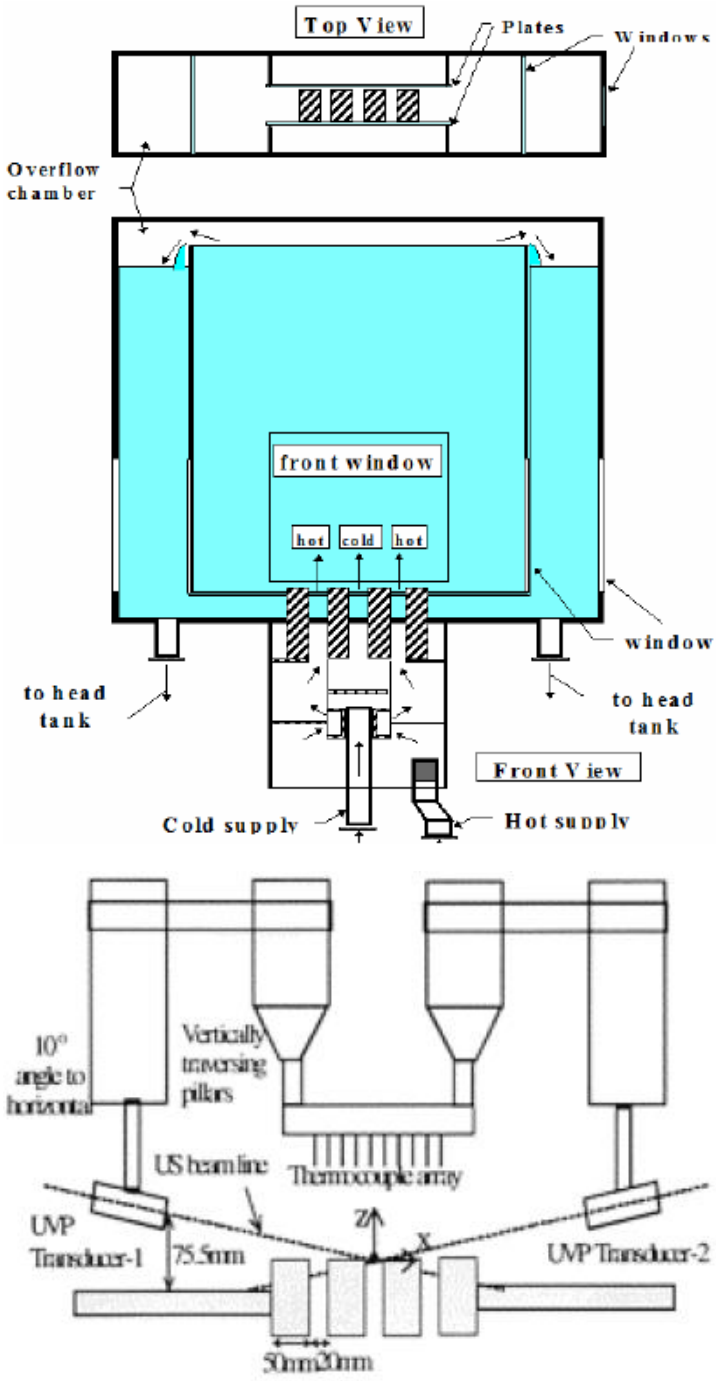

Figure 1: (a). Schematic of the triple-jet test section with inner and outer enclosures. A similar configuration for dual-jet is proposed. (b). Schematic of ultrasound velocimetry and temperature measurement set-up and simulation results for a triple-jet

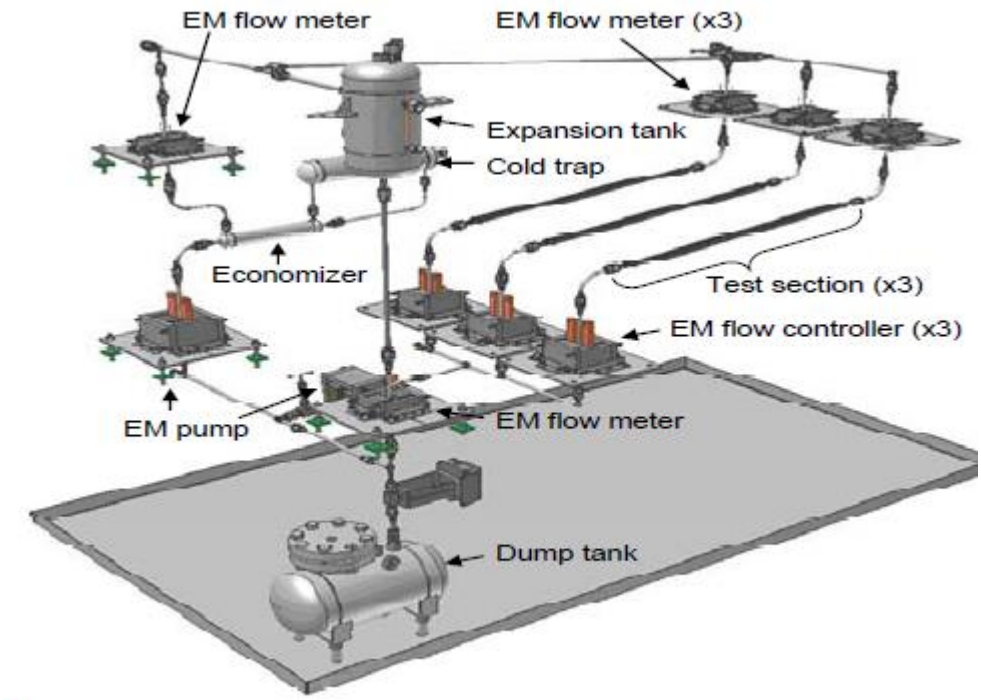

Figure 2: Schematic of a small sodium loop facility at DOE laboratory. Proposed separate effects facilities will have many of the same features and specifications for components exchange options. Initial test section will be to study thermal mixing of two parallel jets.

PI1, Permanent Magnet Velocity Probe

The permanent magnet velocity probe (PMP) reported by von Weissenfluh, Kapulla and coworkers in sodium will be further developed with present day electronics. Earlier the inability to track the non-linearity in the magnetic 'inductance' with temperature hindered full application in tube bundle heat transfer experiments. However, as the temperature dependence is well documented, the measured non-linearity can be monitored with present day electronics and software, relative to a reference. The PMP thus provides independent means to cross-check UDV/UDT measurements.

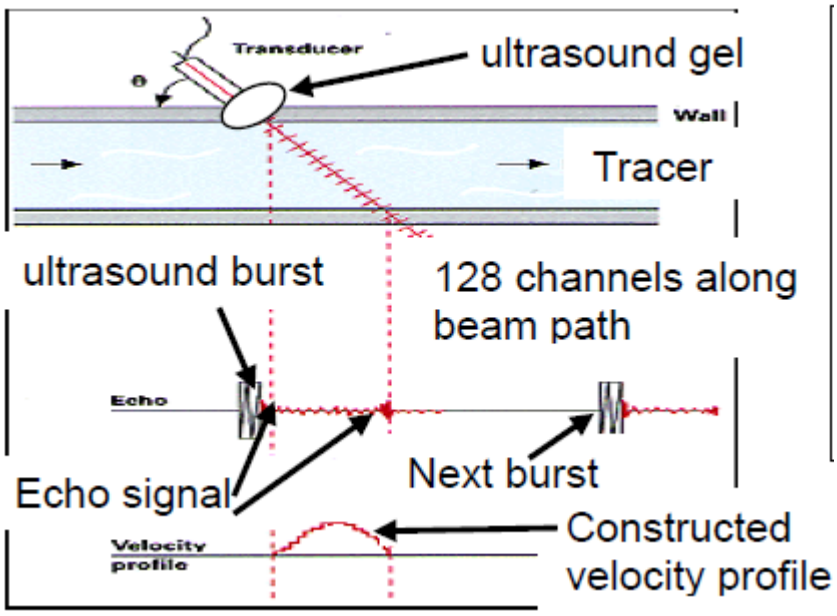

Figure 3: Principle of ultrasound Doppler velocimetry (udv) as applied to pipe-flow as an example. Transducer can be in- or ex-situ and has to be acoustically coupled to medium (solid & liquid). US burst is emitted, then echo from reflections oversampled to construct velocity profile along beamline; thus spatio-temporal.

PI2 – Tasks 2 and 3, Data Characterization for Validating Thermofluid Simulations
In the large body of 'classic' experimental studies on SFRs (LWRs) used to validate nuclear simulation tools, data collection focused largely on measuring integral behavior over large control volumes. At the time, this approach was consistent with the limited means of (mostly) pointwise instrumentation; typically yielding mean values of temperature, pressure, and flow.

Further, the experiments were scaled based on familiar dimensionless parameters such as the Reynolds, Prandtl, or Grashof numbers. While these parameters describe the characteristic turbulence effects in the system, they do not provide information regarding the turbulence spectrum. In fact, the results were not necessarily intended to validate turbulence models but rather to encompass integral and engineering correlations.

Today, higher resolution CFD codes can correctly model many (single-phase) phenomena; however, they have to thoroughly undergo V&V. This requires test data having spatial resolution and bandwidth comparable to that of the simulations. As the available higher fidelity or spatiotemporal data on LM is limited, besides designing and constructing a separate effects test facility, PI2 will collect, reduce and characterize higher fidelity data from broadened base of LM TH studies. In fact, PI2 has been work with LM-targets for high energy physics experiments and for spallation neutron source (SNS) applications. He has performed thermofluid experiments with Hg with small fluid inventories (~1-2 liters), and supported the spallation source convective heat transfer experiments where Hg flow rates were 1500 liter/min. UDV (as above) was used to characterize flows and has similarly been used for engineering and design of other spallation sources worldwide. The existing database and related LM-dynamo experiments will be compiled in the context of the V&V SOW. Furthermore, PIV image files using neutron radiographic images in a seeded Pb-Bi flow were collected from a Japanese research project.

These data will be recovered to develop and benchmark simulation tools and help identify the development path for future LM experiments. In the SNS studies, both fluid and thermal field measurements were made; detailed flow field measurements were made using UDV. In fact, UDV measurements were validated against LDV data in experiments using water, and then used to acquire prototypic data in a full scale Hg-loop. PI1 also compared UDV versus LDV in water in single-jet flow. Data has been used to validate steady-state CFD code predictions facilitating the optimization of target designs and assessing system safety. UDV data, along with other velocimetric methods, will be recovered/re-evaluated to assess the relative applicability of UDV for constructing turbulence field spectra suitable for validation of the unsteady turbulence models used in CFD simulations of thermal mixing of jets. Additional heat transfer data taken under prototypic convective conditions using multiple measurement techniques will also be investigated and used for code validation.

Task 4. PI3 will lead computational simulations of these experiments using LES and RANS methodologies developed as part of the advanced SHARP code suite at PI3's institution. PI3 will simulate near-to-exact experimental conditions defined by PI1 and PI2; further generate spatiotemporally averaged data from simulations to 'match' experimental measurement methods.

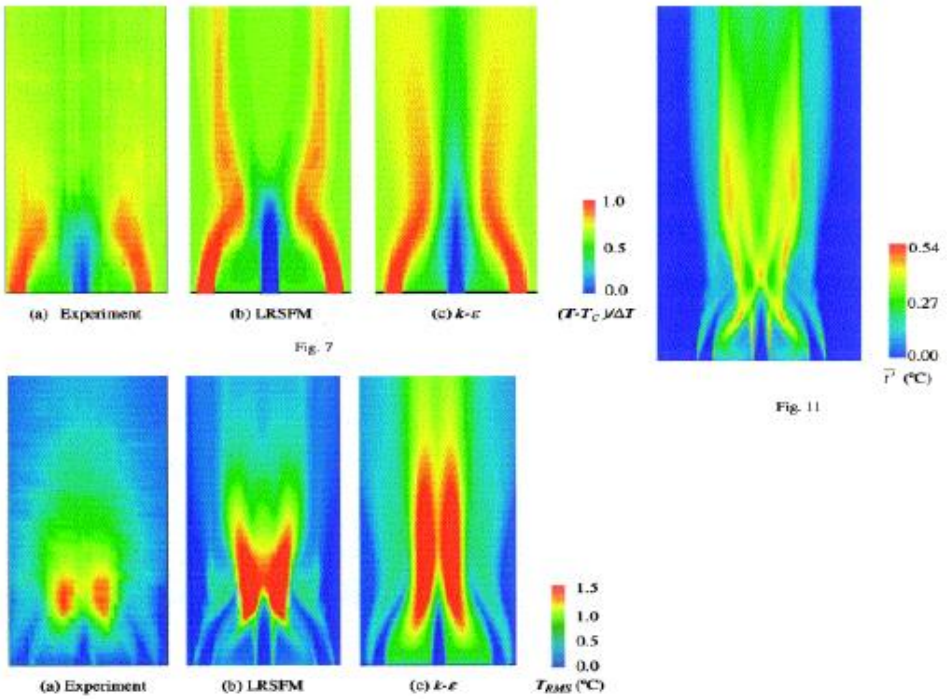

Figure 4: Compare results reported by Kimura and co-workers on thermal-mixing of a non-isothermal triple jet flow. Form left to right, color contours of the experimental result, simulation using a low Re-number stress and heat flux (LRSFM) model and simulation using κ–ε model. The top figure show velocity data while the lower show temperature contours. Contour at right shows the LRSFM predicted mean square temperature fluctuation

As part of the SHARP project, the range of applicability of RANS, LES and DNS methods in the simulation of thermofluid phenomena in LMFRs is being assessed, with the goal of defining a multi-resolution strategy in which high-resolution methods are used to improve the accuracy

of the engineering models in lower-resolution methods (PI3, et al. 2008). Initial efforts focused on the prediction of fluid dynamics and heat transfer in wire-wrapped fuel bundles. However, as shown by Fig. 4 (above) Kimura, Nishimura and co-workers reported DNS, LRSFM and κ−ε based simulation results for thermal mixing of a triple-jet. Recent efforts have focused on the mixing of the jet flows that appear at the outlets of the fuel assemblies (see PI3, et al., 2009). Similar simulations efforts are underway internationally and at least one other DOE laboratory.

In RANS simulations, turbulence effects on bulk characteristics are approximated using a relatively simple engineering closure model. In LES, one directly computes only the energy-carrying large scales of motion while explicitly modeling the energy transfer to the unresolved (sub-grid) scales. In DNS all turbulent fluctuations are modeled directly and predictions are subject only to the constraints of the Navier-Stokes equations. While the high Reynolds numbers and long domain lengths of reactor design simulation preclude the use of DNS for even single sub-channels, the application of LES to assembly scale simulations and RANS simulations to whole-core or other large component simulations is achievable.

PI3 will lead the development of computational models of the proposed experimental geometries using the commercial CFD code Star-CD for steady and unsteady RANS simulation and an advanced DOE laboratory code for unsteady RANS and LES simulations. Computational meshes will be developed from CAD representations using automatic meshing tools associated with the SHARP project and/or STAR-CCM+. Simulations will be completed using standard closure models and solvers associated with each code. Initial models will be used to guide the development of the experiments, including the identification of instrumentation locations. Final CFD models will be based on as-built geometry while experiments are completed; final "blind" simulations will use measured boundary conditions.

Task 5. PI1, PI2 and PI3 will jointly validate and verify to the extent possible the experimental results against the computational simulations. The team will also quantify the associated uncertainties. Uncertainties in experiments will be estimated via standard propagation of error analysis. Initial estimates of uncertainties in CFD simulations will consider the effects of mesh resolution and closure model selection. The effects of statistical fluctuations in boundary conditions will be estimated by variation of boundary parameters in steady state. Unsteady simulations will attempt to replicate the statistical fluctuations if sufficient data can be provided from the experimental measurements. Additional analyses using standard Monte Carlo driven variations of additional selected parameters, such as thermophysical properties, may be completed in year three if warranted.

Current scaling methods are based on non-dimensional parameters which describe the characteristic or average turbulence behavior of a system but provide little or no insight into the distribution of turbulence length or time scales within a system. The proposed matched pair of experiments will facilitate the development of methodologies for improved scaling of advanced experiments supporting advanced simulation tool validation.

ROLES and RESPONSIBILITIES: There are two faculty from separate universities (PI1, 2) and two DOE laboratory co-investigators, PI3 and 4, contributing to the project. PI1, 2 have primarily responsibility to design and construct respective separate effects test facilities with advice from PI4, and to undertake experiments per Tasks 2 and 3. PI1, 2 and 3 will jointly undertake Tasks 1 and 5. PI3 will have lead responsibility for Task 3 and define prototypic conditions to PI1 and 2; PI3 will also 'adapt' simulations results to reflect the characteristics of

experimental spatiotemporal data so obtained. Technical staff at each university will assist PI1 and 2.

DESCRIPTION of FACILITIES to be UTILIZED: The team proposes design and construction of two new separate effects test facilities using LMs with a DOE laboratory's existing facility as a benchmark standard. Both university PIs, PI1 and PI2, are in close proximity to two other DOE laboratories with major facility know-how and are thus uniquely positions to receive expert support. All three PIs have liquid metal thermal-hydraulics expertise. The computing infrastructure of the university and DOE laboratory will be utilized. Additional details are contained in the 'Capabilities' document.

LOGICAL PATH TO ACCOMPLISHING SCOPE and TASK DESCRIPTION

Project Coordination (PI1, 2, 3 and 4): This work includes grant administration, coordination with a DOE lab to obtain prototypic test conditions, and periodic reporting. Since the five tasks involve a detailed understanding of the CFD, V&V and experimentation, the project coordination will involve meeting with the DOE lab PIs and other representatives active in AFCI, to discuss the proposed simulations, experimentation and the compromises that have to be made to operate the proposed separate effects facilities. We have identified the following tasks:

Task 1. Learn current status of work PI3's institution; define PI1's and PI2's specific scope of work to support and broaden DOE laboratory's computational and experimental efforts and separately investigate related instrumentation, scaling and data analysis issues.

Task 2. PI1 and 2 to design and construct small-scale separate effects thermal mixing facility in consultation with PI4; test should yield thermal mixing data. Test sections and auxiliary loop components should be adaptable to the existing DOE laboratory Na-loop for collaboration.

Task 3. PI1 and 2 to define and conduct thermal mixing experiments that are similar but broaden and encompass the parameter-space covered by PI3's computational study.

Task 4. PI3 will lead computational simulations of these experiments using DNS, LES, RANS methods developed by the SFR modeling and simulation 'team' at PI3's institution. PI3 will simulate near-to-exact experimental conditions defined by PI1 and PI2; further generate spatiotemporally averaged data from simulations to 'match' experimental measurement methods.

Task 5. PI1, 2 and 3 will jointly validate and verify to the extent possible the experimental results against the computational simulations. The team will also quantify the associated uncertainties.

PROJECT SCHEDULE: Scope of work is to be completed over a 3-year time span.

Tasks (below),[PIs] Quarters (right) >	1	2	3	4	5	6	7	8	9	10	11	12
Write guidance doc., expt'l data needs for adv. SFR design & safety analysis. [participants - ALL]	X	X										
Write guidance doc., V&V, application of advanced TH simulation methods, SFR design. [ALL]	X	X										
Design, construct and shakedown separate effects facilities; construct jet thermal mixing test sections. [PI1, PI2]	X	X	X	X								
Develop and demonstrate advanced instrumentation for experiments. [PI1,PI2, PI4]		X	X	X	X	X	X	X				
Conduct simulations in phases [PI3]		X	X		X	X		X	X		X	
Develop spatiotemporal data mgmt & processing strategies and methods, integrate to high-resolution V&V practices [PI3]			X	X	X	X	X	X	X			
Initial separate effects tests [PI1, PI2]				X	X	X						
Develop experimental benchmark database that is accessible to users [PI1,2,4]						X	X					
Follow-up separate effects tests.[PI1,2]							X	X	X	X		
Do V&V, UQ along with experiments; provide feedback; 'adapt' simulations to expt'l data [ALL]									X	X	X	
Graduate students. [PI1, 2]	X	X	X	X	X	X	X	X	X	X	X	X
Reports:Quarterly, Annual and peer-reviewed. [ALL]	X	X	X	X	X	X	X	X	X	X	X	X

Deliverables: The proposed work will be reported in Quarterly progress reports, Annual reports at the end of each year, conference and journal paper.

CHALLENGES TO ACCOMPLISH TASKS and INNOVATIONS TO MEET CHALLENGES

One of the anticipated challenges in this SOW is to properly coordinate the experimental, modeling and computational tasks across the institutional partnership. Fortunately the co-PIs are well-acquainted with each other and are currently working or have previously worked collaboratively. PI1 and PI2 are also in proximity to two additional DOE laboratories and thus have a broad expertise base to access. In order to minimize unnecessary customization in the proposed separate effects facilities, we will use the existing DOE facility as the reference and to the extent possible match their specifications. The following are anticipated challenges and brief descriptions of means by which we will address them. That is, we with respect to:

1) Developing guidance document outlining experimental data, V&V and UQ needs for SFR reactor design and safety analysis, we will collaboratively prepare such a document. The team is well-versed in the LM literature and has access to LM experts.

2) Designing and constructing a heated jet mixing experiment with proper turbulence scales to simulate thermal striping, we selected a dual-jet configuration that is well-documented relative to single-jet, triple-jet and mixing layers, both experimentally and computationally. This minimizes unanticipated challenges. Further we have to standardized the test facility.

3) Developing and demonstrating advanced instrumentation, both universities use a common UDV instrument and transducer (sensor). Both the UDT and PMP can be tested at both facilities as well as at the DOE facility.

4) Establishing data management and processing strategies to facilitate higher resolution V&V and UQ practices, PI1 and 2 will support the agreed upon practices. This includes an effort to identify capabilities, gaps and needs for data reduction, characterization, cross-correlation, visualization and comparison in existing software.

5) Completing CFD simulations of the dual-jet thermal mixing problem, PI3 has extensive experience and computing infrastructure to undertake Tasks 4 and 5.
6) Overall effort, PI1, 2 and 3 have access to official and unofficial channels to access and request experimental and computational database associated with single- and triple-jet studies conducted at the foreign national institutes and universities.

INFORMATION, DATA and PLANS: All key information has been presented in technical scope.

QUALITY ASSURANCE: The team will use the following QA/QC approach, consistent with the graded approach established by the offices for GNEP Technical Integration and AFCI.
• All work will be recorded in lab notebooks. These notebooks will include: statement of objective/description of specific work to be done or reference to approved planning document/implementation that addresses those topics, identification of method(s) and computer software used, identification of any samples, or measurement/test equipment used description of the work as it was performed, results obtained, names of those performing the work, and dated initials/signature, name(s) of individuals making the entries, Description of changes made to methods used. Description of problems encountered and resolution.
• Lab notebooks shall be reviewed yearly by project supervisors to verify there is sufficient detail to: 1) Retrace the investigations and confirm the results, or 2) Repeat the investigation and achieve comparable results, without recourse to the original investigator.
• Training on proper use and maintenance of lab notebooks will be conducted yearly.
• For each major piece of equipment used, a record of drawings, operational procedures, material certifications and calibrations will be maintained.
• Certificates of completion of radiation safety and chemical safety will be maintained for each researcher required to have this training.

REFERENCES

DOE, Nuclear Energy Research Initiative (NERI), on 03/16/2009, www.nuclear.energy.gov/neri/
Hayashida, H., M. Ueda, PI1 and K. Ara, 8th Int. Conf. Nucl. Eng., ICONE-8, Baltimore, MD April 2-6, 2000.
Kapulla, R., Sigg, B., Horanyi, S. and Hudina, M., Exp.Therm. Fluid Sci., 20, 3-4, 115, February 2000.
Kimura, N., M. **Nishimura** and H. Kamide, JSME Int. J., Ser. B, 45, 3, Special Issue Int. Conf. Power and Energy Sys., p.592, 2002
Nishimura, M., PI1, N. **Kimura** and H. Kamide, Nucl. Eng. and Design, 200 (1), 77, 2000.
PI1, Atomic Energy Soc. Japan, J. Nucl. Sci. and Technol., 36[6], Jun 1999.
PI1 and N. Kimura, Nuclear Engineering and Design, 188, 49-73, 1999.
PI3, P.F. Fischer, A. Siegel, and J. Smith, Proc. Int'l Congress Adv. Power Plants (ICAPP'08), Anaheim, CA, Paper No. 8252, Jun 2008,.
PI3, P. Fischer, A. Siegel and J. Smith, Proc. ICAPP '08, Anaheim, CA , 2008
PI3, S. Lomperski, P. Fischer, A. Obabko, Proc. ICONE-17, Brussels, Belgium, Jul 2009.
Takeda,Y., M. Harada, Ed., Fluid Control and Measurements, 2-6 September, Tokyo, Pergamon Press, 1985.
Von Weissenfluh, T. and Sigg, B., 5th Beer-Sheva Seminar on Magneto-hydrodynamic (MHD) Flows and Turbulence, Jerusalem, Mar 2-6, 1987.

APPENDIX C

RCCS EXPERIMENTAL RESULTS

Baseline Condition (Runs 052 and 058)

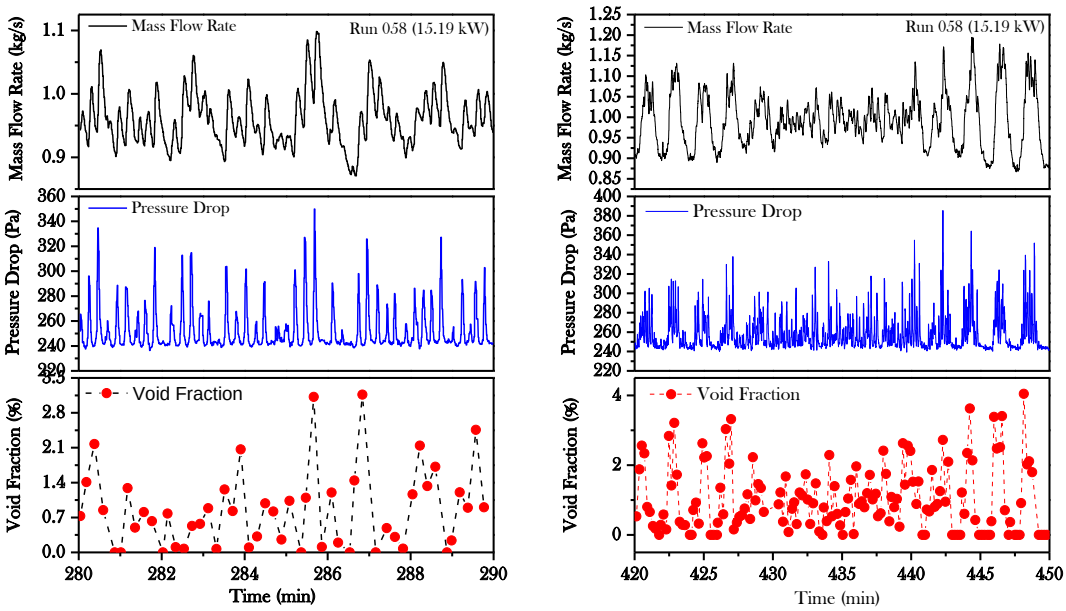

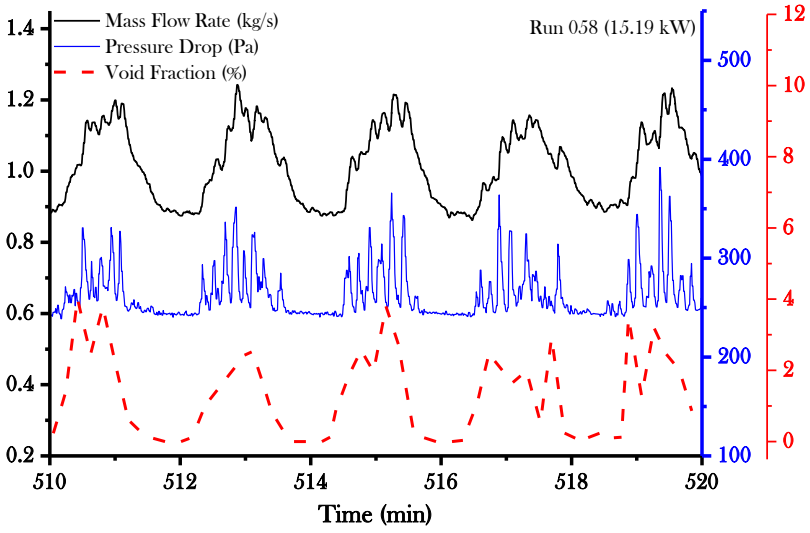

Power Investigation (Runs 054, 058, 059, 061)

Run 054

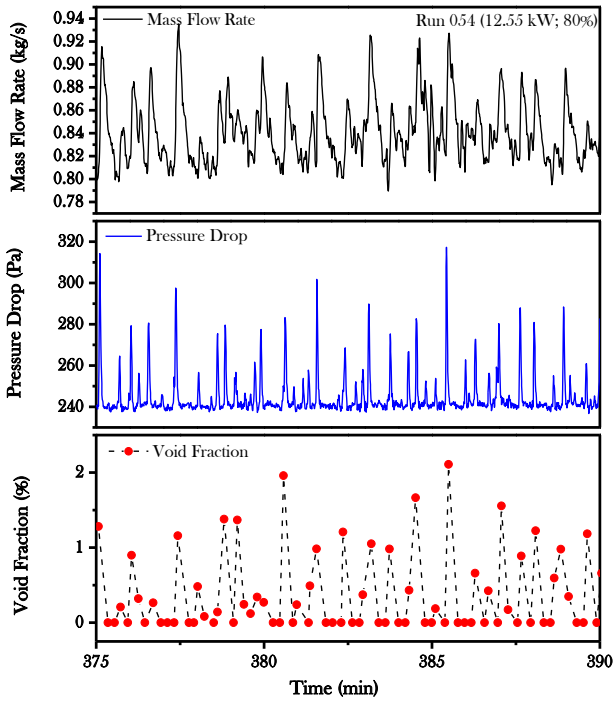
Mass Flow Rate
Run 054 (12.55 kW; 80%)
Mass Flow Rate (kg/s)
0.94
0.92
0.90
0.88
0.86
0.84
0.82
0.80
0.78
Pressure Drop
Pressure Drop (Pa)
320
300
280
260
240
Void Fraction
Void Fraction (%)
2
1
0
375
380
385
390
Time (min)

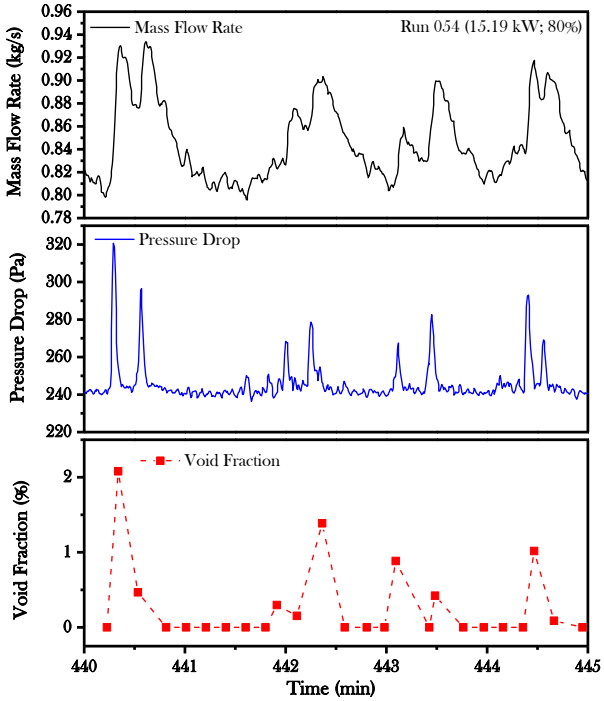
Mass Flow Rate
Run 054 (15.19 kW; 80%)
Mass Flow Rate (kg/s)
0.96
0.94
0.92
0.90
0.88
0.86
0.84
0.82
0.80
0.78
Pressure Drop
Pressure Drop (Pa)
320
300
280
260
240
220
Void Fraction
Void Fraction (%)
2
1
0
440
441
442
443
444
445
Time (min)

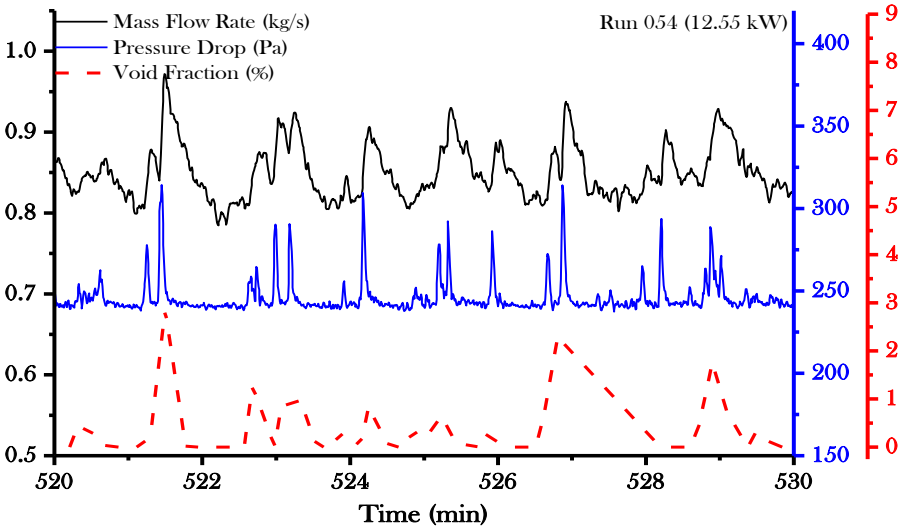
Mass Flow Rate (kg/s)
Pressure Drop (Pa)
Void Fraction (%)
Run 054 (12.55 kW)
1.0
0.9
0.8
0.7
0.6
0.5
400
350
300
250
200
150
9
8
7
6
5
4
3
2
1
0
520
522
524
526
528
530
Time (min)

Run 059

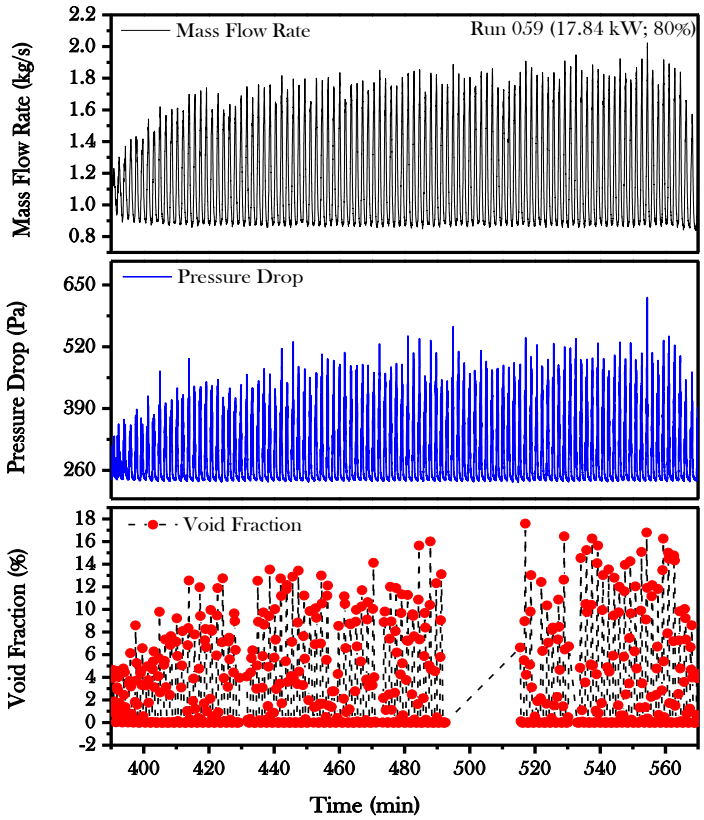
Mass Flow Rate
Run 059 (17.84 kW; 80%)
Mass Flow Rate (kg/s)
2.2
2.0
1.8
1.6
1.4
1.2
1.0
0.8
Pressure Drop
Pressure Drop (Pa)
650
520
390
260
Void Fraction
Void Fraction (%)
18
16
14
12
10
8
6
4
2
0
-2
400
420
440
460
480
500
520
540
560
Time (min)

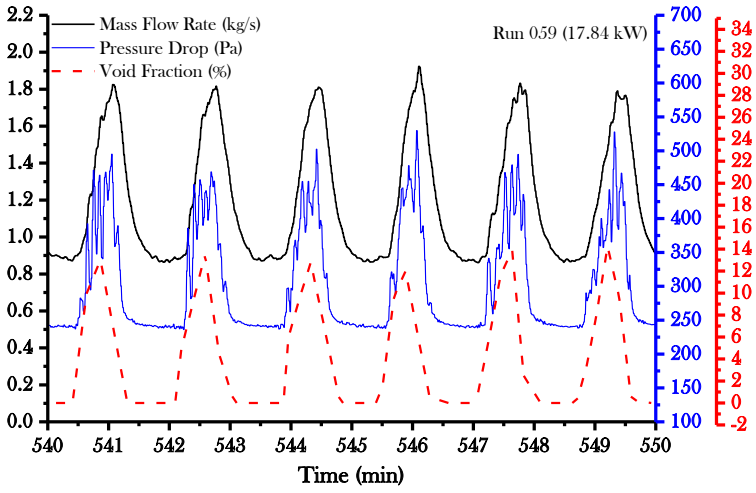
Mass Flow Rate (kg/s)
Pressure Drop (Pa)
Void Fraction (%)
Run 059 (17.84 kW)
Time (min)

Run 061

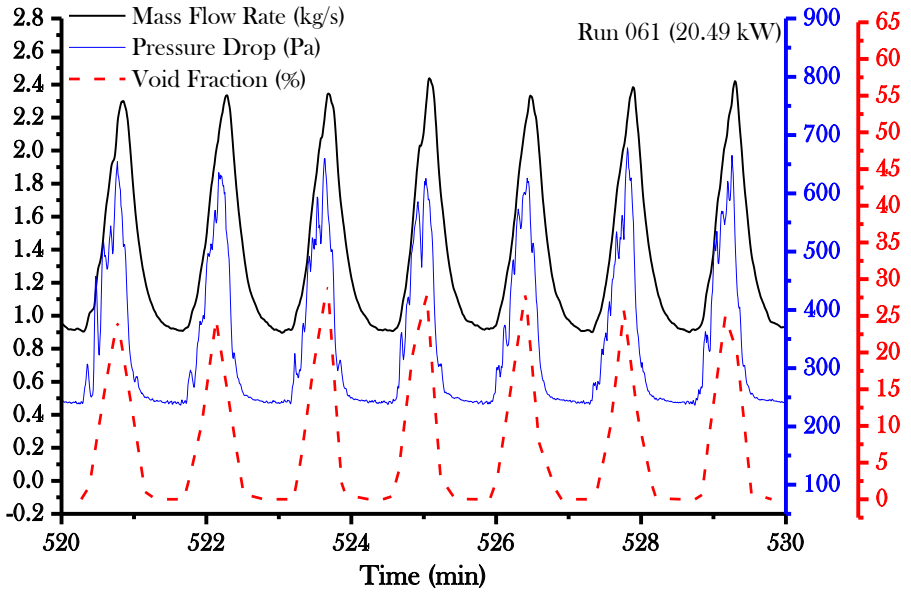
Mass Flow Rate (kg/s)
Pressure Drop (Pa)
Void Fraction (%)
Run 061 (20.49 kW)
Time (min)

Tank Inventory (Runs 050, 051, 058)

Run 050

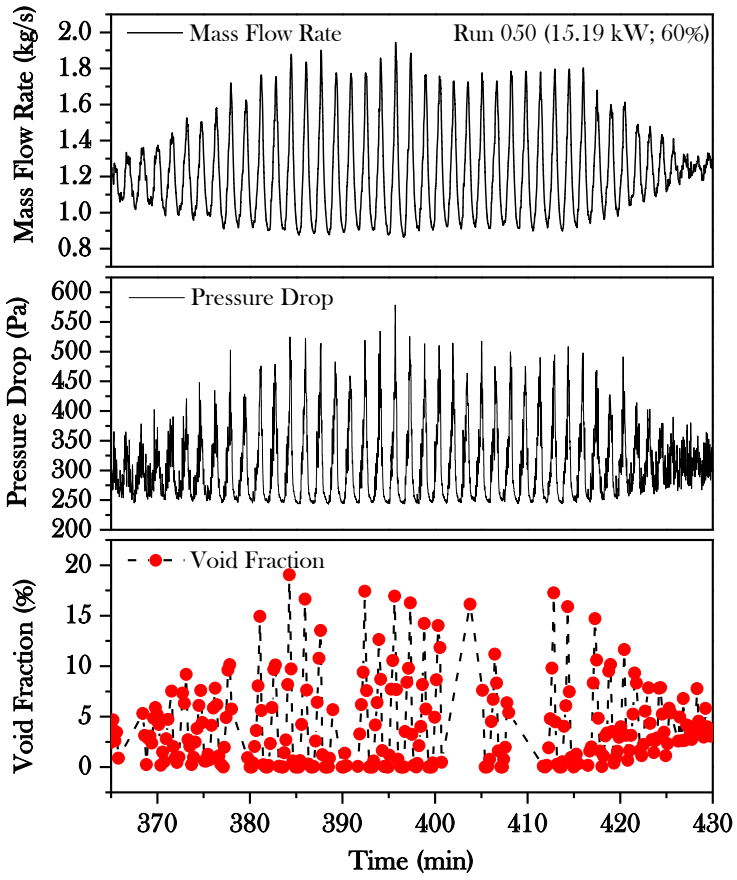

Tank depletion through accelerated drain (Run 055)

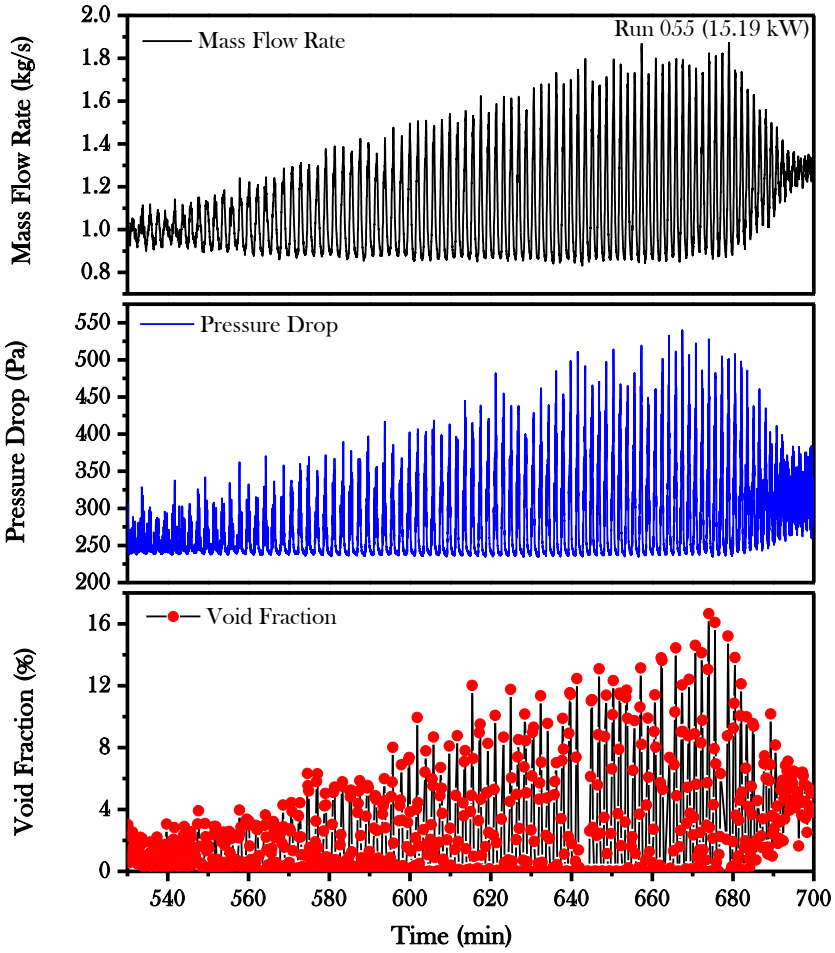

APPENDIX D

PUBLICATIONS

1. **Published in Proceedings of 8th International Topical Meeting on Nuclear Thermal-hydraulics, Operations and Safety (NUTHOS-8), Shanghai, China, October 10-14th, 2010**

Computational Fluid Dynamic Simulations of Jet Momentum Transport in Liquid Metals

Lee Tschaepe[1], O. Omotowa[2], R. Davis[2], A. Ruggles[1], D. Pointer[3] and A. Tokuhiro[2]

1- University of Tennessee, 315 Pasqua Engineering Building, Knoxville, Tennessee USA 37996; ltschaep@utk.edu, aruggles@utk.edu
2- University of Idaho, 1776 Science Center Drive, Idaho Falls, Idaho USA 83402-1575; tokuhiro@uidaho.edu, +1-208-533-8102
3- Argonne National Laboratory, Argonne, Illinois 60439 USA; dpointer@anl.gov

ABSTRACT

Several DOE laboratories are obtaining high resolution experimental data for validation and verification of computational fluid dynamics and multiphysics tools for the prediction of thermo-hydraulic phenomena in sodium fast reactor systems. The multiphysics code COMSOL is used to simulate two closely spaced jets entering a plenum in order to guide design of an experiment for acquisition of high resolution data for such a flow. COMSOL provides two default turbulence models, k-epsilon and k-omega. There exist within each of these turbulence models various options to tailor fit the model to the flow physics of interest. These turbulence models are first compared against existing literature simulations for a single vertical water jet injected into a pool of water to determine the ability of COMSOL to replicate well established data sets. This also provides the opportunity to tune the turbulence models to replicate the physics of the well-known single jet isothermal flow. Finally, simulations for two mixing jets are performed with mercury and with sodium, the fluids to be used in the experiments, and the outcomes are compared. These two mixing jet simulations are also compared with integral analytic mass and momentum balances to examine the simulation fidelity to these balances. The results of these computational efforts to support experiment design are presented.

KEYWORDS

COMSOL, jet, turbulence, mercury, sodium.

1. INTRODUCTION

The impetus for this work is the desire of several department of energy (DOE) laboratories to obtain high fidelity data sets characterizing the flow field for two liquid metal jets vertically impinging a pool. These data sets will be used for verification and validation of computational fluid dynamics (CFD) codes. These codes will be employed to model and develop sodium fast reactor systems. Prior to the design and construction of the test facilities, it is necessary to understand the temporal and spatial variations in velocities and temperatures to be measured. The multiphysics code COMSOL is the tool chosen to guide the design of the experimental facilities that will be constructed to obtain the data used for verification and validation.

A typical velocity component in a turbulent flow fluctuates randomly in time about a mean value. It is the sum of this fluctuation and the mean value that corresponds to the measured quanta. The mean and fluctuating components of any variable are:

$$\bar{Q} = \frac{1}{T}\int_{t_0}^{t_0+T} Q\,dt \tag{1}$$

$$Q' = Q - \bar{Q} \tag{2}$$

Noting the fluctuating nature of turbulent velocity, pressure, and temperature components and assuming constant material properties, the incompressible continuity equation.

$$\nabla \cdot V = 0 \tag{3}$$

is rewritten as the time average continuity equation

$$\frac{\partial \bar{u}}{\partial x} + \frac{\partial \bar{v}}{\partial y} + \frac{\partial \bar{w}}{\partial z} = 0 \tag{4}$$

The Navier-Stokes equation

$$\rho \frac{DV}{Dt} = \rho g - \nabla p + \mu \nabla^2 \mathrm{V} \tag{5}$$

can similarly be rewritten in time average form

$$\rho \frac{D\bar{V}}{Dt} + \rho \frac{\partial(\overline{u_i' u_j'})}{\partial x_j} = \rho g - \nabla \bar{p} + \mu \nabla^2 \bar{V} \tag{6}$$

The $\overline{u_i' u_j'}$ term in the mean momentum equation is the turbulent inertia tensor. In turbulent flow this term is not negligible. This term adds an additional nine unknown terms to the Navier-Stokes equations. The turbulent inertia tensor is often combined with the stress tensor

$$\rho \frac{D\bar{V}}{Dt} = \rho g - \nabla \bar{p} + \nabla \cdot \tau_{ij} \tag{7}$$

$$\tau_{ij} = \mu \left(\frac{\partial u_i}{\partial x_j} + \frac{\partial u_j}{\partial x_i} \right) - \rho \overline{u_i' u_j'} \tag{8}$$

Though the turbulent inertia tensor is combined with the stress tensor, these terms are not stresses. In a similar fashion to the continuity and momentum equations, the mean energy equation is obtained

$$\rho c_p \frac{D\bar{T}}{Dt} = -\frac{\partial (q_i)}{\partial x_i} + \bar{\Phi} \tag{9}$$

$$q_i = -k \frac{\partial \bar{T}}{\partial x_i} + \rho c_p \overline{u_i' T'} \tag{10}$$

where the second term on the right hand side of Equation 10 represents the turbulent heat flux term. Collectively, these equations introduce several new unknowns and several modeling approaches have been developed to manage the complexity. The correlation of these models to experimentally obtained data allows for validation of a CFD code like Fluent or a multiphysics code like COMSOL.

2. WATER VALIDATION:

The capability of COMSOL to reproduce vetted data for a single vertical water jet injected into a pool of water is explored prior to performing the mercury and sodium 2 jet simulations. The COMSOL k-epsilon and k-omega models are employed for turbulence modeling. Rodi indicates that the k-epsilon model can be used to model free shear flows. However, two constants, C_μ and $C_{\varepsilon 2}$, should be modified to improve agreement with experimental results. The constant C_μ of the Wilcox k-omega model, as implemented in COMSOL, is modified from the default value of 0.09. The values listed in Table 1 and associated with the k-epsilon model are historically determined via experiments. The values listed in Table 1 and associated with the k-omega model are closure constants for the k and omega equations used in the simulations.

Table 1. K-ε and K-ω Constants

k-ε		k-ω	
$C_{\varepsilon 1}$	1.44	α	0.52
$C_{\varepsilon 2}$	1.8533	β_0	0.072
σ_k	1	$\beta_{0,k}$	0.09
σ_ε	1.3	σ_k	0.5
C_μ	0.05	σ_ω	0.5
turbulent kinetic energy	0.005	C_μ	0.05
turbulent dissipation rate	0.005	turbulent length scale	0.01
		turbulence intensity	0.05

The simulation geometry shown in Figure 1 for the water validation closely mimics the experimental setup used by Tokuhiro (1999). The main difference is the simulation employs a reduced test section height. A heat transfer module, describing the fluid properties, is used in addition to the stated turbulence models for each of the simulations. Though what are presented are isothermal cases, inclusion of this module allows for the evaluation of the material properties at varying temperature ranges without manual input of the properties. Figure 1 displays the pertinent boundary conditions that are applied for the isotropic single jet injected vertically into a pool of water. Since two modeling modules are used, two boundary conditions at every boundary are required, excluding continuity boundaries. For all walls, the wall offset in viscous units is 1000. This assumes that the flow near the walls is of little concern and should be valid as long as the jet does not directly impact the walls. The assumption that the simulated jet flow field does not impact the wall is visually verifiable through COMSOL post processing menus. To satisfy the heat transfer module at the walls, the boundary condition is chosen to be thermal insulation. The flow inlet boundary conditions prescribe the velocity as 0.5 m/s and the inlet temperature as 293.15 K. The outlet boundary conditions prescribed are zero pressure and convective flux. Figure 2 displays the mesh density at the outlet used in the simulation for the single water jet. It was determined, through iterations, that an increased mesh density at the flow outlet is beneficial to the conservation of mass. The total number of elements and degrees of freedom in the k-epsilon simulation are 7236 and 63469, respectively. The total number of elements and degrees of freedom in the k-omega simulations are 9576 and 97731. A stationary segregated iterative solver is used for the present simulations. The employed segregated solver breaks the problem into three groups consisting of velocity and pressure components, log(d) and log(k) for the k-epsilon solver (log(w) and log(k) for the k-omega solver), and Tf and Jf. Each group uses a Direct (PARDISO) solver and iterates until the solution converges below 1E-3.

Prior to comparing the COMSOL simulations to experimental results, the simulations are juxtaposed with theoretically determined mass and momentum balances. The integral transport equation is:

$$\frac{d}{dt}\iiint \rho c dV + \oiint \rho c(\vec{v})\vec{n}dA = \iiint \rho\varphi dV + \oiint \vec{J}\vec{n}dA \tag{11}$$

where c 1, $\vec{J} = 0$, and $\varphi = 0$ yields mass conservation. It is assumed for all conservation analysis that the solution is at steady state, and the fluid is incompressible. Applied to the COMSOL mesh and geomentry in Figure 2, the mass conservation

$$v_{out} = \frac{v_{in}A_{in}}{A_{out}} \tag{12}$$

returns an outlet velocity of 0.0714285714 m/s. The COMSOL predicted outlet velocity for the k-omega simulation is 0.0715714286 m/s. The mass flow errors for the k-epsilon and k-omega simulations are 0.8% and 0.2%, respectively.

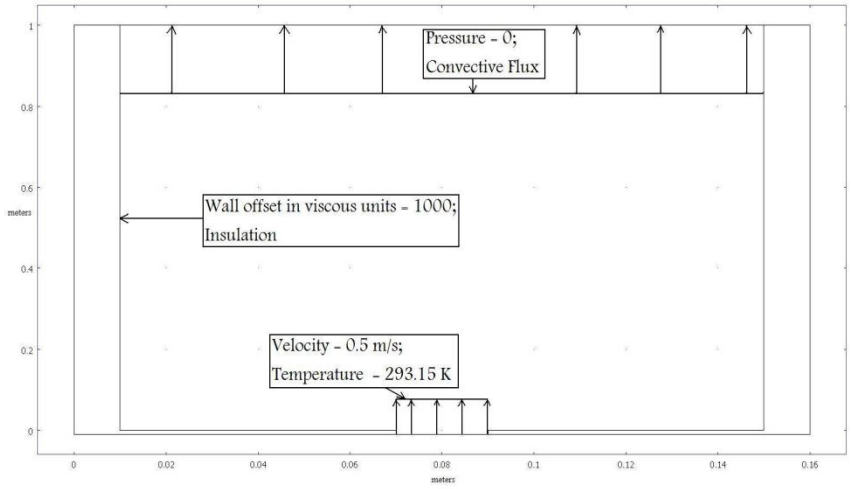

Figure 1. Single Jet Boundary Conditions

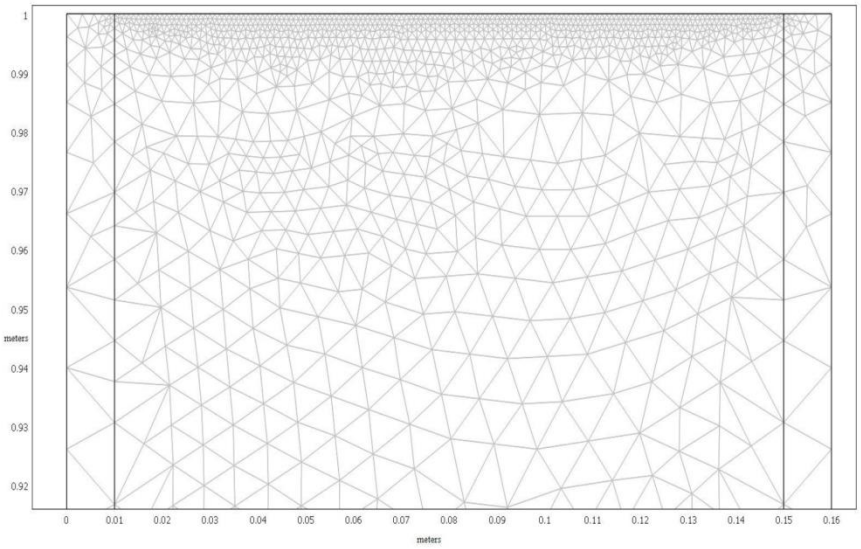

Figure 2. Single Jet Mesh Density

The integral momentum balance is represented by Equation 11 with $c = \vec{v}$, $\vec{j} = \bar{\bar{\tau}} - p\bar{\bar{I}}$, and $\varphi = \vec{g}$. Applying these new constraints to Equation 11 and neglecting viscous effects yields:

$$p_{in} = \frac{\rho g}{A_{out}}[hA_{out} + v_{in}^2 A_{in}] \tag{13}$$

The outlet boundary is assumed to be maintained at 0 Pa. The calculated inlet pressure is is 10170.4543 Pa. The k-epsilon and k-omega simulated inlet pressures are 9923.95975 Pa and 9964.2331 Pa, respectively. The resulting errors for the k-epsilon and k-omega simulations are 2.4% and 2%. These variations from the theoretical results can potentially be attributed to a coarse mesh.

Figure 3-4 are comparisons of the COMSOL k-epsilon and k-omega models to existing literature data for the decay of the centerline velocity versus axial distance and the half radius half max. It is apparent that the COMSOL k-epsilon model show reasonable agreement with these data. The COMSOL k-epsilon simulation results in a slightly non-linear decay of the centerline velocity. However, the COMSOL k-epsilon simulation results remain bounded by previous experimental results for methane, air, and water. The jet half radius comparison shows that the COMSOL k-epsilon simulation predicts a slope which mimics the historical data. These results lend confidence to the COMSOL k-epsilon simulations. The k-omega results do not perform well under the applied conditions. It significantly over predicts the decay of the centerline velocity and the slope of the k-omega velocity prediction in Figure 3 is much steeper than prior experimental results. The k-omega predicted jet half radius is also inconsistent with prior experimental results. The poor performance of the k-omega may be due to overzealous diffusion parameters used to obtain a stable solution for the k-omega simulation. Unless significant improvement can be made, the k-omega model as implemented in COMSOL will not be used for the future development of the mercury and sodium separate effects facilities.

3. LIQUID METAL SIMULATIONS

The premise of the experimental setup is that two vertical jets will be combining under free turbulence and will be uninfluenced by wall effects. For the experiments of interest, the temporal fluctuations of the measured quanta, temperature and velocity, are likely large where the jets first combine. Temporal fluctuations will be smaller further away from the jet inlets. CFD methods employing LES models, or DNS methods, can reproduce both temporal and spatial attributes of the mixing jets. The capability to measure and to model these fluctuations are of interest to CFD validation efforts. While COMSOL using RANS models will not deliver time resolved turbulence outcomes, these simulations are still quite useful to the early design effort.

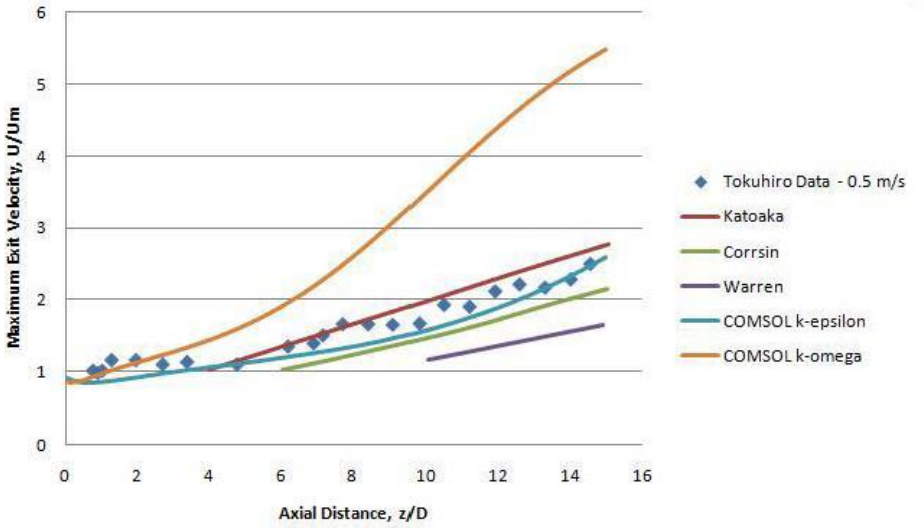

Figure 3. Decay of the Centerline Velocity versus Axial Distance

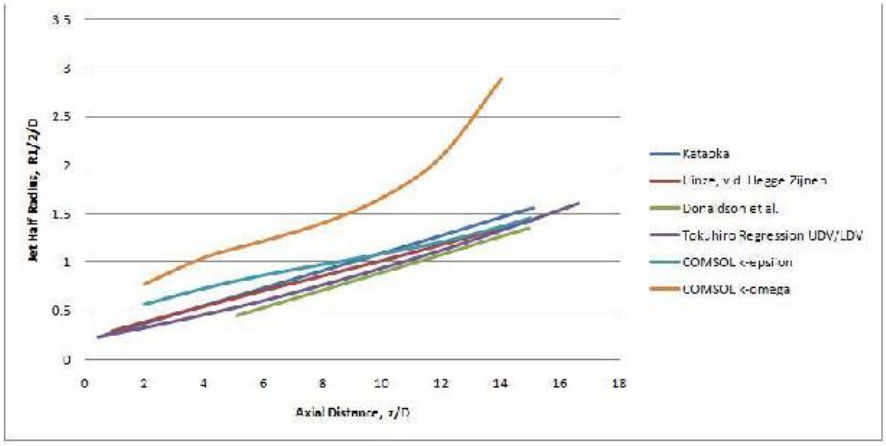

Figure 4. Jet Half Radii versus Axial Distance

Based on jet theory and historical experiments (in non-liquid metals) for a single round jet: The mean velocity profile does not become self similar until x/D > 20. The stream wise velocity fluctuations become self similar at x/D = 50, and the transverse velocity fluctuation components become self similar at x/D = 70. It is at this point that the singular jet is considered to have reached a self preserving state. The presented two jet simulations assume an x/D = 160.

The inlet diameter of each jet is 0.00635 m. The mercury flow rate is 2 L/min. This flow rate results in a jet inlet velocity of 0.526 m/s for mercury at 293 K. To effectively relate the momentum simulations between the investigated fluids, they are examined at similar Reynolds numbers. The jet inlet velocity for sodium is 3 m/s at 400 K. The multiphysics code COMSOL is used to simulate theoretical outcomes for each test section. The results for the COMSOL k-epsilon and k-omega velocity fields are presented in Figures 5-6.

It is apparent that, as currently implemented, there are significant differences between the k-epsilon and k-omega results. The k-epsilon and k-omega results presented in Figure 5 visually resemble each other, more so than the k-epsilon and k-omega results of Figure 6. This is likely due to the fact that an isotropic diffusion of 0.4 is needed to obtain convergence for the sodium k-omega simulation. Isotropic diffusion is not required to obtain convergence in the other three simulations.

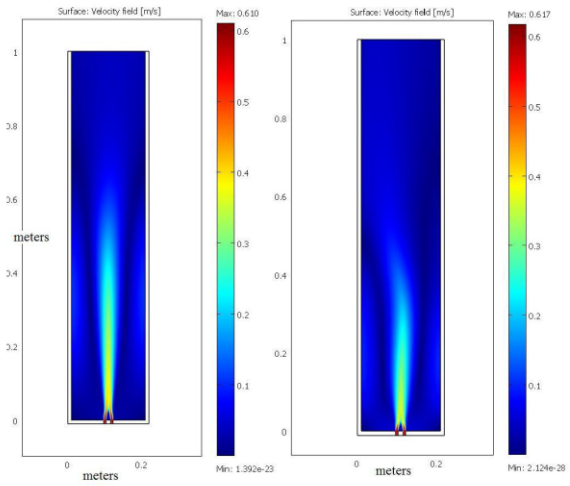

Figure 5. k-epsilon (left) and k-omega (right) Simulations of Mercury Velocity Profile

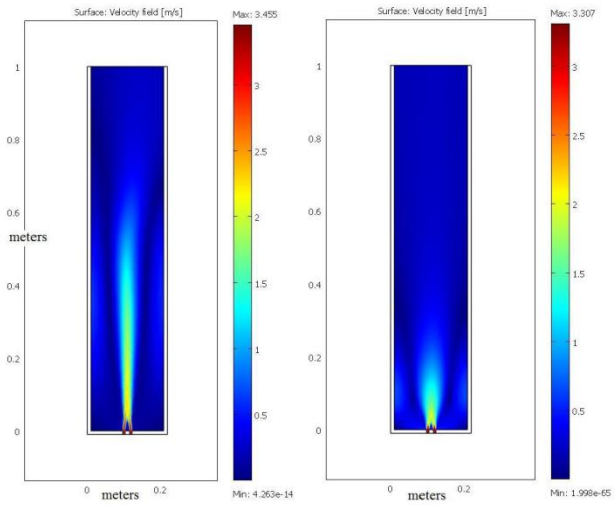

Figure 6. k-epsilon (left) and k-omega (right) Simulations of Sodium Velocity Profile

Similar to the water validation, analytic mass and momentum balances are performed to determine, to the extent possible, the validity of the simulations. The theoretical and simulated solutions for the mass and momentum balances are compared in Table 2.

Table 2. Mass and Momentum Comparisons

Mercury				
Solutions	Exit Velocity	Error	Inlet Pressure	Error
analytic	0.033401		132996.3642	
k-ε	0.034155	0.02257	134857.5293	0.013994105
k-ω	0.03379	0.01165	135030.8849	0.015297566
Sodium				
Solutions	Exit Velocity	Error	Inlet Pressure	Error
analytic	0.1905		8530.13589	
k-ε	0.19137	0.00457	9341.525197	0.095120326
k-ω	0.191235	0.00386	9866.320079	0.156642779

The computed error between the theoretical inlet pressure and the simulated inlet pressure for the sodium simulations is significant. A basic mesh refinement study was performed in order to reduce this error. However, limitations on the available computation resources prevented further mesh refinement and error reduction. Mesh refinement forces the simulation towards the theoretical solution.

4. CONCLUSION

COMSOL is used to guide the design of an experimental facility for gathering high resolution data for mixing of two liquid metal jets. The default settings provided by COMSOL serve as a starting point for jet simulation, with the k-epsilon model providing reasonable fidelity to legacy data for single jet flows. The k-omega model appears to be too diffusive using the recommended settings, and significant work remains to tune the models to the particular flow physics of interest. Once the appropriate models are instituted, work to design the experimental facility for high resolution data collection can be completed.

Going forward, the high resolution data expected for the two jet mixing experiments will allow a more complete validation of turbulence models for this flow situation. The data will include better spatial resolution and some temporal resolution of the mixing flow structure for the two jets in liquid metal. More advanced turbulence modeling approaches, such as LES, will benefit from the more challenging validation data.

5. REFERENCES

1. Bashir, J., Uberoi, M. S.: Phys. Fluids, 18[4], 405 (1975).
2. Chen, C. J., Rodi, W.: "Vertical Turbulent Buoyant Jets - A review of experimental data", Pergamon Press, Oxford, England, (1980).
3. Cheremisinoff, N. P., Ed.: "Encyclopedia of Fluid Mechanics, Dynamics of Single-Fluid Flows and Mixing", Vol. 2, Gulf Publ., Houston, USA, (1986).
4. Corrsin, S., Uberoi, M. S.: NACA TN 1865, (1949).
5. D. C. Wilcox, "Turbulence Modeling for CFD," 2nd ed. DCW Industries, 1998.
6. Donaldson, C. duP., Gray, A. E.: AIAA J., 4, 2017 (1966).
7. Expancel tracer powder, Expancel, Tokyo, Japan.
8. Harris, P. R.: The densimetric flows caused by the discharge of heated two-dimensional jets beneath a free surface, Ph.D. Thesis, Univ. of Bristol, Dept. Civil Eng., Bristol, U.K. (1967).
9. Hinze, J. O., van der Hegge Zijnen, B. G.: Appl. Sci. Res., 1A, 435 (1949).
10. Kataoka, K.: Modeling turbulent jets with variable density, in "Encyclopedia of Fluid Mechanics, Dynamics of Single-Fluid Flows and Mixing", (Cheremisinoff, N. P., Ed.), Vol, 2, Chap. 20, Gulf Publ., Houston, USA, (1986).
11. Kataoka, K., Shundoh, H., Matsuo, H.: J. Chem. Eng. Jpn., 15, 17 (1968).
12. Kimura, N., Tokuhiro, A., Miyakoshi, H.: 8th Int. Topical Meeting on Nuclear Reactor Thermal Hydraulics, NURETH-8, Kyoto, Japan, Vol. 3, 1724 (1997).
13. Kiser, K. M.: AIChE J., 9, 386 (1963).
14. Kotsovinos, N. E.: J. Fluid Mech., 81, 25 (1977).
15. Kristmanson, D., Danckwerts, P. V.: Chem. Eng. Sci., 16, 267 (1961).
16. Rodi, W. Turbulence Models and Their Application in Hydraulics, Brookfield, Brookfield, Vt. 1984.

17. Sawada, T., Tokuhiro, A., Aritomi, M., Eds.: Proc. USDJ'97 A Seminar Flow Measur. using Ultrasound Doppler Methods, Keio Univ., Yokohama, Japan, 10-11 Nov. (1997).
18. Schetz, J. A., Fuhs, A. E., Eds.: "Handbook of Fluid Dynamics and Fluid Machinery", Vol. 1, John Wiley & Sons, New York, USA, (1996).
19. Schlichting, H.: "Boundary Layer Theory", (6th ed.), Chap. 24, McGraw-Hill, New York, (1968).
20. Takeda, Y., Dury, T., Bauer, G. S.: 8th Int. Topical Meeting on Nuclear Reactor Thermal Hydraulics, NURETH-8, Kyoto, Japan, Vol. 3, 1252 (1997).
21. Takeda, Y.: Exp. Therm. Fluid Sci., 10, 444-453 (1995).
22. Takeda, Y., Haefeli, M.: Proc. 2nd World Conf. Exp. Heat Transfer, Fluid Mech. And Thermodynamics, Dubrovnik, Yugoslavia, 23-28 June, (1991).
23. Takeda, Y.: Inst. J. Heat Fluid Flow, 8, 313-318 (1986).
24. Takeda, Y.: JSME Int. J., Fluid Therm. Eng., B38[1], 8-16 (1995).
25. Takeda, Y., Kobashi, K., Fischer, W. E.: Exp. Fluids, 9, 317 (1991).
26. Takeda, Y.: Nucl. Eng. Des., 126, 277-284 (1990).
27. Takeda, Y.: Nucl. Technol., 79, 120-124 (1987).
28. Takeda, Y.: Proc. 3rd World Conf. on Exp. Heat Transfer, Fluid Mech. and Thermodynamics, (Kelleher, M. D., et al. ed.), Honolulu, Hawaii, USA, Oct. 31-Nov. 5, 126-131 (1993).
29. Takeda, Y.: Proc. 4th Int. Topical Meeting Nuclear Reactor Thermal Hydraulics, NURETH-4., Karlsruhe, Germany, (1989).
30. Takeda, Y., Samec, K., Kobayashi, K.: ASME-FED, Vol. 128, Exp. And Num. Visualization, ASME Winter Annu. Meeting, Atlanta, Georgia, USA, Dec., (1991).
31. Takeda, Y.: Velocity measurement by ultrasound Doppler shift method, "Fluid Control and Measurements", (Harada, M., Ed.), Pergamon, Tokyo, Japan, (1985).
32. Teufel, M., et al.: Flow Measur. Instrum., 3, 95 (1992).
33. Tokuhiro, A. "Experimental Investigation of a Vertical Planar Jet by Ultrasound and Laser Doppler Velocimetry", Journal of Nuclear Science and Technology, Vol. 36, No. 6, p. 540-548. June 1999.
34. Tokuhiro, A., Kimura, N., Kobayashi, J., Miyakoshi, H. : Proc. 6th Int. Conf. on Nuclear Engineering, ICONE-6, San Diego, CA, USA, CD-ROM, Session 7.09, ICONE-6058 (1998).
35. Tokuhiro, A., Kimura, N., Miyakoshi, H.: 8th Int. Topical Meeting on Nuclear Reactor Thermal Hydraulics, NURETH-8, Kyoto, Japan, Vol. 3, 1712 (1997).
36. Ultrasound Velocity Profile monitor, Model X-1, Met-Flow SA, Lausanne, Switzerland, (1992).
37. White, F. Viscous Fluid Flow, 3rd ed. McGraw Hill, New York, New York, 2006.

2. Proceedings of 2012 International Congress on Advances in Nuclear Power Plants (ICAPP-12), Chicago, IL, June 24-28th ,2012

Proceedings of ICAPP '12
Chicago, USA, June 24-28, 2012
Paper 12269

BENCHMARK STUDIES OF THERMAL JET MIXING IN SFRS USING A TWO-JET MODEL

Olumuyiwa A. Omotowa, Richard Skifton, Akira Tokuhiro
University of Idaho - Idaho Falls
1776 Science Center Drive, Idaho Falls, ID 83401
Tel :(208)-533-8151, Email:omot6968@vandals.uidaho.edu

ABSTRACT

To guide the modeling, simulations and design of Sodium Fast Reactors (SFRs), we explore and compare the predictive capabilities of two numerical solvers COMSOL and OpenFOAM in the thermal jet mixing of two buoyant jets typical of the outlet flow from a SFR tube bundle. This process will help optimize on-going experimental efforts at obtaining high resolution data for V&V of CFD codes as anticipated in next generation nuclear systems. Using the k-ε turbulence models of both codes as reference, their ability to simulate the turbulence behavior in similar environments was first validated for single jet experimental data reported in literature. This study investigates the thermal mixing of two parallel jets having a temperature difference (hot-to-cold) ΔT_{he}= 5°C, 10°C and velocity ratios U_c/U_h =0.5, 1. Results of the computed turbulent quantities due to convective mixing and the variations in flow field along the axial position are presented. In addition, this study also evaluates the effect of spacing ratio between jets in predicting the flow field and jet behavior in near and far fields.

I. INTRODUCTION

Safety is important to the design and operation of nuclear reactors and plants alike. Old and new designs have therefore incorporated advanced mechanisms to ensure safety in order to meet design certification and safety review process of the US NRC and other regulatory agencies across the world. One of the safety concerns to the Liquid Metal Fast Reactor (LMFR) designs is the thermal striping phenomena. This phenomenon describes the effect of the random temperature fluctuations of poorly mixed streams of coolant flow interactions from different sub-assemblies with temperature difference of orders of magnitude impinging on the reactor upper core structures The high heat transfer coefficient and diffusivity of liquid metals facilitates the transmission of the temperature fluctuations from the coolant to the structures[1,2,3]. A good understanding of turbulence is necessary for a detailed numerical study of thermal striping [2] .Constant interactions with the structures cause cyclic stresses due to temperature changes and are thought to eventually lead to substantial wear and fatigue of the sub-assembly top plate, upper core structures, supporting grid and other adjoining structures.

As such, the US DOE under the auspices of the Nuclear Energy Universities Program (NEUP) is interested in the collection of high resolution data from high fidelity instrumentation to guide in the design of LMFRs. In support of these, both experimental and computational studies are currently in the works to investigate the thermal-hydraulics. Two separate test facilities are currently being built for data collection purposes using mercury and sodium respectively to predict the detailed temperature and velocity fluctuations as could be seen in a LMFR. Additional experimental data exist for air (Argonne National Laboratory MAX experiments) and water (L. Tschaepe thesis), [4-7] have reported both experimental and numerical results of jet performance using either plane or asymmetric jets with different turbulence models. [7] compared the performance of three turbulence models (k-ε, RS and RNG) in the prediction of the mean flow characteristics and jet spread in the outer shear layer. In addition [2] investigated the effect of grid resolution, domain size and use of different discretization schemes on the different turbulence models. The computational study carried out by Velusamy et.al reported that a grid size of the order of 1mm gave a reasonable accurate prediction of temperature fluctuation in the fluid and solid. Also, [8] investigated the influence of velocity ratio on flow injection at the region closest to the jets and [9] studied the influence of the streamwise fluctuating velocity components.

This paper investigates thermal jet mixing of two parallel slot jets having a temperature difference (hot-to-cold) ΔT_{he}= 5°C, 10°C and velocity ratio U_c/U_h =0.5, 1 at the core outlet zone of a SFR from a numerical study perspective. The study examines the effect of temperature and velocity ratios on the fluid entrainment and the development of the jets.

Proceedings of ICAPP '12
Chicago, USA, June 24-28, 2012
Paper 12269

II. MODEL DESCRIPTION

As part of efforts to obtain high fidelity temporal and spatial data for code development, verification and validation, a high resolution numerical model is developed. Detailed analysis and modeling of the thermal stripping phenomenon requires knowledge of the multi-physics at multi-scales in order to capture the transport mechanisms. This can be achieved using finite element based codes or multi-physics codes. We explore the predictive capabilities of COMSOL and OpenFOAM to guide the modeling, simulations and design. The dimension of the test section is 260mm in height and 158mm in width (see Figure 1). Two parallel jets with 0.00635m diameter (D) each and a spacing S=2D are positioned in the middle of the tank. The dimensions were determined based on the availability of liquid sodium. For each temperature difference, two scenarios were computed. The first scenario has an iso-velocity condition while the second scenario has a velocity ratio $U_c = 0.5U_h$. The $U_h$jet exit Reynolds number was 2.92 x 10^4 , corresponding to an exit velocity of 2.3m/s Furthermore, T_c= 473K and T_h = 483K or 478K

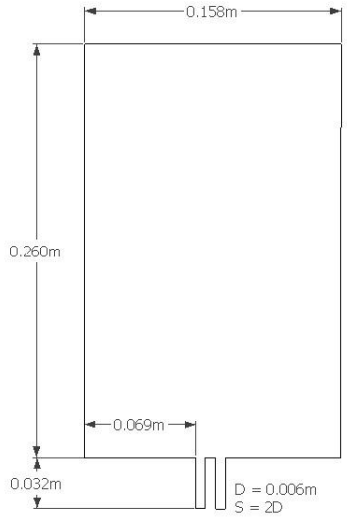

Figure 1: A schematic of the 2-D computational model

Benchmark:

Experimental data reported by Tokuhiro (1999) for a single jet using water as the working fluid was utilized to benchmark two CFD based codes: COMSOL Multi-physics 3.5a and OpenFOAM 2.1.0 for turbulent mixing in an LMFBR. A comparison of the jet half radius and decay of the centerline velocity plots were made and compared to those reported by Tokuhiro using Ultrasonic Doppler and Laser Doppler Velocimetries (UDV, LDV) techniques for measurements and data collection.

Numerical Model:

Using COMSOL (ver. 3.5a) a finite element based multi-physics code and OpenFOAM (ver. 2.1.0) the RANS equations were solved for the 2-D steady state problem. To resolve the turbulent flow, the k-ε turbulence model was employed for closure approximations in the two numerical solvers. The turbulent kinetic energy 'k'and turbulence dissipation rate 'ε' are derived from the relationships (i) and (ii) respectively.

$$\boldsymbol{k} = \frac{3}{2}(\boldsymbol{UI})^2 \qquad \text{(i)}$$

$$\boldsymbol{\varepsilon} = \frac{\boldsymbol{C_\mu^{3/4} k^{3/2}}}{\boldsymbol{0.075L}} \qquad \text{(ii)}$$

Where **U** is the inlet velocity and **I** is the turbulence intensity which for this study is taken as 0.05. C_μ is an empirical constant defined below and L is the characteristic length scale.

TABLE I: Empirical constants in the k-ε turbulence model

	C_μ	$C_{1\varepsilon}$	$C_{2\varepsilon}$	σ_k	σ_ε
Standard $k-\varepsilon$ *model*	0.09	1.44	1.92	1.0	1.3

II.A. Boundary Conditions (COMSOL)

Computational modeling was developed using the heat transfer module in COMSOL Multiphysics 3.5 with the thermal-fluid interaction subset. COMSOL solvers are based on a set of non-linear algorithms and a set of linear system solvers. The simulations were for a single jet benchmark study with water and a two-jet model. Figure 2 shows the schematic of two vertical jets into a pool. Each of the two jets nozzles has a hydraulic diameter of 0.02m and three different scenarios were investigated as will be described in the model development section. Initial pool temperature was set at 293K and inner walls are set to have thermal wall function. This function is used based on the assumption that the flow field is free of wall effects and the heat flux across the fluid-solid interface is proportional to the difference between the wall fluids on the opposite side of the viscous boundary layer.

Proceedings of ICAPP '12
Chicago, USA, June 24-28, 2012
Paper 12269

II.B. Boundary Conditions (OpenFOAM)

A similar setup was used to define the boundary conditions in OpenFOAM 2.1.0. A solver based on the SIMPLE algorithm was used. With inlet conditions of velocity and temperature to match the four scenarios stated above. The outlet conditions were set as a free surface to a pool, which entails no viscous forces. Lastly, the walls were set to represent the no-slip condition and logarithmic wall functions were used to represent the boundary layer.

Table II: Boundary Conditions for COMSOL and OpenFOAM Simulations

COMSOL

Boundary	**Type**	**Parameters**
Inlet (jet entrance)	Velocity	U= 2.3m/s
		$L_T = 0.01$
		$I_T = 0.05$
	Temperature	Jet 1= 473K
		Jet 2= 483K or 478K
Outlet	Pressure	
	No viscous stress	
	Convective flux	
Walls	Logarithmic wall function	Wall offset d_w= h/2
	Insulation/ Symmetry	

OpenFOAM

Boundary	**Type**	**Parameters**
Inlet (jet entrance)	Velocity	U= 2.3m/s
	Temperature	Jet 1= 473K
		Jet 2= 483K or 478K
Outlet	Pressure	
	No viscous stress	
	Zero Gradient	
Walls	Logarithmic wall functions	
	No slip	

Relationships between the turbulent intensity 'I_T', turbulent kinetic energy 'k', turbulent length scale 'L_T' and dissipation 'ε' have been described with equations 'i' and 'ii' respectively above. The logarithmic wall function helps to model and describe momentum transfer in turbulent flows at solid-fluid interface. It also accounts for near wall effects and pressure variations in low and high Re-number turbulence models with a clear assumption that the flow is parallel to the wall. 'd_w' describes the distance of the computational domain from the real wall.

II.C. Meshing

Both COMSOL and OpenFOAM simulations were discretized using a total of 202426 mesh points. Equal number of boundary and vertex elements was utilized. The computational grid was made fine enough to capture the physics at the regions of interest (see Figure 2). An iterative tolerance level of $1e^{-6}$ was set as the convergence criterion for both simulations.

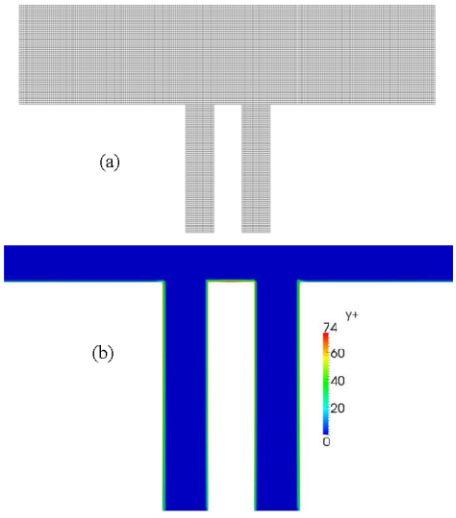

Figure 2. a) Discretization of the fluid domain: Structured mesh grid system for both COMSOL and OpenFOAM, abbreviated. b) y^+ values near the high shear regions of the flow.

III. SIMULATION RESULTS AND DISCUSSIONS

III.A. Velocity Field Analysis

Along the axial position of the flow field, two distinct variations can be observed. The jet velocity decreases, i.e. decays and also the radial spread of the jet, both due to diffusion of momentum.

Proceedings of ICAPP '12
Chicago, USA, June 24-28, 2012
Paper 12269

Leading off from the wall between the two jets there can be seen distinct characteristics about the flow. The axial velocity profile in Fig. 3 clearly shows the three characteristic regions of jet flow namely the converging, merging and combining regions.

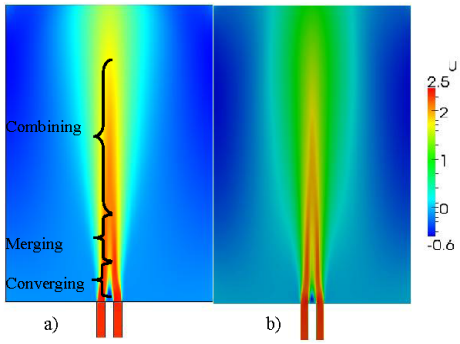

Figure 3. Surface field magnitude plot of streamwise velocity for ΔT=5°C at velocity 2.3m/s with S=2D for (a) COMSOL and (b) OpenFOAM

These profiles are compared in Figure 4 between the cases of $\Delta T_{hc} = 5°C$ and $\Delta T_{hc} = 10°C$ with $U_c/U_h = 1$.

The difference between the two codes is the way that each software computes dissipation rate, in other words, either,

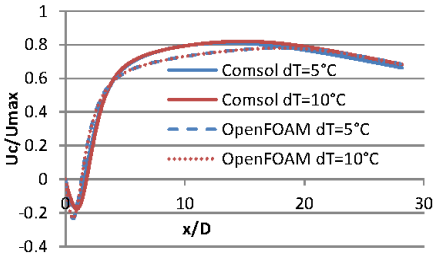

Figure 4. Centerline velocity profile for different temperatures (dT) at 2.3m/s

OpenFOAM computes the dissipation too soon or, conversely, COMSOL computes it too late. Regardless, the trends can be seen.

Point x/D=0 along the jet orifice surface to the x/D=1.65 for COMSOL is symbolic of the region where the inner shear layers of the jet begin to merge (converging region). The converging region is climaxed at the merge point for both temperature differences ΔT=5°C and 10°C. Corresponding merge point measured using OpenFOAM was approximately x/D=1.23. The region between the merge point (x/D=1.65 for COMSOL and x/D=1.23 for OpenFOAM) and combine point (x/D= 15.1 for COMSOL and OpenFOAM) represents the merging region where the mixing of the two jets begin. The combine point represents the location where the maximum streamwise mean velocity is reached along the symmetry plane and beyond that point, self-similarity is attained. Though taking a second look at Fig. 3, we identified the combine point for the ΔT=10°C case using OpenFOAM to be at x/D=16.8.

When the velocity between the two jets is varied, because the velocity of the hotter jet is twice that of the cold jet, the rate of entrainment of the surrounding fluid near the nozzle of the faster jet is higher that from the cold jet. This therefore establishes a lower pressure region between the two jets and causes the cold jet to diverge from the vertical path previously shown as seen in Fig.3. The momentum of the cold jet is entrained within the fluid between the two jets and causes both jets to diverge until they impinge the wall boundary (Figure 4).

III.B. Turbulent Kinetic Energy Analysis

The contributions of the turbulent kinetic energy are presented at different axial locations in order to observe the mean kinetic energy associated with the eddy structures. Detailed analysis is however not shown in this paper for the turbulent Reynolds stresses components.

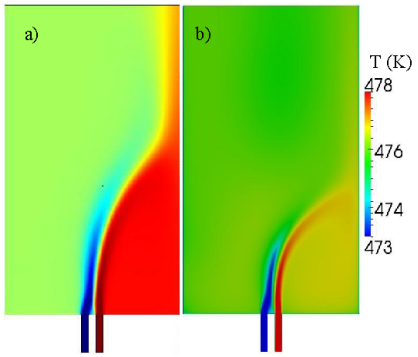

Figure 5. Temperature field for non-isothermal condition (ΔT=5°C) at V_h= 0.5 using a) COMSOL and b) OpenFOAM.

This horizontal shift is quantified by comparing the turbulent kinetic energy because TKE associates the mean kinetic energy to the eddies as shown in the two software packages at specific locations from the jet orifice (Figure 6).

The turbulent kinetic energy is measured across the flow field at axial locations (x/D=2, 5 and 10) as shown in Figure 6.

Proceedings of ICAPP '12
Chicago, USA, June 24-28, 2012
Paper 12269

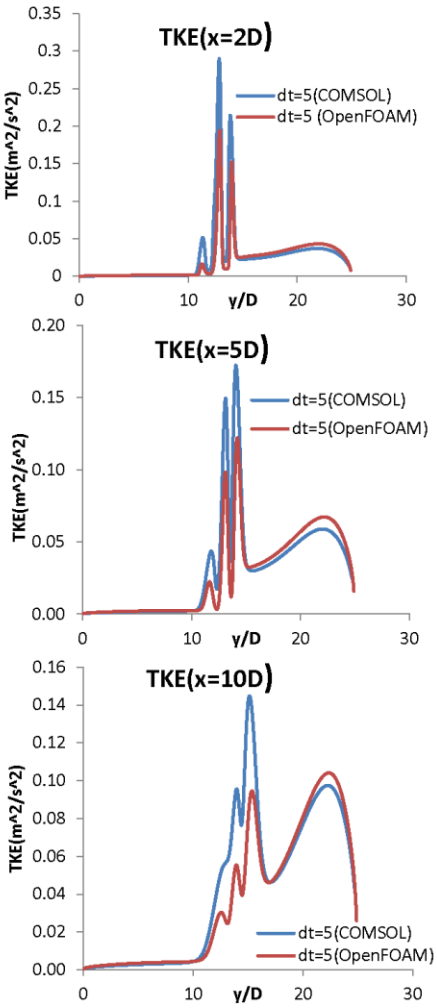

Figure 6. Turbulent kinetic energy 'k' across the flow field at x/D=2, 5 and 10 for ΔT_{hc}=5°C at U_c/U_h= 0.5 (COMSOL vs. OpenFOAM)

IV. JET SPACING

We investigated the effect of spacing between multiple jets on the flow field. Using the ΔT_{hc}=5°C at U_c/U_h=1, we simulated three cases of S=2D, 5D and 7D respectively.

The magnitude of the entrainment region of the flow increases with increased spacing, conversely the magnitude of the combining point decreasing with combining flow (see Figure 7).

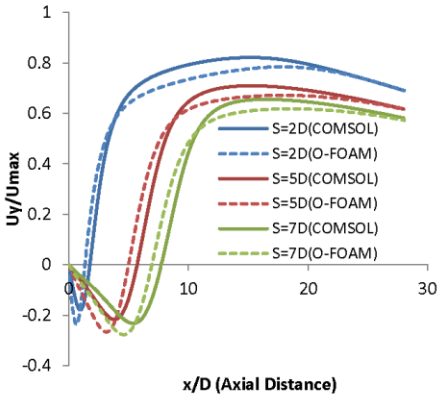

Figure 7. Effect of jet spacing on fluid entrainment in the converging region.

We investigated the effect of spacing on the streamwise velocity along the axial direction. We observed that with increasing spacing from S/D=2, 5 and 7, the converging region became further broadened thereby causing a shift in the merge point further in the near field. The trend indicated a linear relationship between the spacing and the merge point. This means that an increase in the spacing between both jets will lead to a merge point farther into the far field. It is however anticipated that at some threshold S/D value, there will be little or no interaction between the jets. The jets will then transition from a linear relationship between merge point and S/D to more of an asymptotic region.

V. CONCLUSIONS

Quantity and high quality information is needed in the design and modeling of Sodium Fast Reactors (SFR). This study has looked specifically at the thermal striping of two momentum driven jets representing the outlet flow from coolant channels within a SFR tube bundle. The present work was analyzed using two CFD codes, namely, COMSOL and OpenFOAM which are of interest to the benchmark studies. The velocity data calculated using both codes show similar trends in the decay of the centerline velocity and temperature levels. Thermally speaking, having a temperature drop between the two jets did not affect the jets momentum and/or magnitude to any

Proceedings of ICAPP '12
Chicago, USA, June 24-28, 2012
Paper 12269

considerable amount. In contrast, having the jets velocities vary by a factor of 2 caused the jets to diverge to one direction or the other. However, either case of the divergence or the vertical streaming of the jets will lead to problems within the upper plenum, causing stresses on components and eventually thermal fatigue. In addition, our investigation of the effect of spacing between multiple jets revealed that there is a shift in the merge point further in the near field and there is a linear relationship between the spacing and the merge point.

ACKNOWLEDGMENTS

This work performed at the University of Idaho was funded by US DOE under the NEUP-09-321 contract "Data collection methods for validation of Advanced Multi-Resolution Fast reactor Simulations". Also the significant contributions of our colleagues at the Center for Advanced Energy Studies (CAES) to this paper are gratefully acknowledged.

NOMENCLATURE

D – diameter of the jet
ε – turbulent dissipation rate
I_T – turbulence intensity
k – turbulent kinetic energy
L_T – turbulent characteristic length scale
S jet spacing
T temperature
$U_{c,h}$ – jet velocity (hot or cold)
x,y – axial position, transverse position
y^+ - dimensionless wall distance (u^*y/ν)

REFERENCES

1. A.T. TOKUHIRO and N. KIMURA, "An Experimental Investigation on Thermal Striping: Mixing Phenomena of a Vertical Non-buoyant Jet with Two Adjacent Buoyant Jets as Measured by Ultrasound Doppler Velocimetry," Nuclear Engineering and Design, **188**, 1, p.49, (1999).

2. K VELUSAMY et al, "CFD Studies in the Prediction of Thermal Stripping in an LMFBR, " 2007 OECD-NEA Report", p. 253, (2007).

3. D. TENCHINE, "Some Thermal-Hydraulic Challenges in Sodium Cooled Fast Reactors," Nuclear Engineering and Design. **240**, p.1195, (2010).

4. A. TOKUHIRO, "Experimental Investigation of a Vertical Planar Jet by Ultrasound and Laser Doppler Velocimetry," Journal of Nuclear Science and Technology, **36**, 6, p.540, (1999).

5. M. WAKAMATSU et al, "Attenuation of Temperature Fluctuations in Thermal Stripping," Journal of Nuclear Science and Technology, **32**, 8, p.752, (1995).

6. E.A ANDERSON and R.E SPALL, "Experimental and Numerical Investigation of Two-Dimensional Parallel Jets," *Journal of Fluid Engineering*, **123**, 401 (2001).

7. J.C.S. LAI and A. NASR, "Two Parallel Plane Jets: Comparison of the Performance of Three Turbulence Models" *Proc. of the Institution of Mechanical Engineers*, June 1, 1998, 212, p. 379, Part G: Journal of Aerospace Engineering , (1998)

8. N. FUJISAWA, K. NAKAMURA and K. SRINIVAS, "Interaction of Two Parallel Plane Jets of Different Velocities," *Journal of Visualization*, **7**, 135 (2004).

9. Tawfik J.A and Arimilli R.V, "Influence of inlet fluctuations on the development of the turbulent two-stream mixing layer", *Proc. of COMSOL conference* , Boston, (2010)

10. L.TSCHAEPE et al, "Computational Fluid Dynamics Simulations of the Jet Momentum Transport in Liquid Metals, "*Proc of 8th Int. Topical Meeting on Nuclear Thermal-Hydraulics, Operations and Safety (NUTHOS-8),* Shanghai, China, October 10-14, 2010.

11. R.K CHANDRAN et al, "Investigation of the Thermal Stripping in Prototype Fast Breeder Reactor using Ten Jet Water Model," Heat Transfer Engineering, **32**, 5, p.369, (2011).

12. H. ELBANNA and S. GAHIN, "Investigation of Two Parallel Jets," Journal of American Institute of Aeronautics and Astronautics (AIAA), **21**, 7, p. 986, (1983).

13. N. KIMURA et al, "Experimental Investigation on Transfer Characteristics of Temperature Fluctuation from Liquid Sodium to Wall in Parallel Triple-jet," International Journal of Heat and Mass Transfer, **50**, p.2024, (2007).

3. Proceedings of 15th International Topical Meeting on Nuclear Reactor Thermal-Hydraulics (NURETH-15), Pisa, Italy, May12-17, 2013

The 15th International Topical Meeting on Nuclear Reactor Thermal - Hydraulics, NURETH-15
Pisa, Italy, May 12-17, 2013

NURETH15-492

POWER INVESTIGATIONS ON THE TWO-PHASE BEHAVIOR AND INSTABILITY IN AN EXPERIMENTAL REACTOR CAVITY COOLING SYSTEM WITH WATER

D. Lisowski[1], O. Omotowa[2], A. Tokuhiro[2], M. Anderson[1], M. Corradini[1]
[1]University of Wisconsin – Madison 1500 Engineering Drive, Madison, WI 53711. USA.
[2]University of Idaho – Moscow.

dlisowsk@wisc.edu

ABSTRACT

To address the issue of long-term decay heat removal, advanced high temperature gas reactors (HTGR) can utilize passive cooling systems. With water as the working fluid, these systems operate in passive mode during an accident transient, providing heat transport from the reactor pressure vessel (RPV) in the cavity to the outside atmosphere entirely through natural circulation. Of the designs under consideration, the water-cooled reactor cavity cooling system (RCCS) has emerged as a leading concept for decay heat removal in the Next Generation Nuclear Plant (NGNP). A primary concern is the development of flow instabilities arising from a local perturbation, with the potential for undesirable effects on heat removal performance. To evaluate the performance and instability regions in a water cooled RCCS design, a scaled experimental facility was constructed modeling a 5° sector and ¼ axial extent of a full scale concept prototype. Instrumented to appropriately guide experimental practices, measurements of key thermal hydraulic data such as water temperatures, pressure drop, mass fluxes, and void fractions are presented. Experiments for two-phase conditions characterize the magnitude and behavior of flow oscillations at varying power levels. An evaluation of the two-phase behavior is given, with continued testing in progress.

1. INTRODUCTION

Passive heat removal systems provide the opportunity to remove decay heat from a nuclear reactor pressure vessel (RPV) to an ultimate heat sink without the need for off-site AC or on-site DC power. Recent design efforts have identified the Reactor Cavity Cooling System (RCCS), as a natural circulation system that offers simplicity and safety with a high level of performance. To confirm the viability of the RCCS as a long-term solution for passive decay heat removal continued progress in investigating the thermal-hydraulic behaviour, performance, and thermal stability bounds must be made.

2. RCCS OPERATION

Using water as the working fluid, the RCCS operates in passive mode during an accident condition, rejecting heat from the RPV to the atmosphere via a system of water tubes, cooling panels, and water storage tanks. As the water rises in temperature and reaches saturation, the release of steam into the atmosphere serves as the ultimate heat sink. The Nuclear Regulatory Commission (NRC) has indicated that for water cooled passive safety systems, a 72-hour cooling inventory must be available before water storage tanks can be replenished. Since the design is

The 15th International Topical Meeting on Nuclear Reactor Thermal - Hydraulics, NURETH-15 NURETH15-492
Pisa, Italy, May 12-17, 2013

still under active development, a concept has been drafted by the authors using openly available literature, with the concrete containment of the General Atomic Modular High Temperature Gas Reactor (MHTGR) as the basis. Details of our concept design and scaling methods are documented in previous publications (Lisowski, 2011).

3. NATURAL CIRCULATION STABILITY

Due to the inherent nature of buoyancy driven natural circulation loops, flow instabilities must be considered when designing and analyzing a system. At a stable-steady state condition, the driving forces (buoyancy) and losses (frictional) balance in equilibrium. However, when a perturbation occurs in the system, this balance can be upset and oscillations can arise and propagate. Such a perturbation is readily introduced when operating at two-phase conditions, as these systems are transient dominated. Flow instabilities will arise under certain conditions, and can be undesirable in process systems since a continued oscillation may cause forced mechanical vibrations, effect local and integral heat transfer characteristics, and even induce boiling crises, such as CHF, burn out, dry out (Boure, 1973).

3.1 Type-I & Type-II Instabilities

Integral to their design, natural circulation loops provide relatively little frictional or minor restrictions to flow within the pipes. For a perturbation arising within the loop such as a change in void fraction, the influence by the change in driving head creates a temporary flow excursion, and can result in a flow oscillation that peaks at several times the original flow rate. Classified as 'Type-I', they are occur at low power and low pressure conditions, (van der Hagen, 2000), and observed most often as a result of flashing phenomena or fluctuations in hydrostatic head that begin in the unheated portions of a loop.

The presence of two-phase flow within a natural circulation loop can form a dynamic coupling between multiple feedback effects and the integral system behavior. Dependent on the changes in single and two-phase pressure drop, they can exhibit a high level of complexity due to non-linear effects. These 'Type-II' instabilities are most frequently introduced at high powers and low flow conditions in the form of flashing-induced DWO, pressure waves, thermal oscillation, among others.

3.2 Phenomena Induced Instabilities

Flow instabilities occur as the result of a perturbation, and are not themselves cause for flow excursions. Thus they require some other mechanism, or phenomena, to induce a perturbation and resulting onset of flow instability. One example is when a condition exists that upon traveling through a heated section, the fluid temperature becomes greater than the saturation temperature at the exit of the chimney. The driving hydraulic pressure suppresses a change in phase that would otherwise have occurred, thus it can exits the channel without ever entering a gas phase and result in boiling. As the fluid rises in elevation into the unheated sections, it may reach its local saturation temperature and instantaneously flash void. This process of vapor generation is not created by heat from the outside, but instead a change in operating conditions due to the decrease in hydrostatic head. (Zhang, 2004). The result can induce a pure flashing instability, or a flashing-induced density wave oscillation (DWO).

The 15th International Topical Meeting on Nuclear Reactor Thermal - Hydraulics, NURETH-15 NURETH15-492
Pisa, Italy, May 12-17, 2013

4. EXPERIMENTAL FACILITY

The ¼ scale RCCS constructed at the University of Wisconsin – Madison serves primarily to investigate accident scenarios prototypic of a ¼ scale passive decay heat removal system originally designed for as part of the GA-MHTGR. Standing 7.6 m tall, a 3 m heated test section serves as the heat source, and a 1,200 L water-mixing tank as the heat sink. The test section is comprised of three parallel riser tubes, separated by fins welded at their centerline. Radiant heaters impose a heat flux onto a three riser tube and fin test section, and is able to achieve peak heat flux and power levels of 25 kW/m^2 at 42.5 kW. Key specifications for results presented in this paper are provided below, with a facility overview in Figure 1.

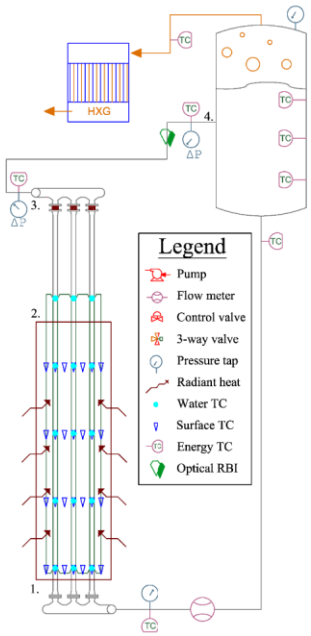

Figure 1: Facility diagram. Points 1 – 2 (unheated riser) , 2 – 3 (heated riser), 3 – 4 (chimney)

The unheated length for the UW-RCCS facility is split among a riser (1.92 m) and chimney segment (0.6 m). While the riser is vertical along the entire length, the chimney includes 3 elbows and a 0.98 m horizontal leg.

Several high-resolution measuring devices were mounted at different locations in the test facility to capture, acquire and record key thermal-hydraulic phenomena. This includes but not limited to an dual tip void fraction probe, magnetic flow meter and pressure transducers.

Table 1: Experiment specifications

Working fluid	water	Unheated length	2.53 m
System pressure	atmospheric	Heated length	3 m
Heat flux	7.67 – 12.52 kW/m^2	D_h of riser, chimney	5.08cm, 10.16cm
Inlet subcooling	19.5 °C	No parallel risers	3

4.1 Local void fraction measurement

Void fraction is one of the key physical parameters that can guide the determination of the flow distribution under two phase flow conditions. Increasing void fraction could have significant changes on the dynamics of the system and affect the heat transfer characteristics. In this study, we used the local void fraction measurements by use of a double tip probe to guide our knowledge of flow distribution in the thermal-hydraulic facility. The device was placed in a vertical section of the chimney to ensure phase stratification would not occur and prevent the measurement of natural bubble behavior.

The probe is an optical, double tip, intrusive probe capable of detecting phase changes based on Snell's law of refraction. The double sapphire tips each has a diameter of 25μm and the spacing between both tips is 500μm. Detailed operating principle and accuracy of the optical probe for two-phase flow measurements has been reported in work performed by (Ferrand, 1987) and (Francois, 2012). Using statistical methods, local void fraction, bubble diameter and interfacial area at superficial gas velocities are measured and analyzed. Data from each optical fiber was sampled at 2MIIz and acquired over a 10 second period for the full duration of each test, from which measurement of time averaged void fraction could be determined

5. TWO-PHASE INVESTIGATIONS

Investigations with the ¼ water cooled RCCS at UW-Madison have been on-going in recent months, and will ultimately encompass a wide range of test conditions and experimental parameters. Characterization of the facility during single phase, steady-state conditions has been completed, and results presented in previous publications (Lisowski, 2012). Recent efforts transitioned to a focus on two-phase conditions, where the system was brought to saturation and subsequent boiling. The results presented in this paper will focus on outlining the baseline behavior of our scaled water RCCS, with a first analysis on a power variation parametric.

5.1 Test procedure

Initial scoping tests at two-phase conditions indicated that the RCCS behavior can be dramatically affected by minimal variations in initial and boundary conditions. The extreme sensitivity exhibited by the facility required establishing a rigid procedure and strict set of initial conditions if high quality and repeatable data was to be obtained.

Two-phase testing began with defining baseline conditions, which were derived from expected operating parameters of the full-scale concept design and logistical considerations for experimental practices. An initial 80% tank inventory (measured to within 4mm), ≈70 °C bulk system temperature, and a 60 minute ramp to the test-specific maximum heater power defined the initial conditions for each test. The heat up period from 70 °C allows the system time to

recover and stabilize from any nonuniformities present, and spans a nominal 5 hours before reaching boiling conditions. To repeatedly capture the approach to boiling, a thermocouple, placed at the steam outlet of the water storage tank, triggers the cold leg of the condensation system once it exceeds 10 °C above ambient. With this trigger, control parameters are held constant for a 4 hour minimum duration, after which the heaters are ramped down over a 10 minute period and power shut off. This procedure was maintained for several experiments to confirm procedures and established repeatability bounds for the facility.

5.2 Power variation results

A test series composed of four tests is presented, with a single variable of integral power investigated for its role on system behavior. Powers of 12.55, 15.19, 17.84, and 20.49 kW of supplied heater power, which resulted in a total heat flux deposition of 7.67, 9.29 10.90, and 12.52 kW/m^2, respectively were selected based on scale levels of decay heat flux of the prototype reactor.

5.2.1 Low Power

At the lowest power investigated, 12.55 kW (7.67 kW/m^2), the system exhibited small amplitude oscillations in the system mass flow rate, Figure 2, with fluctuations reaching maximum values of ±12% of the mean flow. Void fractions measured an average 0.42% with a standard deviation 0.62, thus the flow pattern can be characterized as bubbly flow dominated.

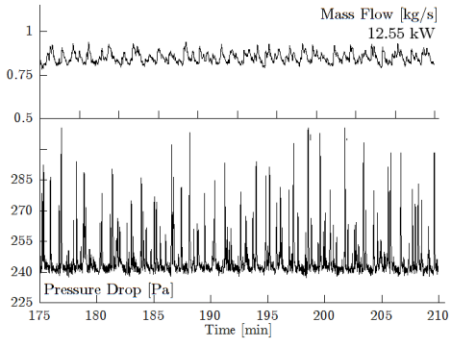

Figure 2: Mass and pressure, 12.55 kW

Nayak (2008) has suggested that amplitude changes of below ±10% can be considered 'stable', while others recommend even a higher threshold of ±30%. The bubble formation did not define any characteristic oscillation frequency for the bulk system behavior, with stable responses in all temperatures and system flow. Static pressure measurements remained within ±1.5% of the nominal value, and indicate that the transient void formation was not sufficient to create large swelling and result in large static pressure fluctuations. Pressure drop measurement along the chimney confirmed the bubble formation and lack of periodicity, Figure 2.

The 15th International Topical Meeting on Nuclear Reactor Thermal - Hydraulics, NURETH-15 NURETH15-492
Pisa, Italy, May 12-17, 2013

5.2.2 Medium Power

At power levels of 15.19 kW (9.29 kW/m^2), early stages A) resemble those observed at low power, with small amplitude fluctuation that lack a definitive period.

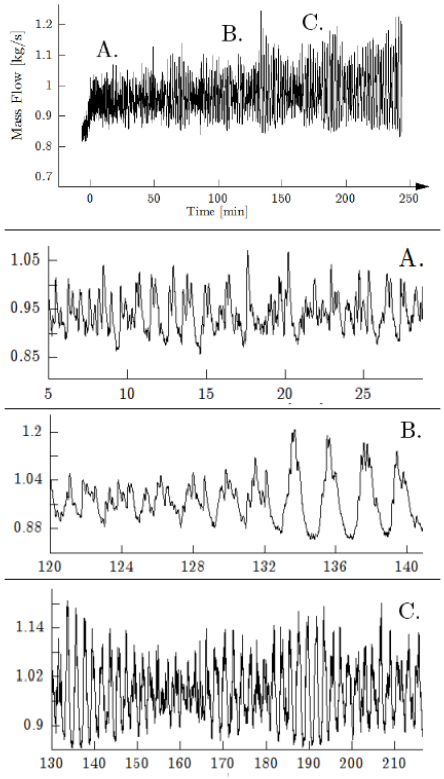

Figure 3: Transient behavior of mass flow rate 15.19 kW. A) chaotic nucleate boiling, B) multimode nucleate / voiding, C) growth and decay of dominant behavior

As the system is allowed to develop with time, voiding in the chimney section is first observed at B) and results in short windows of periodic oscillations in the system flow rate. As bubbles accumulate in the chimney region, they begin to coalesce and form larger voids, aiding in the growth of a full periodic oscillation, and can be observed by smaller peaks within the larger oscillation cycle. The system then enters a multimode region, C), characterized by coupling effects from the combined nucleate boiling and large voiding that falls in and out of defined oscillation periods, resulting in a growth, decay, and return of periodicity. With continued time,

the large voiding becomes more dominant, eventually suppressing the localized fluctuations observed at the start of boiling from small bubbles.

The region that occurs in B) at 15.19 kW has been observed by Wu (1995), who identified the mechanism as 'thermal hydraulic oscillations', whose oscillation periods was classification as either chaotic or periodic 2 – 5 fundamental frequencies per period. These fundamental frequencies present themselves most readily in the pressure drop across the chimney by 4 – 6 distinct peaks. Chiang et al. (2005) classified this as 'natural circulation oscillation', and suggests they are unique to natural circulation loops that contain horizontal sections or bends along the chimney length.

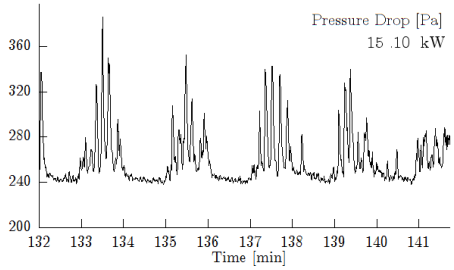

Figure 4: Fundamental frequencies in ΔP oscillations

Experiments by Subki et al. (2004) observed natural circulation oscillations due to hydrostatic head fluctuations in experiments operating at atmospheric conditions. They described initiating criteria as a time varying accumulation of vapor in the chimney region. If such a condition can exists, sufficient accumulation will create a drop in hydrostatic head pressure in that region and subsequent increase in system flow. Upon refilling with a liquid phase, the head increases and the process repeats.

5.2.3 High Power

At high powers, 17.84 and 20.49 kW (10.90 and 12.52 kW/m^2 respectively), system flow oscillations were observed immediately upon the onset of boiling. The flow rate was characterized by full periodic flow excursions that returned to a constant and stable baseline, and followed a smooth sinusoidal shape, Figure 5. Mass flow rate fluctuations on the order of 145% and 192% were observed at heat fluxes of 10.90 and 12.52 kW/m^2, with average and peak void fraction exceeding 5% and 20%, respectively, for both tests.

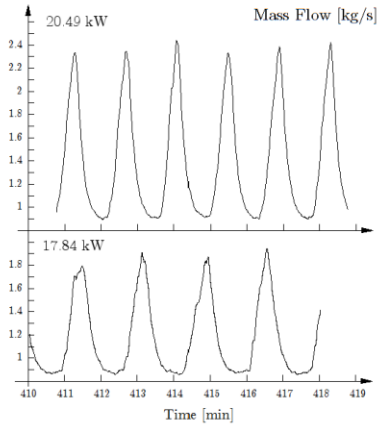

Figure 5: Periodic sinusoidal flow oscillations observed at 17.84 and 20.49 kW

Temperatures of the bulk fluid experience out-of-phase oscillations in the chimney region, and in-phase oscillations in the heated section, indicating that void formation occurs in the adiabatic chimney and not the heated section.

Additionally, the pressure drops in the chimney response in-phase with the system flow rate, confirming the boiling boundary location and suggesting that the mechanism of flashing was present. A summary of results from the four power variation tests are given in Table 1.

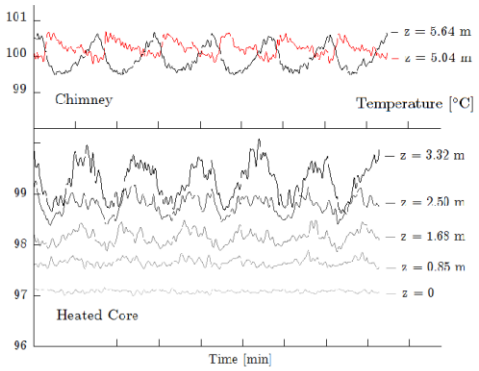

Figure 6: In-phase temperature oscillations along heated section,
out-of-phase oscillations in adiabatic section of chimney. 20.49 kW

Table 2: Summary of power variation

	12.55 kW	15.19 kW	17.84 kW	20.49 kW
q'' [kW/m^2]	7.67	9.29	10.90	12.52
α_{mean} [%]	0.427	0.934	2.218	4.975
α_{max}	2.861	6.272	17.43	30.56
σ	0.439	0.895	3.504	7.850
m_{mean} [kg/s]	0.85	0.97	1.17	1.35
$\Delta m/m$	14.6	28.3	146.6	199.1
$\Delta P_{drop}/P_{drop}$	36.4	62.5	139.7	196.5
$\Delta P_{static}/P_{static}$	2.10	2.53	4.47	6.58
T [s]	-	120.6	104.3	86.30
τ_{system}	-	112.9	95.39	82.67

5.3 Phase Portrait

The chaotic and periodic classification of the behavior at varying powers can be further examined by a drawing a phase portrait, which allows for the illustration of any coupling or relation between system variables. The flow rate and pressure drop were chosen, and are presented in Figures 7. These present a clear behavior at high powers, indicating an elliptically shaped operating region for flow and pressure parameters. The illustration at lower powers lacks clarity in defining a discrete operating region, with flow-pressure coupling observed at all values within the measurement bounds.

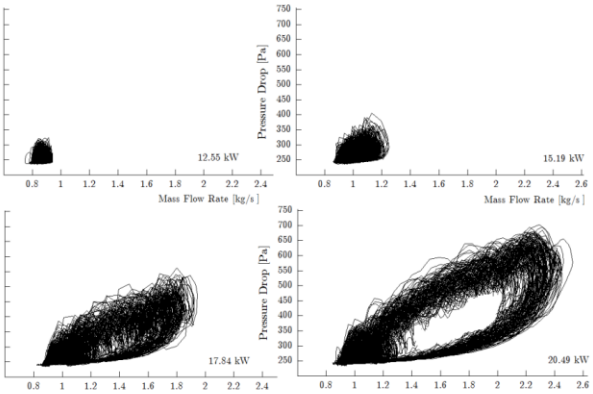

Figure 7: Phase portraits. Chimney pressure drop & flow rate.
Chaotic: a) 12.55 kW, b) 15.19 kW Periodic: c) 17.84 kW, d) 20.49 kW

The 15th International Topical Meeting on Nuclear Reactor Thermal - Hydraulics, NURETH-15 NURETH15-492
Pisa, Italy, May 12-17, 2013

5.4 Spatial – Temporal Analysis

The behavior observed at all but the lowest heat flux can easily be characterized by periodic flow and large void phenomena in an adiabatic chimney. Several two-phase behavior results have been published on water cooling natural loops that exhibit similar behavior. Based on the work of Bouer (1973) and Furuya (2005), they proposed criterion for identification of these instabilities which assumes a typical period of DWO, which they defined as one-and-a-half to two times the fluid transit time through the chimney region. If the experimental oscillation period agrees with this transit time, Eq. (1), they proposed that it can indicate a prototype characteristic of flashing induced density wave oscillations. They found correlation with over 150 experimental data points to this trend, regardless of pressure, heat flux, or inlet subcooling.

$$\tau_{chimney} = \frac{V_{chimney}}{Q_{bulk}} \tag{1}$$

Marcel et al. (2010) proposed a modification to the typical period for a DWO to include half of the heated core along with the chimney, Eq. (2), where Q_{bulk} is the mean volumetric flow rate of the fluid measured at a subcooled section, $V_{chimney}$ is the volume within the chimney piping, and V_{core} is the total volume of the heated section. Agreement of this transit time with the measured oscillation period would also suggest a density wave character of flashing induced oscillations.

$$\tau_{channel} = \frac{V_{chimney} + 0.5V_{core}}{Q_{bulk}} \tag{2}$$

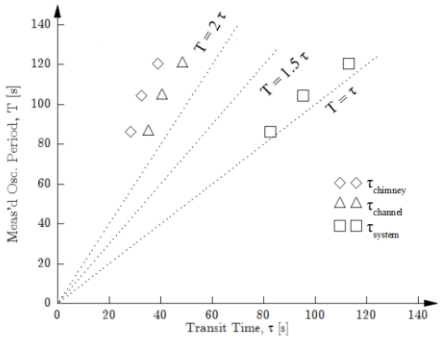

Figure 8: Characteristic transit times and measured period

The oscillation period of experimental data at 12.55, 17.84, and 20.49 kW was compared against these transit times, and presented in Figure 8. Transit times defined by both the chimney and channel region did not match the criteria established for DWO, and fell outside the bounds of the 1.5 – 2 transit times region. The authors have identified a characteristic transit that that represents the observed flow oscillations as being nearly that of the transit time for a subcooled fluid to travel the length of the entire system, water tank outlet to tank inlet, Eq. (3).

$$U_{system} = \frac{\forall_{downcomer} + \forall_{core} - \forall_{chimney}}{Q_{bulk}} \tag{3}$$

6. CONCLUSION

The ¼ scale RCCS at UW-Madison has been investigated for the effects of power variations at saturation conditions in the ranges of 7.67 – 12.52 kW/m^2. Stable two-phase flow was observed at low heat fluxes, with nucleate bubbly flow driving fluctuations in flow rate that did not vary more than +14%. Upon increasing the power to 9.29 kW/m^2, the system exhibit three primary mechanisms of oscillations: bubbly flow fluctuations, natural circulation oscillations due to hydrostatic head fluctuations with individual contributions from fundamental frequencies, and initial periods of large void formation. At the highest powers, smooth sinusoidal oscillations were observed that suggest a flashing behavior. Characteristic transit times were compared to oscillation periods, and it was concluded that DWO were not observed at any of the tests conducted. From phase portraits, the behavior at low powers was defined to be chaotic, while those at higher power have been defined as periodic. Continued efforts are ongoing, with investigating into the system behavoir at higher pressures, varying system inventories, and restricted inlet conditions.

7. ACKNOWLEGDEMENTS

The authors wish to acknowledge support from the Department of Energy, with funding provided under the project number NEUP 09-202.

8. NOMENCLATURE

D_h	Hydraulic dia.	[m]
m	Mass flow rate	[kg/s]
q"	Heat flux	[kw/m^2]
Q	Flow rate	[m^3/s]
T	Period	[s]
$\forall$	Volume	[m^3]
Greek		
α	Void fraction	[%]
σ	Standard deviation	
τ	Transit time	[s]
Subscripts		
Bulk	System averaged	
Channel	Core – chimney	
Chimney	Unheated length	
System	Tank out → Tank in	

9. REFERENCES

[1] "Preliminary Safety Information Document for the Standard MHTGR" HTGR-86-024, Volume 1, Amendment #13. US Department of Energy, (1992)

[2] Bouré , J.A., Bergles, J.E., Tong, L.S., "Review of two-phase flow instability". *Nucl. Eng. Des.* Vol. 25, pp. 165–192, (1973)

[3] Chiang, J.H., Aritomi, M., Mori, M., "Fundamental study on thermo-hydraulics during start-up in natural circulation boiling water reactors, (ii) natural circulation oscillation induced by hydrostatic head fluctuation". *J. Nucl. Sci. Technol.* Vol. 30-3, pp. 203–211, (1993)

[4] Ferrand, F., Dautrey, B., et al., "Process in technology and signal treamente of mono and bi-optical probes for two phase flow measurements", European Two-Phase Flow Group Meeting, Trondheim (1987)

[5] Francois, F., Garnier, J., Cubizolles, G., "A new data aquisition system for binary random signal application in multiphase flow measurements", *Meas. Sci. Technol.*, Vol. 14, pp. 929-942, (2003)

[6] Furuya, M., Inada, F., van der Hagen, T.H.J.J., "Flashing induced density wave oscillations in a natural circulation BWR – mechanism of instability and instability map", *Nucl. Eng. Des.*, Vol., 235, pp. 1557 – 1569, (2005)

[7] Lisowski, D., et al., "Experimental Studies of NGNP Reactor Cavity Cooling System with Water", *Proc. of the 2011 ICAPP*,, Nice, France (2001)

[8] Lisowski, D., et al., "Results from a Scaled Reactor Cavity Cooling System with Water at Steady State", *Proc. of the 2012 ICAPP*, Chicago, IL US, (2012)

[9] Marcel, C.P., et al., "Experimental investigations on flashing-induced instalibities in one and two-parallel channels: a comparative study", *Exp. Thermal and Fluid Science*, Vol. 34, pp. 879 892, (2010)

[10] Nayak, A. K., & Vijayan, P. K., "Flow instabilities in boiling two-phase natural circulation systems: A review", *Science and Technology of Nuclear Installations*, 1–15. (2008).

[11] Subki, M. H., Aritomi, M., et al., "Multi parameter effect of thermohydraulic instability in a natural circulation boiling water reactor during startup", *JSME International Journal*, Series B, Vol. 47, No. 2, pp. 277 – 237, (2004).

[12] van der Hagen, T.H.J.J., at el., "Reactor experiments on type-I and type-II BWR stability", *Nucl. Eng. Des.*, Vol. 200, pp. 177-185, (2000).

[13] Wu, C.Y., Wang, S.B., Pan, Chin., Chaotic oscillations in a low pressure two-phase natural circulation loop under low power and high inlet subcooling conditions. *Nucl. Eng. Des.*, Vol. 162, pp. 223-232, (1996)

[14] Zhang, Y.J., X.T. Yang, and S.Y. Jiang. "Analysis of Special Two-Phase Flow Instabilities at Full Power Natural Circulation Reactor Conditions." *Kerntechnik.* 69.4, 149-153 (2004)

4. Published in International Journal of Multi-phase Flow, January 2014

International Journal of Multiphase Flow 60 (2014) 135–148

Contents lists available at ScienceDirect

International Journal of Multiphase Flow

journal homepage: www.elsevier.com/locate/ijmulflow

Influences of boil-off on the behavior of a two-phase natural circulation loop

D.D. Lisowski *, O. Omotowa [1], M.A. Muci, A. Tokuhiro [1], M.H. Anderson, M.L. Corradini

University of Wisconsin – Madison, 1500 Engineering Drive, Room 839, Madison, WI 53706, USA

ARTICLE INFO

Article history:
Received 6 May 2013
Received in revised form 15 December 2013
Accepted 18 December 2013
Available online 28 December 2013

Keywords:
Two-phase
Natural circulation
Boil-off
Water storage tank
Passive safety

ABSTRACT

This experimental study investigates the thermal hydraulic behavior and boiling mechanisms present in a natural circulation loop experiencing boil-off. Extended duration tests with inventory loss were conducted to examine the transient behavior of a test loop under constant heat load. Five different stages of natural circulation flow were identified: single-phase heating, transitional nucleate boiling, hydrostatic head fluctuations, stable two-phase flow, and geysering. The water level in the storage tank was observed to play an important role in the stability of the system as it directly influences the hydrostatic pressures and, therefore local saturation temperatures. It would found that changes in inventory can shift the boiling boundary to different segments of the loop, whose geometry and orientation dictate the flow regime and ultimately the system behavior. With continued loss of inventory, a break in the loop occurs and induces flow stagnation with geysering in the heated region. Further operation results in severe degradation of heat removal, with a potential for burn out and possible structural damage. For safety-related applications, the venting of steam can extend the long-term cooling time window for heat removal and is of significant practical interest.

Published by Elsevier Ltd.

1. Introduction

Natural circulation loops have been widely adopted in industrial settings, relying on natural forces (e.g. gravity and density difference) to efficiently transport heat without the need for active power sources. In areas of nuclear engineering, they have emerged as a leading focus area for passive safety, offering a solution to long-term core cooling and decay heat removal (Pope et al., 2009). With a robust design, these systems have become an integral part of the power plant design which requires no human intervention during an accident transient (Burgazzi, 2007).

Of the concepts under consideration, several use water as a primary working fluid where operating conditions are expected to reach saturation and subsequent two-phase flow. The venting of steam into the atmosphere serves as the ultimate heat sink, and hence these designs operate at low pressures.

While offering an extensive array of benefits, these systems often exhibit complex and uncertain thermal hydraulic behavior. Of primary concern is the development of flow instabilities: both global (e.g. continuous and increasing flow oscillations) and local (e.g. possible burn out or material fatigue). Additionally, the system will undergo dynamic changes in behavior and performance as the coolant inventory decreases due to boil-off from venting steam. To ensure successful application of these systems, this oscillating behavior must be understood. This includes, but is not limited to, knowledge of the behavior and magnitude during prototypic conditions with an ultimate goal of creating a shift from uncertainty to predictability.

Several studies have addressed the thermal hydraulic analysis of boiling water natural circulation, including both fundamental and application focused investigations. Chen et al. (2001) investigated the hysteresis effect on a double channel natural circulation loop, which suggested that the operating state to be a path function that depended not only on the operating conditions but the process approaching it. Moreover, multiple operating states were found to be theoretically possible for a given heating power at low pressures and large inlet subcooling cooling (Jeng and Pan, 1994).

Experimental validation of a cooling loop for passive safety of the AES-2006 nuclear plant design (Bakhmet'ev et al., 2009) was performed with effects of varying water levels in a bulk storage tank, including considerations for repeated replenishment. Additionally, the natural circulation behavior of a VVER-440 with a small break, loss-of-coolant accident (Puustinen, 2002) considered the transition from single to two-phase, with a focus on influences from the break size. While these studies presented a general insight into the heat removal performance with changes in inventory, the quantitative details specific to the boiling mechanisms, modes of operation, and thermal hydraulic behavior were not

* Corresponding author. Current address: 9700 South Cass Ave Argonne, IL 60439-4840, USA. Tel.: +1 630 252 1128.
E-mail address: dlisowski@anl.gov (D.D. Lisowski).
[1] Address: University of Idaho, Idaho Falls, ID 83402, USA.

0301-9322/$ - see front matter Published by Elsevier Ltd.
http://dx.doi.org/10.1016/j.ijmultiphaseflow.2013.12.005

given. Additionally, their geometry for natural circulation is significantly different from our design.

In other more relevant studies, a role of an auxiliary tank in semi-closed two-phase natural circulation loops (Lee and Kim, 1999; Kim and Lee, 2000) was presented. Fundamental phenomena specific to two-phase flow was examined, where an emphasis was placed on a mapping of the flow stability. Six different modes of loopwise natural circulation were identified by varying heat flux, inlet subcooling, and expansion tank line restrictions. The work observed velocity and enthalpy fluctuations at the heater exit propagating along the loop, directly affecting the flow at the heater inlet. Though the instantaneous system pressure was not fixed due to the inertia of the liquid column, a constant time averaged pressure head (inventory) was imposed due to an outflow condition in the tank and short test durations.

The studies by Lee and Kim (1999) and Kim and Lee (2000) are more relevant to our investigations because of the similarity in natural circulation geometry. However, they did not examine the case for varying levels of hydrostatic head in their auxiliary tank, a feature that parallels our water storage tank and is of key interest with respect to heat and mass transfer. Therefore, in this paper, the authors will address the thermal hydraulic behavior of a natural circulation test loop undergoing a reduction in inventory, with a focus on the boiling mechanisms and two-phase flow regimes.

2. Experiment description

The test facility as shown in Fig. 1 is housed within a 7.6 m tall structure and contains a downcomer (DC), three parallel channels (risers), two header plenums, chimney, and a water storage tank. The volume of all the network piping is 120 l, a factor of ten smaller than the water storage tank. The total form loss of the network piping was determined from separate testing at isothermal forced flow conditions. Represented as the pressure loss coefficient, $K = 2\Delta P/\rho u^2$, where ΔP is the frictional pressure drop, ρ the fluid density, and u the inlet velocity. A summary of values across the loops segments are provided in Table 1.

The risers extend 5.4 m in total length, but only the lower 3 m resides within the heated core. Power is delivered from thirty-four radiant heaters, supplying up to 42 kW at 25 kW/m^2. Experiments presented in this paper maintained a constant 15.19 kW, uniformly imposed from the heaters surface onto the cooling tubes. Effects from asymmetric heating profiles and variations in integral power can be found in previous work by the authors (Lisowski et al., 2013a). It was found that during asymmetric heating conditions in single phase, the skewed heat flux profile did not incur a large split in the flow distribution among parallel channels. This was due to combined effects of both convection inside the cavity, and conduction along the cooling fins between the riser tubes.

Above the core outlet, the unheated region (2.5 m) is split among the upper risers (1.9 m), a common outlet header plenum, and single chimney pipe (0.6 m) before finally entering the water storage tank. While the risers are vertical along their entire length, the chimney contains multiple bends that result in both horizontal and vertical segments, Fig. 2.

The heated core is heavily insulated to reduce parasitic losses to the environment, which is built upon a matrix of Microtherm® LW-Board and Pyrogel-XL. Networking plumbing and water storage tank are insulated by KFlex, a closed cell elastomeric material for use in low temperature heating, ventilation, and air-conditioning (HVAC) applications. Evaluations of the heat loss from the core enclosure and networking plumbing indicate that a nominal 84% of the supplied heater power is ultimately transferred into the working fluid. This was confirmed by an evaluation of thermal power within the heated region, which followed a form of the steady-flow thermal energy equation, $Q = \dot{m}C_p\Delta T$ (Q is the power within the test section, $\dot{m}$ the system mass flow rate, C_p the fluid specific heat at inlet conditions, and ΔT the temperature rise across the test section). References in the text to 'inlet' and 'outlet' temperatures are made to this region of energy balance, and encompasses the heated test section only.

Several high-resolution devices, listed in Table 2, are placed throughout the test loop to measure key thermal hydraulic behavior. A magnetic volumetric flow meter is positioned at the liquid inlet into the risers, surface and fluid thermocouples at multiple points throughout the loop, and a dual-tip void fraction probe in the vertical segment leading to the tank. Fluid temperatures are measured with type-K, ungrounded, small diameter (3.175 mm) thermocouples placed at the centerline of the flow. Within the chimney region, exposed thermocouples of similar type and diameter were selected for their smaller (0.1 s) response time. Dynamic changes in tank inventory are measured by a static pressure transducer at the riser inlet, normalized by a pressure transducer in the gas space of the tank above the water level. Individual contributions from natural boil-off and accelerated drain are measured by two additional magnetic flow meters, one placed after the steam condenser and a second near a control valve off a side port on the tank, respectively. Data from these instruments are sampled and recorded at a rate of 2 Hz.

Local void fractions where measured by the use of a double tip optical probe, capable of detecting phase changes based on Snell's law of refraction. The sapphire tips each have a diameter of 25 μm, with the spacing between both tips set to 500 μm. A data acquisition unit collects and converts analog signals from the probe into a logic waveform, where a 'low' 0 V signal corresponds to a water phase and a 'high' 5 V corresponds to a gas phase. Statistical methods, similar to those employed by Aprin et al. (2007), were used to translate the logic signals into measurements of void fraction and superficial gas velocities. Signals are sampled at a rate of 10 kHz, and written onto the computer disk in discrete time intervals to prevent exceeding the software buffer limitations. Final time averaged void fractions are presented which span a period of 10 s, logged continuously for the full duration of our tests.

2.1. Water storage tank

The water storage tank plays an important role for heat transfer in the system. Providing a means of both inventory recirculation and boil-off discharge, this dual mode of operation further classifies our test loop as semi-closed.

At saturation conditions, two-phase flow enters the tank and creates a penetrating jet that mixes with the bulk fluid in the pool. Largely subcooled, the pool condenses part of the entering two-phase jet mixture as the lower density mixture rises to the surface. Larger steam bubbles exit from the surface of the pool and enter the condensation network as boil-off discharge, while the heavier subcooled liquid falls to the bottom before entering the downcomer for recirculation. The quality of the exiting steam, or liquid carryover, was not measured for the tests conducted in this paper.

Boil-off discharge is collected from a vent positioned above the tank gas space and transferred to a flat plate heat exchanger via a 19 mm steam hose. A condensation return line then feeds into a separate, open reservoir, with care taken to maintain near atmospheric pressures by preventing liquid slugs forming within the lines.

Frictional pressure losses in the condensation network result in a minor but important back pressure for the steam flow. Separate effects testing at the expected test conditions created an elevated system pressure, nominally 2 kPa above atmospheric, within the gas space of the storage tank.

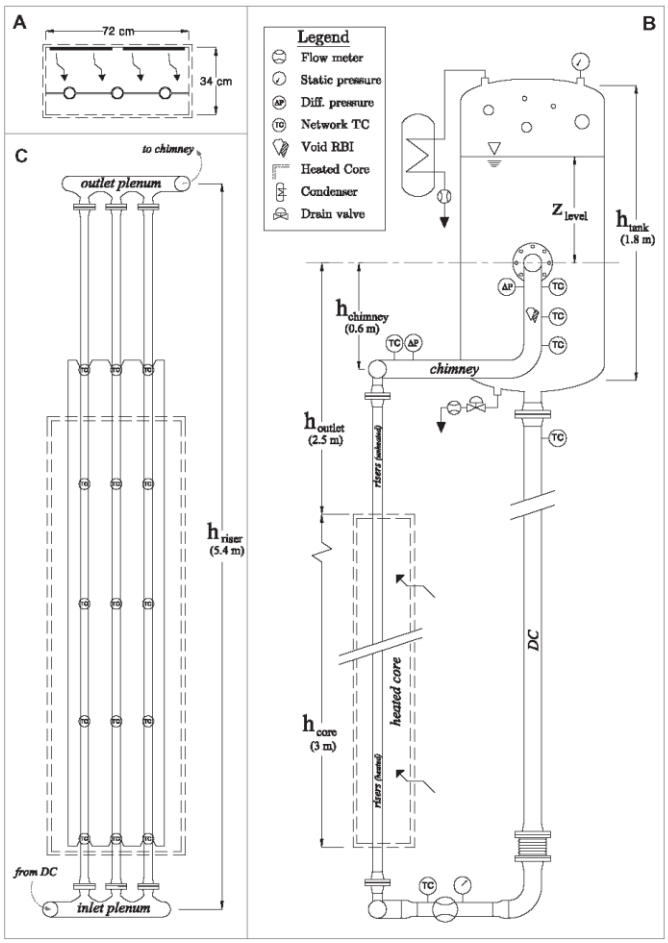

Fig. 1. Diagram of facility components and key features, elevations referenced to tank inlet centerline. (A) Heated cavity, plan view. (B) Test section with inlet and outlet headers, front view. (C) Full facility, side view.

Table 1
Loop component dimensions and loss factor.

Component	Volume (l)	Diameter (cm)	*K*-factor (–)
DC, lower network	58.9	10.2	2.78
Risers	40.2	5.1	8.72
Chimney	21.9	10.2	3.10
Water tank	1,200	91.4	–
Steam network	–	*Variable*	40

3. Experiment procedure

Experimental results have shown that after reaching steady operation, the system will behave in a predictable and quasi-steady state condition (Lisowski et al., 2013b). Thus for a given set of constant boundary conditions, the system behavior is a function only of the tank inventory at that point in time. To study this behavior through full tank depletion, we will explore the stages of the test loop as it experiences a reduction in inventory with time. Full tank depletion will be defined when adequate cooling or safe operation of the test loop is no longer possible due to the reduced fluid inventory, typically preceded by a break in the circuit and stagnation of system flow rates.

Under nominal conditions, natural boil-off to full tank depletion would require operating at saturation for approximately 45 h, an undesirable duration given the demands required for the operator. Thus, to examine the effects of extended duration boil-off an auxiliary drainage system was implemented to facilitate experimental practices and reduce total run times. To ensure that the system did not introduce additional influences or unwanted effects, a series of

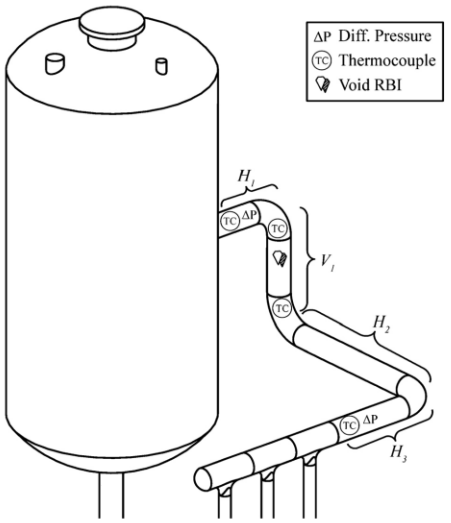

Fig. 2. Upper network and storage tank, with references for instrumentation and piping orientations.

Table 2
Instrumentation specifications.

Measurement	Type	Range	Uncertainty
Temperature	Type-K	1250 °C	±0.2 °C
System flow	76 mm Magnetic	±600 l/min	±0.2% + 1 mm/s
Drain rate	13 mm Magnetic	150 l/min	±0.5%
Differential pressure	Differential	0–6 in H_2O	<0.2%
Fluid static pressure	Static, gauge	0–20 psig	<0.1%
Gas space pressure	Static, gauge	0–1 bar	±0.5% + 0.5 mbar
Water level	Inferred[a]	0–182 cm	±1.7 cm
Void fraction	Dual-tip optical probe	0–100%	<0.5%

[a] Based on static and gas pressure transducers.

scoping tests were performed that compared the behavior with natural and accelerated depletion rates. Natural boil-off tests were performed at starting tank inventories of 80%, 70%, and 60% (z_{level} = 72, 55, and 22 cm) and allowed to maintain steady operation for a period of 4 h, that is the power remained constant and no forced drain was initiated. Comparisons were made to tests undergoing accelerated drain in addition to natural boil-off, where system parameters were examined at times of equal tank levels. Variations in absolute drain rate were also examined, which reduced the overall time scale for inventory loss by a factor of 10–30 from natural boil-off. Finally, repeatability tests were performed under all configurations. Across these tests, measured systems values at matched tank levels fell within a 4% range, ascertaining the feasibility of accelerated tank drain to investigate the effects of natural boil-off.

Tests presented in this paper were performed at baseline conditions, defined by an initial 80% tank inventory (z_{level} = 72 cm), system bulk temperature less than 60 °C, and a one hour power ramp to 15.19 kW. After the onset of natural circulation but prior to data collection, the system is allowed a minimum stabilization period of 240 min to resolve any residual thermal stratification and allow the mass of the steel piping to reach a thermal equilibrium. Given the large inventory, saturation conditions are typically reached 150 min after stabilization, or 400 min into a test. With onset of boiling, a period of 45 min was allotted before enabling forced drain. The tests were concluded shortly upon reaching tank depletion, avoiding material damage to the facility when heat removal became insufficient.

4. Results

The full time history of the system flow rate is presented in Fig. 3, where the test loop experienced continued loss of inventory from natural boil-off and drain. Forced drain began at t = 440 min at a constant rate of 1.10 l/min, later increased to 3.15 l/min at t = 615 min. The tank inventory time history, referenced to z_{level}, is shown in Fig. 4 along with contributions from natural boil-off.

Spanning a duration of 745 min, key changes in behavior have indicated five primary operating stages, and have been summarized in Table 3. An analysis of each stage and the physical phenomenon governing transition mechanisms will be provided in following sections.

4.1. Stage A – Single phase heat-up, $t_{300–400}$

While the system remained largely subcooled during the rise in temperature, isolated bubbles were first observed beginning from t = 350 min. Indicated by localized peaking events in the measured pressure drop, they are the result of riser wall temperatures (T_{wall} = 136 °C) exceeding the local fluid saturation temperature ($T_{sat,f}$ = 108 °C). This temperature difference is sufficient to drive the formation of nucleation sites and bubble formation. The localized peak amplitudes averaged 4 Pa during early stages, gradually increasing to upwards of 14 Pa near the approach to boiling. With separation and mixing into the bulk free stream, the voids eventually collapsed and result in no significant effects to the integral system. A summary of system parameters is provided in Fig. 5. The observed rise in pressure within the gas space of the storage tank can be attributed to the minor flow resistance across the condensation network piping and heat exchanger.

4.2. Stage B – Boiling incipience, $t_{400–470}$

The approach to saturation was first observed at t = 394 min, with a rise in both the gas space temperature and pressure of the storage tank, followed by an acceleration of system flow rate from an increase in driving head. Boiling incipience occurred at t = 410 min, indicated by a flattening of the flow rate and onset of system wide perturbations, Fig. 6.

The boiling mechanism through t = 470 min is classified as transitional nucleate boiling. Void fractions (α) measured an average 1.16% with an absolute standard deviation of 0.62, thus the flow pattern can be characterized as bubbly flow dominated. The bubble formation did not define any characteristic oscillation frequency for the bulk system behavior, resulting in a chaotic trend that lacked clarity in a discrete operating region. The bubbly flow created an ideal regime for heat transfer, noted by the gradual reduction in riser wall temperatures.

Static pressure measurements remained within ±1.5% of the nominal value and indicate that the transient void formation was not sufficient to create large swelling or large static pressure fluctuations. The system exhibited small amplitude oscillations in the system mass flow rate with fluctuations reaching maximum values of ±12% of the mean flow. Nayak and Vijayan (2008) has suggested that amplitude changes of below ±10% can be considered 'stable',

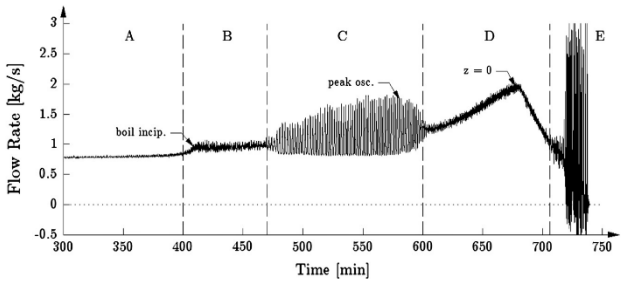

Fig. 3. Full time history of mass flow rate, with stages of interest (A–E) noted.

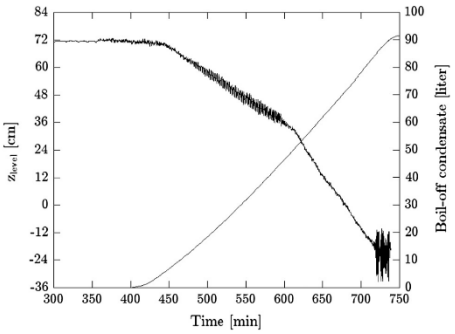

Fig. 4. Full time history of tank inventory, referenced to z_{level}.

while Mochizuki (1992) recommend even a higher threshold of ±30%. Pressure drop measurement along the chimney was characterized by random fluctuations that lacked any defining period or shape, thus suggesting chaotic bubble formation.

Forced inventory loss was initiated at $t = 440$ min, where water was drawn from a side port on the water storage tank and collected into a reservoir.

4.3. Stage C – Periodic oscillations, $t_{470–600}$

With a continued reduction in tank inventory due to boil-off and forced drainage the system parameters at $t = 478$ min shifted away from small, chaotic perturbations and into newly defined periodic behavior. The flow rate in this region is characterized by fully periodic flow excursions that returned to a constant and stable baseline, and followed a smooth sinusoidal shape. The influence on system wide parameters (flow, pressure, temperature, etc.) that occurred during the period from $t = 470–600$ min ($z_{level} = 64–37$ cm) is shown in Fig. 7. Temperatures of the fluid experienced out-of-phase oscillations in the chimney region, and in-phase oscillations in the heated section, Fig. 8, indicating that void formation is formed in the adiabatic chimney and not the heated section.

4.3.1. Boiling mechanism

The phenomenon occurring in this region has been classified as 'natural circulation oscillations' (Chiang et al., 1993), 'thermal hydraulic oscillations' (Wu et al., 1996), or 'hydrostatic head fluctuations' (Subki et al., 2004). Their initiating mechanism is unique to boiling water loops that operate at low or atmospheric pressure, with an additional criterion of horizontal sections or bends along the chimney length. An identifying trait is the presence of 2–5 fundamental frequencies within the measured oscillations, a characteristic that will be examined in later sections. Finally, this mechanism can induce large amplitude flow oscillations and under certain conditions coupled with flashing to induce density wave oscillations (DWO).

Hydrostatic head fluctuations (HHF) can proceed in the following steps: first, a condition must exist where an insufficient vapor generation rate results in an accumulation of voids in horizontal section of network piping. With continued time, new vapor enter the region, where incoming bubbles coalesce and accumulate in the voided section. This accumulation grows, leading to a decrease in hydrostatic head onto the fluid below. Since the driving head from the cold downcomer remains the same, the circulation rate increases and forces the large voided region out and subcooled water in. Finally, a decrease in flow rate then occurs from a now increased hydraulic head, allowing the process to start again and repeat (Chiang et al., 1993).

Not readily apparent in the system flow rate alone, this mechanism is revealed with insight into the local chimney pressure drop, void fraction, and temperature phases. Each oscillation of the chimney pressure drop contains 4–8 void growths, which present themselves as distinct peaks in the measured data, Fig. 9. The rate of vapor generation is insufficient to induce a large system wide flow excursion, but instead allows smaller voids in the

Table 3
Summary of five operating regions.

	Stage	t_{start} (min)	Span (min)	z_{level} (cm)	$\dot{G}_{boil-off}$ (l/min)	$\dot{G}_{system}$ (l/min)	$\dot{x}$ (%)	ΔP (Pa)	ΔT_{core} (°C)	$\Delta T_{chimney}$ (°C)
A	Single-phase	300	100	72.00	–	50.62	0.18	227	3.19	0.36
B	Transitional nucleate boiling	400	70	72.00	0.16	60.09	1.16	259	2.86	0.36
C	Hydrostatic head fluctuations	470	130	62.95	0.25	68.45	2.92	296	2.52	0.18
D	Stable two-phase flow	600	100	34.81	0.28	99.71	17.44	516	1.85	−0.57
E	Geysering	700	35	−13.68	0.18	49.33	37.67	–	1.98	−1.31

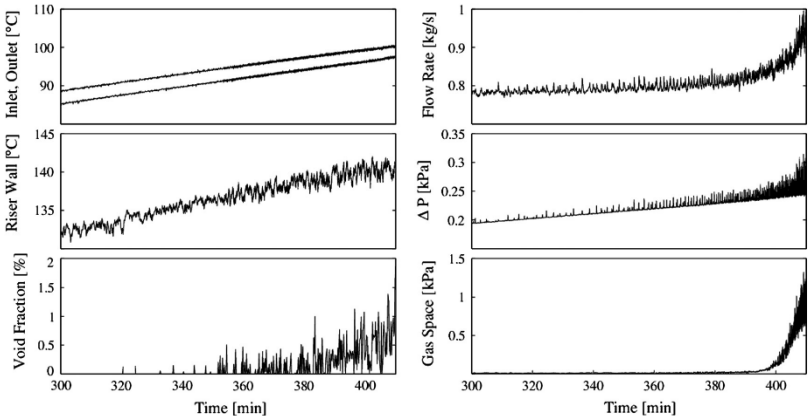

Fig. 5. Details of system parameters for stage A, t = 300–400.

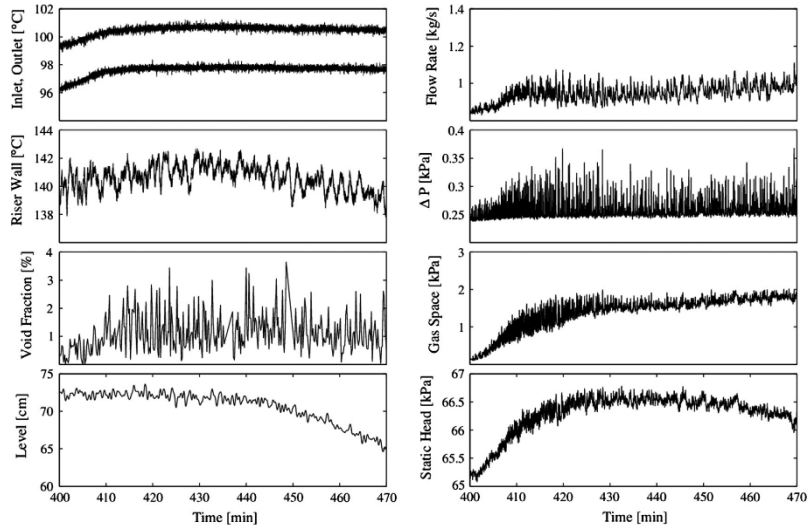

Fig. 6. Details of system parameters for stage B, t = 400–470.

chimney region to coalesce and aid in the growth of a defined periodic oscillation.

The presence of additional modes within a larger system oscillation can further examined by a time domain frequency analysis. The amplitude spectrum of the chimney pressure drop was obtained through a fast Fourier transform of the data from t = 510–560 min, a stage characterized by large periodic oscillations. The results, provided by Fig. 10, indicate a first fundamental frequency of 0.009 Hz (~110 s) and represent the primary system wide fluctuations. Four additional peaks represent the higher order harmonics (integer products of the fundamental), and exhibit frequencies of 0.0175, 0.0261, 0.035, and 0.044 Hz. These harmonics are characteristic of the magnitude, or state, of the HHF instability mechanism and not necessary defined by the experimental apparatus. The work by Wu et al. (1996) observed nearly identical frequencies (0.0098, 0.020, 0.030, 0.040 Hz), yet their test conditions defined 4 kW of heater power, an inlet subcooling of 56 °C, and a chimney piping 19.8 mm in diameter. However, individual contributions from the localized peaks can be observed at a frequency of 0.15 Hz (~7 s), a period unique to the geometry and operating conditions.

From the onset of periodic oscillations, the gradual increase in system wide amplitude spanned a duration of 100 min until reaching a maximum at t = 578 min, where measured oscillations in system parameters exceeding 160% of their baseline values. With a nominal period of 100 s, the void fraction transitioned from 0%

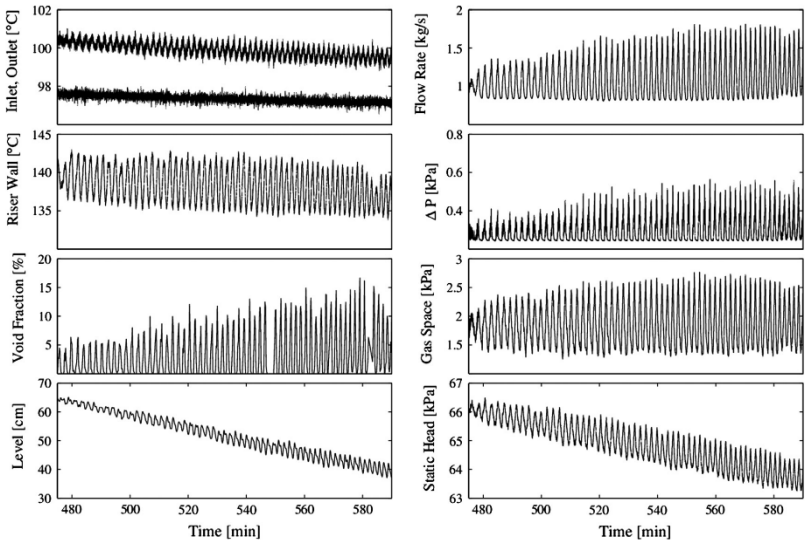

Fig. 7. Details of system parameters for stage C, t = 470–600.

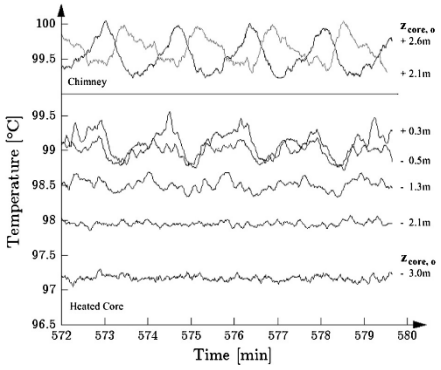

Fig. 8. In-phase oscillations in heated region, out-of-phase in chimney during stage C. Elevations referenced to core outlet.

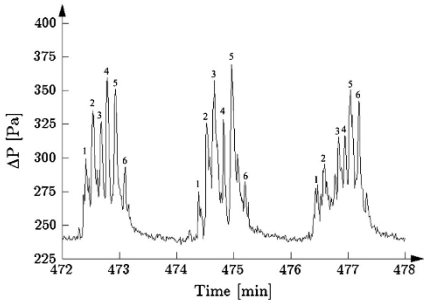

Fig. 9. Local peaks from void excursions within larger oscillation of pressure drop measurements, hydrostatic head fluctuations occurring during stage C.

to upwards of 18% at each oscillation peak. This behavior is a result of the sudden flow excursion, reducing the residence time and thus enthalpy addition in the heated region to such a degree that subcooled liquid can travel through the full extents of the network piping. An analysis of the superficial vapor and liquid velocities provide insight into the flow regimes of the two-phase flow. Data from t = 560–562 min is shown in Fig. 11, tracing the steps across a single flow excursion. Beginning from subcooled liquid (off figure), a path from bubbly to slug flow and returning to bubbly flow is presented.

Immediately after the point of maximum oscillations, a reversal in behavior was observed: system wide oscillations ceased to grow and instead underwent decay with time. Over a period of only 10 flow oscillations, the instabilities became completely suppressed and transitioned to a continuous boiling regime, Fig. 12, indicated by an average void fraction that remained near 5%.

The growth, maximization, and subsequent dampening signify critical points in the operating state and stability of the system. As the system progresses in time and experiences a decrease in tank level, local saturation temperatures are reduced while the rate of enthalpy addition remains the same. Thus, voids begin to form at a lower elevation, oscillation periods decrease, and the boiling boundary transitions to a new physical location. The oscillation period of the system flow rate from t = 460–600 min is shown in Fig. 13, decreasing from 140 to below 80 s.

Description of the void formation and boiling boundary movement, however, will require a more thorough explanation. Given the complex nature of the adiabatic chimney, critical

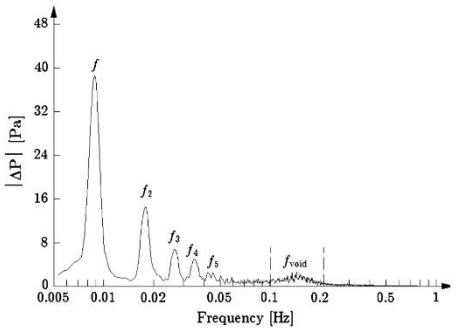

Fig. 10. Fundamental periods characterizing the hydrostatic head fluctuation phenomenon of stage C, determined from the chimney pressure drop at t = 510–560.

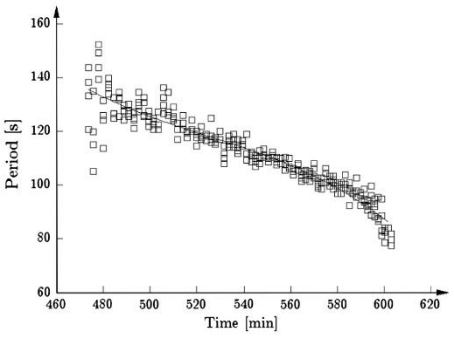

Fig. 13. Oscillation period time history during period of large system oscillations in stage C.

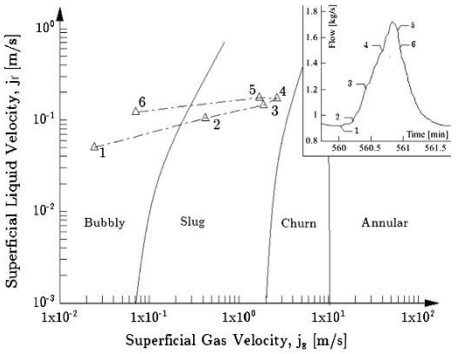

Fig. 11. Two-phase flow regime map of a brief time window near point of maximum periodic oscillations within stage C, t = 560–561.

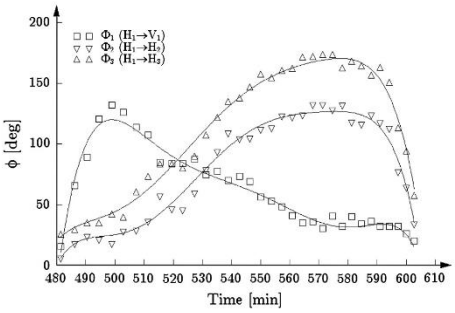

Fig. 14. Phase shift of chimney fluid temperatures during period of growth and decay in system oscillations, stage C.

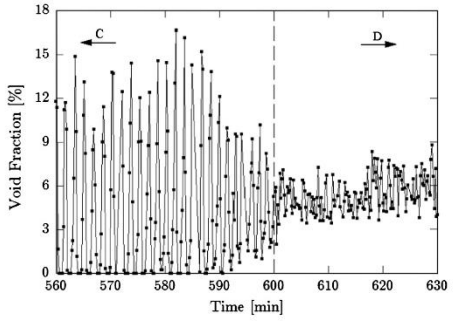

Fig. 12. Void fraction, transition from periodic to continuous, stage C–D.

transition points occur at elbows where the joining pipe is horizontal or vertical in orientation. The movement of the boiling boundary and location of large void growth can be characterized by examining the oscillation behavior of individual measurements along the chimney length. The phase shift of two measurement points serves as insight into the hydraulic phenomenon occurring in the middle region; e.g. out-of-phase measurements suggest the formation of new voids, in-phase suggest the passing of a continuous medium, gas or liquid. Earlier we isolated the void formation to a region above the core by observing an overall phase shift; we will now examine the specific transient phase-lag to identify the localized movement of large voids.

Local fluid temperatures of four temperature measurements along the chimney length were examined for their individual oscillation periods, and compared against one another to identify a phase angle shift. Referenced to a common location at the tank inlet, a time history of three phase shifts from t = 480–610 min is shown in Fig. 14, with physical locations in the facility provided by previous Fig. 2.

Beginning from t = 480 min, prior to the start of large flow oscillations, a 0° phase-shift can be observed across the full length of the chimney for all three phases. At this point in time, system inventory had been reduced by 208 l (166 liters from forced drain, and 42 l from natural boil-off), and corresponded to a z_{level} of 65 cm (12 cm below initial). Local void fractions did not exceed 1.2%, indicating that only small bubbles were present at this point in time. Voiding occurs primarily at the last horizontal segment leading to the tank, H_1, where they are able to rise to the top pipe

wall, create a stratified flow condition, and incur a minimal influence to the bulk system behavior.

When the system enters a period of sinusoidal shaped and periodic oscillations at t = 485 min, a steep rise in the angle of Φ_1 (the calculated phase shift from tank inlet, H_1, to the lower vertical segment, V_1) emerges first. Characterized by void fractions that alternate between 0 and an averaged 6%, the two-phase behavior regime has transitioned from continuous bubbly flow to alternating slug flow induced by hydrostatic head fluctuations. The formation of large voids during t = 485–520 min was found to occur in regions of H_1, V_1, and the elbow connecting the two. The 120° peak of Φ_1 at t = 500 min serves as a key point of reference: large void formation at times prior occurs above the elbow and near the inlet of H_1, and times after occur below the elbow and near the outlet of V_1.

As the amplitude of system flow oscillations grow between t = 520–580 min, a rise in Φ_2 (calculated phase shift from tank inlet, H_1, to outlet of the large horizontal chimney leg, H_2) and Φ_3 (calculated phase shift from tank inlet, H_1, to outlet of the test section, H_3) and attenuation of Φ_1 confirm the boundary has moved past H_1 and fully into V_1. When voiding occurs is this vertical segment, a large bubble formed from the accumulation of incoming vapor can span the entire flow cross sectional area. The growth and movement of this large bubble is able to create a significantly higher pressure drop than a bubble of identical volume in a horizontal leg (Subki et al., 2004).

With continued decrease in water levels voiding occurs at lower elevations in the chimney, resulting in an effect that is able to play a major role in influencing the system behavior. A complete 180° phase shift by Φ_3 is observed at t = 580 min, which is found to match the times of maximum system wide oscillations. The shift indicates large void growth is occurring at a location equidistant from the points used in calculating Φ_3. Based on engineering drawings of the facility, this location was determined to lie exactly at the base of V_1, an equal 1.08 m arc length from either chimney inlet or outlet.

The oscillating region is finally concluded when the void boundary moves into the horizontal segment H_2 and the phase shift returns to zero. The oscillations are dampened from combined effects of a sufficiently high vapor generation rate to prevent accumulation of bubbles, and void formation occurring in a horizontal segment where the gas and liquid phases can stratify.

Considerations were made into the occurrence of density wave oscillations (DWO), which exhibit a similar behavior to hydrostatic head fluctuation due to the presence of a 180° phase shift in oscillations between the chimney inlet and outlet. Both mechanisms are widely observed in boiling water natural circulation systems; however density wave oscillations exhibit a more complex coupling onto system parameters, constitutive relations, and loop geometry. Classically DWO's are the result of multiple regenerative feedback mechanisms present in the system flow, vapor generation rate, and channel pressure drop (Bouré et al., 1973). Their phenomenon stems from a density difference between the inlet and outlet fluid states, which can trigger a delayed and alternating feedback from the subcooled liquid inertia and compressibility of the two-phase mixture. Physical systems will often observe DWO as the basis for influence or coupling onto other instability modes (e.g. flashing-induced DWO), and readily propagate during a start-up transient or in the presence of parallel channels.

Unique to DWO are a characteristic time period of nearly one and a half to twice the time required for a fluid to pass through the channel, Eq. (3), defined as including the full length of the chimney region along with half of the heated core (Marcel et al., 2010). The transit time of the channel, τ_{ch}, is defined in terms of the volume of the chimney ($V_{chimney}$), core (V_{core}), and the bulk volumetric flow rate, (Q_{bulk}).

$$\tau_{ch} = \frac{V_{chimney} + 0.5V_{core}}{\dot{Q}_{bulk}}. \quad (3)$$

While the behavior observed in this work shares similar characteristics to DWO's, the authors do not believe the instability mode in this region is directly attributed to a pure DWO phenomenon. Transit times defined by the channel region fell outside of the DWO operating zone for the majority of the times sampled, Fig. 15, and only matched criteria for a DWO during a short period shortly after the point of maximum system oscillations, from t = 589–595 min. The authors have instead identified a characteristic transit time that represents the observed flow oscillations during the full growth and decay of oscillations and is defined as τ_{system}, the transit time for a subcooled fluid to travel the length of the entire system (tank outlet to tank inlet), Eq. (4), and can be viewed as a means to further identify the mechanism of hydrostatic head fluctuations observed in this work.

$$\tau_{system} = \frac{V_{DC} + V_{core} + V_{chimney}}{\dot{Q}_{bulk}} \quad (4)$$

4.4. Stage D – Continuous circulation, $t_{600-700}$

By t = 605 min the mean circulation rate reached had increased to 1.22 kg/s, resulting in a vapor generation in the system sufficient to create a stable, continuous two-phase circulation condition that exhibited no large periodic amplitude oscillations. The entire chimney became partially voided, transporting a continued stream of bubbles from the risers above the heated core to the tank inlet. The increased circulation and void generation rate prevent an accumulation of voids, halting the hydrostatic head fluctuations observed previously. System flow rates and pressure drops were observed to undergo a gradual increase in magnitude while saturation temperatures continued to decrease, Fig. 16.

A critical point was reached at t = 680 min and z_{level} = −5 cm, where a "knee" occurs in the flow rate due to the level falling below the lower lip of the inlet pipe. With a reduction of driving head from the tank outlet and downcomer, the circulation rate began a gradual decrease. One might expect the flow to experience an abrupt halt since the rectangular loop has essentially been reduced to an open U-loop. However, the flow continues to circulate from two effects: the temperature difference within the vertical length of the cold downcomer and hot riser tubes and swelling from void generation.

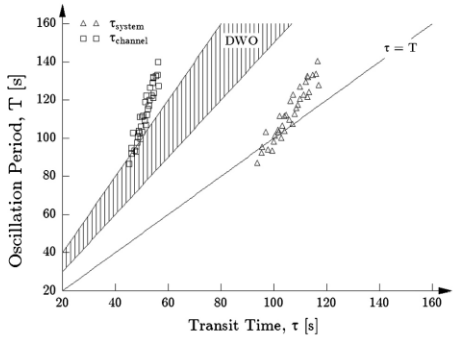

Fig. 15. Transit time and oscillation periods, stage C.

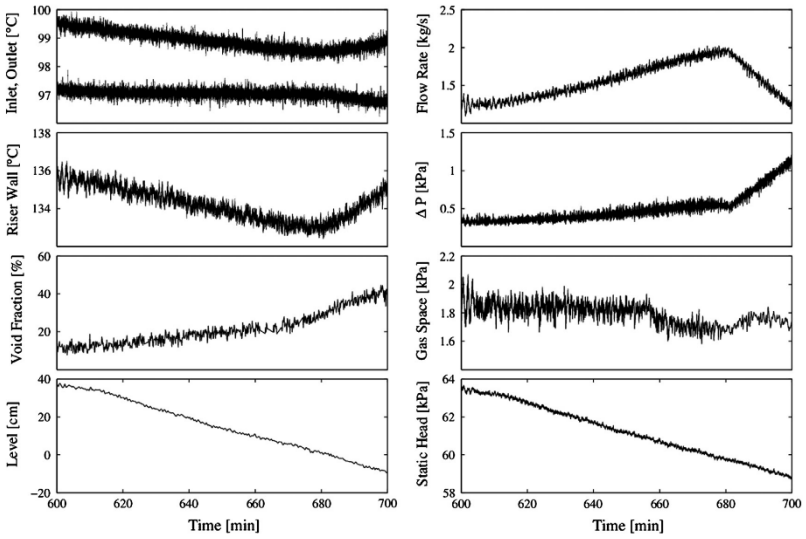

Fig. 16. Details of system parameters for stage D, t = 600–700.

Due to the reduction in flow rate, an absolute temperature increase was observed at the walls of the riser tubes, and together with a deviation in temperatures through the heated and water storage tank, Fig. 17, they suggest a drop in the total heat transfer by the system. Additionally, with equal enthalpy supplied but reduced flow rate, the balance in thermal energy manifested itself by a large rise in outlet and smaller drop in inlet fluid temperatures.

4.4.1. Boiling mechanism

The classification of the system behavior can be further examined by a drawing a phase portrait, which provides an illustration into the coupling or relation between variables. The flow rate and chimney pressure drop were chosen, and are presented in Fig. 18. The behavior observed in stage B, t = 410–470 min, lacks clarity in defining a discrete operating region and is characteristic of a chaotic flow-pressure coupling. Within stage C, t = 470–600 min, an elliptically shaped operating region is visible in the relation between flow and pressure parameters. The periodic nature outlines a discrete path that bounds both the pressure drop and flow rate. Lastly in stage D, t = 600–700 min, a linear rise is evident from the tight coupling of parameters. Without an elliptically operating region, the behavior in this region also suggests a chaotic relation.

4.4.2. Two-phase flow pattern

A statistical analysis was performed to describe the two-phase behavior by constructing normalized probability density functions (PDF). Similar methods have been applied by Jones and Zuber (1975) for air–water flow in a rectangular channel, and Aprin et al. (2007) for boiling hydrocarbons in complex geometry. They summarized that the PDF will exhibit a single peak at low void fractions for bubbly flow, a single peak at high void fractions for annular flow, and twin peaks for slug like flows. Similar observations have been made by Matsui (1984), however he notes that

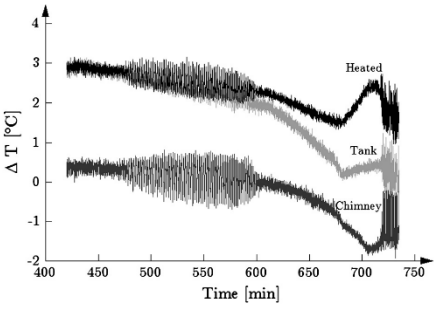

Fig. 17. Temperature rise across various segments for the full time history at two-phase conditions.

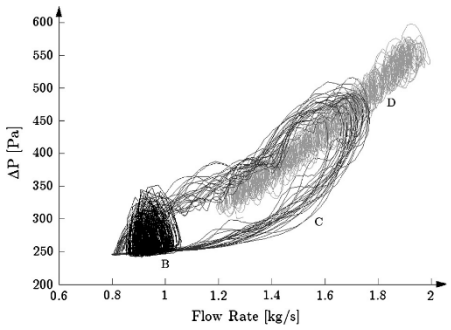

Fig. 18. Phase portrait of flow rate–pressure drop coupling observed in stage B–D.

when the length of observation exceeds the gas dominate portion of slug like flows, PDF shape will resembling that of a normal type.

Interpretation of the void fraction distribution within stages A–D is presented by four PDF plots, shown in Fig. 19. Data collected over the full duration of each stage would be inappropriate given the time varying progression of measured void fractions, thus a quasi-steady sub-stage was selected. Details of the PDF construction, together with a summary of statistical parameters, are provided in Table 4. The kurtosis, κ, of a PDF measures the concentrations of experimental values around a localized peak, while the skewness, γ, provides a measure of asymmetry. The kurtosis and skewness for normal (Gaussian) distribution will approach expected values of $\kappa = 3$ and $\gamma = 0$.

The PDF form of stages A and B is characterized by low void fraction events that occur near their peak, or mode, values and suggests the presence of small bubbly flow. A high kurtosis ($\kappa = 6.3$, 3.9) results from the sharp, narrow shape of the curve, while the skewness ($\gamma = 1.59$, 1.02) explains the asymmetry and bias towards lower void fractions.

The PDF of stage C shows a wider spread in the measured range of void fraction, and exhibits a long 'tail' that extends from the base. The shape shows moderate asymmetry ($\gamma = 0.79$) but lacks a sharp peak due to a near-Gaussian kurtosis ($\kappa = 2.7$). While the hydrostatic head fluctuation mechanism occurring in stage C results in a varying bubbly-slug flow regime, the slug residence time, or relative time spent at higher void fraction regimes, is insufficient to produce the twin peak shape observed by others.

The PDF of stage D begins to resembles that of a Gaussian distribution, with kurtosis ($\kappa = 2.2$) and skewness ($\gamma = 0.06$) approaching those of expected values. Given the high mean void fraction but symmetric shape of the PDF, the flow is representative of an intermittent bubbly regime with alternating presence of small and large bubbles whose diameters fall within a size distribution according to a Gaussian curve (Aprin et al., 2007).

4.5. Stage E – Core voiding, $t_{700-735}$

Flow continued for a period of 40 min past the observed "knee" and subsequent reduction of circulation rate. A critical level, Δz_{crit}, is noted by the water level when the effects of thermal expansion and void swelling are insufficient to carry fluid over into the tank. The result is a break of the water surface and subsequent stagnation of system circulation. Observed at $z_{level} = -19$ cm (14 cm below the lip of the tank inlet) average void fractions and loop temperatures differences were measured at 50% and a 2 °C, respectively. A summary of system parameters is provided in Fig. 20. The flat line in the differential pressure ($t = 715–735$) is due to instrument saturation when the level fell below the 'low' pressure port, whose signal was now dominated by changes in hydrostatic head instead of frictional and thermal differences. Similarly, the dotted regions shown in the void fraction curve ($t = 700–705$, $t = 708–723$) are the result of software limitations and the very large number of voiding events that occurred.

Table 4
Void fraction PDF analysis: statistically summary and sub-stage time window.

Stage		$\bar{\alpha}$ Mean	α_{min} Min.	α_{max} Max.	σ Std. dev.	γ Skewness	κ Kurtosis
A	$t = 380–400$	0.37	0.00	1.86	0.31	1.59	6.32
B	$t = 430–450$	1.05	0.01	3.65	0.65	1.00	3.99
C	$t = 560–580$	4.27	0.00	14.89	3.64	0.80	2.72
D	$t = 620–640$	15.28	7.20	23.03	3.38	0.04	2.22

Voiding occurs entirely in the core region due to enthalpy addition, with the boiling boundary traveling further down the core with time. Out-of-phase oscillations between the core inlet and outlet are observed at the initial stages, transitioning to fully in-phase as the boundary moves to the core inlet, Fig. 21. At this point in time, the level has fallen well below the tank inlet, creating a break in the water circuit and forming a U-loop geometry. With large steel piping and low frictional losses of our facility, the little restriction to flow excursions creating an oscillating bidirectional behavior in the system flow rate.

4.5.1. Boiling mechanisms

The boiling mechanism at this stage is characterized by periodic flow excursions followed by an incubation (no boiling) period. Termed geysering, it is most commonly observed when a vertical column of liquid is heated from the bottom (Kyung and Lee, 1994). The events repeat by a series of three events: an initial period subcooled flow stagnation, incubation and enthalpy addition, and violent ejection of fluid. The phenomenon is distinguishable to those nearby an active experiment, creating an audible effect that easily transmits through steel piping and insulation.

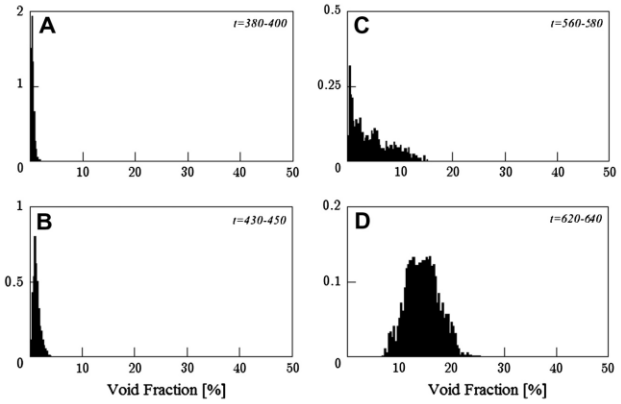

Fig. 19. Normalized PDF of void fractions within a quasi-steady window of stage A–D.

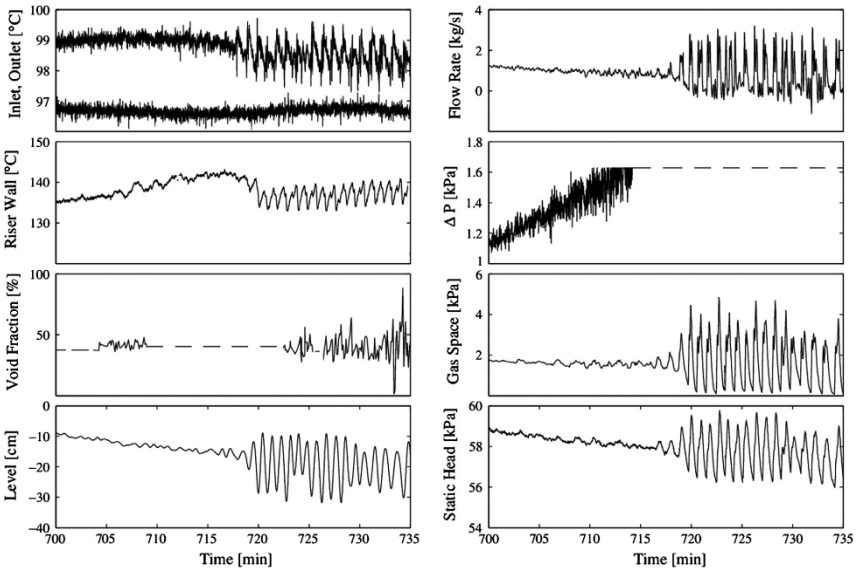

Fig. 20. Details of system parameters for stage F, $t = 700$–735. Dashed lines indicate unavailable data (void fraction) or saturated instrumentation (pressure drop).

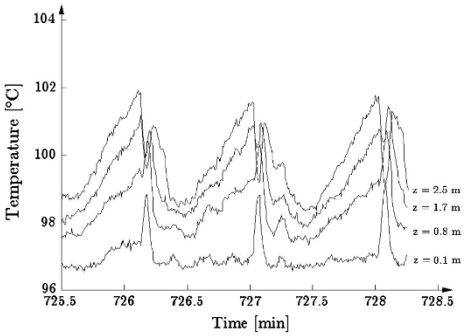

Fig. 21. Voiding of riser tubes within heated core, end of stage E. Elevations referenced from inlet to heated core.

Typically occurring due to the presence of superheat near the base of the column, Kuncoro et al. (1995) observed one subtle difference when investigating this phenomenon in natural circulation systems with water: the violent ejection of fluid occurs by a pattern induced fast propagation boiling and not superheating. Griffith (1962) described this pattern boiling by a series of chain reactions: when a bubble is first formed in the pipe it creates a reduction in hydrostatic pressure for the fluid below, decreasing the saturation temperature for points lower in elevation. A second bubble is then formed and this process is repeated, propagating downward to the base of the column until reaching a position where the fluid remains subcooled even at lowest pressures within the loop.

The power was removed and test concluded at $t = 735$ min due to an inventory insufficient to provide adequate cooling and maintain structural integrity of the test facility. This point marked a 'fully depleted' tank condition, which measured a water level 15 cm below the lip of the tank inlet ($z_{level} = -20$ cm). A total inventory loss of 620 l occurred within a period of 735 min, where 530 l were removed from forced drain and 90 l due to natural boil off. Without forced drain and considering natural boil-off only, the system would have maintained adequate heat removal performance for a period of 44.75 h after boiling incipience. When considering that a nominal 6.5 °C/h single phase heating rate would bring the system to saturation conditions from an initial temperature of 30 °C in only 10.8 h, the venting of steam allows for a substantially extended time window of adequate heat removal operation.

5. Scaling considerations

In extending these results to other facilities at different scales, it is desirable to preserve or otherwise predict the system behavior and nominal flow patterns. Applications to different scale or same fluid installations may be appropriate if an accurate and systematic scaling process was established. Such a study of thermal hydraulic scaling requires an effort where experiments at different scales are complemented by analysis. This work is the first step in such an effort and as such a full characterization would extend past the scope of the presented paper.

Integral scaling of system behavior has been documented for similar facilities, in particular the Natural Convection Shutdown Heat Removal Test Facility at Argonne National Lab (Tzanos and Farmer, 2006). While construction of their water based facility was never realized, our design shares a common framework and thus we agree with their analysis and believe it is well suited to serve as a basis. Scaling using a reduced axial length, and following simplified one-dimensional conservation equations for mass, energy, and momentum, they developed similarity relationships

that govern primary, system level parameters such as heat flux, ΔT, and velocity, among others.

Based on this reduced axial length scale and integral system scaling for the natural circulation loop, it is expected that under single-phase or two-phase conditions, the gravitational driving head and frictional resistances are preserved by the Froude and Friction numbers. The scaling analysis of Ishii et al. (1998) suggested that the energy transfer and kinematics, or more specifically flashing phenomena and the rate of vapor generation, may be also preserved by maintaining similarities in nondimensional characterization of phase change and sub-cooling phenomena. For a boil-off influenced system, however, the dynamics of the flashing phenomena in the chimney is largely due to the geometry, heat input from the core (heated section) and decreasing hydro-static head. Therefore an additional phase change number may be introduced a means to partially account for the head pressure change across the chimney. However, this addition cannot be guaranteed to satisfy the full scaling requirements and thus we do not expect this effect to be properly scaled at different scales.

Details pertaining to local effects, such as transport in the storage tank, have been published in previous work by the authors (Lisowski et al., 2011). It was found that single and two-phase operating conditions required unique scaling constraints, and could not be satisfied by a single, static tank configuration. The primary criterion established was maintaining the aspect ratio of the storage tank (length/diameter) and number of inlet jets, which would ensure preservation of the buoyant plume rise times from two-phase discharge.

For similar systems with varying axial lengths, one may preserve the integral system behavior with relatively high confidence if appropriate scaling processes are implemented. Additionally, if the total amount of vapor generated is scaled correctly, two-phase phenomena such as flashing may also be preserved. However, effects specific to local behavior, or when boil-off is present, the scaling may require additional constraints and cannot be guaranteed to satisfy requirements under all operating conditions. Furthermore, changes to the fundamental piping geometry or configuration may be overwhelmingly difficult to account for. Given the complex coupling of natural circulation phenomena, scaling distortions are inevitable and must be anticipated.

6. Conclusion

This experimental study investigated the thermal hydraulic behavior and boiling mechanisms present in a natural circulation loop experiencing boil-off. Five primary operating stages were identified and have been classified by the mode of two-phase natural circulation.

Initial stages prior to boiling incipience (A) presented a gradual rise in system temperatures with occasional bubble release from riser tube wall superheat. Stages immediately after saturation (B) exhibited stable but chaotic nucleate voiding in a small bubbly flow regime due to the boiling boundary occurring at a horizontal segment nearest to the tank inlet. Later stages (C) see a shift in boiling location to the vertical leg; however, due to a low vapor generation rate, bubbles could accumulate, coalesce, and create large voids. This phenomenon, described as hydrostatic head fluctuations, created alternating periods of liquid and two-phase slug flow. When this boundary again moves down the vertical leg and into the horizontal segment nearest the riser outlet (D), the rate of void generation was sufficient to prevent the time varying accumulation of voids, and allowed the system to enter a stable and continuous two-phase operating region. The flow regime during this period is classified as an intermittent bubbly regime with alternating presence of small and large bubbles. Finally, when the water level fell below a critical level, z_{crit}, a break in the water loop occurred and resulted in flow stagnation (E). Significant degradation in the heat transfer was observed, at which point heat removal would be insufficient to maintain safe operation of the system.

These effects ultimately are an artifact of the complex chimney geometry, heating rate, and hydrostatic pressure from the tank inventory. Changes in hydrostatic pressure are able to shift the boiling boundary to different segments of the chimney, whose geometry and orientation dictate the flow regime and ultimately the system behavior. At low vapor generation rates, void growth at or prior to a horizontal segment will result in a stratified regime and stable operating state. If the boiling boundary occurs at or prior to a vertical segment, a condition can exist where bubbles coalesce to form large voids that strongly influence the system stability. However, if the rate of vapor generation is sufficiently high to prevent an accumulation of voids, it can surpass the effects described previously and result in a stable, continuous two-phase flow regime.

For safety–critical applications where truly passive means of heat removal is required, natural circulation water loops have the potential to offer a high level of performance with relative simplicity. If the venting of steam can be incorporated, they can offer a significantly extended time window for successful heat removal and operation.

Acknowledgment

The authors wish to acknowledge support from the Department of Energy, with funding provided under the Project Number NEUP 09-202.

References

Aprin, L., Mercier, P., Tadrist, L., 2007. Experimental analysis of local void fractions measurements for boiling hydrocarbons in complex geometry. Int. J. Multiphase Flow 33, 371–393.
Bakhmet'ev, A.M. et al., 2009. Experimental validation of the cooling loop for a passive system for removing heat from the AES-2006 protective envelope design for the Leningradskaya nuclear power plant site. Atom. Energy 106, 148–152.
Burgazzi, L., 2007. Thermal–hydraulic passive system reliability-based design approach. Reliab. Eng. Syst. Saf. 92, 1250–1257.
Bouré, J.A., Bergles, A.E., Tong, L.S., 1973. Review of two-phase flow instability. Nucl. Eng. Des. 25, 165–192.
Chen, W.L., Wang, S.B., Twu, S.S., Chung, C.R., Pan, C., 2001. Hysteresis effect in a double channel natural circulation loop. Int. J. Multiphase Flow 27, 171–187.
Chiang, J.H., Aritomi, M., Mori, M., 1993. Fundamental study on thermo-hydraulics during start-up in natural circulation boiling water reactors, (ii) natural circulation oscillation induced by hydrostatic head fluctuation. J. Nucl. Sci. Technol. 30–3, 203–211.
Griffith, P., 1962. Geysering in liquid-filled lines. In: ASME AiChE Heat Transfer Conference, 62-HT-39.
Ishii, M., Revankar, S.T., Leonardi, T., Dowlati, R., Bertodano, M.L., Babelli, I., Wang, W., Pokharna, H., Ransom, V.H., Viskanta, R., 1998. The three-level scaling approach with application to the Purdue University Multi-Dimensional Integral Test Assembly (PUMA). Nucl. Eng. Des. 186, 177–211.
Jeng, H.R., Pan, C., 1994. Multiple steady-state solution for a two-phase natural circulation loop with subcooled boiling. In: Proc. 4th Int. Topical Meeting on Nuclear Thermal Hydraulics, Operations and Safety, Taipei, Taiwan, 9A1–9A8.
Jones Jr., O.C., Zuber, N., 1975. The interrelation between void fraction fluctuations and flow patterns in two-phase flow. Int. J. Multiphase Flow 2, 273–306.
Kim, J.M., Lee, S.Y., 2000. Experimental observation of flow instability in a semi-closed two-phase natural circulation loop. Nucl. Eng. Des. 196, 359–367.
Kuncoro, H., Rao, Y.F., Fukuda, K., 1995. An experimental study on the mechanism of geysering in a closed two-phase thermosyphon. Int. J. Multiphase Flow 21, 1243–1252.
Kyung, I.S., Lee, S.Y., 1994. Experimental observations on flow characteristics in an open two-phase natural circulation loop. Nucl. Eng. Des. 150, 171–187.
Lee, S.Y., Kim, Y.L., 1999. An analytical investigation of role of expansion tank in semi-closed two-phase natural circulation loop. Nucl. Eng. Des. 190, 353–360.
Lisowski, D., Albiston, S., Scherrer, R., Haskin, T., Anderson, M., Tokuhiro, A., Corradini, M., 2011. Experimental studies of NGNP reactor cavity cooling system with water. In: Proc. ICAPP 2011, CD-ROM, #11116.
Lisowski, D., Haskin, T., Tokuhiro, A., Anderson, M., Corradini, M.L., 2013a. A study on the behavior of an asymmetrically heated reactor cavity cooling system with water in single phase. Nucl. Technol. 183, 7.

Lisowski, D., Omotowa, O., Anderson, M., Corradini, M.L., 2013. Power investigations on the two-phase behavior and instability in an experimental reactor cavity cooling system with water. In: Proc. of NURETH15.

Marcel, C.P. et al., 2010. Experimental investigations on flashing-induced instabilities in one and two-parallel channels: a comparative study. Exp. Therm. Fluid Sci. 34, 879–892.

Matsui, G., 1984. Identification of flow regimes in vertical gas-liquid two-phase flow using differential pressure fluctuations. Int. J. Multiphase Flow 10, 711–719.

Mochizuki, H., 1992. Experimental and analytical studies of flow instabilities in pressure tube type heavy water reactors. J. Nucl. Sci. Technol. 29, 50–67.

Nayak, A.K., Vijayan, P.K., 2008. Flow instabilities in boiling two-phase natural circulation systems: a review. Sci. Technol. Nucl. Install., 1–15.

Pope, M.A., Lee, J.I., Hejzlar, P., Driscoll, M.J., 2009. Thermal hydraulic challenges of gas cooled fast reactors with passive safety features. Nucl. Eng. Des. 239, 840–854.

Puustinen, M., 2002. Natural circulation flow behavior at reduced inventory in a VVER geometry. Nucl. Eng. Des. 215, 99–110.

Subki, M.H., Aritomi, M., et al., 2004. Multi parameter effect of thermohydraulic instability in a natural circulation boiling water reactor during startup. JSME Int. J. B, 277–286.

Tzanos, C.P., Farmer, M., 2006. Feasibility Study for Use of the Natural Convection Shutdown Heat Removal Test Facility (NSTF) for Initial VHTR Water-Cooled RCCS Shutdown (ANL-GenIV-079), Technical Report. Nuclear Engineering Division, Argonne National Lab.

Wu, C.Y., Wang, S.B., Pan, C., 1996. Chaotic oscillations in a low pressure two-phase natural circulation loop under low power and high inlet subcooling conditions. Nucl. Eng. Des. 162, 223–232.

5. Submitted for Publishing in the Proceedings of 2014 International Congress on Advances in Nuclear Power Plants (ICAPP-14), Charlotte, NC, April 6-9th ,2014

Proceedings of ICAPP 2014
Charlotte, USA, April 6-9, 2014
Paper 14395

Off-normal Characteristic Two-Phase Flow Behavior in the Water-cooled MHTGR-RCCS with Decay Heat Variation

Olumuyiwa OMOTOWA [1], Darius LISOWSKI [2], Mark ANDERSON [3], Akira TOKUHIRO [1], Mike CORRADINI [3]

[1] *Dept. of Mechanical Engineering, University of Idaho, 1776 Science Center Dr., Idaho Falls, ID, USA 83402*
[2] *Argonne National Laboratory, 9700 S Cass Ave., Lemont, IL 60439*
[3] *Dept. of Engineering Physics, University of Wisconsin, 1500 Engineering Dr., Madison, WI, USA 53711*

Tel: *(208)-357-8003*
Email: *omot6968@vandals.uidaho.edu*

Abstract – In the conceptual modular high temperature gas-cooled reactor (MHTGR), the reactor cavity cooling system (RCCS) is designed for decay heat removal. Following the occurrence of a design basis accident (DBA) such as a loss of forced circulation, the RCCS operation is designed to transition from the active to passive decay heat removal mode. A water-cooled RCCS, consisting of multiple standpipes will provide cooling via natural circulation heat transfer by removing the decay heat from the reactor pressure vessel (RPV) to an ultimate heat sink. The decay heat load on the full-scale RCCS during a transient event varies over time with an estimated peak power of 1.5 MW. This paper experimentally investigates the two-phase phenomena in a three channel natural circulation loop at different radiative-convective thermal loads representing decay heat, and the corresponding effect on the thermal-hydraulic behavior and performance of a scaled RCCS test facility.

I. INTRODUCTION

Natural circulation cooling is a passive safety feature in advanced reactor designs for decay heat removal purposes. It also provides simplicity and a basis for making advanced designs more economical and hence more competitive. For this reason, the modular high temperature gas-cooled reactor (MHTGR) is designed with a natural circulation passive cooling feature hitherto referred to as the Reactor Cavity Cooling System (RCCS). This is designed to remove decay heat from the reactor pressure vessel (RPV) following a design basis accident (DBA) such as a loss of forced circulation (LOFC).

While other natural circulation passive systems have been designed and several studies have been performed with respect to primary system core heat removal in boiling water reactors (BWRs), the characterization of the complex two-phase thermalhydraulics of the system presents a unique challenge. Aritomi *et.al* (1993) investigated these systems behavior under forced circulation and at the onset of natural circulation immediately after the loss of forced cooling (pump trip transient) using two channels. The authors showed that in-phase instability occurs in both channels under natural circulation but the flow is stable under forced circulation with increase in heat flux. Boure *et.al* (1973), described the physical mechanisms and the parameters that influence flow instabilities to include system geometry, operating conditions and boundary conditions.

This paper is organized as follows: Section II gives the description of key features of a water-cooled RCCS for the MHTGR. In Section III, a description of the structural features and instrumentation on a ¼ - scale RCCS test facility at the University of Wisconsin – Madison is given. Section IV focuses on experimental efforts representing the influence and individual contribution of different scaled decay heat loads to the thermal-hydraulic behavior of the RCCS following a transient. Section V discusses the experimental results based on the semi quantitative characterization of two-phase flow behavior of the RCCS using characteristic flow parameters at different heat flux. The thermalhydraulics, characterized by chaotic and periodic oscillatory flow behavior of key system parameters are quantified and analyzed using a simple but pertinent metric, the full-width half maximum method. Finally, in Section VI, the concluding remarks are presented.

II. REACTOR CAVITY COOLING SYSTEM (RCCS)

The conceptual design is based off the GA-MHTGR reactor design with modular core power of 350 MWt. The RCCS for the GA-MHTGR is an ex-vessel natural circulation passive safety system that constitutes the volume between the RPV and the concrete structures. The primary function of the RCCS is the removal of residual heat from the RPV to an ultimate heat sink (atmosphere) while also keeping the reactor cavity and structural surface

temperatures within safe limits [van Staden (2004)]. Using water as the working fluid, the RCCS during normal plant operations remains functional in the active mode using equipment protection cooling circuit (EPCC) pumps for circulating water from the heat sink (storage tanks) to the riser tubes, extracting heat from the cavity and returning sub-cooled liquid into the tank. A secondary cooling line is used to maintain system temperatures by drawing water from the tanks through a heat exchanger located outside the containment. The heat loss from the RPV to the reactor cavity during steady state normal operations is approximately 700 kW [DOE, 1992].

Following a DBA such as a D-LOFC leading to a SCRAM, the RCCS operations transitions to a passive mode and operates under natural circulation heat transfer. Under this scenario, the decay heat through the RPV, as a result of the in-vessel radioactive decay of the fission products, continually increases and peaks at about 1.5 MW [DOE, 1992]. Fig.1 shows the decay heat curve for a conceptual MHTGR design immediately after shutdown. The expected decay heat over time after shutdown can be described in the form, (Ragheb, 2013)

$$P_s = P_o 6.48[(t_s^{-0.2} - (t_s + t_o)^{-0.2}] \quad (1)$$

where P_o and $P_s$are the reactor powers before and after shutdown respectively, t_s is the corresponding time past shutdown and t_o is the reactor operation time in days. This is based on the assumption that the reactor operated for at least a year before shutdown.

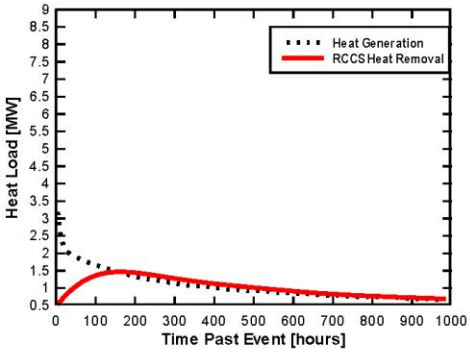

Fig. 1: Reactor power and RCCS heat removal following a design basis accident [DOE, 1992]

III. WATER-COOLED RCCS

The conceptual RCCS design used as a basis for these studies has approximately 227 risers and 9 sets of overhead storage tanks. All risers are connected through hot and cold headers representing the upper and lower plenum respectively. An illustration of a full scale RCCS design with the riser forming a curtain along the concrete walls is given in Fig. 2.

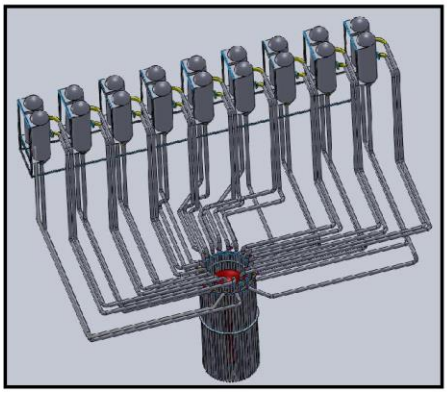

Fig. 2: Schematic of a full scale RCCS (author's view- not to scale)

III.A. UW-Scaled RCCS Test Facility

To predict the thermal-hydraulic behavior of the full scale RCCS, a ¼ scale test facility has been built (i.e. UW-RCCS Test Facility) to simulate the decay heat from a RPV wall to the RCCS through a heated reactor cavity. The scaled UW-RCCS test facility uses water as the working fluid, and a 1200 litre overhead storage tank serving as a heat sink. Total height of the integral facility is 7.8 m. This represents a ¼ axial length scale of the conceptual design. All radial dimensions were preserved on a 1:1 ratio. Detailed scaling analysis of the facility has been reported by Lisowski et.al (2011), with a summary of scaled quantities provided in Table 1. The test loop consists of three parallel risers connected along their centerlines with fins to enhance heat transfer, a downcomer, upper and lower plenums connecting all three risers, an upper (chimney) and lower pipe network, and a heated cavity. Each riser measures 5 m in length, an inner diameter of 0.051 m and the pitch to diameter ratio of risers is 4. The length of the downcomer is 5.8 m and the inner diameter is 0.1016 m.

Initial confirmatory analysis indicates that the mode of decay heat transfer from the vessel wall is on average 80% radiation and 20% convection. The decay heat was simulated using 34 electrically heated radiant heaters, designed to accommodate heat load of 42.5 kW corresponding to a heat flux of 25 kW/m^2. A 3 m section along each riser is exposed to the rejected heat from the radiant heaters, leaving an unheated section at the bottom and top of each riser. Due to the height of the test facility, support was built to dampen flow-induced vibrations, which readily present themselves during two-phase testing. A schematic of the UW-RCCS test facility depicting the overall natural circulation loop structure is shown in Fig. 3.

To capture the thermal-hydraulic processes during operation, the test facility is fully equipped with pressure, temperature and flow (point A in Fig. 3) sensors.

Table 1: Summary of Scaled Quantities

Parameter	Notation	Scaled Ratio
Axial length scale	l_R	0.25
Radial scale	$A_{o,R}$	1
Power	$Q_{o,R} \approx \sqrt{l_R}$	0.5
Heat flux	$q''_R \approx 1/\sqrt{l_R}$	2
Velocity	$U_{o,R} \approx \sqrt{l_R}$	0.5
Temperature difference	ΔT_R	1

A high resolution magnetic volumetric flow meter is positioned along the inlet to the lower plenum, a differential pressure transmitter for pressure drop measurement in the chimney, type K thermocouples well distributed to give both bulk fluid and pipe surface temperatures and a dual tipped optical probe (point B in Fig. 3) to measure local void fraction in the chimney close to the inlet of the heat sink. Uncertainties associated with all instruments were quantified based on their rated conditions (mass flow meter: ±0.2% + 1mm/s, pressure drop: <0.2%).

IV. METHODOLOGY

Following the occurrence of an accident, it is assumed that the reactor is immediately shutdown and the reactor power decreases. Heat removal via conduction and radiation to the RCCS begins to provide cooling. Since the RCCS is a function of the RPV temperature, the heat loss to the RCCS varies during the transient event. Steady state operating conditions were modeled based on sets of scaled boundary conditions representing the conceptual design. Single-phase, steady-state thermal-hydraulic analyses have been detailed in Lisowski et.al (2011). The influence and individual contribution of different scaled decay heat loads (12.55, 15.19, 17.84 and 20.49 kW) to the thermal-hydraulic behavior of the RCCS are presented. The prototypic system response incorporating all individual power schemes and representing decay heat removal of the RCCS during transition from normal to off-normal operation in the sudden event of an accident was also investigated but not reported in this paper.

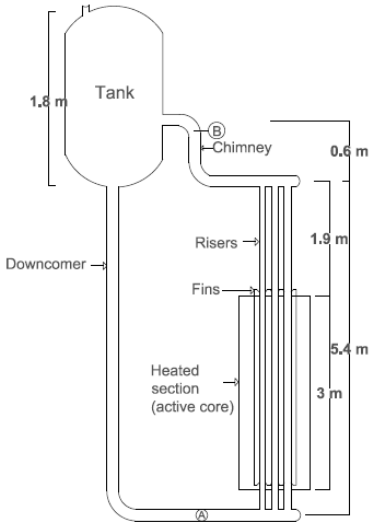

Fig. 3: Schematic of University of Wisconsin's ¼ -scaled Water-Cooled RCCS Test Facility

IV.A. Boundary Conditions and Procedure

For all experiments reported in this paper, initial fluid volume prior to testing were maintained at a nominal 80% tank volume (960 litres). Average bulk fluid temperature at the start of the experiment was 65°C and all experiments were carried out at atmospheric pressure. To prevent thermal shock on the electric heaters, a one hour ramp-up period was set until reaching the desired power scheme. Table 2 shows the average heat-up rate for each experiment. With continuous heat addition to the system, the fluid remains in single phase until the riser tube surface temperatures are high enough to initiate nucleate boiling. This indicates the transition phase leading to boiling at fluid saturation temperatures. The system is kept under two-phase boiling conditions for approximately 4 hours until the power is gradually ramped-down, marking the end

of each experiment. Discussions are provided in the following result and analysis section.

Table 2: *Scaled decay heat load from the RPV, corresponding heat flux and heating rate for each power scheme.*

Decay heat load (kW)	Heat flux (kW/m^2)	Heating rate (°C/min)
12.55	7.27	0.084
15.19	9.29	0.112
17.84	10.9	0.157
20.49	12.52	0.173

V. EXPERIMENTAL RESULT AND ANALYSIS

Performance metrics used to characterize the system behavior include the bulk system mass flow rate, chimney pressure drop, and tank inlet void-fraction. Previous results at steady-state single phase experimental suggest a linear behavior [Lisowski et.al, (2011)] with increasing power. At riser wall temperatures 'T_w', in excess of 4-40°C above the saturation temperature of water, local and bulk nucleate boiling heat transfer regime is observed between the single phase and inception of boiling. This is shown in ***region A*** of Fig. 4 (a-d). Surface bubble dynamics at nucleation sites, release of bubbles from the surface, coalescence and collapse of bubbles under local sub-cooling as captured by the pressure and flow measuring devices, show as perturbation in the time response of their signals. Isolated bubbles were initially formed in the left riser within the heated region but they were immediately suppressed upon release; however, with increasing riser surface temperatures, more bubbles formed and coalesced in the center and right risers. They hence make their way into the chimney region above the heated cavity and the effect is subsequently detected by the pressure drop transmitter. A summary of measured parameters in the boiling regime is given in Table 3.

At elevated temperatures close to saturation, the amplitude of flow oscillations increases, leading to a sudden rise in all system parameters. More frequent large voids are hence observed, then the onset of full boiling as illustrated by ***region B*** in Figure 4(a-d). The same effect led to an increase in pressure drop measurements and also an increase in the void fraction, hence confirming the presence of voids and the location of the boiling boundary in the chimney.

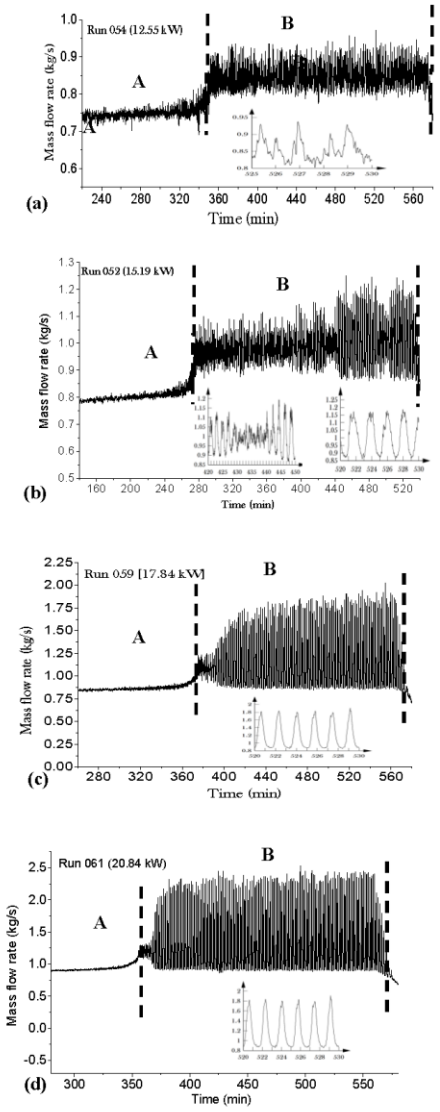

Fig. 4(a-d): Characteristic system flow rate at different decay heat loads: (A). Transition region (local and bulk nucleate boiling regime) (B).Dynamic system behavior during boiling. Insets: Resolved response over a ten minutes time frame.

Table 3: Average dynamic system measurements in the boiling region.

Heat flux (kW/m²)	Mass Flow (kg/s)		Press. Drop (Pa)		Void Fraction (%)	
	Mean	σ	Mean	Σ	Mean	σ
7.27	0.85	0.03	245.37	9.36	0.32	0.47
9.29	0.99	0.07	256.62	18	0.96	0.94
10.9	1.16	0.31	292.94	70.81	2.89	4.07
12.52	1.33	0.45	327.48	117.13	5.49	8.15

Flow measurements corresponding to low input heat flux (7.27 kW/m²) show a charateristic chaotic oscillatory behavior due to the high density ratio between liquid water and its vapor under two-phase conditions. This translates to low natural circulation flow rate. Increasing the input heat flux, the oscillatory behavior is more periodic (see Figure 4(a-d) insets). A plot of the average period of oscillation during the two-phase boiling region for each experiment also indicates that with increasing decay heat flux, the periods become much smaller as shown in Figure 5. Experiment performed at 9.29 kW/m², exhibit a combination of chaotic and periodic oscillatory behavior with the flow oscillations increasing in amplitude and dampening in a cyclic pattern in increments of 20, 32, 48 min. until a more periodic behavior is established as shown in Fig. 5b.

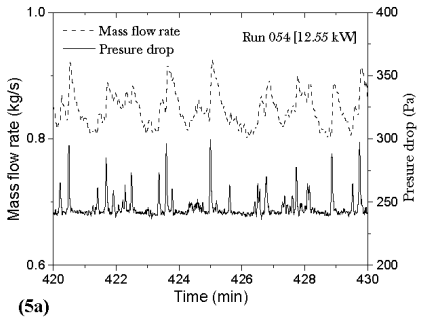

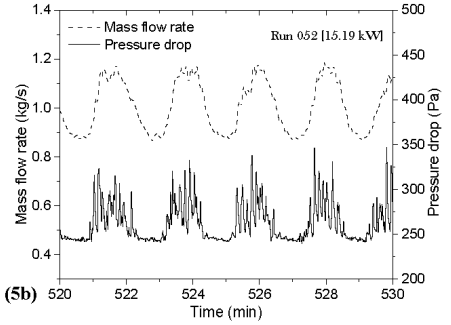

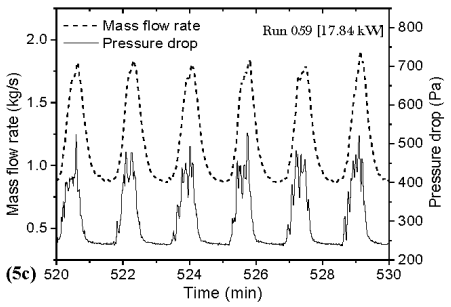

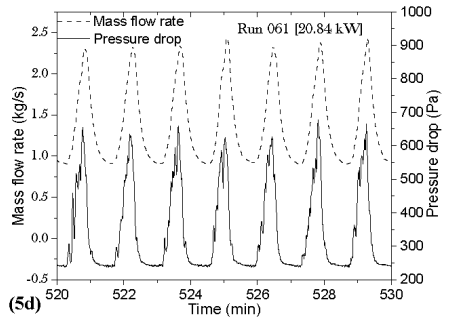

Fig. 5(a-d): In-phase oscillatory response of the system flow rate and pressure drop measurements in the chimney region for decay heat load experiments

To further understand the dynamics and flow mechanism downstream in the area above the heated core, statistical analysis is used to resolve and analyze the chaotic and periodic oscillatory behavior observed in the pressure drop and void fraction results of each experiment in two-phase regime. The full width at half maximum (FWHM) concept describes the 'peakedness' of the oscillatory behavior, given that the phenomena is periodic and gives a good estimate of the standard deviation of the signal. Multiple samples of oscillatory behavior were taken from the instant when the oscillations are deemed established, or in a period of quasi-steady state after the onset of boiling, approximately two hours into boiling, and within the last hour of each power scheme experiment. All resolved peaks were fitted using a Gaussian model of the form,

$$y = y_o + \frac{Ae^{\frac{4\ln(2)(x-x_c)}{\omega^2}}}{\omega\sqrt{\frac{\pi}{4\ln(2)}}} \qquad (2)$$

where y_o is the baseline offset, A is the total area under the curve from the baseline, x_o is the center of the peak and ω is the width of the peak at half height.

Figs. 5(a)-(d) depict the expanded time-dependent mass-flow and pressure traces at four representative scaled decay heat loads and corresponding heat fluxes. They correspond to a segment of Figs. 4(a)-(d). These traces were characterized using the FWHM method, as guided by a Gaussian 'fit' onto the traces. In order to facilitate the following phenomenological explanation, we depict the flow room delineated into three spatial regions, R1, R2 and R3. The region R1 consists of the standpipes and piping up to the tank. Thermal energy is provided in this region to the standpipes within the heated section. R2 consists of the tank (with large relative volume) and R3, consists of the downcomer piping, down to the bottom of the standpipe and including the mass-flow meter. The estimated FWHM values of the pressure drop and the void fraction (from similar time-dependent traces) are shown in Fig. 6 and Fig. 7. We noted that the pressure drop was measured across R1 to R2, while the void fraction was measured near the inlet into R2.

There is a coupling of both mass, momentum and energy transport into all three regions and their corresponding relative volumes. Under single phase buoyant circulation and initial sub-cooled boiling the loop retains a continuous single-phase but with increasing, convected enthalpy content. At the onset of flashing flow, near the top of R1, the temperature of the fluid is constrained to the local saturation temperature because of phase change.

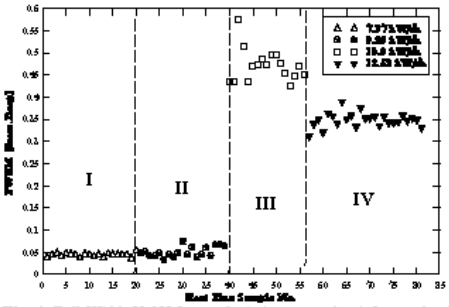

Fig. 6: Full Width Half Max analysis (pressure drop) for resolved peaks at different heat flux.

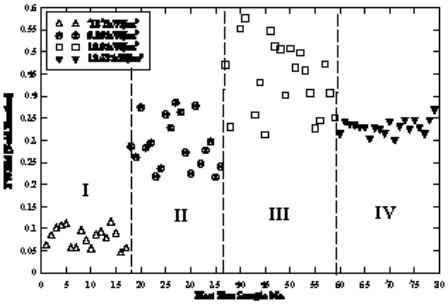

Fig. 7: Full Width Half Max analysis (void fraction) for resolved peaks at different heat flux.

However, the nearly thousand-fold reduction in density (vapor vs. liquid), there is increasing momentum 'injection' into the storage tank. The pressure trace at lower heat/heat flux input show mixed, quasi periodicity due to fluctuations in flashing and its interaction with the rest of the loop, R2 and R3. The mass-flow traces, measured at the bottom of R3, are correlated to mass flow but indicate increasingly periodic signature with increase in heat flux. That is, as heat flux increases and flashing flow persists, the momentum transfer into R2 and R3 increasingly are observed by mass flow measurement. Thus although pressure-based FWHM points are small in magnitude in Fig. 6, regions "I" and "II", the void-based FWHM are scattered and immediately larger in "II" in contrast to "I". At yet larger 17.81 kW and 20.84 kW heat input, both the momentum and heat input out of the standpipe and into the tank (R2) and downcomer (R3) regions establish peaked, periodic flow throughout the loop. This is characterized by regions "III" and "IV" in Figs.6 and 7. The relative capacity of the tank can only isolate the downcomer region for a short-time; thereafter flashing flow 'drives' periodicity in the entire loop. When circulation is thus established at

20.84 kW, the pressure drop is slightly smaller as correspondingly distribution of the void assumes a periodic flashing (interfacial) flow past the void sensor probe. We surmise that at 17.81 kW the flashing flow into the tank (R2) and thus the interfacial area fluctuation still experience heat transfer in the tank which is highly agitated, though we believe continued investigations are required to fully understand this behavior.

VI. CONCLUSION

Initial scaling analysis and experimental practices have shown that in single phase circulation, the test loop exhibits a linear system response. However, upon the onset of flashing flow from the standpipes into the storage tank, the thermalhydraulics becomes non-linear and transitions from one accommodated by the capacity (inertially and thermally) of the tank to increasingly flashing flow driven throughout the loop. We have experimentally investigated four power heating cases to further examine this non-linear behavior and quantify the performance bounds. Our results support an indication that the thermal and inertial capacity of the tank will prolong the eventual process of depletion of the liquid inventory via over-pressurization and relief valve expulsion of the RCCS liquid inventory. These findings were observed without degradation to the heat removal performance of the scaled RCCS test facility, though continued efforts must be made to fully understand this non-linear behavior.

ACKNOWLEDGMENTS

The authors wish to acknowledge the support of the US DOE for providing the funds for this research under the DOE/NEUP-09-202 "Experimental Studies of Reactor Cavity Cooling System".

NOMENCLATURE

DBA	Design Basis Accident
D-LOFC	Depressurized Loss of Forced Circulation
DOE	Department of Energy
EPCC	Equipment Protection Cooling Circuit
FWHM	Full Width at Half Maximum
LOFC	Loss of Forced Circulation
MHTGR	Modular High Temperature Gas-cooled Reactor
NEUP	Nuclear Energy University Program
RCCS	Reactor Cavity Cooling System
RPV	Reactor Pressure Vessel
UW	University of Wisconsin-Madison

REFERENCES

1. M. Aritomi, J.H. Chaing, and M. Mori, "Geysering in Parallel Boiling Channels", *Nuclear Engineering and Design*, 141, 111-121 (1993).
2. N. Watanabe, M.H. Subki, H. Kikura and M. Aritomi, "Thermal-hydraulic Instability Characteristics in Natural Circulation Parallel Boiling Channels Upflow System Under Low Pressure", *Proc. of 12th Int. Conf. on Nuclear Engineering (ICONE12)*, Vol. 1, 697-704, Arlington VA, USA (2004).
3. J.A. Boure, A.E., Bergles and L.S. Tong, "Review of Two Phase Flow Instability", *Nuclear Engineering and Design*, Vol. 25, 165-192 (1973).
4. R. ZBoray, W.J.M De Kruijf, T.H.J. Van der Hagen and R. Uddin "Investigating the Non-linear Dynamics of Natural Circulation, Boiling Two-Phase Flows", *Nuclear Technology*, 146, 244-256 (2004).
5. P. van Staden Martin, "Analysis of Effectiveness of Cavity Cooling System", *Proc. of 2nd International Topical Meeting on High Temperature Reactor Technology*, Paper 20, Beijing, China (2004)
6. Department of Energy (DOE), "Preliminary Safety Information Document for the Standard MHTGR", Technical Report, *HTGR-86-024*, Vol. 1, Amendment 13 (1992)
7. D. Lisowski, M. Albiston, A. Tokuhiro, M. Anderson and M. Corradini, "Experimental Studies of NGNP Reactor Cavity Cooling System with Water", *Proc. of 2011 Int. Congress of Advances in Nuclear Power Plants (ICAPP)*, Paper 11116, Nice, France (2011).
8. D. Lisowski, O. Omotowa, M. Anderson, A. Tokuhiro and M. Corradini, "Power Investigations on the Two-Phase Behavior and Instability in an Experimental Reactor Cavity Cooling System with Water" *Proc. Of NURETH 15*, Pisa, Italy, May 12 – 15 (2013).
9. M.M. El-Wakil, "*Nuclear Heat Transport*", 2nd ed. American Nuclear Society (1993).
10. F. Inada, M. Furuya and A. Yasuo, "Thermo-hydraulic instability of boiling natural circulation loop induced by flashing (analytical consideration)", *Nuclear Engineering and Design*, 200, 187-199 (2000).
11. S. Narayanan, B. Srinivas, S. Pushpavanam and S.M. Bhallamudi, "Non-linear dynamics of a two phase flow system in an evaporator: The effects of (i) a time varying pressure drop (ii) an axially varying heat flux" , *Nuclear Engineering and Design*, 178, 279-294 (1997).
12. G. Cammarata, A. Fichera and A. Pagano, "Non-linear Analysis of a Rectangular natural Circulation

Loop", *Int. Comm. Heat Mass Transfer*, 27, 1077-1089 (2000).
13. V. Jain, A.K. Nayak, P.K. Vijayan, D. Saha and R.K. Sinha, "Experimental investigation on the flow instability behavior of a multi-channel boiling natural circulation loop at low pressures", *Experimental Thermal and Fluid Science*, 34, 776-787 (2010).
14. M.H. Subki, M. Aritomi, N. Watanabe, H. Kikura and T. Iwamura, "Transport Mechanism of Thermohydraulic Instability in Natural Circulation Boiling Water Reactors during Start-up", *Journal of Nuclear Science and Technology*, 40, 918-931 (2003).
15. NGNP Technology Development Road Mapping Report: Reactor Cavity Cooling System", NGNP-CTF MTECH-TDRM-016, Westinghouse LLC (2008).
16. M. Ragheb, "Decay Heat Generation in Fission Reactors", Chapter 8, University of Illinois, Urbana-Champaign, (2013).